

# Implementation and evaluation of V/f and vector control in high-speed PMSM drives

G.L. Kruger

13039210

---

Dissertation submitted in partial fulfilment of the requirements for the degree *Magister  
Ingeneriae* in Computer and Electronic Engineering at the Potchefstroom campus of the  
North-West University

---

Supervisor: Prof. S.R. Holm

Assistant Supervisor: Mr. A.J. Grobler

May 2011

## Akademiese Administrasie

### PLEGTIGE VERKLARING

#### Plegtige verklaring deur student

Hiermee verklaar ek \_\_\_\_\_ die ondergetekende dat die skripsie/  
verhandeling/proefskrif getitel,

\_\_\_\_\_

wat ek aan die Noordwes-Universiteit ter voldoening/gedeeltelike voldoening aan die vereiste van die \_\_\_\_\_-graad, hiermee inhandig, my eie werk is, dit volgens die vereistes taalversorg is en dat dit nie reeds aan 'n ander universiteit ingehandig is nie.

Ek verstaan en aanvaar dat die eksemplare wat vir eksaminering ingehandig word, die eiendom van die universiteit is.

Handtekening van student \_\_\_\_\_ Universiteitsnommer \_\_\_\_\_

Geteken te \_\_\_\_\_ hierdie \_\_\_\_\_ dag van \_\_\_\_\_ 20.....

Verklaar voor my hierdie \_\_\_\_\_ dag van \_\_\_\_\_ 20.....

Kommissaris van Ede: \_\_\_\_\_

\_\_\_\_\_

#### Plegtige verklaring deur studieleier/promotor/navorsingsdirekteur

Hiermee verklaar ondergetekende:

- 1.1 dat die genoemde student 'n goedgekeurde module vir die betrokke kwalifikasie bygewoon het en die werk van die module uitgevoer het of werk gedoen het wat deur die Senaat goedgekeur is;
- 1.2 dat die student aan die minimum duur van studie voldoen soos voorgeskryf in die jaarboek;
- 1.3 dat hy/sy derhalwe gemagtig word om sy/haar skripsie verhandeling/proefskrif in te handig;
- 1.4 dat die registrasie/wysiging van titel goedgekeur is;
- 1.5 dat die aanwysing/wysiging van eksaminatore goedgekeur is en
- 1.6 ander voorskrifte soos vervat in die Handleiding vir nagraadse studie nagekom is.

Handtekening Studieleier/Promotor: \_\_\_\_\_ Datum: \_\_\_\_\_

Handtekening Navorsingsdirekteur: \_\_\_\_\_ Datum: \_\_\_\_\_

\_\_\_\_\_

# Abstract

**Keywords:** Permanent-magnet synchronous machine (PMSM), vector control, volts-per-hertz (V/f) control, voltage source inverter, speed observer, dead-time compensation

The McTronX research group, at the Potchefstroom campus of the North-West University, has been researching Active Magnetic Bearings (AMBs). A fully suspended, flywheel energy storage system (FESS) has been developed. Due to excessive unbalance on the rotor, the motor drive could not be tested up to its rated speed. In the interim, until the rotor can be balanced and other rotor dynamic effects have been investigated, the group decided that the existing drive control should be improved and tested on a high-speed permanent magnet synchronous motor (PMSM), using normal roller element bearings.

In order to test the motor control a second (identical) PMSM, mechanically coupled to the former, operates in generator mode which serves as the torque load. Two different control algorithms, namely V/f and vector control, are designed and implemented on a rapid control prototyping system, i.e. dSPACE<sup>®</sup>. The V/f control is an open-loop, position sensorless technique, whilst the vector controller makes use of a position sensor.

From the design and implementation it became clear that the vector control is more robust, in the sense that it is less sensitive on parameter variations and disturbances. It can start up reliably even under full load conditions.

The V/f control is an attractive alternative to the vector control, especially in AMB systems, where it may be difficult to mount the position sensor, has to operate in a hazardous environment not suited to the sensor or could degrade the reliability of the AMB system. The cost of the position sensor is not really a concern compared to the cost of an AMB system. The V/f control is more suited to fan and pump applications, which has a low dynamic requirement. The V/f control has high startup currents and is not recommended for applications requiring a high starting torque or fast acceleration during operation.

The inverter, which drives the PMSM, also had to be developed. With regard to the motor control, the effects of inverter non-idealities had to be accounted, especially for the V/f control.

The implemented control algorithms were tested up to 20krpm. Discrepancies between the expected and actual results are discussed. Overall, the controllers performed as desired. Generally, the project goals have been reached satisfactorily.

---

# Acknowledgements

I would like to thank my advisor, Prof. Robert Holm, for his encouragement, sober advice and the stories about aeroplanes.

Thank you to Mr. André Grobler, my assistant-supervisor, for his friendly nature and helping me with winding of one of the PMSM stators. Through trial and error it took us weeks, but by now we're pro machine winders and could do it in a day, literally!

Without the physical high-speed PMSMs (despite the faults), I would not have been able to test the controllers, hence, thank you to Dr. Eugén Ranft and Mr. Cornelius Ranft for the mechanical design and construction of the PMSMs. Also, thank you to Mr. Dewald Herbst for the layout of the sensor and interface boards.

I would also like to thank M-Tech Industrial, THRIP and the North-West University for funding this project and allowing me to further my studies.

Thank you to *all* of the other McTronX research group members for their interest in the project and the coffee break talks.

Last, but not least, I would like to thank my parents and family for their encouragement and support.

---

*“<sup>2</sup>Aan U, o God, kom ’n lofsang toe in Sion: geloftes moet betaal word <sup>3</sup>aan U wat die gebed verhoor. Na U toe sal alle mense kom <sup>4</sup>om hulle skuld te bely. Ons sondes het ons ingehaal, maar U maak ons daarvan vry.” Psalm 65: 2-4*

---



# Contents

<b>1</b>	<b>Introduction</b>	<b>1</b>
1.1	Background . . . . .	1
1.1.1	General background of electric machine control . . . . .	1
1.1.2	Background specifically leading to this project . . . . .	2
1.2	Problem Statement . . . . .	3
1.3	Issues to be addressed . . . . .	3
1.4	Research methodology . . . . .	4
1.4.1	Literature study . . . . .	4
1.4.2	PMSM modelling . . . . .	4
1.4.3	Control system modelling . . . . .	4
1.4.4	Hardware specification and procurement . . . . .	5
1.4.5	System integration . . . . .	5
1.4.6	Control implementation and evaluation . . . . .	5
1.5	Dissertation overview . . . . .	5
<b>2</b>	<b>Literature study</b>	<b>7</b>
2.1	Background . . . . .	7
2.1.1	Machine classification and comparison . . . . .	7
2.1.2	Applications . . . . .	9
2.2	PMSM drive modelling . . . . .	9
2.2.1	PMSM models available in the literature . . . . .	9
2.2.2	Mathematical model of the PMSM . . . . .	10
2.2.2.1	Stationary three-phase flux linkage . . . . .	11
2.2.2.2	Three- to two-phase coordinate transformation . . . . .	13

---

2.2.2.3	Stationary to rotating coordinate transformation . . . . .	14
2.2.2.4	Voltage model of the PMSM in the rotor reference frame . . . . .	15
2.2.2.5	Electromagnetic torque . . . . .	17
2.2.2.6	Rotor dynamic equation of motion . . . . .	19
2.2.2.7	State-space model . . . . .	19
2.2.2.8	Space vectors . . . . .	20
2.2.3	PMSM parameter identification . . . . .	20
2.2.3.1	PMSM circuit parameters from terminal measurements . . . . .	20
2.2.3.2	Least squares parameter identification of the PMSM . . . . .	21
2.2.4	Inverter modelling . . . . .	23
2.2.4.1	Inverter control . . . . .	24
2.2.4.2	Inverter non-ideality compensation . . . . .	28
2.2.4.3	Determination of phase-to-neutral voltages . . . . .	31
2.3	PMSM control strategies . . . . .	32
2.3.1	V/f Control . . . . .	32
2.3.1.1	Principle of operation . . . . .	32
2.3.1.2	Stabilization . . . . .	33
2.3.1.3	Efficiency . . . . .	34
2.3.2	Vector control . . . . .	34
2.3.2.1	Principle of operation . . . . .	34
2.3.2.2	Current control loop . . . . .	35
2.3.2.3	Different control objectives . . . . .	36
2.3.2.4	Field weakening . . . . .	37
2.3.3	Sensorless vector control . . . . .	37
2.3.4	Direct torque control . . . . .	40
2.3.4.1	Principle of operation . . . . .	40
2.3.4.2	DTC control features . . . . .	41
2.4	Summary . . . . .	41

---

<b>3</b>	<b>Controller design</b>	<b>43</b>
3.1	Design preliminaries	43
3.1.1	PMSM parameters	43
3.1.2	PMSM simulation model	44
3.2	Vector control	44
3.2.1	Current control	45
3.2.1.1	Linearized model via feed-forward terms	45
3.2.1.2	Digital control design preliminaries	49
3.2.1.3	Current control design	52
3.2.1.4	Current control simulation	56
3.2.2	Speed signal extraction	61
3.2.2.1	Numerical differentiation	61
3.2.2.2	Speed observer	63
3.2.2.3	Modified speed observer	66
3.2.3	Speed control	71
3.2.3.1	Speed control design	71
3.2.3.2	Speed reference generator	74
3.2.3.3	Simulation model	75
3.2.3.4	Simulation results	77
3.2.4	Load torque control	81
3.3	V/f Control	84
3.3.1	Constant flux linkage control	84
3.3.2	Linearized PMSM model	86
3.3.3	Stabilization	89
3.3.3.1	Unstable open-loop operation	89
3.3.3.2	Reduced order model	89
3.3.3.3	Stabilization via synchronous frequency modulation	94
3.3.3.4	Low speed boost voltage	98
3.3.3.5	Verification of stabilization with synchronous frequency modulation	99
3.3.4	High efficiency control	100

3.3.5	Current measurement decoupling . . . . .	102
3.3.6	V/f control simulation . . . . .	103
3.3.6.1	Simulation model . . . . .	103
3.3.6.2	Simulation results . . . . .	107
3.4	Inverter non-ideality compensation . . . . .	113
3.4.1	DC bus disturbance rejection . . . . .	113
3.4.1.1	Introduction . . . . .	113
3.4.1.2	DC bus rectifier and capacitor model . . . . .	114
3.4.1.3	Control simulation models with disturbance rejection . . . . .	115
3.4.1.4	Disturbance rejection simulation response . . . . .	117
3.4.2	Dead-time compensation . . . . .	120
3.4.2.1	Dead-time average value model . . . . .	120
3.4.2.2	Control models with dead-time compensation . . . . .	120
3.4.2.3	Dead-time compensation simulation results . . . . .	122
3.4.3	Duty cycle quantization noise suppression . . . . .	124
3.4.3.1	Introduction . . . . .	124
3.4.3.2	Control models with quantization noise suppression . . . . .	124
3.4.3.3	Quantization noise suppression simulation results . . . . .	125
3.5	Summary . . . . .	126
<b>4</b>	<b>Implementation issues</b>	<b>129</b>
4.1	Drive layout . . . . .	129
4.2	Specification of drive components . . . . .	131
4.2.1	IGBT Voltage rating . . . . .	131
4.2.2	IGBT Current rating . . . . .	131
4.2.3	Inverter thermal verification . . . . .	132
4.2.4	Rectifier design . . . . .	135
4.2.4.1	Filter inductance design . . . . .	136
4.2.4.2	DC bus capacitor design . . . . .	140
4.2.4.3	Three-phase diode bridge . . . . .	142
4.3	Isolation and protection . . . . .	143

4.3.1	Three-phase transformer . . . . .	143
4.3.2	DC bus inrush current limiting . . . . .	143
4.3.3	Inverter dead-time selection . . . . .	144
4.3.4	Inverter snubber capacitors . . . . .	144
4.3.5	Inverter current limiting . . . . .	145
4.3.6	DC bus overvoltage protection . . . . .	147
4.3.7	Controller protection from sensor signals . . . . .	147
4.4	Drive sensors . . . . .	148
4.4.1	Voltage and current sensors . . . . .	148
4.4.2	Temperature sensors . . . . .	149
4.4.3	Position sensor . . . . .	149
4.4.3.1	Sensor mounting . . . . .	150
4.4.3.2	Communication to controller . . . . .	150
4.4.3.3	Offset zeroing . . . . .	151
4.5	EMI . . . . .	151
4.5.1	Shielding and filtering . . . . .	151
4.5.2	Synchronized sampling of sensor signals . . . . .	153
4.6	Computation improvements . . . . .	155
4.7	Summary . . . . .	155
<b>5</b>	<b>Controller results</b>	<b>157</b>
5.1	PMSM drive protection . . . . .	157
5.1.1	Inrush current limiting . . . . .	157
5.1.2	Inverter current limiting . . . . .	158
5.1.3	Inverter dead-time . . . . .	160
5.2	Vector Control . . . . .	161
5.2.1	Current control results . . . . .	161
5.2.2	Speed control results . . . . .	164
5.2.2.1	Speed control ripple . . . . .	164
5.2.2.2	Speed control ramp response . . . . .	166
5.2.2.3	Speed control frequency response . . . . .	166

5.3	V/f Control . . . . .	167
5.3.1	Speed control ramp response . . . . .	167
5.3.2	Speed control frequency response . . . . .	169
5.4	Control efficiency . . . . .	170
5.5	Control evaluation . . . . .	171
5.6	Summary . . . . .	172
<b>6</b>	<b>Conclusion and recommendations</b>	<b>175</b>
6.1	Conclusions . . . . .	175
6.1.1	Vector control . . . . .	175
6.1.2	V/f control . . . . .	175
6.1.3	Design methodology . . . . .	175
6.2	Recommendations . . . . .	176
6.2.1	Sensorless vector control . . . . .	176
6.2.2	Unification of V/f and sensorless vector control . . . . .	176
6.2.3	Mechanical vibration and bearing losses . . . . .	177
6.2.4	Drive recommendations . . . . .	178
6.2.4.1	Sensor and interface board redesign . . . . .	178
6.2.4.2	Brake circuit . . . . .	178
6.2.4.3	Three-phase transformer . . . . .	179
6.2.4.4	Influence of PWM switching frequency on total drive losses . . . . .	179
6.3	Closure . . . . .	179
	<b>References</b>	<b>180</b>
<b>A</b>	<b>Parameter identification</b>	<b>189</b>
A.1	PMSM circuit parameters from terminal measurements . . . . .	189
A.2	PMSM mechanical parameters from calculation . . . . .	190
A.3	Least squares parameter identification of the PMSM . . . . .	191
<b>B</b>	<b>Detail mechanical drawings</b>	<b>195</b>
B.1	Detail rotor assembly . . . . .	195
B.2	Detail stator assembly . . . . .	195
<b>C</b>	<b>Files on CD</b>	<b>199</b>

# List of Figures

2.1	Electrical Machine Categories (Combination of [1, 2]) . . . . .	8
2.2	Conceptual PMSM drive. . . . .	9
2.3	Cross-sectional view of PMSM. . . . .	11
2.4	Three-phase IGBT inverter. . . . .	24
2.5	Voltage output with sine-triangle modulation. . . . .	25
2.6	Voltage output with hysteresis modulation. . . . .	27
2.7	Voltage space vectors [3]. . . . .	28
2.8	DC bus voltage disturbance rejection. . . . .	29
2.9	Dead-time effect. . . . .	30
2.10	Current ripple due to dead-time distortion. . . . .	31
2.11	Open loop V/f control. . . . .	33
2.12	Vector control. . . . .	35
2.13	Sensorless vector control [4]. . . . .	38
2.14	Direct torque and flux control [5] . . . . .	41
3.1	PMSM simulation model (motor). . . . .	45
3.2	PMSM simulation model sub-domains. . . . .	46
3.3	dq0 transformations. . . . .	47
3.4	PMSM model user-interface. . . . .	48
3.5	Measured current vs. actual current due to sampler delay. . . . .	49
3.6	Zero-order hold approximation error. . . . .	52
3.7	Current control block diagram. . . . .	53
3.8	Bode diagram of current control open-loop gain. . . . .	54
3.9	Bode diagram of current control closed-loop gain. . . . .	55

3.10 Current control step response. . . . .	56
3.11 Current control model interfaced with PMSM model. . . . .	56
3.12 Current control simulation model. . . . .	57
3.13 Feed-forward linearization terms. . . . .	57
3.14 Measurement delay decoupling. . . . .	58
3.15 PI control model with anti-windup. . . . .	58
3.16 Third harmonic injection term. . . . .	59
3.17 Inverter simulation model. . . . .	60
3.18 Current step response with performance measures. . . . .	61
3.19 Speed from position via backward difference. . . . .	62
3.20 Numerical differentiation algorithm response. . . . .	63
3.21 Bode diagram for observer speed transfer function. . . . .	65
3.22 Speed and load torque observer. . . . .	66
3.23 Speed observer step response. . . . .	67
3.24 Modified speed and load torque observer. . . . .	67
3.25 Modified speed observer step response. . . . .	69
3.26 Modified speed observer Bode diagram. . . . .	69
3.27 Observer frequency response, $\alpha = 0.65$ . . . . .	70
3.28 Speed control block diagram. . . . .	71
3.29 Speed control stability margins. . . . .	72
3.30 Speed control closed-loop Bode diagram. . . . .	73
3.31 Closed-loop speed-control step response. . . . .	73
3.32 Speed reference generator for vector control. . . . .	75
3.33 Top level of speed control simulation model. . . . .	75
3.34 Combined speed and current control. . . . .	76
3.35 Measurement decoupling, speed observer and voltage feed-forward linearization. . . . .	77
3.36 PI speed controller. . . . .	77
3.37 Speed control step response, $\alpha = 1$ . . . . .	78
3.38 Speed control step response with underestimated motor parameters and input, $\alpha = 0.65$ . . . . .	78



3.39 Speed control step response with overestimated motor parameters and input, $\alpha = 1.35$ . . . . .	79
3.40 Speed ramp and torque load step response. . . . .	79
3.41 Current response to speed ramp and load torque step without measurement de- coupling and feed-forward linearization. . . . .	80
3.42 Response with quantizer included. . . . .	80
3.43 Speed response comparison with different modulation schemes. . . . .	81
3.44 PMSM simulation model (generator). . . . .	82
3.45 Motor and generator interconnection. . . . .	83
3.46 PMSM generator control. . . . .	83
3.47 Motor assist soft-switching. . . . .	84
3.48 PMSM variables in the synchronous reference frame. . . . .	85
3.49 Root loci of open-loop V/f control. . . . .	89
3.50 Block diagram of linearized mechanical dynamics. . . . .	90
3.51 Bode diagram of exact and reduced order model for $\omega_{r0} = 2\pi 50 \text{ rad.s}^{-1}$ . . . . .	93
3.52 Bode diagram of exact and reduced order model for $\omega_{r0} = 2\pi 60 \text{ rad.s}^{-1}$ . . . . .	94
3.53 Rearranged open-loop V/f control block diagram. . . . .	94
3.54 Dependence of electromechanical spring constant ( $K_{e0}$ ) on operating point. . . . .	95
3.55 Compensation of speed perturbation in the feedback path. . . . .	95
3.56 Simplified block diagram of open-loop V/f control with stabilization loop. . . . .	97
3.57 Damping ratio as a function of operating speed. . . . .	98
3.58 Root loci of open-loop V/f control with stabilization loop ( $k_c = \frac{10}{ \omega_{r0}^* }$ ). . . . .	100
3.59 Zero reactive power control loop. . . . .	102
3.60 Top level of V/f control simulation model. . . . .	103
3.61 Speed reference generator for V/f control. . . . .	104
3.62 Lower level of V/f control simulation model. . . . .	104
3.63 V/f control stabilization from power perturbation . . . . .	105
3.64 Calculation of resultant terminal voltage. . . . .	106
3.65 V/f control high efficiency loop implementation. . . . .	106
3.66 Calculation of enable signals of the different control loops. . . . .	107
3.67 V/f control response with and without stabilization loop. . . . .	108

3.68 Startup response with and without boost voltage. . . . .	108
3.69 Torque load step response, at $\omega_{r0} = 20$ krpm, with and without the high efficiency loop. . . . .	109
3.70 Response with and without current measurement decoupling. . . . .	109
3.71 Current response with mismatch in controller's permanent magnet flux linkage. .	110
3.72 Current response with mismatch in controller's stator inductance. . . . .	111
3.73 Current response with mismatch in controller's stator resistance. . . . .	112
3.74 Open-loop feed-forward control of phase current. . . . .	112
3.75 Feed-forward control of phase current with positive feedback compensation of resistive voltage drop. . . . .	113
3.76 Current control with positive feedback. . . . .	113
3.77 Rectifier and bus capacitor model. . . . .	114
3.78 V/f control with DC bus disturbance rejection. . . . .	115
3.79 Voltage reference to duty cycle conversion. . . . .	115
3.80 Average value inverter model. . . . .	116
3.81 Current harmonic suppression. . . . .	116
3.82 Vector control with DC bus disturbance rejection. . . . .	117
3.83 Vector control response without DC bus disturbance rejection. . . . .	118
3.84 DC bus response to vector control without disturbance rejection. . . . .	119
3.85 V/f control response without DC bus disturbance rejection. . . . .	119
3.86 Large scale V/f control response without DC bus disturbance rejection. . . . .	120
3.87 Dead-time average value model. . . . .	120
3.88 Dead-time average value model included with inverter. . . . .	121
3.89 Dead-time compensation. . . . .	121
3.90 Vector control model with dead-time compensation. . . . .	122
3.91 V/f control model with dead-time compensation. . . . .	122
3.92 Vector control with dead-time compensation. . . . .	123
3.93 V/f control with dead-time compensation . . . . .	123
3.94 Delta-sigma modulator. . . . .	125
3.95 Current response to vector control with quantization noise suppression. . . . .	126
3.96 V/f control response with quantization noise suppression. . . . .	126

4.1	Functional relationship block diagram. . . . .	130
4.2	Inverter thermal model. . . . .	132
4.3	Three-phase rectifier. . . . .	136
4.4	Three-phase diode bridge rectifier forward characteristic. . . . .	142
4.5	Anti-aliasing filter and zener voltage clamp circuit. . . . .	148
4.6	Non-contact, angular position sensor [6]. . . . .	150
4.7	Functional diagram of position sensor interfaced with controller. . . . .	151
4.8	Common mode current due to parasitic capacitance. . . . .	152
4.9	Conversion of common mode to differential mode signals. . . . .	153
4.10	IGBT gate and synchronization clock. . . . .	154
5.1	Charging of DC bus capacitors with inrush current limiting. . . . .	158
5.2	Over current protection test circuit. . . . .	159
5.3	Overcurrent protection measurement. . . . .	160
5.4	Inverter dead-time protection verification. . . . .	161
5.5	Current control step response. . . . .	162
5.6	Bode diagram of closed-loop current control closed-loop transfer characteristic. . . . .	163
5.7	Bode diagram of closed-loop current control open-loop transfer characteristic. . . . .	163
5.8	Reduced gain and bandwidth of current control open-loop transfer characteristic, due to dead-time effect. . . . .	164
5.9	Rotor response to small motoring torque (0.07 Nm). . . . .	165
5.10	Spectral comparison of speed controller results with high (designed) and low gain. . . . .	166
5.11	Speed ramp response of vector control with 1 N.m torque load step. . . . .	167
5.12	Bode diagram of closed-loop speed controller with designed gain. . . . .	168
5.13	Bode diagram of speed control with reduced gain. . . . .	168
5.14	Speed ramp response of V/f control with 1 N.m torque load step. . . . .	169
5.15	Bode diagram of V/f speed control. . . . .	170
5.16	Efficiency comparison between vector and V/f control with 50 % rated load torque. . . . .	171
A.1	PMSM excitation for least squares parameter identification. . . . .	192
B.1	Detail rotor assembly [7]. . . . .	196
B.2	Detail machine assembly [7]. . . . .	197



# List of Tables

2.1	Inverter switching state vectors. . . . .	24
3.1	PMSM parameters . . . . .	44
4.1	Summary of thermal verification. . . . .	135
4.2	T400-26 core parameters. . . . .	138
4.3	Electrolytic capacitor parameters. . . . .	141
A.1	Line-Line measurements for PMSM #A. . . . .	189
A.2	Line-Line measurements for PMSM #B. . . . .	189



# Nomenclature

ADC	Analogue-to-Digital Converter
DSP	Digital Signal Processor
DTC	Direct Torque Control or Dead-time Compensation
EKF	Extended Kalman Filter
FOC	Field Oriented Control
PD controller	Proportional and derivative controller
PI Controller	Proportional and integral controller
V/f Control	Volt/frequency Control
VSI	Voltage source inverter
ZOH	Zero-Order Hold
AC	Alternating Current
AMB	Active Magnetic Bearing
BDCM	Brushless DC Motor
CAS	Computer Algebra System
DC	Direct Current
DQ model	Direct-Quadrature model
dq0 transformation	direct-quadrature-zero transformation
emf	Electromotive force [V]
FE	Finite Element
FESS	Flywheel Energy Storage System
IGBT	Insulated Gate Bipolar Transistor

---

IM	Induction Machine
mmf	Magnetomotive force [A.turns]
PM	Permanent Magnet
PMSM	Permanent Magnet Synchronous Machine
rms	root-mean-square
rpm	revolutions per minute
SM	Synchronous Machine
SVM	Space vector modulation
$i_d$	Instantaneous d-axis current [A]
$\mathbf{i}_{dq0}$	Instantaneous current vector in dq0 reference frame [A]
$\mathbf{v}_{dq0}$	Instantaneous voltage vector in dq0 reference frame [V]
$\omega_m$	Rotor mechanical frequency [rad/s]
$\omega_r$	Rotor electrical frequency [rad/s]
$\omega_s$	Stator electrical frequency [rad/s]
$i_a, i_b, i_c$	Instantaneous a, b and c phase current [A]
$i_q$	Instantaneous q-axis current [A]
$P$	Power [W]
$v_a, v_b, v_c$	Instantaneous a, b and c phase voltage [V]
$v_{DC}$	Instantaneous DC bus voltage [V]
$v_d$	Instantaneous d-axis voltage [V]
$v_q$	Instantaneous q-axis voltage [V]
$T_c$	Inverter switching/carrier period [s]
$T_s$	Controller sample period [s]
$\lambda_p$	Stator flux linkage due to rotor permanent magnet [Wb.turns]
$L_s$	Stator phase inductance [H]
$R_s$	Stator phase resistance [ $\Omega$ ]
$z_p$	Number of pole pairs

---



---

$B$	Viscous friction loss [N.m.s/rad]
$J$	Rotor polar moment of inertia [N.m.s <sup>2</sup> /rad]



# Chapter 1

## Introduction

### 1.1 Background

#### 1.1.1 General background of electric machine control

In the not so recent past, DC machines were the main contender for variable speed control whilst AC machines were mainly used for constant speed applications because they were run from constant frequency supplies [1].

The development of semiconductor technology for the use of power electronics enhanced the available control techniques for DC and AC machines. Not only did it enhance the available control techniques but new control techniques were realised.

The control signals for the semiconductor switches were generated with logic circuitry. The advent of micro-controllers eased the development for control circuitry by increasing flexibility and decreased the complexity by decreasing component count<sup>1</sup>.

Researchers also realised that the electrical machines could now be designed differently to suit new applications and that they needn't worry if it was possible to control these machines. The control effectivity was however another matter, but semiconductor performance and the attainable control complexity increased by leaps and bounds.

Semiconductor technology played an important role, because the electrical quantities that were fed to the machine could be better controlled. The characteristics of the machine itself have also improved, due to research in the materials from which the machine is constructed. Permanent magnets made from rare earth materials, with high coercivity<sup>2</sup> and residual magnetism gives the permanent magnet synchronous machine better characteristics than induction and brushed DC machines [8].

Despite the higher efficiency of variable speed machines, Monajemy asserts that the variable speed machine is still being underutilized because its operational boundary is determined in the

---

<sup>1</sup>Although it may be argued that the complexity has only shifted from hardware to software.

<sup>2</sup>Thereby decreasing the chance of possible demagnetisation by motor control currents.

same manner as for constant speed machines. He goes forth to present the concept of constant power loss as the correct operational boundary, which results in higher utilisation [9].

The permanent magnet synchronous machine (PMSM) is replacing other types of machines in some applications. When compared to direct current, induction and synchronous machines, the PMSM has higher efficiency, reliability and lower maintenance. Its operational performance, such as higher torque to inertia ratio, less torque ripple and higher power factor is also superior to other types of machines [10, 2]. One drawback of using PMSMs is its higher cost, mainly due to rare earth magnets used in its construction [2]. In time, a return on investment is made due to energy (cost) savings due to higher efficiency of the PMSM. It is expected that as with other technologies, the cost will come down as alternative materials are discovered, production methods are refined and competition between manufacturers ensue.

The good characteristics of the PMSM has ensured many applications, which include electric vehicles [11, 12], machine tool spindles, starter/generator units [13], robotics, aerospace actuators [8], electric wheelchairs [14], fan-type applications [4] and turbo compressors [15].

Despite the good machine characteristics of the PMSM, its usefulness relies to a great extent on the performance of the system which it is controlled by. There are mainly two control strategies for the PMSM (which has been adopted from the induction machine control theory), namely  $V/f$ <sup>3</sup> and Vector control.  $V/f$  is an open loop control method, whilst Vector control is a form of closed loop control. Various factors influence the performance and cost of these two control strategies, such as: the use of a position encoder or implementing a sensorless control technique, computational ability of the controller required, quickness of response, attainable stability and operational efficiency of the machine.

### 1.1.2 Background specifically leading to this project

The need to implement and test the control of a high-speed surface mount PMSM at the *School of Electrical, Electronic and Computer Engineering, North-West University* has been identified based on the results of a previous project [16].

The project focused on the development of a three-phase power amplifier for a surface mount PMSM used in a high-speed flywheel energy storage system (FESS) and not on the control algorithm of the PMSM. In order to decrease bearing and windage loss, the flywheel was suspended in a depressurised enclosure by active magnetic bearings (AMB)<sup>4</sup>. Since the load of the machine required low dynamic response, the open-loop  $V/f$  control was deemed sufficient.

Unfortunately, the flywheel could not be spun to its designed maximum speed of 30 000 rpm due to excessive rotor unbalance which exceeded the specified requirements of the AMBs. The AMB control currents are driven into saturation to counter the unbalance force. Amongst other things, this non-linearity causes the AMBs to become unstable after a certain rotational speed has been exceeded.

---

<sup>3</sup>Read as:  $V$  over  $f$ .

<sup>4</sup>The AMB control was the focus of a different project [17].

Besides the instability due to the active magnetic bearings, a V/f controlled PMSM becomes unstable by itself after a certain rotational speed, by losing synchronism with the drive control currents. A stabilisation loop was implemented in the control, but could not be validated at high speed due to the aforementioned impediment<sup>5</sup>. The electromagnetic design of the PMSM could also not be verified at high speed. Hence, the need to test the control and electromagnetic design of a high-speed surface mount PMSM similar to the one used in the FESS has been identified. Normal roller element bearings are used instead of AMBs.

Since the previous requirement is not a full justification for a project in itself, there was decided to implement and compare more than one control strategy to enlarge the project scope. By doing so the previously stated requirement will inherently be met whilst aiding the beneficiaries and the research community in general, in the design of PMSM drive control.

## 1.2 Problem Statement

The purpose of this project is to implement V/f and vector control on a high-speed surface mount permanent magnet synchronous machine drive and compare the control strategies according to various performance criteria, on a wide operating range of the PMSM. In order to characterize the operating range a second PMSM is mechanically coupled to the former, which needs to be controlled such that it serves as a variable torque load.

## 1.3 Issues to be addressed

The following project objectives need to be reached in order to reach the final project goal:

- Symbolic models of permanent magnet synchronous machine, of varying complexity, need to be investigated.
- Accurate model parameter identification of the PMSM used.
- Decide on and justify certain performance criteria.
- Procurement of all the necessary hardware.
- Development or procurement of a 3-phase power amplifier (30 A, 350 V, 20 kHz) with fault condition monitoring.
- Implementation of V/f control.
- Implementation of Vector control, using a position encoder for feedback.

---

<sup>5</sup>The author should note that from personal experience from run-up tests of the FESS, the implementation of the stabilisation loop was incomplete due to observed loss of synchronism during some of the tests.

- Modification of V/f and the Vector control such that the second PMSM machine which is mechanically coupled to the first can function as an adjustable torque load.
- The PMSMs have to be controlled up to 30 krpm at 8 kW in parallel (motoring or generating mode).
- Evaluate the measured system performance over a wide operating range, according to the selected criteria and compare it to the simulated system response.

## 1.4 Research methodology

### 1.4.1 Literature study

The design and implementation details of the various control strategies need to be researched in the form of a literature study. The first objective of the literature study is to identify various PMSM models on which the designed controllers can be tested via simulation before hardware implementation.

A second outcome of the literature study is to identify criteria for the comparison of the PMSM's differing performance due to the different control strategies.

### 1.4.2 PMSM modelling

The mathematical models of the PMSM which has been identified during the literature study needs to be implemented in a simulation package, such as The Mathwork's Simulink<sup>®</sup>. Models with lesser complexity is used since this saves simulation and development time, but more correct/complex models will also be implemented to validate simulation results and clarify uncertainties.

### 1.4.3 Control system modelling

Once different models have been implemented in Simulink<sup>®</sup>, these models can be used to test the designed controller, relying again on the information gathered during the literature study. Scalar (V/f) and Vector control is implemented. Special attention is then given further to sensorless vector control, flux weakening operation, stability and machine control criteria such as unity power factor operation, maximum efficiency operation and maximum torque control. The conditions required for the second PMSM to function as a load will also be clarified during this phase.

#### 1.4.4 Hardware specification and procurement

The modelled control systems are implemented on physical PMSMs. High-speed surface mount permanent magnet synchronous machines has been development at the *School of Electrical, Electronic and Computer Engineering, North-West University*.

The specification for the power electronics needed in the drive needs to be calculated, after which 3-phase IGBT modules meeting the specification will be procured. A power amplifier, consisting of the IGBT modules, driver circuitry and current sensors are integrated.

A signal conditioning circuit for all the sensors are developed, so that it can be safely connected to the dSPACE<sup>®</sup> control boards. Sensors as required for the system control and system performance evaluation is procured.

A cooling solution for the system is procured and installed, as experience has shown that improper cooling of the system may hamper its performance and thus the range of obtainable operation. Cooling of the system is also important from a safety point of view, since the material strength is dependent on temperature, which becomes a concern when the machine is operating at high speed.

#### 1.4.5 System integration

The PMSMs, power electronics, sensors, controller and cooling of the system are integrated. Part of the integration procedure is the modification of the designed control models in Matlab/Simulink<sup>®</sup>, such that it is implemented on the dSPACE<sup>®</sup> controller. The sensor calibration also forms part of the integration phase.

#### 1.4.6 Control implementation and evaluation

Due to noise and idealized control models, a system never performs exactly as simulated, which is why validation on a real system is performed. The different control strategies will be evaluated by specifying different control criteria and using the second PMSM as a virtual load. The measured system response will be used to calculate the performance criteria.

### 1.5 Dissertation overview

An overview of the chapters to follow

**Chapter2: Literature study** The literature study is a compilation of the relevant topics required as background for the design the PMSM controller. This includes: a presentation of the mathematical model of the PMSM and inverter, and methods of determining the PMSM model parameters. The operational principle of the different types of PMSM controllers is also presented.

**Chapter 3: Controller design** The detail design of the vector and V/f controllers are presented in this chapter. The designed controllers are verified via simulation.

**Chapter 4: Implementation issues** Practical implementation issues, such as integration of the drive sub-assemblies, inverter hardware design, controller protection and control algorithm optimisation is presented in this chapter.

**Chapter 5: Controller results** The implemented controller results are presented in this chapter. For comparison, the same type of controller tests is performed as during the simulation. The comparison of the measured controller response of the actual system to the simulation results is viewed as the validation of the controllers.

**Chapter 6: Conclusion and recommendations** Based on the controller results, a conclusion is drawn with regard to the efficacy of each of the designed controllers.



## Chapter 2

# Literature study

The aim of the literature study, for this project, is to become acquainted with all the relevant aspects of PMSM control, in order to be able to design and implement the vector and V/f controllers. These aspects consist out of the background theory of the different types of electrical machines, modelling of the PMSM and inverter and the principle of operation of the different type of controllers.

### 2.1 Background

#### 2.1.1 Machine classification and comparison

A classification of electric machines is given in figure 2.1. Further comparison between the application characteristics of the brushless DC motor (BDCM) and PMSM is done in [2]. Both machines require an AC source on the stator to produce a torque. The main difference is that the PMSM back electromotive force (emf) is sinusoidal whilst the BDCM back emf is trapezoidal. The lower harmonics in a sinusoidal wave implies lower harmonic losses which favours the PMSM at higher speeds.

Advantages of PMSMs over other types of machines are [10, 2]:

- Higher torque to inertia ratio than the induction machine (IM) and the wound-rotor synchronous machine (SM).
- Lower maintenance and higher reliability than brushed DC machines and SMs, because of the absence of brushes and slip rings, respectively.
- Higher efficiency than IMs and SMs, because of no copper losses on the rotor.
- Do not require magnetizing current on rotor for its functional operation, implying decreased complexity.

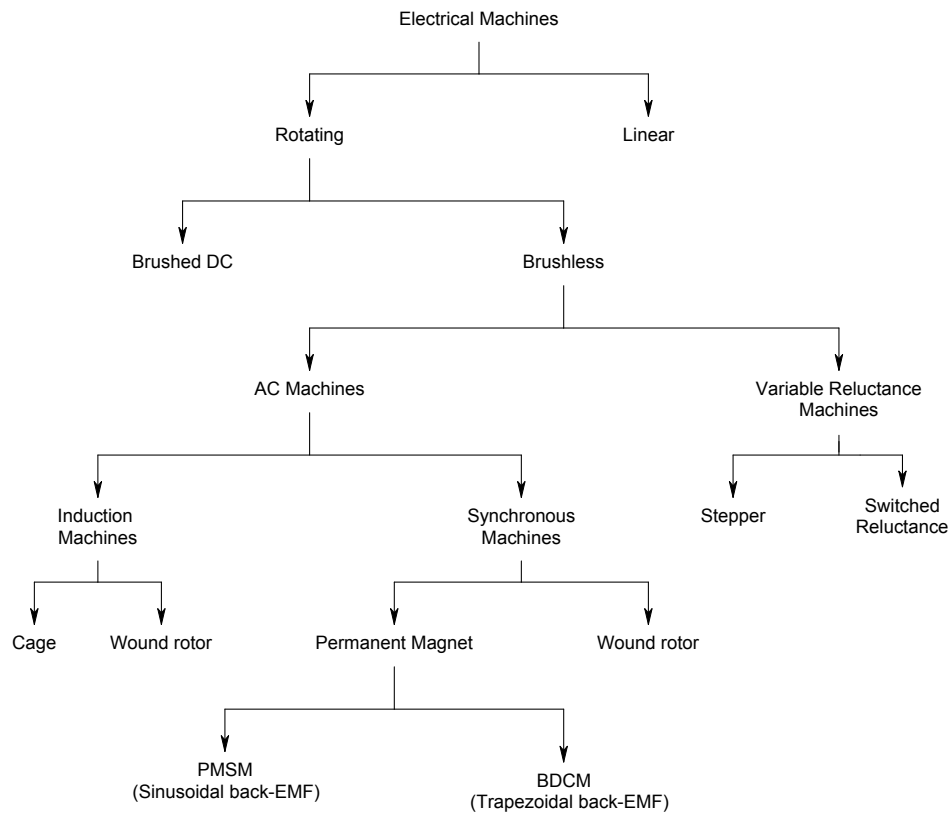


Figure 2.1: Electrical Machine Categories (Combination of [1, 2])

- Higher power factor is possible which lowers the inverter's required VA rating.
- Lower inertia implies faster torque response, in case of a load disturbance.
- Less torque ripple in the case of slot-less PMSMs.
- A lighter rotor implies less frictional loss and longer operating life of the bearings.

The main drawbacks of PMSMs are [2]:

- Higher cost of materials and construction in comparison to other machines.
- Smaller flux weakening region than for the IM.
- Lower operating temperatures allowed than for an IM due to the Curie temperature of the permanent magnets.

The advantages of the PMSM overshadow the disadvantages and a possible return on investment is made due to higher operating efficiency.

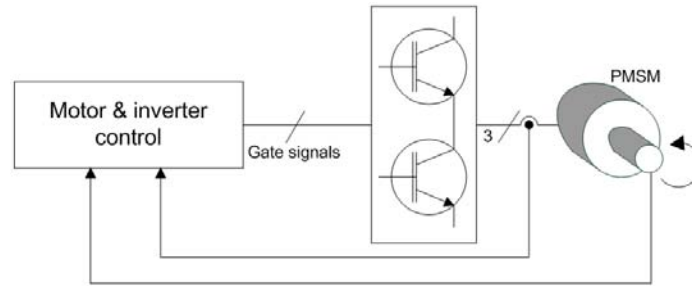


Figure 2.2: Conceptual PMSM drive.

### 2.1.2 Applications

The good characteristics of the PMSM has ensured many applications, which include electric vehicles [11, 12], machine tool spindles, starter/generator units [13], robotics, aerospace actuators [8], electric wheelchairs [14], fan-type applications [4] and turbo compressors [15].

## 2.2 PMSM drive modelling

The model of the PMSM drive can roughly be subdivided into three components: models of the PMSM, inverter and control driving the motor. This partitioning is shown in figure 2.2. In this section the literature is consulted for the modelling of each of these different sub-components.

### 2.2.1 PMSM models available in the literature

To design a controller for a PMSM, one needs an accurate model of the machine with which simulations can be done. If a state-space model is available, the inverse of the model can be cascaded with the reference input in a controller. This is the principle of open-loop control. When there is feedback of state variables, the requirements on the accuracy of the inverse model is not so stringent because the resulting error itself is used as an actuating signal in closed-loop control. In certain non-linear systems, an accurate model even with closed-loop control is necessary to achieve adequate performance. An example of this is servo control of a PMSM.

There is differentiated between models that are very accurate, but computationally inefficient and models which are less accurate but are useful for the real-time control of a system on a digital signal processor (DSP).

Hadžiselimović *et al.* presents a non-linear dynamic model of a PMSM. Several factors are accounted for such as winding distribution, material properties, slots and saturation. The model is verified with a finite element (FE) analysis. The authors conclude that the model is the most complete model known to them and is suitable for control design [18].

Another model that takes complex dynamics into account is presented by Jing *et al.* This model, like the previous model, accounts for various factors including a non-smooth air gap (slots). The

analysis investigates stability using bifurcation theory. The model is general and thus applicable to future PMSM designs [19].

The Direct-Quadrature (DQ) model of a PMSM is presented in [20] and a Matlab/Simulink<sup>®</sup> simulation model is developed from the mathematical model. The DQ model is obtained by using the direct-quadrature-zero (dq0) transform on the three-phase variables in the stationary reference frame, to obtain two-phase variables in a reference frame rotating synchronously with the rotor. The dq0 transformation was originally developed by Park for synchronous machines [21]. The advantage of this transformation is that the components of the stator current causing torque (i.e. the component which is perpendicular to the magnetic axis of the rotor permanent magnets) and (de-)magnetization are distinguished. It is not only used for simulation purposes but is also used by the vector controller. The vector control is also named Field Oriented Control (FOC) in the literature, because the magnetic axis of the stator currents is oriented with respect to the magnetic axis of the rotor to satisfy a certain control criterion. For non-salient machines as an example, if the angle is oriented perpendicularly, then maximum torque per current is produced.

In Mohammed *et al.* [22], a physical phase variable model of the PMSM is presented. The model is a circuit model and acquires the parameter values in the model from a dynamic FE analysis. It is demonstrated that the model delivers more accurate simulation results than the DQ model and is more computationally efficient than the full FE analysis. It may also be used for control.

A multiple-input multiple-output (MIMO) state-space model of the PMSM is developed by [23]. The method of linearizing the model is discussed. Another source which uses the linearized PMSM model is [24], in order to investigate the small signal dynamics of the machine for stability analysis. The derivation of the symbolic linearized models of electric machines, including the PMSM, is presented in [25]. A method of determining a numerical linearized model is presented in [26] using Matlab/Simulink<sup>®</sup>.

### 2.2.2 Mathematical model of the PMSM

The different models presented in Section 2.2.1 are by no means exhaustive. During the literature study it became apparent that the standard model used for the control system modelling and design is the DQ model of the PMSM.

There are three main approaches to derive the DQ model of the PMSM (the multiple methods are due to the fact that the stator of the different machine types are essentially the same)<sup>1</sup>:

- In [28] the dynamic model of the induction machine is derived. To obtain the PMSM model the terms in the model involving rotor currents are dropped and a flux linkage term is added to the d-axis flux linkage expression to account for the rotor flux due to the permanent magnets.

---

<sup>1</sup>In fact, it can be shown that the DC and AC machines are special cases of a mathematically general machine named the “doubly fed” machine. The general machine theory is attributed to G. Kron [27].

- Even more naturally, the PMSM can be viewed as a special case of the synchronous machine where the rotor electrical dynamic equation is neglected and the field current terms due to the rotor in the voltage equation of the stator are assumed constant, as done in [29, 3].
- The model can also be derived in its own right from first principles.

It should be noted that the mathematical model of the permanent magnet stepper motor is exactly the same as for the PMSM [29, 30]. The difference lies in the model parameter values themselves and not in the symbolic expression of the PM stepper motor (e.g. high saliency in the PM stepper motor).

A summary of the key steps to derive the DQ model is presented in the next subsections, for a more thorough derivation of the PMSM model the reader is referred to [3, 28, 29, 25, 30].

### 2.2.2.1 Stationary three-phase flux linkage

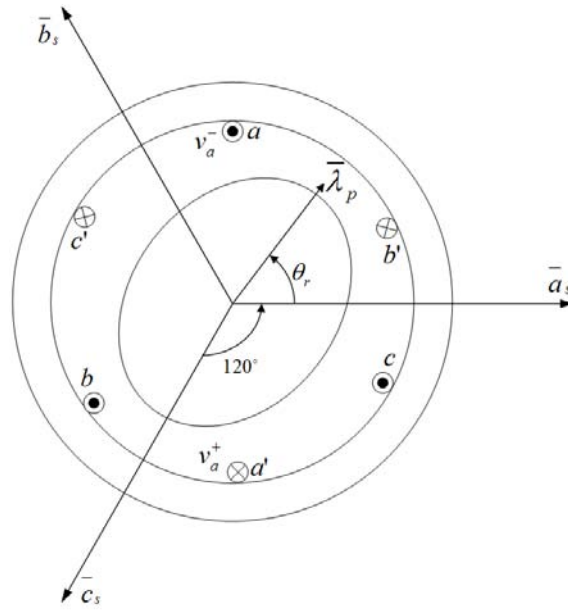


Figure 2.3: Cross-sectional view of PMSM.

The PMSM is depicted as in figure 2.3, which includes the salient rotor, stator back iron and three phase windings. If an external voltage,  $v_a$ , is connected to phase-a with polarity as shown, a current will flow into the page (crossed terminal) through the winding and back out of the page (dotted terminal), returning to the source. The resulting magnetic axis of phase-a,  $\bar{a}_s$ , is determined by Faraday's right hand rule. Since the current is delivered by the voltage source, the source is delivering power, thus the voltage convention used is motoring mode. The rotor angular position,  $\theta_r$ , is measured from the stator phase-a magnetic axis to the peak magnetic axis of the rotor, i.e. the rotor d-axis.

The windings are depicted physically  $120^\circ$  from each other, thus the motor is a two pole motor. The symbolic model of the PMSM can easily be modified afterwards, to account for the actual number of physical poles, by multiplying the physical angle with the number of pole pairs,  $z_p$ , to obtain an angle in electrical degrees. Also, the concentrated windings with  $N$  turns are in reality sinusoidally distributed, which can be accounted for by a winding factor,  $k_w$ , in the actual number of turns:

$$N = k_w N_{actual} \quad (2.1)$$

The derivation assumes a wye-connected motor, thus the accented winding terminals are connected in an isolated neutral point. The instantaneous three-phase current can be relatively arbitrarily controlled, but with the constraint that the currents have to sum to zero, due to the isolated neutral point assumption:

$$i_a + i_b + i_c = 0 \quad (2.2)$$

The three-phase flux linkage of the PMSM can be expressed as [3]:

$$\begin{bmatrix} \lambda_a \\ \lambda_b \\ \lambda_c \end{bmatrix} = \begin{bmatrix} L_{aa} & L_{ab} & L_{ac} \\ L_{ba} & L_{bb} & L_{bc} \\ L_{ca} & L_{cb} & L_{cc} \end{bmatrix} \begin{bmatrix} i_a \\ i_b \\ i_c \end{bmatrix} + \lambda_p \begin{bmatrix} \cos(\theta_r) \\ \cos(\theta_r - \frac{2\pi}{3}) \\ \cos(\theta_r + \frac{2\pi}{3}) \end{bmatrix} \quad (2.3)$$

where  $\lambda_p$  is the flux linkage due to the permanent magnet on the rotor.  $L_{xx}$  and  $L_{xy}$  is the stator self and mutual phase inductances, respectively. The subscript notation for the mutual inductance,  $L_{xy}$ , is such that a flux produced by phase-y couples with phase-x.

Equation 2.3 can be written in a shorter form as:

$$\boldsymbol{\lambda}_{abc} = \mathbf{L}_{abc} \mathbf{i}_{abc} + \boldsymbol{\lambda}_p \quad (2.4)$$

where the correspondence to equation 2.3 makes it unnecessary to clarify which terms are vectors and which terms are matrices, except to note that matrices and vectors are depicted in bold to distinguish them from scalars.

Note that the self and mutual phase inductances are dependent on the rotor angular position,  $\theta_r$ . The self inductance can be expressed as [29]:

$$\begin{aligned} L_{aa}(\theta_r) &= L_l + L_{m0} + L_{mp} \cos(2\theta_r) \\ L_{bb}(\theta_r) &= L_l + L_{m0} + L_{mp} \cos(2\theta_r + \frac{2\pi}{3}) \\ L_{cc}(\theta_r) &= L_l + L_{m0} + L_{mp} \cos(2\theta_r - \frac{2\pi}{3}) \end{aligned} \quad (2.5)$$

where  $L_l$  is the leakage inductance,  $L_{m0}$  is the mean magnetizing inductance and  $L_{mp}$  is half of the peak-to-peak variation of the magnetizing inductance due to the rotor angular position. Note the double frequency dependence on  $\theta_r$ . This is because for one physical rotation the

variation in reluctance due to the permanent magnets reach a peak for each magnetic pole. For a multiple pole machine, equation 2.5 is still valid if  $\theta_r$  is replaced by the rotor angle in electrical radians:

$$\theta_{re} = z_p \theta_r \quad (2.6)$$

As stated in [3], the sign of  $L_{mp}$  is dependent on the permanent magnet placement on the rotor. For a surface mount PMSM, the permeability of the rotor is lower in the q-axis direction due to the permanent magnet. Thus, the phase-a inductance is at a maximum when the rotor is aligned with the magnetic axis of phase-a, corresponding to a positive  $L_{mp}$ . For a surface mount PMSM the absolute magnitude of  $L_{mp}$  is small.

The mutual inductances between each set of the stator phases are expressed as [29]:

$$\begin{aligned} L_{ab}(\theta_r) = L_{ba}(\theta_r) &= -\frac{1}{2}L_{m0} + L_{mp} \cos(2\theta_r - \frac{2\pi}{3}) \\ L_{bc}(\theta_r) = L_{cb}(\theta_r) &= -\frac{1}{2}L_{m0} + L_{mp} \cos(2\theta_r) \\ L_{ac}(\theta_r) = L_{ca}(\theta_r) &= -\frac{1}{2}L_{m0} + L_{mp} \cos(2\theta_r + \frac{2\pi}{3}) \end{aligned} \quad (2.7)$$

The factor of a  $\frac{1}{2}$  in the first term is ascribable to the  $120^\circ$  phase displacement of the magnetic axis of each phase. Thus, the amount of flux produced by phase-b which couples with phase-a is equal to the dot product between the flux vector and the vector normal to the windings of phase-a, i.e. the magnetic axis of phase-a. Hence:  $\bar{b} \cdot \bar{a} = \cos(\frac{2\pi}{3}) = -\frac{1}{2}$ . The negative sign associated with the  $\frac{1}{2}$  term, is present because the components of each phase pair which are parallel is flux opposing with respect to the other phase which couples with it.

The argument of the cosine function can be explained by noting that the peak mutual coupling between phase-a and phase-b, influenced by the rotor saliency, is obtained when:

$$\begin{aligned} 2\theta_r - \frac{2\pi}{3} &= \pm\pi \\ \therefore \theta_r &= -\frac{\pi}{6}, \frac{5\pi}{6} \end{aligned} \quad (2.8)$$

Therefore, it can be seen that the maximum mutual flux linkage between phase-a and phase-b is obtained when the rotor magnetic axis is aligned such that the mean path between the two phases are at a minimum<sup>2</sup>.

### 2.2.2.2 Three- to two-phase coordinate transformation

The three-phase flux linkage of equation 2.3 can be transformed to a two-phase flux linkage. The constraint in the transformation is that the resultant flux in the air gap has to be conserved, in

<sup>2</sup>Figure 2.3, depicts the case when the absolute mutual flux linkage between phase-a and phase-b is at a minimum.

which case the permanent magnet is “unaware” of the transformation and the resulting torque for the two-phase model is the same as for the three-phase model. The transformation to obtain a two-phase model from the three-phase model is known as the Clarke transform [3]. Since the coordinate system is stationary with respect to the stator, the two-phase inductance is still a function of the rotor angular position.

The advantage of the three- to two-phase transformation is most apparent when the three-phase system is assumed balanced and a zero sequence component of the current is impossible due to an (assumed) isolated neutral connection. Thus, the three-phase currents reduce to two linearly *independent* currents,  $i_\alpha$  and  $i_\beta$ .

Even though useful due to the mathematical simplification of the equations, the three- to two-phase transformation can be viewed as an in-between step for an even more simplifying transformation presented in section 2.2.2.3. Therefore, the reader is referred to [3] for the mathematical details of the Clarke transformation.

### 2.2.2.3 Stationary to rotating coordinate transformation

The two-phase stationary model can be transformed to a rotating coordinate system, so that the resulting variables are stationary with respect to the rotor, hence the inductance dependence on the rotor angular position disappears. The transformation need not be done on the two-phase coordinate system but can just as well be performed on the three-phase variables, to obtain two-phase variables which are stationary with respect to the rotor. This transformation, as mentioned previously in section 2.2.1, is known as the dq0 or Park transformation [21]. The two-phase flux linkages in the rotor reference frame, using the transformation presented in [29] is<sup>3</sup>:

$$\lambda_{dq0s} = K_s^r \lambda_{abcs} \quad (2.9)$$

with

$$K_s^r = \frac{2}{3} \begin{bmatrix} \cos(\theta_r) & \cos(\theta_r - \frac{2\pi}{3}) & \cos(\theta_r + \frac{2\pi}{3}) \\ -\sin(\theta_r) & -\sin(\theta_r - \frac{2\pi}{3}) & -\sin(\theta_r + \frac{2\pi}{3}) \\ \frac{1}{2} & \frac{1}{2} & \frac{1}{2} \end{bmatrix} \quad (2.10)$$

The subscript,  $s$ , denotes that the transformation is carried out on stator variables. In the case of an induction machine the subscript for the rotor would be  $r$ . Since the PMSM does not have a rotor circuit, ambiguity is not a problem, thus the subscript is dropped in future use. The superscript  $r$  denotes that the variables are transformed to the synchronous reference frame. The reader should note that there is more than one form of this transformation in the literature due to the arbitrary choice of alignment of the phase-a axis with either the d-axis or q-axis. The case presented in equation 2.10 assumes alignment between phase-a and phase-d when  $\theta_r = 0$ .

<sup>3</sup>The transformation notation of [25] is used in modified form.



Not only can the transformation be applied to the variables numerically, but it can also be applied symbolically to the flux linkage model by substituting equation 2.3 into equation 2.9 as follows:

$$\begin{aligned}
 \lambda_{dq0} &= \mathbf{K}^r \lambda_{abc} \\
 &= \mathbf{K}^r \mathbf{L}_{abc} \mathbf{i}_{abc} + \mathbf{K}^r \lambda_p \\
 &= \mathbf{K}^r \mathbf{L}_{abc} (\mathbf{K}^r)^{-1} \mathbf{i}_{dq0} + \mathbf{K}^r \lambda_p
 \end{aligned} \tag{2.11}$$

where  $\mathbf{i}_{dq0} = \begin{bmatrix} i_d & i_q & i_0 \end{bmatrix}^T$  and the inverse of the dq0 transformation is [29]:

$$(\mathbf{K}^r)^{-1} = \begin{bmatrix} \cos(\theta_r) & -\sin(\theta_r) & 1 \\ \cos(\theta_r - \frac{2\pi}{3}) & -\sin(\theta_r - \frac{2\pi}{3}) & 1 \\ \cos(\theta_r + \frac{2\pi}{3}) & -\sin(\theta_r + \frac{2\pi}{3}) & 1 \end{bmatrix} \tag{2.12}$$

Equation 2.11 can be simplified into the following form:

$$\lambda_{dq0} = \mathbf{L}_{dq0} \mathbf{i}_{dq0} + \lambda_r \tag{2.13}$$

where the substitutions  $\mathbf{L}_{dq0} = \mathbf{K}^r \mathbf{L}_{abc} (\mathbf{K}^r)^{-1}$  and  $\lambda_r = \mathbf{K}^r \lambda_p$  have been made.

The trigonometric simplification procedure to obtain  $\mathbf{L}_{dq0}$  and  $\lambda_r$  is presented in appendix C.1. The simplification results in:

$$\mathbf{L}_{dq0} = \begin{bmatrix} L_d & 0 & 0 \\ 0 & L_q & 0 \\ 0 & 0 & L_l \end{bmatrix} \tag{2.14}$$

and

$$\lambda_r = \lambda_p \begin{bmatrix} 1 \\ 0 \\ 0 \end{bmatrix} \tag{2.15}$$

where the inductances on the diagonal are

$$L_d = \frac{3}{2} (L_{m0} + L_{mp}) + L_l \tag{2.16}$$

and

$$L_q = \frac{3}{2} (L_{m0} - L_{mp}) + L_l \tag{2.17}$$

#### 2.2.2.4 Voltage model of the PMSM in the rotor reference frame

With the use of Faraday's law of induction and including the resistive voltage drop, the voltage equation for the PMSM in the stationary reference frame can be written as [25]:

$$\mathbf{v}_{abc} = \mathbf{r}_s \mathbf{i}_{abc} + p \lambda_{abc} \tag{2.18}$$

where  $p$  is the time derivative operator ( $\frac{d}{dt}$ ) and  $\mathbf{r}_s$  is the resistor matrix given by:

$$\mathbf{r}_s = \begin{bmatrix} r_s & 0 & 0 \\ 0 & r_s & 0 \\ 0 & 0 & r_s \end{bmatrix} \quad (2.19)$$

The three-phase voltage equation is transformed to the rotor reference frame as:

$$\begin{aligned} \mathbf{v}_{abc} &= \mathbf{r}_s \mathbf{i}_{abc} + p \boldsymbol{\lambda}_{abc} \\ \left( (\mathbf{K}^r)^{-1} \mathbf{v}_{dq0} \right) &= \mathbf{r}_s \left( (\mathbf{K}^r)^{-1} \mathbf{i}_{dq0} \right) + p \left( (\mathbf{K}^r)^{-1} \boldsymbol{\lambda}_{dq0} \right) \\ \therefore \mathbf{v}_{dq0} &= \mathbf{K}^r \mathbf{r}_s (\mathbf{K}^r)^{-1} \mathbf{i}_{dq0} + \mathbf{K}^r p \left( (\mathbf{K}^r)^{-1} \boldsymbol{\lambda}_{dq0} \right) \end{aligned} \quad (2.20)$$

The first term on the right hand side of equation 2.20 can be simplified as follows:

$$\begin{aligned} \mathbf{K}^r \mathbf{r}_s (\mathbf{K}^r)^{-1} \mathbf{i}_{dq0} &= \mathbf{r}_s \mathbf{K}^r (\mathbf{K}^r)^{-1} \mathbf{i}_{dq0} \\ &= \mathbf{r}_s \mathbf{i}_{dq0} \end{aligned} \quad (2.21)$$

where the commutative law does not in general hold for matrix multiplication, i.e.  $\mathbf{AB} \neq \mathbf{BA}$ , but could be applied in this case, because  $\mathbf{r}_s$  is diagonal. The second term of equation 2.20 can be expanded by applying the chain rule:

$$\begin{aligned} \mathbf{K}^r p \left( (\mathbf{K}^r)^{-1} \boldsymbol{\lambda}_{dq0} \right) &= \mathbf{K}^r p \left( (\mathbf{K}^r)^{-1} \right) \boldsymbol{\lambda}_{dq0} + \mathbf{K}^r (\mathbf{K}^r)^{-1} p \boldsymbol{\lambda}_{dq0} \\ &= \mathbf{K}^r p \left( (\mathbf{K}^r)^{-1} \right) \boldsymbol{\lambda}_{dq0} + p \boldsymbol{\lambda}_{dq0} \end{aligned} \quad (2.22)$$

The simplification of the first term in equation 2.22 is shown in appendix C.1, of which the result is:

$$\mathbf{K}^r p \left( (\mathbf{K}^r)^{-1} \right) = \omega_r \mathbf{J} \quad (2.23)$$

where the skew symmetric matrix,  $\mathbf{J}$ , is defined as:

$$\mathbf{J} = \begin{bmatrix} 0 & -1 & 0 \\ 1 & 0 & 0 \\ 0 & 0 & 0 \end{bmatrix} \quad (2.24)$$

The off-diagonal elements in the transformation matrix  $\mathbf{J}^4$  show that there is cross-coupling between the dq-axes.

Using the previous results in this section, the voltage equation of the PMSM in the rotor reference frame is:

$$\mathbf{v}_{dq0} = \mathbf{r}_s \mathbf{i}_{dq0} + \omega_r \mathbf{J} \boldsymbol{\lambda}_{dq0} + p \boldsymbol{\lambda}_{dq0} \quad (2.25)$$

---

<sup>4</sup>The symbol for the transformation matrix  $\mathbf{J}$ , must not be confused for the rotor polar moment of inertia,  $J$ .

Note how the voltage equation could *not* intuitively be written as:

$$\mathbf{v}_{dq0} = \mathbf{r}_s \mathbf{i}_{dq0} + p \boldsymbol{\lambda}_{dq0} \quad (2.26)$$

but that the three-phase voltage equation had to be transformed to obtain equation 2.25. The derivative could not be applied directly to the two-phase flux linkage, because the dq0 transformation matrix,  $\mathbf{K}^r$ , is itself a function of time.

### 2.2.2.5 Electromagnetic torque

There exist several methods of deriving the electromagnetic torque from the PMSM model. Chiasson derived the expression from the electromagnetic torque using the Lorentz force equation [30]. In his thesis on sensorless vector control, Batzel derived the electromagnetic torque with the energy method [3]. An intuitive method, pointed out by de Kock, is that the electromechanical energy conversion is due to the speed voltage [31]. From equation 2.25, the back-emf (or speed voltage) is denoted as:

$$\mathbf{e}_{dq0} = \omega_r \mathbf{J} \boldsymbol{\lambda}_{dq0} \quad (2.27)$$

The power delivered across the air-gap of the PMSM is then [31]:

$$\begin{aligned} P_o &= \mathbf{e}_{abc}^T \mathbf{i}_{abc} \\ &= \left( (\mathbf{K}^r)^{-1} \mathbf{e}_{dq0} \right)^T \left( (\mathbf{K}^r)^{-1} \mathbf{i}_{dq0} \right) \\ &= \mathbf{e}_{dq0}^T (\mathbf{K}^r)^{-1T} (\mathbf{K}^r)^{-1} \mathbf{i}_{dq0} \\ &= \mathbf{e}_{dq0}^T \begin{bmatrix} \frac{3}{2} & 0 & 0 \\ 0 & \frac{3}{2} & 0 \\ 0 & 0 & 3 \end{bmatrix} \mathbf{i}_{dq0} \end{aligned} \quad (2.28)$$

In the literature, because the term  $(\mathbf{K}^r)^{-1T} (\mathbf{K}^r)^{-1}$  did not simplify to yield the identity matrix, the transformation matrix of equation 2.10 is known as the power variant transform. The dq0 transformation for which the term  $(\mathbf{K}^r)^{-1T} (\mathbf{K}^r)^{-1}$  *does* result in the identity matrix is known as the power invariant dq0 transformation, given by:

$$\mathbf{K}_s^r = \sqrt{\frac{2}{3}} \begin{bmatrix} \cos(\theta_r) & \cos\left(\theta_r - \frac{2\pi}{3}\right) & \cos\left(\theta_r + \frac{2\pi}{3}\right) \\ -\sin(\theta_r) & -\sin\left(\theta_r - \frac{2\pi}{3}\right) & -\sin\left(\theta_r + \frac{2\pi}{3}\right) \\ \sqrt{\frac{1}{2}} & \sqrt{\frac{1}{2}} & \sqrt{\frac{1}{2}} \end{bmatrix} \quad (2.29)$$

The zero sequence current component can be ignored in equation 2.28, because of the previously stated assumption that the neutral wye connection is isolated, thus:

$$P_o = \frac{3}{2} \mathbf{e}_{dq}^T \mathbf{i}_{dq} \quad (2.30)$$

Substituting the expression for  $e_{dq0}$ , equation 2.27, into equation 2.30:

$$\begin{aligned}
 P_o &= \frac{3}{2} (\omega_r \mathbf{J} \boldsymbol{\lambda}_{dq})^T \mathbf{i}_{dq} \\
 &= \frac{3}{2} \omega_r \boldsymbol{\lambda}_{dq}^T \mathbf{J}^T \mathbf{i}_{dq} \\
 &= \frac{3}{2} \omega_r \begin{bmatrix} \lambda_d & \lambda_q \end{bmatrix} \begin{bmatrix} 0 & 1 \\ -1 & 0 \end{bmatrix} \begin{bmatrix} i_d \\ i_q \end{bmatrix} \\
 &= \frac{3}{2} \omega_r (\lambda_d i_q - \lambda_q i_d)
 \end{aligned} \tag{2.31}$$

Substituting the dq-axis stator flux linkages:

$$\lambda_d = L_d i_d + \lambda_p \tag{2.32}$$

$$\lambda_q = L_q i_q \tag{2.33}$$

into equation 2.31 and simplifying, yields:

$$P_o = \frac{3}{2} \omega_r (\lambda_p i_q + (L_d - L_q) i_q i_d) \tag{2.34}$$

The output power, shaft torque and rotational speed are related by:

$$P_o = T_e \omega_m \tag{2.35}$$

Using the relation for the electrical and mechanical speed,  $\omega_r = z_p \omega_m$ , equation 2.35 is expressed in electrical speed as:

$$P_o = T_e \frac{\omega_r}{z_p} \tag{2.36}$$

Substituting the output power expression from equation 2.34, into equation 2.36 and solving for the electromagnetic torque, yields:

$$T_e = \frac{3}{2} z_p (\lambda_p i_q + (L_d - L_q) i_q i_d) \tag{2.37}$$

The terms  $\lambda_p i_q$  and  $(L_d - L_q) i_q i_d$  are known as the reaction and reluctance torques, respectively. For a surface mount PMSM the dq-axes inductance is nearly equal, so that equation 2.37 can be approximated by:

$$T_e \approx \frac{3}{2} z_p \lambda_p i_q \tag{2.38}$$

The torque constant, which is a characteristic machine parameter, is defined as the coefficient which is multiplied with the torque producing current in equation 2.38. Thus the torque constant is:

$$K_t = \frac{3}{2} z_p \lambda_p \tag{2.39}$$

The electromagnetic torque can then be expressed as:

$$T_e = K_t i_q \quad (2.40)$$

which is similar in form to that of the separately excited DC machine. Therefore, the PMSM has the advantage that it can be controlled to have the same performance as the separately excited DC machine, without the disadvantages due to the brushes and commutator.

### 2.2.2.6 Rotor dynamic equation of motion

In order to simulate the PMSM model the dynamic equation for motion need to be included. The second order differential equation is:

$$J\ddot{\theta}_m = T_e - T_l - B\dot{\theta}_m \quad (2.41)$$

where  $J$  is the polar moment of inertia,  $T_e$  is the electromagnetic torque,  $T_l$  is an external load torque and  $B$  is the viscous friction loss coefficient. The terms on the right hand side of equation 2.41 is the resultant torque,  $T_r$ , which accelerates the rotor, ie.:

$$J\ddot{\theta}_m = T_r \quad (2.42)$$

Equation 2.42 is of the same form as Newton's second law of motion.

### 2.2.2.7 State-space model

For simulation purposes, the voltage is usually the input to the PMSM model (since the input from the inverter is a voltage) and the current is the output of interest.

Since the model is a differential equation, it is useful to express the rate of change of current as the output. The current is then obtained by numerical integration, because equation 2.25 is non-linear (due to the product between two dependent variables, i.e.  $\omega_r$  and  $\lambda_{dq0}$ ) for which an analytical solution is not possible. This is known as the state-space representation of the PMSM model and is useful for simulation and controller design purposes. The resulting state-space formulation of the PMSM model is [24]:

$$\begin{aligned} p i_d &= -\frac{1}{\tau_s} i_d + \omega_r \sigma i_q + \frac{v_d}{L_d} \\ p i_q &= -\frac{\omega_r}{\sigma} \left( \frac{\lambda_p}{L_d} + i_d \right) - \frac{1}{\sigma \tau_s} i_q + \frac{v_q}{L_q} \\ p \omega_m &= \frac{3}{2J} z_p (\lambda_p i_q + L_d (1 - \sigma) i_q i_d) - \frac{1}{J} B \omega_m - \frac{1}{J} T_l \end{aligned} \quad (2.43)$$

where  $\tau_s = \frac{L_d}{r_s}$  is the d-axis stator electrical time constant and  $\sigma = \frac{L_q}{L_d}$  is the saliency factor.

### 2.2.2.8 Space vectors

In the literature there exists an alternative notation for expressing the AC machine equations named space vector notation<sup>5</sup>. The DQ quantities are expressed as complex numbers, where the direct and quadrature axis quantities are respectively the real and imaginary parts of the electrical quantity under consideration. This has the added advantage that the two equation machine model can be expressed as one complex equation. Transforming the machine variables to a different reference frame is then performed simply by multiplying the quantity by a unit magnitude complex number, since multiplying in the complex plane is an additive operation between the complex quantities' angles. This corresponds to rotating the complex number with respect to a new coordinate reference frame [32].

One unnatural adoption by some of the researchers who use space vectors is the manner in which they go about pretending that electrical quantities such as the current space vector,  $\vec{i}_s$ , has spatial significance. The current appears to have a spatial attribute due to the spatial orientation of the windings carrying the current and the consequent spatial orientation of the resulting magnetic flux. The currents are thus actually scalar quantities and the windings should be expressed as vectors as done by Hoeijmakers in [33, 34].

### 2.2.3 PMSM parameter identification

FE analysis is one method used to determine the model parameter values used in the model and control. This method is especially useful if non-linear effects, such as saturation of the machine inductance, need to be included. In [31] an FE analysis is performed on a permanent magnet assisted reluctance machine. The non-linear inductance, as a function of current, is included in the machine model as well as in the current control, in the form of a look-up table (LUT). The LUT is composed from FE analysis results.

The surface mount PMSM has a relatively large air-gap compared to the slotted PMSM. The large air gap causes the stator flux to be dominated by the permanent magnet on the rotor and not that much by the stator current. The resulting inductance of the machine is also much more linear than for the slotted PMSM due to the large air gap. Thus, it is sufficient to consider the electrical parameters as linear. These circuit parameters can be measured by a resistive-inductive-capacitive (RLC) impedance measurement unit. The RL measurements on the terminals of the machine need to be converted in order to be used in the DQ model of the PMSM.

#### 2.2.3.1 PMSM circuit parameters from terminal measurements

Chiasson shows in [30] the method to calculate the two-phase equivalent parameters from terminal measurements. With the rotor held fixed, a line-line terminal measurement is made with

---

<sup>5</sup>Quantities expressed in this reference frame are simply called space vectors, except for the scalar quantities such as the rotor speed  $\omega_r$ .

the third phase open-circuited.

In order to interpret the RL measurement of this configuration, the three-phase electrical equation is observed [30]. Expanding equation 2.18, with the rotor held fixed ( $\omega_r = 0$ ), is:

$$\begin{bmatrix} v_a \\ v_b \\ v_c \end{bmatrix} = \begin{bmatrix} r_s & 0 & 0 \\ 0 & r_s & 0 \\ 0 & 0 & r_s \end{bmatrix} \begin{bmatrix} i_a \\ i_b \\ i_c \end{bmatrix} + \begin{bmatrix} L_{m0} & -\frac{L_{m0}}{2} & -\frac{L_{m0}}{2} \\ -\frac{L_{m0}}{2} & L_{m0} & -\frac{L_{m0}}{2} \\ -\frac{L_{m0}}{2} & -\frac{L_{m0}}{2} & L_{m0} \end{bmatrix} \begin{bmatrix} p i_a \\ p i_b \\ p i_c \end{bmatrix} \quad (2.44)$$

where the inductance is assumed independent of the angular position, since this dissertation deals with surface mount PMSMs. Also, the leakage inductance is included with  $L_{m0}$ . Subtracting the second row from the first, yields:

$$v_{ab} = v_a - v_b = r_s (i_a - i_b) + \left( L_{m0} - \left( -\frac{L_{m0}}{2} \right) \right) p i_a - \left( L_{m0} - \left( -\frac{L_{m0}}{2} \right) \right) p i_b \quad (2.45)$$

Substituting,  $i_b = -i_a$  into equation 2.45 and simplifying, results in:

$$v_{ab} = 2r_s i_a + 3L_{m0} p i_a \quad (2.46)$$

Therefore, for this measurement setup, the phase resistance is one half and the phase inductance is a third of the RL measurement. The phase inductance can then be substituted into equation 2.16 to obtain the d-axis inductance.

For PMSMs with saliency, the calculation is done with the rotor position held as to yield maximum inductance and repeated in the position which yields minimum inductance. With respect to equation 2.44, this corresponds to replacing  $L_{m0}$  with  $L_{m0} + L_{mp}$  and  $L_{m0} - L_{mp}$  for the maximum and minimum inductance cases, respectively. Equation 2.46 would then result as:

$$v_{ab} = 2r_s i_a + 3(L_{m0} \pm L_{mp}) p i_a \quad (2.47)$$

Substituting  $\hat{L} = L_{m0} + L_{mp}$  into equation 2.16 yields the d-axis inductance, whilst substituting  $\check{L} = L_{m0} - L_{mp}$  into equation 2.17 yields the q-axis inductance.

A disadvantage of this method is that none of the mechanical parameters can be determined. Also note that the flux linkage,  $\lambda_p$ , due to the rotor permanent magnets, cannot be determined from stand-still terminal measurements. This measurement technique is also not appropriate to determine the non-linear, current dependent, inductance. In such a case the current should be balanced (the third winding should not be left open-circuited), for which the terminal resistive and inductive characteristic has to be derived, similar to the derivation of equation 2.46.

### 2.2.3.2 Least squares parameter identification of the PMSM

The PMSM model parameters, both mechanical and electrical, can be obtained by a least squares parameter identification technique as presented by Chiasson in [35, 30]. The technique

consists of post processing data, captured from a motor run-up test. The least squares parameter identification requires that the PMSM model, such as the state-space equation 2.4, be rewritten in what is called the regressor form of the model [30]:

$$\mathbf{y} = \mathbf{W}\mathbf{K} \quad (2.48)$$

where  $\mathbf{y} = \begin{bmatrix} v_d & v_q \end{bmatrix}^T$ . The input vector is no longer the state variables, but is now the parameters of the PMSM model, i.e.  $\mathbf{K} = \begin{bmatrix} r_s & L_s & \lambda_p & J & B & T_l \end{bmatrix}^T$ . The regressor matrix is:

$$\mathbf{W} = \begin{bmatrix} i_d & (pi_d - \omega_r i_q) & 0 & 0 & 0 & 0 \\ i_q & (pi_q + \omega_r i_d) & \omega_r & 0 & 0 & 0 \\ 0 & 0 & -\frac{3}{2}z_p i_q & p\omega_m & \omega_m & \text{sgn}(\omega_m) \end{bmatrix} \quad (2.49)$$

where  $\text{sgn}(\cdot)$  is the sign function,  $\omega_r$  and  $\omega_m$  is the rotor speed in electrical and mechanical radians per second, respectively.

Since the captured data is in discrete time form, equation 2.48 is evaluated at each discrete time step,  $t_n = nT$ , where  $T$  is the sampling period. Thus,  $\mathbf{y} = \mathbf{y}(nT)$ .

If there is no noise in the system and each signal in the regressor matrix could be measured perfectly and the PMSM exhibits no unmodelled dynamics, then the left and right hand sides of equation 2.48 would be equal at each sampling instant. Then equation 2.48 constitutes a linear system of equations and the desired model parameters would simply be:

$$\mathbf{K} = (\mathbf{W})^{-1} \mathbf{y} \quad (2.50)$$

In any real world system there exist errors in the measurement due to measurement noise, finite word length effects and unmodelled dynamics. Therefore, the exact solution at two different time steps would in general not be equal. Combining the system of equations for two measurements into one set of equations reveals that there are more equations than unknowns. This constitutes an overdetermined system of equations.

The method of least squares produces the “closest” solution,  $\mathbf{K}^*$ , to an overdetermined system of equations. In general  $\mathbf{K}^*$  is not a solution to the equations produced at any specific time step, but instead the least squares solution minimizes the sum of errors squared of each set of equations. The sum of errors squared is defined as:

$$\mathbf{E}(\hat{\mathbf{K}})^2 = \sum_{n=1}^{n=N} \mathbf{e}_n^T \mathbf{e}_n \quad (2.51)$$

where the error at each individual time step is the difference between the measurement of that time step and the output of some assumed solution ( $\hat{\mathbf{K}}$ ), i.e.  $\mathbf{e}_n = (\mathbf{y}_n - \hat{\mathbf{y}}_n)$ . It can be shown that equation 2.51 is minimized when [30]:

$$\mathbf{K}^* = \mathbf{R}_W^{-1} \mathbf{R}_{Wy} \quad (2.52)$$



where

$$\mathbf{R}_W = \sum_{n=1}^N \mathbf{W}^T(nT) \mathbf{W}(nT) \quad (2.53)$$

and

$$\mathbf{R}_{Wy} = \sum_{n=1}^N \mathbf{W}^T(nT) \mathbf{y}(nT) \quad (2.54)$$

The residual error is of importance, since it is an indication how well the data could be fit with the optimal gain,  $\mathbf{K}^*$ . In practice, a normalized error is used, since the residual error alone is difficult to interpret because there is nothing to compare it with. The error used for normalization is obtained using the zero vector, i.e.  $\mathbf{E}(\mathbf{0})$ . The error index is defined as [30]:

$$\begin{aligned} \text{Error Index} &= \frac{\mathbf{E}(\mathbf{K}^*)}{\mathbf{E}(\mathbf{0})} \\ &= \sqrt{\frac{\mathbf{R}_y - \mathbf{R}_{yW} \mathbf{R}_W^{-1} \mathbf{R}_{Wy}}{\mathbf{R}_y}} \end{aligned} \quad (2.55)$$

The error index gives an indication of how well the parameters could fit the data, but it does not give an indication how well each *individual* parameter has been determined. The amount a certain parameter has to change in order to double the error is known as the parametric error index. If a slight increase/decrease in the optimal parameter,  $K_i^*$ , doubles the total error, it indicates that the system is sensitive to a change in that parameter and that the parameter “explains” the data well with the given model. If a large increase/decrease is required in order to double the error, the part of the model containing that parameter does not have an explanatory role in fitting the data. If it is known that the parameter is important in the model, a large parametric error indicates uncertainty in the numerical value of the parameter. The  $i$ -th percentage parametric error index is defined as:

$$PE_i = \frac{\delta K_i}{K_i^*} \times 100 \quad (2.56)$$

where the  $i$ -th parametric error index,  $\delta K_i$  has been normalized by its parameter value,  $K_i^*$ .

The error index has to be used in conjunction with the parametric error index. For instance, calculating the error indices over a sample range which decrease the error index, but at the expense of increasing the parametric error index, indicates that the model is potentially being over-fit. In other words, the combination of individual bad fitted parameters could have a low total error index.

#### 2.2.4 Inverter modelling

The three-phase inverter, using IGBTs, is as shown in figure 2.4. The O-type connectors represent connections to/from external circuitry, such as the three-phase rectifier feeding the bus

capacitors and the inverter outputs connected to the PMSM. Also not shown is the gate drive circuitry of the IGBTs. Each IGBT has its own freewheeling diode to ensure a commutation path for currents carried by inductive loads. The top and bottom switch for a phase is called an inverter leg. Depending on the instantaneous inverter state the current can freewheel from one inverter leg to another or back to the bus capacitors.

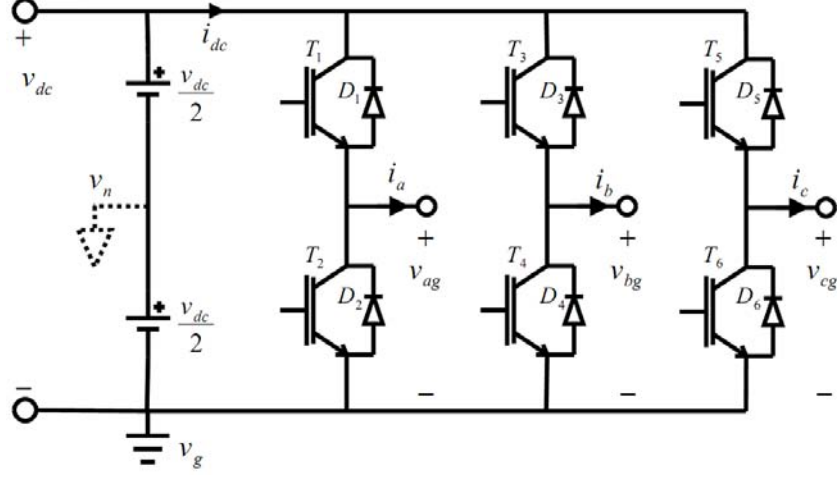


Figure 2.4: Three-phase IGBT inverter.

The instantaneous transistor on/off condition for the six switch inverter, determines the state of the inverter. Each inverter leg has two permitted switching states. The third possible state of both top and bottom switches in an inverter leg conducting simultaneously is not allowed, since this short circuits the bus capacitors which destroys the switches. Thus, for three inverter legs there are 8 possible states ( $2^3$ ) which may be represented by a state vector. Since the bottom switch is the complement of the top switch, the state vector can be denoted by the state of just the top switches. The state vectors are summarized as in table 2.1.

Table 2.1: Inverter switching state vectors.

Switch state	$T_5$	$T_3$	$T_1$
$S_0$	0	0	0
$S_1$	0	0	1
$S_2$	0	1	1
$S_3$	0	1	0
$S_4$	1	1	0
$S_5$	1	0	0
$S_6$	1	0	1
$S_7$	1	1	1

#### 2.2.4.1 Inverter control

The purpose of the three-phase inverter is to act as a controllable voltage source. The transistors can be controlled in a linear fashion, i.e. the gate charge is controlled in order for the output

voltage to equal the commanded voltage. In low power applications<sup>6</sup>, the resulting losses may be acceptable, but not in medium to high power applications such as in motor control.

In order to limit the losses, the switches are controlled either fully on or completely off. Thus carrying either the full load current with little voltage drop across the switch, or no current with a large voltage drop across the switch. In order to satisfy the requested voltage, the switch states are varied in turn (modulated), so that the average output voltage equals the requested voltage. The method used to vary the switch states in order to satisfy a control request (in the average) is known as the modulation scheme. With any modulation scheme a voltage or a current command can be enforced. In the case of a current command, the current is fed back using negative feedback. The current error is then used to generate a voltage command. Hence, the inverter considered in this dissertation is of the voltage source inverter (VSI) type. Different modulation schemes, with different advantages and disadvantages, are used in practice. A review of the main types of modulation schemes follow.

**Sine-triangle modulation** One method of controlling the switching of the inverter is to compare the voltage command with a triangle signal. If the voltage command is greater than the triangle, the top switch in an inverter leg is on and if the triangle is less than the voltage command the bottom switch is on. In the steady state of the PMSM, the voltage command is sinusoidal, thus the modulation scheme is known as sine-triangle modulation<sup>7</sup>. The sine and triangle wave comparison with the resulting output is as shown in figure 2.5. The output voltage, with a peak value of  $\frac{v_{dc}}{2}$ , is measured with respect to the fictitious neutral in figure 2.4. For the inverter to behave linearly, the reference voltage,  $v^*$ , has to be in range of the triangle peaks,  $\pm \hat{v}_c$ . Near and beyond these limits, the inverter is said to operate in the overmodulation region.

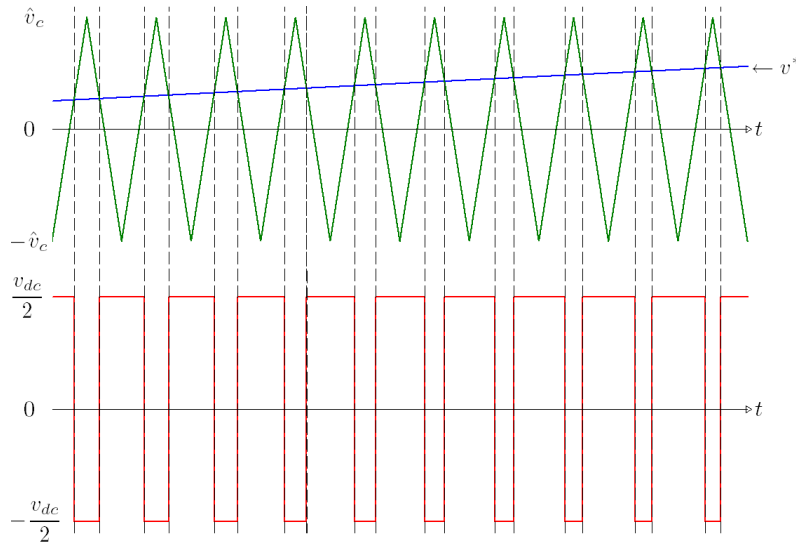


Figure 2.5: Voltage output with sine-triangle modulation.

<sup>6</sup>An audio amplifier is an example.

<sup>7</sup>In the literature, sine-triangle modulation is often called pulse width modulation (PWM), although the strict definition of PWM, such as that by Krause *et al.*, refers to another type of modulation [25].

In this case, linear operation refers to the average output signal. The window of this average is calculated over a switching period of the inverter,  $T_c$ , and is referred to as the fast-average<sup>8</sup>. The gain of the inverter in the linear region is [36]:

$$\begin{aligned} G(v_{dc}) &= \frac{\bar{v}_{xn}}{\bar{v}_{xn}^*} \\ &= \frac{v_{dc}}{2\hat{v}_c} \end{aligned} \quad (2.57)$$

where  $\bar{v}_{xn}$  is the average output voltage in phase x with respect to the fictitious neutral, the starred variable is the reference voltage. Equation 2.57 shows that the gain is a function of the bus voltage,  $v_{dc}$ , therefore a ripple in the bus voltage will cause a current ripple in the load. In an analogue PWM controller a low frequency drift in the triangle wave peak will also cause a disturbance in the load currents. Digital controllers have the advantage that the triangle wave can be kept constant. Analogue PWM controllers can generate the triangle wave as a function of the bus voltage, thereby rejecting the bus voltage ripple to a certain extent. With proper controller implementation, both digital and analogue PWM controllers can compensate for the bus disturbance. The digital controllers are more resistant to electromagnetic interference generated by the fast switching of the transistors.

Equation 2.57 also reveals that the maximum peak voltage obtainable, assuming linear operation, is equal to  $\frac{v_{dc}}{2}$ . The obtainable peak value of the inverter can be increased by adding a third harmonic to the reference signal. This is known as third harmonic injection. The peak value obtainable for third harmonic injection is  $\frac{v_{dc}}{\sqrt{3}}$  (although the inverter gain is still  $\frac{v_{dc}}{2}$ ). For the derivation as to why third harmonic injection has this property and the implementation thereof, the reader is referred to [25].

**Hysteresis modulation** Another modulation scheme, known as hysteresis modulation, generates the switching signals by placing a hysteresis window around the reference signal. The actuated signal is fed back and compared to the windows. If the signal crosses a window the switches are switched in such a manner so as to drive the signal towards the opposite window. The operation of hysteresis modulation is illustrated in figure 2.6, where  $H_w$  is the window size. Hysteresis modulation is non-linear so that a gain for the fast-average input-output relationship cannot be derived. As opposed to sine-triangle modulation, which can operate in open-loop, the hysteresis modulation cannot operate without feedback.

One of the earliest drive models and simulations in the literature study has been that of [10]. A state-space model of the d-q motor model and the controller is given. The effects of the inverter switches are included. A comparison between PWM and hysteresis inverter modulation schemes is also carried out. It is found that PWM may cause a lag in the control, but as long as the switching period is less than one tenth of the system time constant, the resulting lag is negligible. Hysteresis control causes a high switching frequency which is inversely proportional

<sup>8</sup>The average over a period of the modulating signal is zero in the steady state.

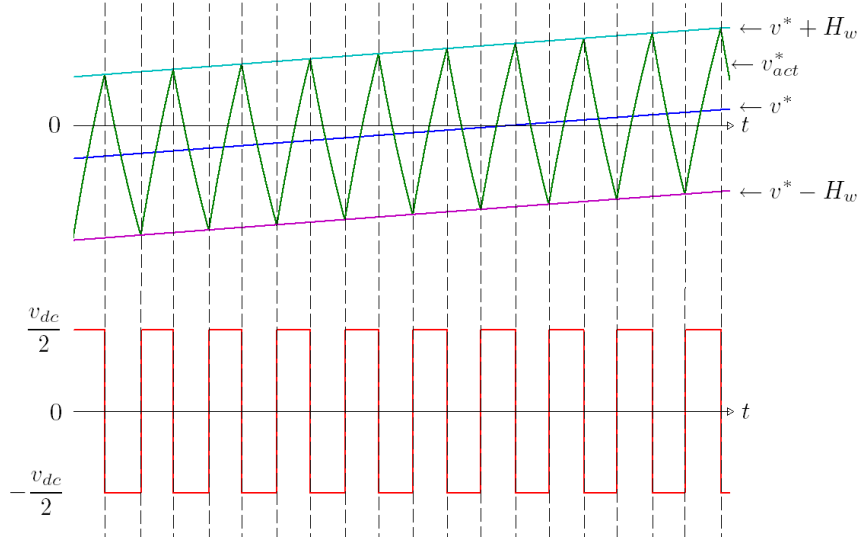


Figure 2.6: Voltage output with hysteresis modulation.

to the size of the hysteresis window. Hysteresis control has higher switching losses than the PWM switching technique. The increase in current tracking accuracy per increase in frequency is not as significant for the hysteresis controller as for the PWM controller. High-speed PMSMs have a small phase inductance, which implies a small time constant. This favours hysteresis current control, because it does not have the mentioned lag, but requires an inverter that can withstand the higher losses.

**Space vector modulation** The sine-triangle and hysteresis modulation schemes control the voltage in each phase independently, which is non-optimal. The switch states in table 2.1 can be represented in diagram form as in figure 2.7, along with the resulting voltage vector for the given switch state. The spatial orientation of the voltage vectors are attributable to the magnetic axis of the resulting flux vector which results from the current that flows for a specific inverter switch state. The origin of the vector nature of the voltage state is thus the same as for the current vector in the space vector model of the PMSM as discussed in section 2.2.2.8. In steady state operation of the PMSM, there is a phase difference between the current vector and the applied voltage vector.

Space vector modulation (SVM) considers in which sector the reference voltage vector resides each switching cycle. The (fast) average reference voltage is obtained as a linear combination of the voltage vectors spanning the sector in which the reference voltage is at that moment. As an example, if the required voltage vector is in sector 1, then:

$$\bar{v}^* = av_1 + bv_2 + cv_0 + dv_7 \quad (2.58)$$

The weights,  $a$  and  $b$ , determine the required fraction of the switching period that the inverter need to be held in a specific state, to obtain the required reference voltage. Since the sum of  $a$

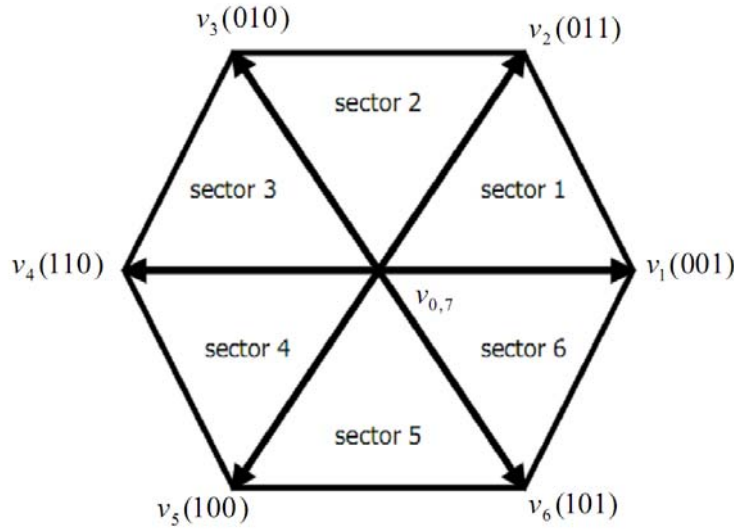


Figure 2.7: Voltage space vectors [3].

and  $b$  is not necessarily equal to the switching period, the remaining time has to be consumed by the zero voltage vector,  $v_0$  and  $v_7$ , which has no influence on the average voltage. The aim of space vector modulation is to switch the inverter states  $S_{0,k,k+1,7}$  in such a sequence so that a minimum number of switch transitions are obtained, thereby minimizing the inverter switching losses and generated harmonics [3]. The peak voltage obtainable by SVM is equal to that of sine-triangle modulation with third-harmonic injection. The reader is referred to [3, 25], for the implementation details of SVM.

#### 2.2.4.2 Inverter non-ideality compensation

The PMSM control design assumes that the inverter is ideal. In reality, the inverter has non-idealities which need to be compensated for, so that the motor control can achieve the performance predicted by the design.

In the overmodulation region of the sine-triangle modulation, the gain of the inverter is non-linear. Rowan *et al.* presents a compensation method to keep the gain linear in the overmodulation region [36].

**DC bus voltage disturbance rejection** As mentioned previously, in the sine-triangle modulation paragraph, a voltage ripple in the bus voltage will cause a current ripple in the motor currents. In the case that the voltage reference is generated by a current error, such as in vector control, the current control loop will reject the voltage ripple. In the case of an open-loop voltage controller, such as V/f control, the DC bus voltage ripple has to be compensated for. The reference voltage generated by the motor control has to be normalized to be within the limits of the PWM triangle for the gate signal generation. This normalization gain is the inverse of the inverter gain in equation 2.57. The inverter inverse gain cascaded with the inverter has a gain

of unity. Therefore, the inverse of the bus voltage disturbance, cancels with the disturbance on the inverter if the instantaneous bus voltage is used to calculate the inverse gain, as depicted in figure 2.8. The bus voltage on which the inverter depends is the instantaneous voltage, whereas the bus voltage used in the controller is an approximation of the fast-average value.

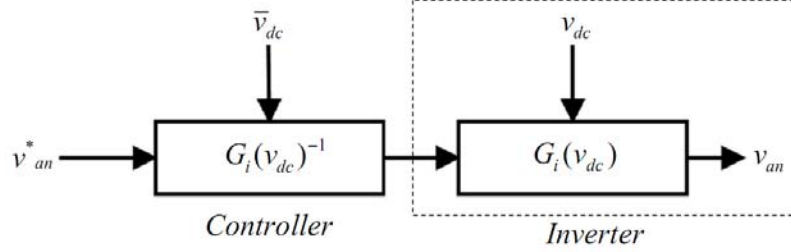


Figure 2.8: DC bus voltage disturbance rejection.

**Dead-time compensation** In order to prevent the top and bottom switch of the inverter from conducting simultaneously, causing a short-circuit known as shoot-through, a delay has to be inserted in the switch transition. This delay,  $T_{dt}$ , is known as dead-time or blanking time. The dead-time distorts the output voltage by causing a small offset in the fast-average of the output voltage, as shown in figure 2.9 (exaggerated). The distortion in the voltage causes a distortion in the PMSM current, hence a ripple in torque too. At low speeds the torque ripple cause startup problems and at higher speeds it contributes to hysteresis and eddy current loss. The current distortion characteristic due to dead-time is shown in figure 2.10.

The distortion near the zero-crossing is known as clamping. The distortion near the peak of a wave is due to the current clamping in another phase and the algebraic relation that the current in the isolated neutral point has to sum to zero. Due to its appearance, the dead-time distortion may be confused for a third harmonic. The zero current clamping is caused due to the inductive nature of the load: the current, which lags the voltage, is forced by the voltage to change polarity, now taking longer due to the decrease in voltage by the dead-time distortion. This explanation is oversimplified and does not explain why the current *clamps*. For a more thorough explanation the reader is referred to [37].

The analytic equation of the offset voltage (fast-average) in phase  $x$ , due to the dead-time is as derived by Ben-Brahim [37]:

$$\Delta v_x = -\frac{T_{dt}}{T_c} V_{dc} \times \text{sgn}(i_x) \quad (2.59)$$

where  $\text{sgn}(i_x)$  is the sign function of the current in phase  $x$  and the other parameters have been defined previously. The offset voltage due to the dead-time can be normalized by the inverter gain of equation 2.57 and be expressed independent of the bus voltage as:

$$\Delta d_x = -2f_c T_{dt} \hat{V}_c \times \text{sgn}(i_x) \quad (2.60)$$

where  $\Delta d_x$  is the effective duty cycle offset and  $\hat{V}_c$  is the peak of the PWM triangle wave. The

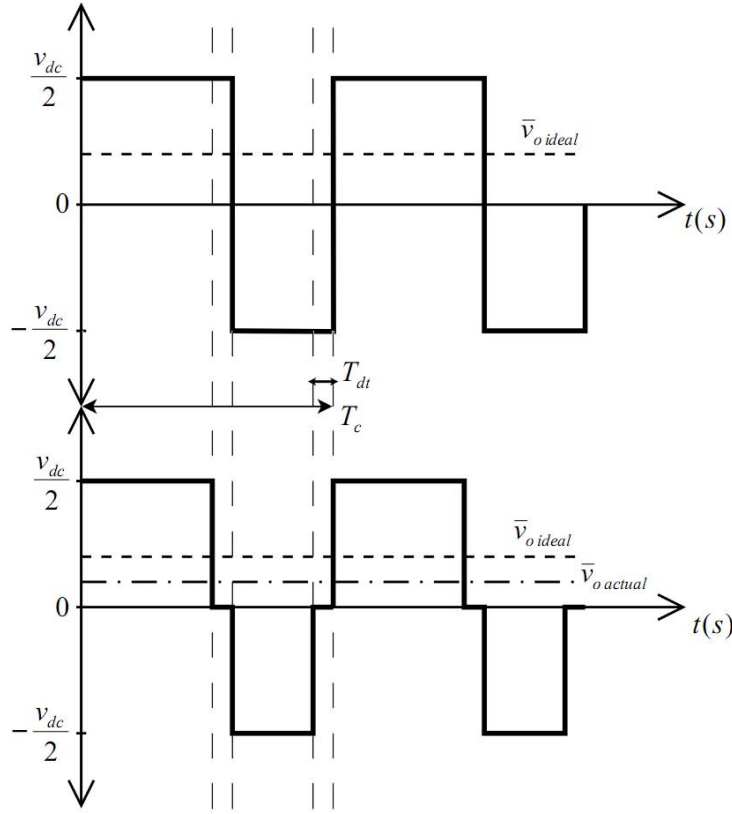


Figure 2.9: Dead-time effect.

analytic expression for the dead-time offset voltage is used as a feed-forward term to cancel (or at least compensate) for the dead-time effect, known as dead-time compensation (DTC). That is, the compensation term is added to the reference voltage to produce a compensated reference voltage as [37]:

$$\begin{aligned} v_c^* &= v^* + \Delta v_x^* \\ &= v^* + \frac{T_{dt}}{T_c} V_{dc} \times \text{sgn}(i_x) \end{aligned} \quad (2.61)$$

where  $\Delta v_x^* = -\Delta v_x$ . Note that the derivation of equation 2.59 accounted only for the dead-time delay and assumed ideal switches and an infinite slope for the switch transitions. Sul *et al.* presents a more accurate analysis, which accounts for device voltage drop and the switch transition slope [38]. During implementation, equation 2.59 is used as a guide that can be adjusted iteratively by observation of the current.

In order to compensate for the dead-time effect, accurate knowledge of the current zero-crossing instant is required due to the presence of the  $\text{sgn}(i_x)$  term. Uncertainty in the current zero-crossings due to noisy measurements and high frequency current harmonics, reduce the effectiveness of the added feed-forward term. To circumvent the effect of the noisy currents, Ben-Brahim suggests that the current reference be used instead of the measured current. He also proposes a



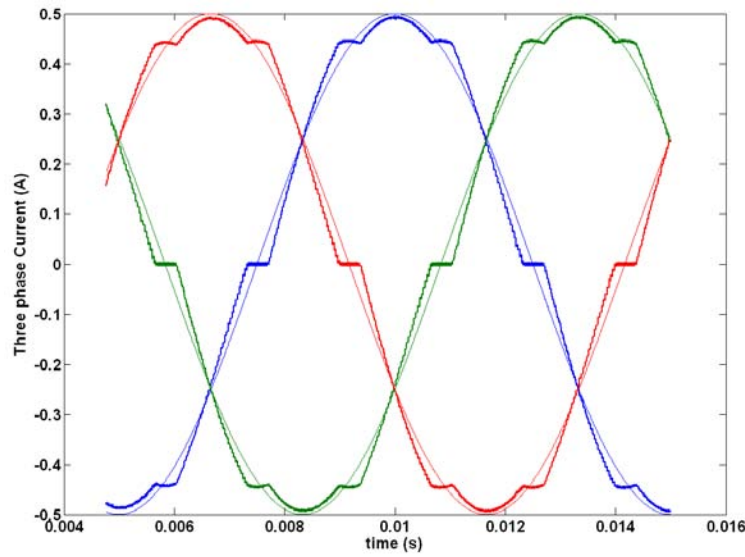


Figure 2.10: Current ripple due to dead-time distortion.

modified form of the conventional compensation technique by using a smooth transition of the current instead of the sign function [39]. The disadvantage of using the current reference is that it is only applicable in the case when the current is controlled, such as in vector control. In the case of an open-loop voltage control, such as V/f control, the measured current has to be used, since there is no current reference available.

A method of compensating for the noise in the current is with the use of a low pass filter. A normal filter would cause a phase lag and would therefore give an erroneous zero-crossing of the current. The phase shift can be prevented if the signal is first transformed to the rotor reference frame, then filtering and transforming back to stationary coordinates. This “extracts” the fundamental component of the current without a phase shift. Such a filtering method is implemented by Wang *et al.* [40].

Instead of compensating for the dead-time in an outer control loop with an average feed-forward signal, Leggate and Kerkman propose a compensation scheme which corrects for the dead-time pulse-by-pulse. This method produces less deviation in magnitude and phase than traditional compensation schemes [41]. Unfortunately, this method requires access to the low level implementation of the gating signals.

#### 2.2.4.3 Determination of phase-to-neutral voltages

The measurement of the phase-neutral voltage is important for parameter identification as presented in section 2.2.3. Vector control with a position sensor requires only the sensing of the motor currents and the rotor angular position, but in certain sensorless vector control schemes, the phase-to-neutral voltages are also important for estimation of the rotor angular position used in the control. Extra cabling, required for the controller to have access to the motor neutral, is

unwanted and depending on the motor design, the neutral connection may be inaccessible for measurement purposes.

The voltage at the isolated neutral connection of the PMSM is *mathematically* equal to the voltage at the fictitious neutral connection. This is not true for the instantaneous voltage, but for the fast-average voltage. This is useful to know because the derived model of the PMSM is in terms of the phase-to-neutral voltages. Hence, the phase-to-neutral voltage can be obtained without having access to the actual neutral connection for measurement. This is done by transforming the measurable phase-to-ground voltage into the phase-to-neutral voltage with [25]:

$$\begin{bmatrix} v_{an} \\ v_{bn} \\ v_{cn} \end{bmatrix} = \frac{1}{3} \begin{bmatrix} 2 & -1 & -1 \\ -1 & 2 & -1 \\ -1 & -1 & 2 \end{bmatrix} \begin{bmatrix} v_{ag} \\ v_{bg} \\ v_{cg} \end{bmatrix} \quad (2.62)$$

where the phase-to-neutral and phase-to-ground voltage is as shown in figure 2.4.

## 2.3 PMSM control strategies

### 2.3.1 V/f Control

#### 2.3.1.1 Principle of operation

The so called V/f control<sup>9</sup> is an open-loop control strategy, i.e. a control strategy with no position or speed sensor feedback. At standstill, a small voltage is applied to the stator of the PMSM, which establishes a stationary stator magnetic field. A torque exists due to the permanent magnet on the rotor that tends to align the rotor with the applied stator field. The frequency of the field established by the stator current is gradually increased, so that the rotor can follow the rotating field. Due to the physical and phase displacement of each phase's magnetic axis, a rotating field is produced.

A back-emf is induced in the stator, due to the change in flux linkage (by the rotating permanent magnets) relative to the stationary stator windings. In order for the torque producing current to be maintained, the terminal voltage has to be controlled to exceed the back-emf, by just the right amount to keep the current magnitude constant. The back-emf is proportional to the rotational frequency of the rotor, as observed in equation 2.27. Thus, the controlled voltage also has to increase proportionally to the rotational speed which explains the name of this type of control. The principle of V/f control is depicted in block diagram form in figure 2.11. This control technique is suited for applications which require low dynamic performance, i.e. a slow change in speed reference and no torque load step change, such as in pump and fan applications [24].

<sup>9</sup>Also called Volts/Hertz or scalar control.

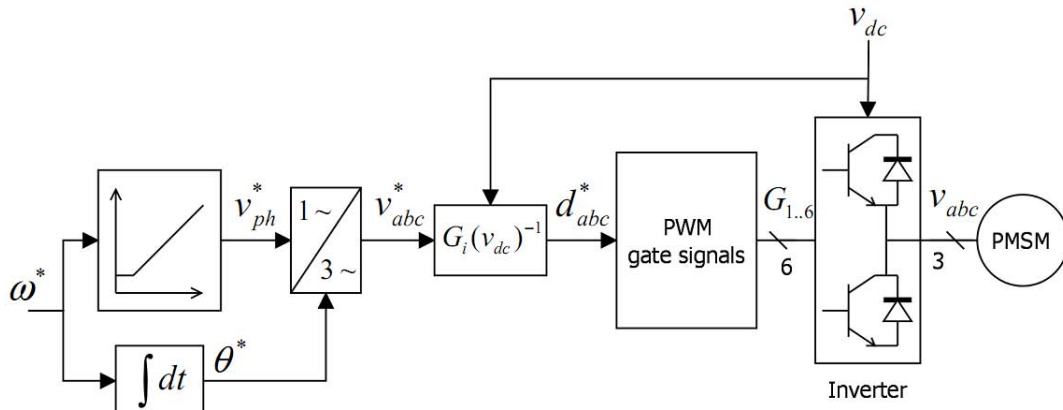


Figure 2.11: Open loop V/f control.

### 2.3.1.2 Stabilization

The induction machine is naturally stable. If the rotor speed decreases, the slip increases, thereby inducing larger torque-producing-current, which stabilizes the machine. The same stabilization effect can be obtained in synchronous machines by adding damper windings on the rotor.

Line-start PMSMs have a damper winding so that they have starting torque like an induction machine [24, 10]. Once it has started up, it locks into synchronism and the damper windings help to keep it in synchronism. Line-start machines are usually of the embedded magnet type, with the damper windings on the periphery of the rotor. These machines have a lower energy density and as discussed previously, the advent of semiconductor technology made inverter-fed PMSMs with variable frequency possible. The inverter-fed PMSM has starting torque without damper windings (hence without the associated losses of damper windings) and has higher energy density due to the fact that the magnets could be placed on the surface of the rotor.

High-speed applications use interior magnets on the rotor, so that the magnets are not subjected to a high centrifugal force. With the aid of a stainless steel jacket over the rotor, improvements on the magnetic material strength and proper adhesive, it became possible to use surface mounted permanent magnet synchronous machines (SPMSM) in high-speed applications [42]. In surface mount PMSMs, the damper windings increase the construction complexity and cost. In high-speed surface mount PMSMs it is even more unfeasible.

Without damper windings which help to keep the machine in synchronism, stability is a problem [24, 10]. A load disturbance or a sudden change in reference frequency will cause the motor to lose synchronism [43]. Also, the PMSM by itself is naturally unstable for a mid-range frequency [24].

Colby and Novotny added active damping by varying the inverter frequency in proportion to the electromechanical power perturbations. They obtained the power perturbations from the measured DC-link current [44].

Others to follow, have continued using similar principles to add stability, but usually using the

three-phase currents to calculate the power perturbations from which a stabilization command is obtained [24, 45]. The three-phase current is also required for dead-time compensation, hence the DC-link current measurement can be dispensed.

Ancuți and Boldea improved the usual stabilization scheme by including a control loop to reject perturbations in the flux linkage as well as in the power. With the added stabilization loops, the V/f control becomes more similar to vector control, in that trigonometric quantities (in effect coordinate transformations) are required. They note that their control is still computationally less intensive than sensorless vector control [46].

The load and machine parameters influence the design of the V/f curve. Zhao *et al.* presents an optimal design of such a curve for PMSMs in super-high-speed applications, which accounts for the stator resistance [47]. The importance of accounting for the stator resistance, for constant flux linkage, is discussed by Blaabjerg *et al.* [24].

### 2.3.1.3 Efficiency

The current in a V/f controlled drive is larger than necessary, i.e. besides the torque producing current a reactive component is also present. The reactive component in the current increases the copper loss.

Colby and Novotny present a search controller for loss minimization. The input power is measured, terminal voltage adjusted and input power is measured again to see if the change in terminal voltage decreased the input power. The stabilization loop prevents the search controller from reducing the real power which would cause the motor to lose synchronism [44].

Itoh *et al.* presents an analytical condition which minimizes the d-axis current by minimizing the reactive power. Thus, stability is provided with the real power perturbations and efficiency is improved by minimizing the reactive power. Their optimization control loop requires knowledge of the phase inductance [45].

Mademlis *et al.* compares the search controller method with an analytic loss model controller. They find that the search controller fails to reach a steady state condition which causes a torque disturbance for each search iteration update to the terminal voltage. Therefore, the analytic loss model method is favoured [48].

## 2.3.2 Vector control

### 2.3.2.1 Principle of operation

Vector or field oriented control (FOC) relies on the dq-coordinate model of the PMSM. The control principle can be explained with the use of the torque expression of equation 2.38, which is repeated here for convenience:

$$T_e = \frac{3}{2} z_p \lambda_p i_q \quad (2.63)$$

The aim of vector control is to control the current to satisfy a torque command (or reference). In the case of speed control, the torque reference is generated by a speed error. The torque reference in turn is used to obtain a current command in the rotor reference frame, with the use of the torque expression. The current command is compared to the actual current from which a rotor reference frame voltage command is generated. The sine-triangle modulator requires that the rotor reference frame voltage command be transformed to the stationary reference frame. The gate signals are then actuated by the inverter. Figure 2.12, illustrates this description of vector control.

Vector control answers the question of how to control the sinusoidal three-phase current in order to yield the required reference torque. The use of the dq0 coordinate transformation is central to the solution. The controlled current is treated as a vector in a reference frame which rotates with the rotor, resulting in a constant reference current after steady state has been reached. The current reference is controlled by a proportional and integral (PI) controller. Since the current reference is at 0 Hz and the integral controller has infinite gain at 0 Hz, a zero steady state error is possible.

There are essentially two control loops: the speed control loop and the inner current control loop. In the case of servo control, the reference speed is generated by a third outer control loop for the angular position.

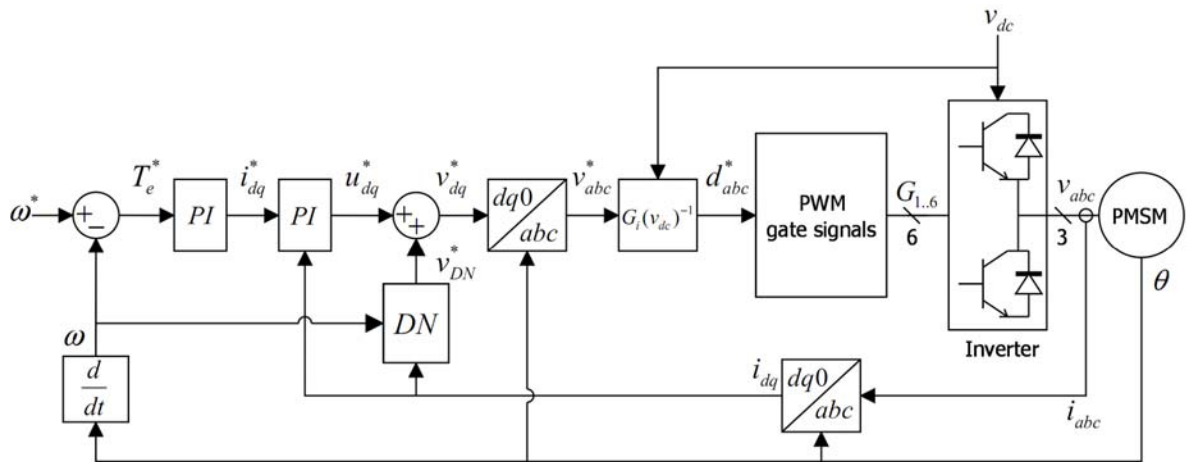


Figure 2.12: Vector control.

### 2.3.2.2 Current control loop

The current control in the synchronous reference frame was first proposed by Kerkman and Rowan. Before the synchronous reference frame current control was proposed, the current reference was transformed to the stationary reference frame from which a voltage command for each phase was obtained with a PI controller in each phase. This control had a limited bandwidth: after a certain rotational frequency the current control was gradually unable to enforce

the current reference. It was also thought that the reduction in gain was due to the motor back-emf. Kerkman and Rowan show that the deficiency of the controller is due to the properties of the stationary current controller and is not due to motor dependencies, such as the back-emf. The synchronous reference frame current regulator has zero steady state error for a much larger frequency range [49].

Lorenz *et al.* also investigates current regulators in the synchronous reference frame and models the current regulator with the use of complex vectors. It is shown that the model of a simple three-phase  $R - L$  load transformed to the synchronous reference frame has a cross-coupling term. Although the synchronous reference frame current controller has zero steady state error, the cross-coupling term degrades the transient performance of the current control. They show that the cross-coupled terms can be decoupled with feed-forward terms, resulting in improved transient current control performance [50]. This is the purpose of the  $DN$  (Decoupling Network) feed-forward term in the block diagram of figure 2.12.

Depending on how the control blocks are arranged, the feed-forward terms may be present in the feedback path. Hence, this type of linearization of the PMSM is better known as feedback linearization as presented by Chiasson *et al.* [51]. Quang and Dittrich use a formal method in which the required feedback terms to linearize certain classes of non-linear systems, are determined systematically. The method is known as exact linearization [32]. In the case of the PMSM model, the required feed-forward terms for linearization can be obtained via inspection of its mathematical model.

For the speed control loop, the current control loop is considered ideal, because the mechanical and electrical time constants are far apart. In servo control systems with low rotor inertia this is not necessarily the case.

### 2.3.2.3 Different control objectives

The vector control described thus far is known as constant current angle control, where the current angle,  $\gamma$ , equals  $90^\circ$ . Krishnan named this constant torque-angle control, where he defined the torque angle as the angle measured from the d-axis to the resultant stator current vector,  $i_s$  [28]. Sarma (and elsewhere in the literature) defines the torque angle,  $\delta$ , as the angle measured from the q-axis to the resultant stator voltage vector,  $v_s$  [52].

A constant current angle of  $90^\circ$  yields the most efficient control because the reactive d-axis current is zero. Different criteria may be used to determine the current angle to realize different control objectives such as: unity power factor control, constant mutual air gap flux linkage control, optimum torque-per-ampere control and flux weakening operation. The aim of the first three types of control is basically to utilize the inverter more efficiently and the flux weakening operation is to drive the motor beyond its rated speed [28].

#### 2.3.2.4 Field weakening

To increase the speed of a PMSM machine beyond the limit imposed by the DC bus voltage, the flux linkage between the stator and rotor needs to be decreased in the d-axis, called flux weakening. This is necessary because at high speed the back-emf exceeds the voltage that can be modulated by the inverter. This limit is imposed by the bus voltage. A higher bus voltage may be selected, but this increases the inverter losses. The inverter switch specification need to be increased and thus the cost. Also, a higher voltage source may not be readily available.

Field weakening is discussed by Pillay and Krishnan as one of the criteria for comparing the BDCM and PMSM operation [2]. Vas *et al.* discusses field weakening and its implementation in vector and direct torque control (DTC) algorithms. Performance features such as torque ripple and quickness of torque response are used to compare the two control algorithms. Instability using DTC in the high-speed region is also stressed [5].

In addition to the adaptive observers presented by Xu and Wang earlier, an adaptive flux weakening algorithm, which is computationally efficient, is also presented [53].

The current control method presented by [4] automatically drives the machine into the flux weakening region once the required DQ voltage has exceeded a certain amount.

#### 2.3.3 Sensorless vector control

In high-speed applications, the use of an encoder to feed back position (and hence speed) information becomes impractical. This is due to the cost and reliability of high-speed position sensors [45].

One approach to addressing this problem is to increase the reliability of the position sensor. Bunte and Beineke propose a method of reducing the systematic errors made by resolvers and encoders (in high performance applications) which give a sinusoidal signal, without a substantial increase in computations [54].

The second approach is to discard the route of using a sensor. There are essentially two sensorless techniques to determine the position and speed of a PMSM, namely high frequency injection and state observers [13]. Sensorless vector control is illustrated in figure 2.13. Instead of feeding back a measured angular position, it is estimated from the measured motor current and terminal voltage.

The high frequency injection technique depends upon the saliency of the machine (different reluctance in the d-axis than in the q-axis). It further assumes that the inverter switching frequency can be modulated high enough to inject these high frequencies, which increases losses in the inverter. Hence, it becomes impractical in machines with low saliency and/or high frequency operation. A high frequency can be obtained either with a high speed or a large number of poles. Despite its dependence on saliency, Staines *et al.* use this technique for a surface mounted PMSM, which has a characteristically low saliency factor. This could be done because of a small

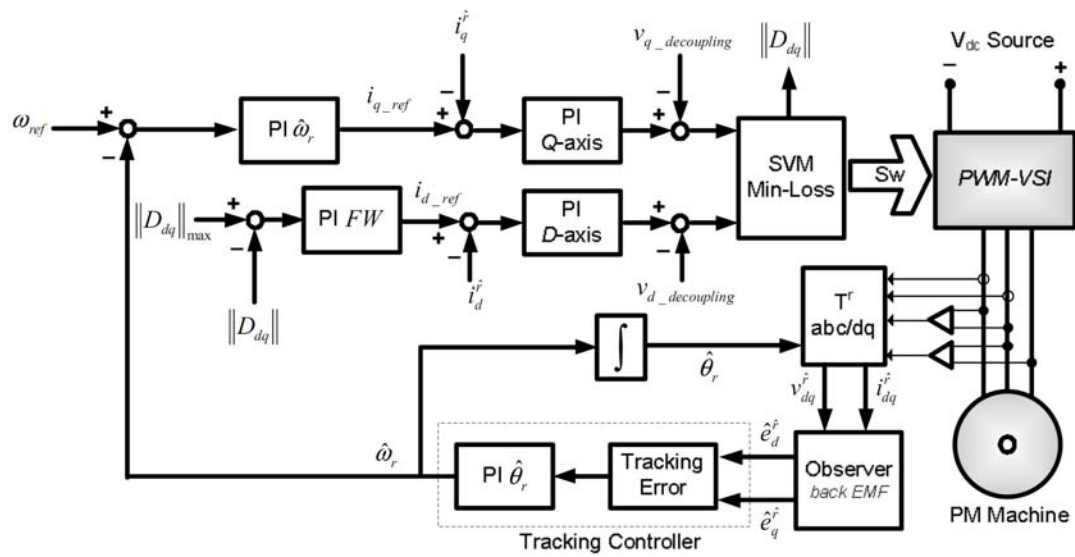


Figure 2.13: Sensorless vector control [4].

amount of saliency that is still present in practice. The experiments were done for a low speed machine (1500 rpm).

Observers measure some of the state variables and incorporate the measurements into an inverse model<sup>10</sup> to approximate other unknown state variables, like position and speed for PMSMs. Another type of observer uses a state model where the error between estimated and measured outputs is used to drive internal model states to that of the physical system, such as the Luenberger observer. Observers suffer at standstill and low speed, because it relies on the measured back-emf of the PMSM, which has a low signal to noise ratio at low speeds [13].

To overcome the problem of sensorless drives at near zero speeds, quasi-sensorless drives have been implemented. This is done by using Hall-effect sensors to determine rotor position at near zero-speeds. As the speed and back-emf increase, the controller may switch over to using only an observer or may use both methods [14, 55, 15]. Other types of quasi-sensorless drives use smart integrated sensor ball bearings [56].

A technique for combining multiple sources of state variable information from observers and sensors, to obtain state variables with less uncertainty is the Kalman filter. Bolognani *et al.* uses an Extended Kalman Filter (EKF)<sup>11</sup>, but only using the dynamic information as an observer for speed and position. Their technique does not require initial knowledge of the mechanical parameters or position [57].

In some cases a predetermined pulse sequence is applied to align the rotor to a known position before starting. In certain applications the rotor is not allowed this alignment step. Hu *et al.* discusses a magnetic pole position identification technique using space vector PWM and confirms its use experimentally. First, the pole magnetic axis is determined, but with a  $180^\circ$  uncertainty,

<sup>10</sup>Feed-forward estimator.

<sup>11</sup>The normal Kalman filter is used for linear systems only, whilst the EKF is appropriate for non-linear systems too, such as the PMSM.



after which the pole polarization is determined using a saturation technique [58]. It is important to note that the measurement pulses do not rotate the rotor. A method that is very similar is suggested by Batzel and Lee [59]. If the rotor is allowed to move then the predetermined pulse sequence may alternatively be used for a dither start up of the machine [59].

Östlund and Brokemper also present a zero to rated speed position detection technique. At standstill it relies on saliency and at higher speeds it uses an observer. The technique is presented for an integrated motor drive, i.e. the drive is deployed with the motor, which makes it acceptable to include very specific machine parameters in the controller [60].

Shinnaka presents a flux-state observer for salient or non-salient machines with very low computational burden, which makes it usable for high frequency control purposes [61].

Another type of observer is to estimate the speed from the measured position signal, instead of using a backward difference approximation for the derivative. Such a method is proposed by Chiasson *et al.* in [51]. It was found that the speed observer yield superior speed resolution in comparison to the backward difference numeric differentiation of the position signal obtained from an encoder position sensor<sup>12</sup>. An encoder cannot measure initial position, but only a  $\Delta\theta$  for each pulse of the encoder is given as output when rotating. Thus the rotor is pre-aligned to a known position,  $\theta_{start}$ , such that the resultant position is obtained by:

$$\theta(t) = \sum \Delta\theta + \theta_{start} \quad (2.64)$$

Yue *et al.* developed a robust adaptive initial-position and speed observer using Lyapunov stability theory. The load inertia and motor parameters are assumed unknown. The observer assumes limited friction and disturbances. The only inputs to the observer are an incremental encoder and stator current signals [62]. This is similar to the observer presented by [51], except that the initial position via pre-alignment is not required.

In cases the dynamic performance requirements are low, such as in fan-type applications, the observer requirements are also lowered. In Sul *et al.* a linear observer is developed, along with a new type of tracking controller using a phase-locked loop, used to track the rotor position and speed. The design steps of the controller are thoroughly presented. Even though it is for a sensorless controller, the design of the current controller and speed control loop is still applicable to a vector controller with position sensor feedback [4].

The load of a machine is part of the plant model. A changing load causes the controller to no longer be optimal and the observers are not as accurate. To account for changes in the system, the controller needs a certain degree of adaptivity. Tursini *et al.* presents a proportional and integral controller gain tuning technique for when the load changes [63].

The non-linear nature of the PMSM causes the use of linear observers with fixed gains to become unstable. To obtain stability the system has to make use of gain scheduling. For each operating

<sup>12</sup>Note that this is not a true “Sensorless” control but it is included in this section because of the use of an observer.

point, the gain of the observer is calculated for the PMSM linearized about that operating point. The optimal controller of Chang *et al.* uses such a gain scheduling technique [23].

Xu and Wang present an adaptive rotor position observer which is required to decrease errors introduced by delay in the measurements of the electrical quantities used in the observer [53]. Xu and Chi address the stability problem that arises when a sensorless vector control algorithm is developed for a motor that runs up to 60 000 rpm. They also note the undesirable effect of sampling delay and continue to develop a flux observer with less phase shift [13].

The switching noise caused by the inverter can be suppressed with the use of a three-phase LC filter. The extra states due to the filter components should be accounted for in the observer of a sensorless drive. A review of different three-phase LC filter topologies and the design of the extended observer, for both the IM and PMSM drives, is addressed in the thesis of Salomäki [64].

## 2.3.4 Direct torque control

### 2.3.4.1 Principle of operation

Similar to vector control, the principle of direct torque control (DTC) can be explained from the torque equation, this time expressed in a different form [65]:

$$T_e = \frac{3}{2} \frac{1}{L_s} z_p |\lambda_s| |\lambda_p| \sin(\delta) \quad (2.65)$$

where the stator flux linkage magnitude is given by:

$$|\lambda_s| = \int |\mathbf{v}_s - R_s \mathbf{i}_s| dt \quad (2.66)$$

Instead of controlling the current to satisfy a reference torque (which is generated by negative feedback of the rotational speed), the torque is controlled directly by controlling the stator flux linkage vector with appropriate stator voltages. The stator voltage in DTC is controlled exclusively with the space vector modulation technique, due to the inherent nature of DTC.

Similarly to vector control, there is a position sensorless version of the DTC. The sensorless DTC is more common which misleads some authors to state that DTC is exclusively a sensorless control technique. The sensorless direct torque controller is shown in figure 2.14. In the position sensor case, the flux estimator makes use of the rotor angular position.

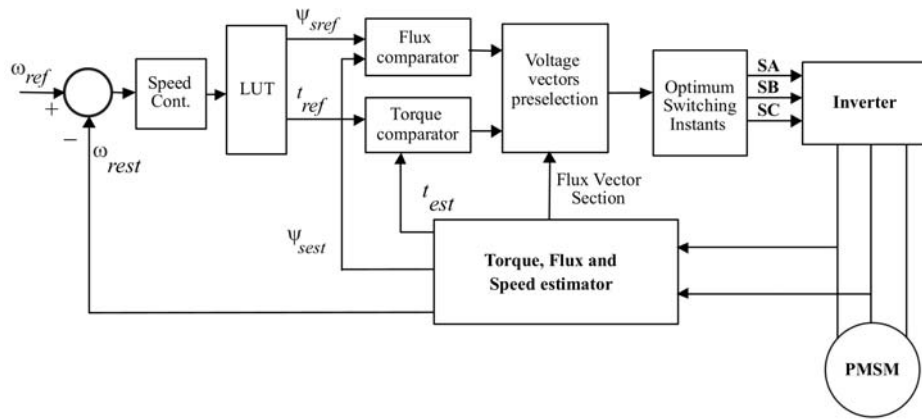


Figure 2.14: Direct torque and flux control [5]

### 2.3.4.2 DTC control features

Direct torque control has some notable characteristics. The torque control dynamics is quicker than that of vector control, but has higher torque ripple than for vector control. The main problem addressed for DTC in PMSM drives is the torque ripple. This is due to the motor reacting differently to the zero voltage vectors than in the induction motor [65]. Vas *et al.* presents a method of reducing the torque ripple for DTC [5].

Similarly to vector control, there are still two control loops, but the current control loop is replaced by a flux linkage control loop. The torque and flux controller is controlled by hysteresis controllers which contribute to torque ripple and variable switching frequency. Taibi *et al.* also present methods to reduce the torque ripple. This is done by a non-hysteresis controller and by injection of a dither signal [66].

DTC is also less dependent on known motor parameters, which increases its robustness. The flux estimator is sensitive to stator resistance variation. The back-emf estimators of sensorless vector control are also sensitive to this parameter [66].

The computational burden of DTC is regarded as lower than that of vector control due to the lack of the dq0 transformations. For the same reason its implementation is claimed to be easier. For a more detailed comparison between DTC and vector control the reader is referred to the article by Merzoug and Naceri [67].

## 2.4 Summary

The important achievements of the literature study can be summarized as follows:

- A mathematical model of the PMSM, appropriate for control development and simulation has been identified. An overview of its derivation has also been presented.

- The method of determining the parameters of the aforementioned PMSM model was presented.
- Aspects of the non-ideal voltage source, in the form of the voltage source inverter, were identified in the literature. Special attention has to be given to the compensation of these effects, since the PMSM control assumes an ideal voltage source.
- An overview of the different PMSM control strategies was given, which introduced the basic operational principle of each control strategy. Important aspects of the V/f controller included the required stabilization and efficiency loops. The two important control loops of the vector controller, namely the current control loop and the speed control loop were also investigated.

## Chapter 3

# Controller design

This chapter presents the design of the V/f and vector controllers. This is preceded by design preliminaries which present the PMSM parameters used in the design and the Matlab/Simulink<sup>®</sup> simulation model of the PMSM used to verify the designed controllers later on in this chapter.

The vector controller design consists out of the design of the current and speed control loops. Special attention on the current control is given with a discussion on the feed-forward terms required to linearize the current control. A derivation of extra decoupling terms which compensates for the delay in the current control (which is important especially at high speeds) is presented. The speed controller design consists out of three parts, namely the design of the reference speed generator, the observer which extracts the PMSM speed from the measured position and the PI speed control gains (which is heavily dependent on the speed observer bandwidth).

The V/f controller design consists of several parts: derivation of the open-loop feed-forward voltage, linearization of the V/f controller to inspect the machine stability numerically, a reduced order model from the linearized machine model from which analytical insight is gained into the lack of damping, design of the stabilization loop and the design of the high efficiency loop. The method of stabilization (as commonly used in the literature) is presented.

The design of both the vector and V/f control is verified via simulation of the motor response to a speed ramp and a torque load step after the motor has reached the reference speed.

The chapter concludes with a section considering the inverter non-idealities which adversely affects the designed controllers. The compensation of the inverter non-idealities are also presented and verified via simulation.

### 3.1 Design preliminaries

#### 3.1.1 PMSM parameters

Throughout the controller design of this chapter, the PMSM parameters as presented in table 3.1 are used, except where indicated. These parameters were obtained with the least squares

identification method discussed in section 2.2.3.2. The Matlab<sup>®</sup> implementation of the least squares identification is presented in appendix A.3.

Table 3.1: PMSM parameters

Parameter description	Symbol	Value	Parametric Error Index
#Pole pairs	$z_p$	1	N/A
Stator inductance	$L_d$	$448 \times 10^{-6} \text{ H}$	9.86
Stator resistance	$r_s$	$0.158 \Omega$	27.1
Stator permanent magnet flux linkage	$\lambda_p$	$49.7 \times 10^{-3} \text{ Wb.t}$	2.24
Rotor polar moment of inertia	$J$	$1.91 \times 10^{-3} \text{ kg.m}^2$	281
Viscous friction loss coefficient	$B$	$90.4 \times 10^{-6} \text{ N.m.s/rad}$	1230
Coulomb friction force	$T_l$	$0.122 \text{ N.m}$	1192

Note the large coulomb friction force, which is uncharacteristic of high-speed PMSMs. This may be due to a number of various causes in the mechanical design and/or assembly procedure.

### 3.1.2 PMSM simulation model

Simulation of the designed controllers in this chapter use a simulation model of the PMSM based on the state-space model presented in section 2.2.2.7. The simulation models presented in this chapter are implemented in Matlab/Simulink<sup>®</sup>. The simulation models are constructed in a hierarchical form of varying levels of abstraction, via the *Subsystem* feature of Matlab/Simulink<sup>®</sup>. The top level of the PMSM simulation model with its immediate lower level is as shown in figure 3.1.

The sub-levels of the electrical and mechanical domain subsystems of figure 3.1, are implemented as shown in figure 3.2.

The implementation of the transformation to and from the rotor reference frame, as used in the PMSM simulation model of figure 3.1, is shown in figure 3.3.

A user-interface for parameter input of the PMSM model is created via the *Mask Subsystem* feature of Matlab/Simulink<sup>®</sup>. The parameter menu is presented in figure 3.4. The entered parameters are those of table 3.1. Note that the peak flux linkage is initialized at the start of simulation by:

$$\lambda_p = \sqrt{2} \frac{E_s}{\omega_s} \quad (3.1)$$

where  $E_s$  is the rated no-load stator rms voltage at the rated stator frequency,  $\omega_s$ .

## 3.2 Vector control

The operational principle of vector control is presented in section 2.3.2. This section's aim is to present the control design of the vector control.

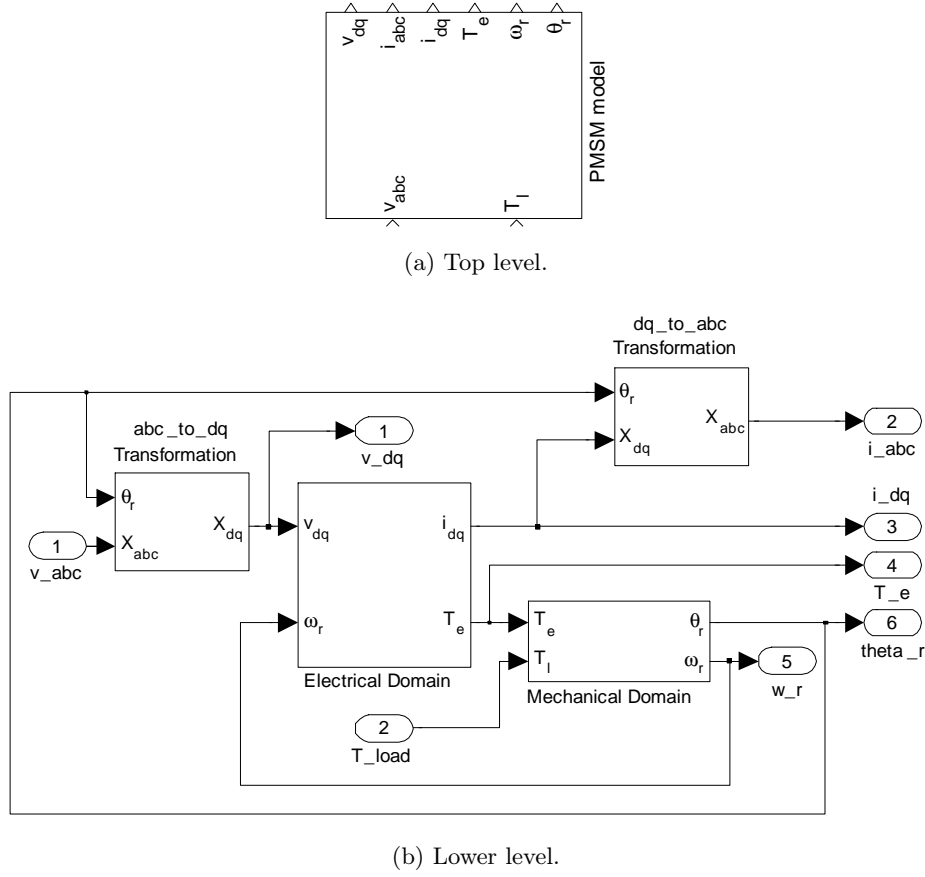


Figure 3.1: PMSM simulation model (motor).

### 3.2.1 Current control

#### 3.2.1.1 Linearized model via feed-forward terms

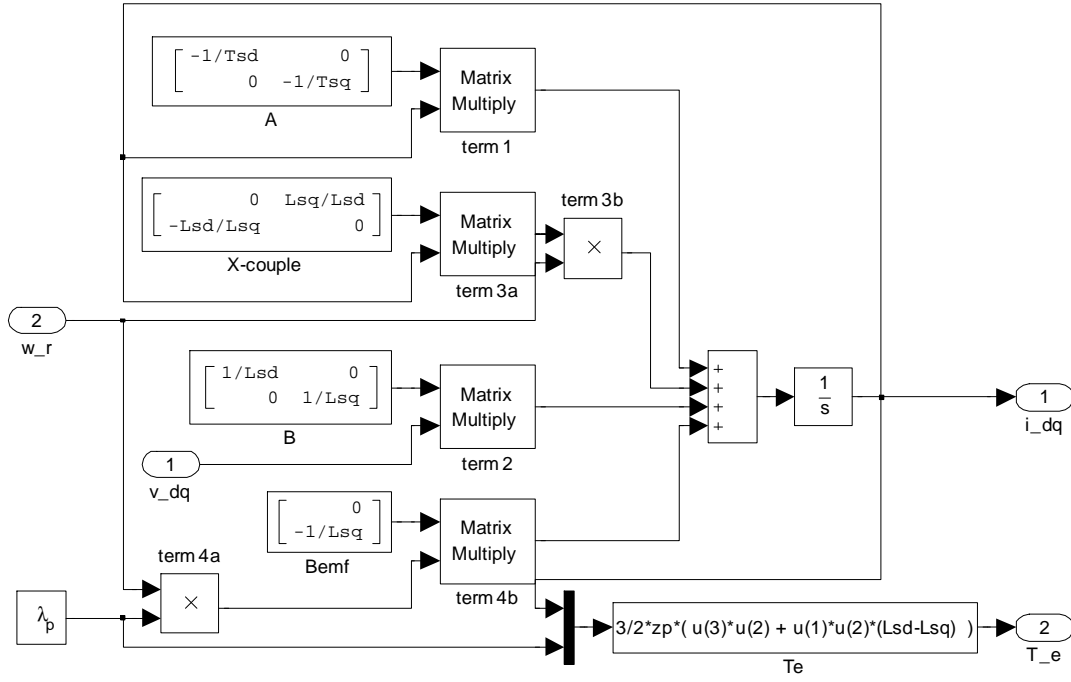
In order to follow a reference speed signal, a torque reference (generated via negative feedback of the speed control loop) has to be actuated. The torque reference is actuated by means of the current control loop. The feed-forward linearization is assumed ideal so that the stator set of differential equations reduce to those of a two-phase  $RL$ -circuit:

$$pi_d = \frac{1}{L_d} (r_s i_d + v_d^*) \quad (3.2)$$

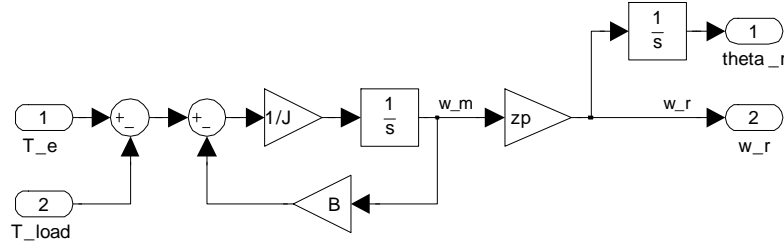
$$pi_q = \frac{1}{L_q} (r_s i_q + v_q^*) \quad (3.3)$$

where  $v_d^*$  and  $v_q^*$  are reference voltages which are generated by the PI current control loop. The feed-forward linearization is performed by adding terms to the reference voltage which cancel with the cross-coupling terms which inherently form part of the PMSM model. The decoupling term is:

$$\mathbf{v}_{dq}^{DN} = -\omega \begin{bmatrix} 0 & L_q \\ -L_d & 0 \end{bmatrix} \begin{bmatrix} i_d \\ i_q \end{bmatrix} \quad (3.4)$$



(a) Electrical domain.



(b) Mechanical domain.

Figure 3.2: PMSM simulation model sub-domains.

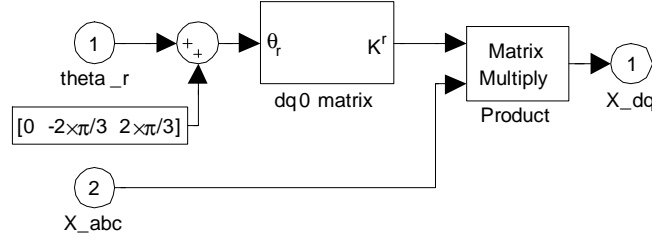
With the plant of the current control loop linearized, classical control design methods are applicable.

Another source of cross-coupling is that due to the anti-aliasing filters, as shown by Sepe and Lang [68]. As with the PMSM model, the cross-coupling can be corrected with feed-forward terms. The cross-coupling terms are derived by transforming the state-space model of the filters in the stationary reference frame to the rotating reference frame. The state-space model of the first-order, three-phase, anti-aliasing filter is:

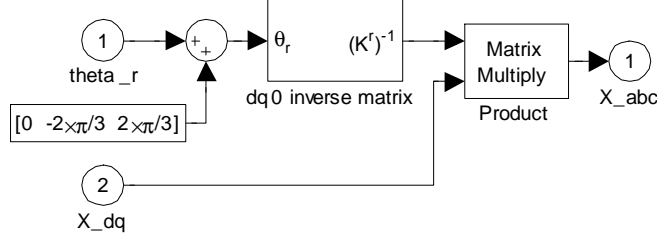
$$p \begin{bmatrix} i_{af} \\ i_{bf} \\ i_{cf} \end{bmatrix} = \begin{bmatrix} -\frac{1}{R_f C_f} & 0 & 0 \\ 0 & -\frac{1}{R_f C_f} & 0 \\ 0 & 0 & -\frac{1}{R_f C_f} \end{bmatrix} \begin{bmatrix} i_{af} \\ i_{bf} \\ i_{cf} \end{bmatrix} + \begin{bmatrix} \frac{1}{R_f C_f} & 0 & 0 \\ 0 & \frac{1}{R_f C_f} & 0 \\ 0 & 0 & \frac{1}{R_f C_f} \end{bmatrix} \begin{bmatrix} i_a \\ i_b \\ i_c \end{bmatrix} \quad (3.5)$$

Note that input and filter signals  $i_x$  and  $i_{xf}$  are not the actual currents, but are voltage signal





(a) Stationary to rotor reference frame.



(b) Rotor to stationary reference frame.

Figure 3.3: dq0 transformations.

outputs from current sensors, which are denoted with current symbols.

The stationary to rotating reference frame transformation for a state-space model is:

$$\begin{aligned}
 p\mathbf{x}_{abc} &= \mathbf{A}\mathbf{x}_{abc} + \mathbf{B}\mathbf{u}_{abc} \\
 p(\mathbf{K}_r)^{-1}\mathbf{x}_{dq0} &= \mathbf{A}(\mathbf{K}_r)^{-1}\mathbf{x}_{dq0} + \mathbf{B}(\mathbf{K}_r)^{-1}\mathbf{u}_{dq0} \\
 \mathbf{K}_r p(\mathbf{K}_r)^{-1}\mathbf{x}_{dq0} &= \mathbf{K}_r \mathbf{A}(\mathbf{K}_r)^{-1}\mathbf{x}_{dq0} + \mathbf{K}_r \mathbf{B}(\mathbf{K}_r)^{-1}\mathbf{u}_{dq0}
 \end{aligned} \tag{3.6}$$

where  $p$  is the time derivative operator,  $\frac{d}{dt}$ . Assuming that system and input matrices are symmetrical, the equations can further be simplified to:

$$\mathbf{K}_r p(\mathbf{K}_r)^{-1}\mathbf{x}_{dq0} = \mathbf{A}\mathbf{x}_{dq0} + \mathbf{B}\mathbf{u}_{dq0} \tag{3.7}$$

The final step in deriving the rotating reference frame state-space model is to apply the chain rule of differentiation to the left-hand-side term. The simplification thereof is the same as for equation 2.22. After simplification, the state-space model in the rotating reference frame becomes:

$$p\mathbf{x}_{dq0} = (\mathbf{A} - \omega_r \mathbf{J})\mathbf{x}_{dq0} + \mathbf{B}\mathbf{u}_{dq0} \tag{3.8}$$

Rearranging the state-space model in terms of the state vector (although implicitly), yields:

$$\mathbf{x}_{dq0} = -\mathbf{A}^{-1}\mathbf{B}\mathbf{u}_{dq0} + \mathbf{A}^{-1}\omega_r \mathbf{J}\mathbf{x}_{dq0} + \mathbf{A}^{-1}p\mathbf{x}_{dq0} \tag{3.9}$$

which reveals the cross-coupling term (due to the skew symmetric matrix  $\mathbf{J}$ ) as the second

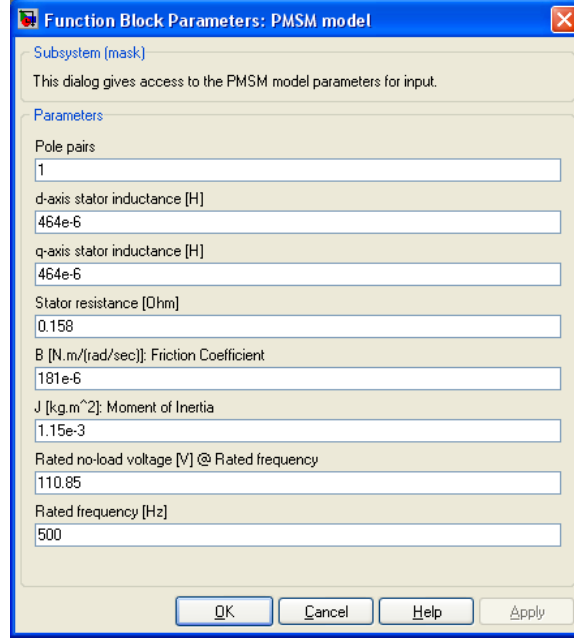


Figure 3.4: PMSM model user-interface.

right-hand side term:

$$\mathbf{x}_{dq0}^X = \mathbf{A}^{-1} \omega_r \mathbf{J} \mathbf{x}_{dq0} \quad (3.10)$$

Since the filter's transfer matrix is diagonal, its inverse is simply the reciprocal of the entries on the diagonal.

The delay of the zero-order hold (ZOH) cause cross-coupling, similar to that due to the phase shift of the anti-aliasing filter. Figure 3.5, depicts the delay as a rotation of the current angle. The erroneous current due to the delay is measured as:

$$\begin{bmatrix} \tilde{i}_d \\ \tilde{i}_q \end{bmatrix} = |\tilde{\mathbf{i}}_s| \begin{bmatrix} \sin(\phi) \\ \cos(\phi) \end{bmatrix} \quad (3.11)$$

where the phase delay is:  $\phi = \omega_r \frac{T_s}{2}$ . The delay is assumed to be half a sampling period,  $\frac{T_s}{2}$ .

Even for a small delay, the coupling from the  $q$ -axis to the  $d$ -axis can be substantial for a large current magnitude,  $|\mathbf{i}_s|$ . For a small delay, the trigonometric functions can be approximated so that the delayed current is given by:

$$\begin{bmatrix} \tilde{i}_d \\ \tilde{i}_q \end{bmatrix} \approx |\tilde{\mathbf{i}}_s| \begin{bmatrix} \omega_r \frac{T_s}{2} \\ 1 \end{bmatrix} \quad (3.12)$$

which shows that for constant current angle control with a current angle of  $\frac{\pi}{2}$ , that the  $q$ -axis current is unaffected, i.e.  $\tilde{i}_q \approx |\tilde{\mathbf{i}}_s|$  and that coupling is mainly from the  $q$ -axis to the  $d$ -axis:  $\tilde{i}_d \approx \tilde{i}_q \omega_r \frac{T_s}{2}$ .

The cross-coupling due to the anti-aliasing filter and sampler delay can be combined to yield

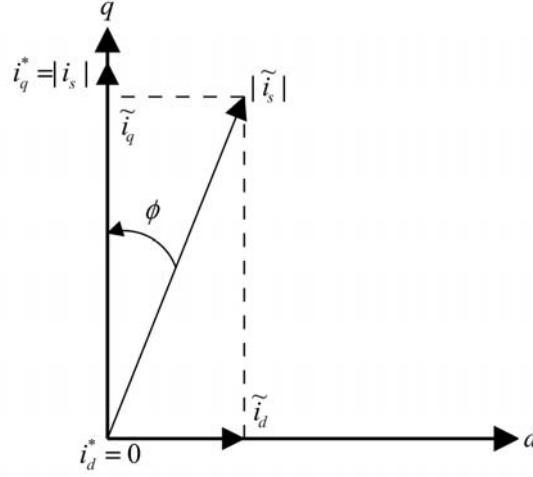


Figure 3.5: Measured current vs. actual current due to sampler delay.

the total cross-coupling in the measured current:

$$\begin{aligned}
 \mathbf{i}_{dq}^X &= \mathbf{A}^{-1} \omega_r \mathbf{J} \mathbf{i}_{dq} + \begin{bmatrix} 0 & \omega_r \frac{T_s}{2} \\ 0 & 0 \end{bmatrix} \mathbf{i}_{dq} \\
 &= \omega_r \begin{bmatrix} 0 & \frac{1}{\omega_c} + \frac{T_s}{2} \\ -\frac{1}{\omega_c} & 0 \end{bmatrix} \mathbf{i}_{dq}
 \end{aligned} \tag{3.13}$$

where  $\omega_c$  is the cut-off frequency of the anti-aliasing filter. Equation 3.13 can be used as a feed-forward correction term in the control to yield a better estimate of the actual current. Note the dependence on the rotational speed, hence the importance of correcting the cross-coupling for high-speed PMSMs.

If the controller's computation frequency can be implemented high enough, then the sampler delay is negligible and the anti-aliasing filter cut-off frequency can be set high, so that feed-forward correction of the cross-coupling may unnecessary. The advantage of using the feed-forward correction is that, even with the added computations (four multiplications and two additions) due to the feed-forward correction, a smaller control frequency may be used.

### 3.2.1.2 Digital control design preliminaries

Due to the control complexity, the control sampling period is constrained by the hardware characteristics on which the control algorithm is executed. Note that the control of both the motor and generator (which serves as a torque load) has to execute on the dSPACE® DS1005 controller. From previous experience with the DS1005 controller, the control frequency is chosen as 10 kHz.

To investigate if the sampling frequency is fast enough, the ratio between the system time constant and the sampling period is inspected. A small ratio has a larger destabilizing effect on

the control system. In the case of the PMSM, the dominating time constant is that due to the stator electrical dynamics:

$$\begin{aligned}\tau_e &= \frac{L_d}{r_s} \\ &= \frac{448 \times 10^{-6}}{0.158} \\ &= 2.84 \times 10^{-3} \text{ s}\end{aligned}\tag{3.14}$$

It can be seen that the electrical time constant,  $\tau_e$ , is roughly twenty five times larger than the chosen control period:

$$\frac{\tau_e}{25} = 113 \mu\text{s} \approx T_s = 100 \mu\text{s}$$

This result would lead one to conclude that the effect of the sampling period is negligible. Unfortunately the non-linear nature of the PMSM also has to be considered. In order for the constant current control to perform well, the current angle has to be controlled at  $\frac{\pi}{2}$ . During the transient response to a step in load torque, the phase difference between reference and actual current angle has to be kept to a minimum. The assumption that the non-linear torque:

$$T_e = K_t i_q \sin(\gamma)\tag{3.15}$$

may be approximated with the linear torque:

$$T_e = K_t i_q C\tag{3.16}$$

rests entirely on how well the current angle can be controlled to be constant *at all times*. At the peak torque producing current angle of  $\frac{\pi}{2}$ , a lag in the phase current angle would decrease the actuated torque and therefore increase the phase lag due to a torque load disturbance even more, resulting in a positive feedback effect. Given a torque load disturbance equal to the rated torque, the deviation of the actual position with respect to the expected position in one sampling period is unnoticeable:

$$\begin{aligned}\Delta\theta_{max} &= \frac{d\omega}{dt} T_s^2 \\ &= \frac{T_e}{J} T_s^2 \\ &= \frac{2.5}{1.9 \times 10^{-3}} (100 \times 10^{-6})^2 \\ &= 13.2 \mu\text{rad}\end{aligned}\tag{3.17}$$

Note the difference in orders of magnitude between the mechanical and electrical time constants:

$$\tau_m = \frac{J}{B} = \frac{1.91 \times 10^{-3}}{90.4 \times 10^{-6}} = 21.1 \text{ s}\tag{3.18}$$

Therefore, the destabilizing effect of the current angle being misaligned with respect to the

permanent magnet angular position due to a torque disturbance is damped due to the rotor inertia. Thus, the controller sampling frequency may be considered sufficient.

The sample-and-hold delay of the analogue-to-digital converter (ADC) needs to be taken into account when designing the current control gains due to the phase lag it introduces in the current control loop<sup>1</sup>. If the sampling frequency is much larger than the closed-loop bandwidth of the controlled system, the delay due to the sample-and-hold can be neglected and the controller can be designed in the  $s$ -plane. This is known as *design by emulation* [31]. The continuous  $s$ -plane transfer function of the controller can then be written in terms of its differential equation representation and be discretized into a difference equation, which is in appropriate form for implementation on a digital signal processor (DSP). The sampling frequency has to be a factor of ten times larger than the closed-loop bandwidth in order for the ZOH delay to be considered negligible, according to de Kock [31]. The delay caused by the ZOH for the chosen sampling period at a rotational frequency of 500 Hz, is  $9^\circ$ . This position delay is of a static nature which cause cross-coupling between the dq-axis of the measured current. Section 3.2.1.1, showed how to compensate for this static phase shift and the preceding paragraph showed that the dynamic phase shift (i.e. the phase shift due to a small signal disturbance) is limited by the rotor inertia.

The phase lag of the ZOH is accounted for in the design of the high-speed PMSM current controller, by designing the controller in the  $z$ -plane, so that stability is assured. The transfer function of the plant and ZOH in the  $z$ -domain is:

$$\begin{aligned} G(z) &= Z[G(s) H_{ZOH}(s)] \\ &= Z\left[G(s) \frac{1 - e^{-T_s s}}{s}\right] \\ &= \frac{z - 1}{z} Z\left[\frac{G(s)}{s}\right] \end{aligned} \quad (3.19)$$

In order to use classical control design methods, such as Bode diagrams, it is preferable to continue the design in the  $w$ -plane by means of performing the bilinear transform on the  $z$ -plane transfer functions. The  $w$ -plane is a good approximation to the  $s$ -plane for frequencies less than:  $\frac{2\pi}{10T_s}$  [69]. The distortion caused by the bilinear transformation can be counteracted by compensating the transfer function before applying the transformation, known as prewarping.

A simpler approach of including the effect of the ZOH is by approximating it by means of a polynomial in the  $s$ -plane. Ridley used a polynomial approximation to a transfer function describing PWM sampling gain in his thesis on small-signal modelling of current-mode controlled dc-dc converters [70]. In fact, the PWM sampling gain he used is the inverse of the ZOH transfer function. The polynomial parameters aimed to fit the PWM sampling term's gain-phase characteristic from 0 Hz to the Nyquist frequency with minimum error. The expression of

<sup>1</sup>The feed-forward correction of the cross-coupling due to delay in the measured current in section 3.2.1.1 is a static compensation. The delay still need to be considered in the dynamics of the control system.

the second order approximation polynomial is of the form:

$$\tilde{H}_e(s) = 1 + \frac{s}{w_n Q_z} + \frac{s^2}{w_n^2} \quad (3.20)$$

where the parameter values:

$$Q_z = \frac{-2}{\pi} \quad (3.21)$$

$$\omega_n = \frac{\pi}{T_s} \quad (3.22)$$

optimise the polynomial fit. The choice of parameters gives a maximum error of 0.2 dB and 3° for frequencies in the range  $[0, \frac{F_s}{2}]$  and equal the gain-phase characteristic of the PWM sampling gain at the end-points of the frequency interval of interest [70].

The PWM sampling gain polynomial is modified to approximate the ZOH transfer function as:

$$\tilde{H}_{ZOH}(s) = \frac{1}{1 - \frac{s}{w_n Q_z} + \frac{s^2}{w_n^2}} \quad (3.23)$$

where the parameter values are unchanged. The first order coefficient sign is changed in order for the phase to be decreasing. The same error for the ZOH approximation is obtained as for the PWM sampling gain for the frequency range of interest as shown in figure 3.6.

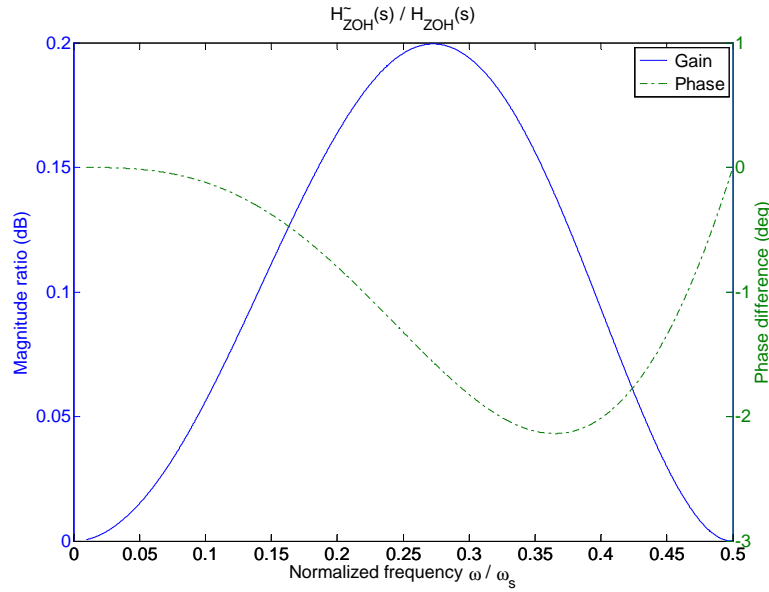


Figure 3.6: Zero-order hold approximation error.

### 3.2.1.3 Current control design

The different elements involved in the q-axis current control are depicted in block diagram form as shown in figure 3.7. The controller gain for the d-axis is the same as for the q-axis, since the

parameters for the dq-axis are assumed equal for the surface mount PMSM.

The transfer functions in the block diagram are functions of the s-plane variable. The discrete nature due to the ZOH is approximated with the s-plane polynomial,  $H_{ZOH}(s)$ , as discussed in the previous section. The controller,  $G_c(s)$ , is a proportional and integral (PI) controller. The DC gain of the inverter transfer function,  $G_i(s)$ , is assumed to have been normalised with respect to the bus voltage,  $v_{dc}$ , in the controller.

The inverter is modelled by a single pole due to half a switching period delay for the PWM control [28]. The inverter switching frequency is selected as 20 kHz, which would result in a small current ripple, no audible noise and not too high in order to limit inverter losses.

The plant for the q-axis is simply that of the RL-circuit due to the feed-forward decoupling,  $v_{qdn}^*$ . The anti-aliasing filter,  $H_f(s)$ , is shown preceding the ZOH transfer function in the feedback path.

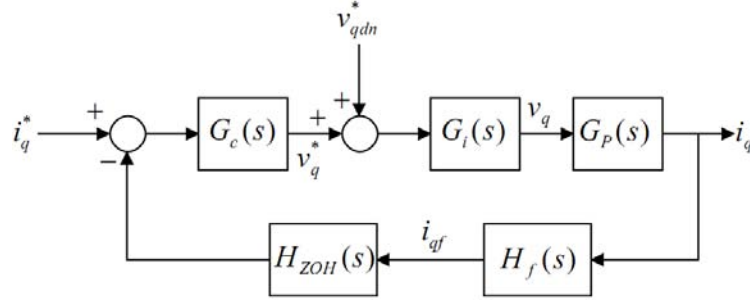


Figure 3.7: Current control block diagram.

One possible choice of the PI controller gain is such that it cancels with the dynamics of the plant (pole-zero cancellation) [4]:

$$\begin{aligned} G_c(s)G_P(s) &= \left(K_p + \frac{K_i}{s}\right) \frac{1}{sL_q + r_s} \\ &= \frac{\omega_c}{s} \left(s\frac{K_p}{\omega_c} + \frac{K_i}{\omega_c}\right) \frac{1}{sL_q + r_s} \end{aligned} \quad (3.24)$$

Hence, in order for the PI controller to cancel with the plant, the gains need to be:

$$K_p = \omega_c L_q \quad (3.25)$$

$$K_i = \omega_c r_s \quad (3.26)$$

The remaining dynamics, after the cancellation, is a pure integrator with a DC gain of  $\omega_c$ . The integrator's DC gain term dominates the total open-loop gain, therefore the term used to calculate the gain at the cross-over frequency is approximately:

$$\begin{aligned} 20 \log_{10} \left( \frac{\omega_c}{\omega} \right) &= 0 \text{ dB} \\ \therefore \omega &= \omega_c \end{aligned} \quad (3.27)$$

thus, the cross-over frequency can be set by specifying  $\omega_c$ . Choosing the cross-over frequency to be 1 kHz, the resulting current control gains are  $K_p = 2.92$  and  $K_i = 993$ . A gain margin of  $\approx 15$  dB and a phase margin of  $\approx 60^\circ$  is predicted, as shown in figure 3.8. Note that the phase delay increases linearly, although it appears non-linear on the logarithmic scale. The prediction of the phase margin for the  $s$ -plane transfer function with the ZOH approximation nearly coincides with that of the exact  $z$ -plane transfer function. The difference in gain margin, 2.6 dB, is due to extra zeros in the  $z$ -plane transfer function.

The resulting integrator-like dynamics of the open-loop system is a desirable feature. An approximation of the closed-loop transfer function is:

$$\begin{aligned} A_{cl}(s) &\approx \frac{\frac{\omega_c}{s}}{1 + \frac{\omega_c}{s}} \\ &= \frac{\omega_c}{s + \omega_c} \end{aligned} \quad (3.28)$$

which is a first order Butterworth filter (maximally flat). This implies no ringing in the range of the current control bandwidth.

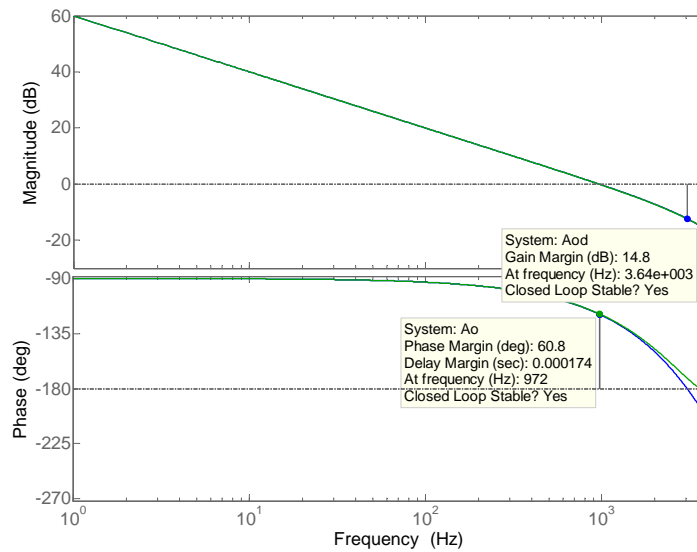


Figure 3.8: Bode diagram of current control open-loop gain.

The closed-loop bandwidth is approximately 1.9 kHz, as shown in figure 3.9. The control frequency is only five times greater than the closed-loop bandwidth, which necessitated that the ZOH delay be taken into account. The bandwidth of the discrete and continuous transfer function is almost equal, showing thus the usefulness of the ZOH approximation in the  $s$ -plane. Note that the phase shift of  $\approx 30^\circ$  at an angular rotation of 500 Hz is not applicable, since the current is controlled in the rotor reference frame, i.e. the angular velocity is effectively at 0 Hz.

The closed-loop bandwidth from the Bode diagram is for a small-signal reference. To verify if a large-signal reference, such as rated current can be excited, the power bandwidth of the controller



is of interest. The power bandwidth is defined as that frequency at which half the maximum power amplifier current can still be enforced without being distorted. Its derivation relies on relating the peak current slew rate that the power amplifier can enforce and the slew rate of a sine wave with amplitude of half the maximum current. The power bandwidth expression relating the power amplifier parameters, is [71]:

$$f_{pbw} = \frac{\hat{m}_i V_{dc}}{\pi \hat{I}_{PA} L} \quad (3.29)$$

where  $V_{dc}$  is the DC bus voltage,  $\hat{I}_{PA}$  is the maximum power amplifier current and  $L$  is the load inductance. The modulation index,  $\hat{m}_i$ , has been added to the expression obtained from the reference. In order to assure that the current is not distorted (as required by the definition), the DC bus voltage value is weighted down with the maximum modulation index which still yields linear operation ( $m_i \approx 0.8$ ). The DC bus voltage for this project is assumed to be at least 311 V. The maximum PMSM current is assumed to be 30 A. The power bandwidth is determined to be greater than 5.5 kHz.

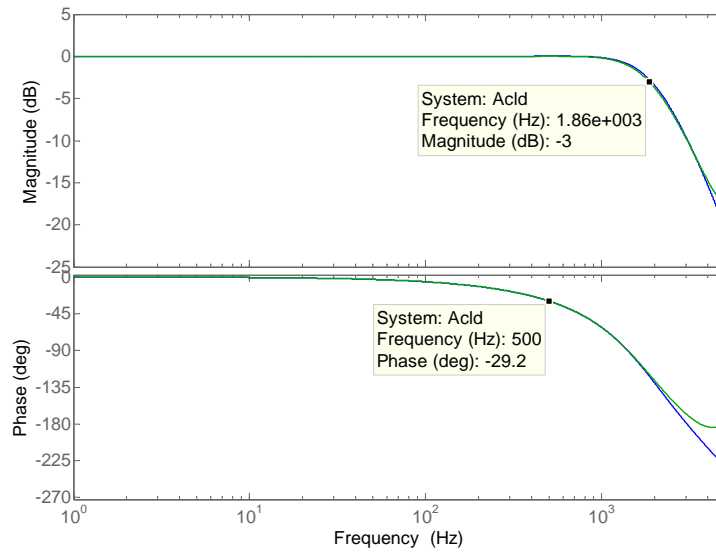


Figure 3.9: Bode diagram of current control closed-loop gain.

The step response for the closed-loop current control (determined from the transfer function) is as shown in figure 3.10. The step response of the continuous transfer function appears as a smoothed version of the pulse transfer function. If the pulse transfer function's response is delayed by half a sampling period, its value at the sampling instants corresponds to the continuous transfer function step response.

Details of the transfer function parameters and calculation of the open- and closed-loop gain is presented in appendix C.4.

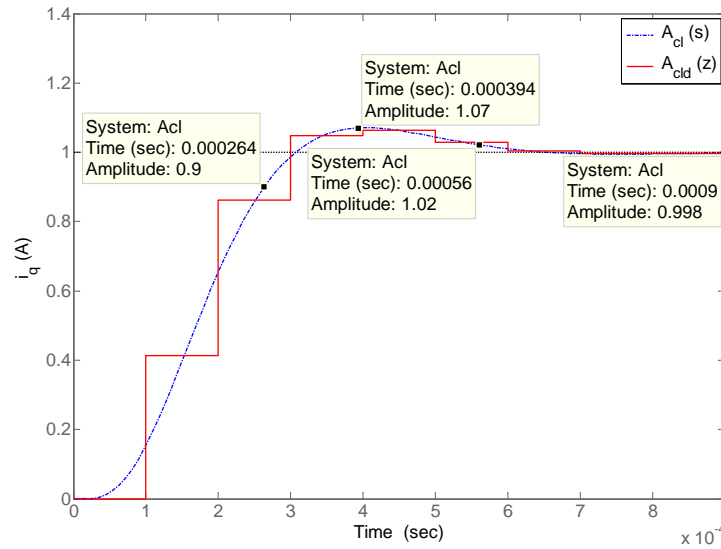


Figure 3.10: Current control step response.

### 3.2.1.4 Current control simulation

The designed current control is verified via a simulation in Matlab/Simulink<sup>®</sup>. The top level of the current controller model, connected to the PMSM model is shown in figure 3.11. The controller receives low pass filtered versions (for anti-aliasing) of the rotational position, speed and three-phase current as inputs.

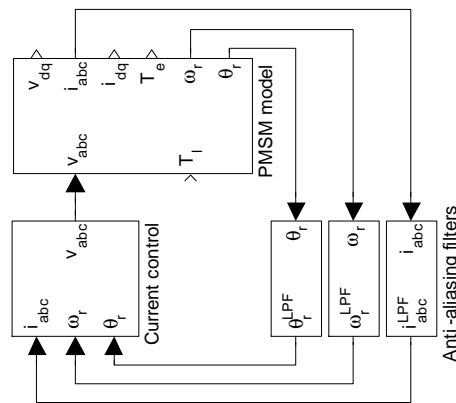


Figure 3.11: Current control model interfaced with PMSM model.

The lower level of the current controller is modelled as shown in figure 3.12. The dq-axis current reference at the top left-hand side serves as control input. The signals used for feedback and feed-forward linearization are the remaining inputs below the current reference, each followed by a ZOH block. The current reference is followed by a saturation block, which limits the current reference to the maximum allowed current value. In effect, the current limit, limits the maximum electromagnetic torque applied to the PMSM.

The saturation is included to verify that its intended operation is obtained. It is important to

model the controller as close as possible to that which is implemented. A modification in the implementation deviating slightly from the designed controller, thought not to be significant, may have unintended complications.

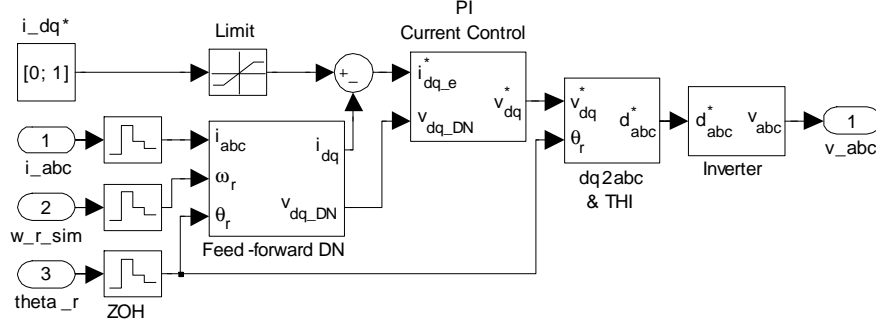


Figure 3.12: Current control simulation model.

The feed-forward decoupling is a partial copy of the PMSM electrical domain model as shown in figure 3.13. Since the feed-forward calculation requires the rotor reference frame current,  $i_{dq}$ , its calculation is done in this subsystem and fed to an output for use in the negative feedback of the current control in the higher level subsystem. The transformation blocks used in the PMSM model are also used in the controller<sup>2</sup>.

The output of the stationary to reference frame transformation is corrected by feed-forward terms which compensate for the coupling caused by the anti-aliasing filter and sampling delay, as presented in equation 3.13. Figure 3.14 presents the implementation of the decoupling as contained in the *AA filter decouple* subsystem.

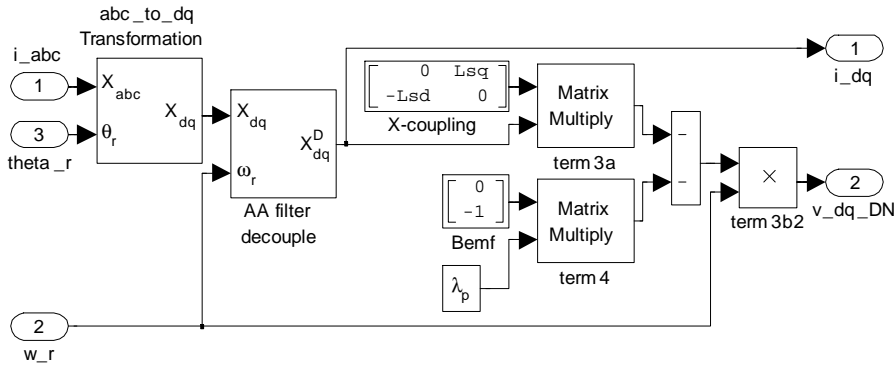


Figure 3.13: Feed-forward linearization terms.

The implementation of the PI controller is as shown in figure 3.15. The controller employs anti-windup for the integrator, as presented by Sul *et al.* [4]. If the saturation block's limit is exceeded, then the difference between its input and output is greater than zero, which weighs the integral input down, so that it never exceeds the limit imposed by the saturation block.

<sup>2</sup>This shows the high degree of code re-usability of Simulink® due to grouping logical atomic code into visual units.

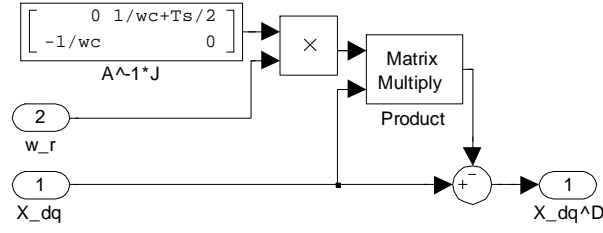


Figure 3.14: Measurement delay decoupling.

An integrator block with anti-windup is available in the Matlab/Simulink<sup>®</sup> library, but the presented anti-windup limits both controller gains with a single saturation block, which is more efficient than using a limited integrator with a second saturation block to limit the sum of the controller gains. Anti-windup of the integrator is important, since it acts to limit excessive overshoot, which is potentially destabilising, in case the PI controller had a large error input for an extensive period. Also note that the feed-forward linearization is added before the saturation, thereby limiting the total reference voltage. The gain in the feedback path of the anti-windup loop is [4]:

$$K_{aw} = \frac{K_i}{K_p} \quad (3.30)$$

The voltage limit of the anti-windup is determined as the product of the maximum allowed duty cycle (which is dependent on the type of inverter modulation) and the inverter gain, i.e.:

$$V_{lim} \left( V_{dc}, \hat{d} \right) = \hat{d} G_i (V_{dc}) = \begin{cases} \frac{V_{dc}}{2} & \text{Sine - Triangle} \\ \frac{V_{dc}}{\sqrt{3}} & \text{Third - Harmonic Injection} \end{cases} \quad (3.31)$$

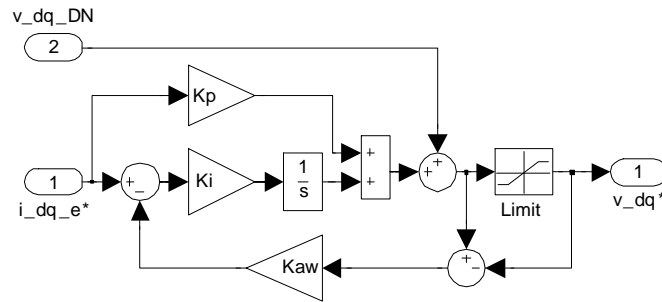


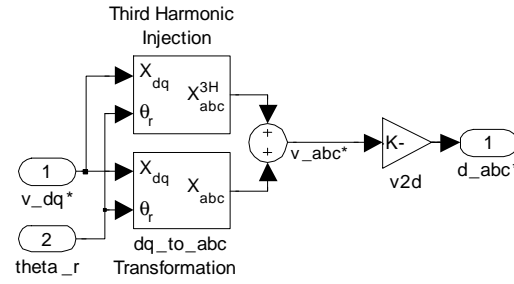
Figure 3.15: PI control model with anti-windup.

The input to the inverter is the sum of the three-phase control voltage and third harmonic injection terms, normalised into a duty cycle value. The calculation of the third harmonic injection term is as shown in figure 3.16. The expression for the third harmonic injection [25]:

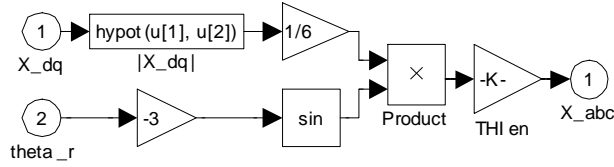
$$v_{abc}^{3H} = \frac{1}{6} \sqrt{v_q^2 + v_d^2} \sin(-3\theta_c) \quad (3.32)$$

is identical for each phase, i.e. no phase shift for the different phases<sup>3</sup>. With a higher obtainable phase voltage with third harmonic injection, field weakening becomes necessary only after a higher rotational speed, thereby increasing the drive efficiency. Via the simulation user-interface the modulation scheme used can be switched between sine-triangle modulation and third-harmonic injection. Depending on the selection, the duty cycle limits are  $\pm 1$  and  $\pm \frac{2}{\sqrt{3}}$  for sine-triangle and third harmonic injection, respectively. The duty cycle limits, together with the inverter gain determines the voltage limit imposed by the PI current controller.

The normalisation is performed with the inverse of the inverter gain inside the  $v2d$  subsystem. In order to yield extra DC bus voltage disturbance rejection, the inverter inverse gain may be computed from a measured DC bus voltage. In an actual drive, the DC bus voltage has to be measured anyway for use in brake circuitry to prevent over-voltage conditions, which pose a danger to the DC bus capacitors and semiconductor switches.



(a) Top level model.



(b) Calculation implementation with THI output enable.

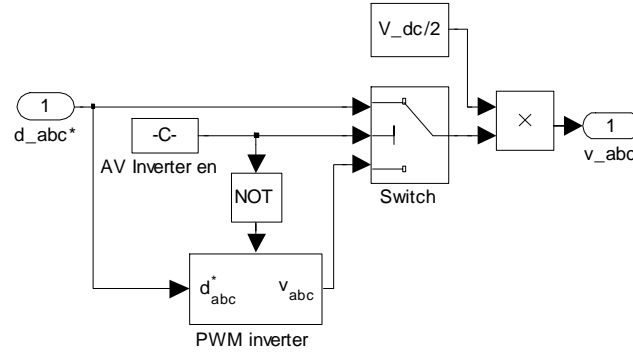
Figure 3.16: Third harmonic injection term.

The inverter is modelled as shown in figure 3.17. Via the controller's user-interface the inverter model can be switched between a PWM switching inverter and an average value inverter. The average value inverter multiplies the input duty cycle by a linear gain term. The combination of the inverter's inverse gain,  $v2d$ , used for normalisation and the average value (linear) gain in effect use the reference voltage directly as the inverter's output. The average value inverter simulates orders of magnitude quicker than the PWM inverter<sup>4</sup>, but the user has to double check that the reference voltage does not drive the inverter into a non-linear region. If the inverter operated in a non-linear region, the simulation response of the average and PWM inverters will

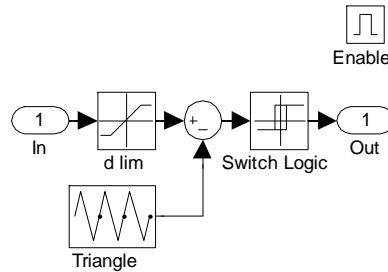
<sup>3</sup>The trigonometric identity may be either sine or cosine, depending on the  $dq0$  transformation convention used. That is whether phase-a is aligned with the d-or q-axis when the rotor angle is aligned with the phase-a magnetic axis.

<sup>4</sup>When the average value inverter is selected, the PWM inverter model is prevented from simulating, by placing it inside an enabled subsystem. To further improve simulation time, the maximum time step ( $h_{max}$ ) is set during initialisation of the simulation depending on whether the average value or PWM inverter has been selected.

differ, in which case the PWM inverter's response is more accurate. The PWM inverter model does not include the effect of dead-time. Models which include the dead-time effect are presented in section 3.4, with regard to dead-time compensation.



(a) Switch between Average value and PWM inverter model.



(b) Implementation of PWM inverter model.

Figure 3.17: Inverter simulation model.

The linear gain used for the inverter is  $\frac{v_{dc}}{2}$ . For design, the DC bus voltage is assumed 311 V. The origin for the DC bus voltage value is clarified in section 4.2. With the third harmonic injection, the peak voltage obtainable by the inverter is approximately 180 V. With the assumed DC bus voltage a peak fundamental voltage before entering over-modulation is 144 V, whilst the peak PMSM voltage at maximum speed (500 Hz) is 156 V, therefore the inverter will operate slightly in the over-modulation region at that speed. The use of field weakening to avoid over modulation is also an option. With third harmonic injection the use of field weakening (which increases motor losses) can in this case be avoided.

The q-axis current step response is shown in figure 3.18, for both the average and PWM inverters. Note how the average inverter's response passes through the PWM inverter's response. To obtain the same accuracy for the PWM inverter as for the average inverter the maximum time step had to be an order of magnitude smaller ( $10 \mu s$  vs  $1 \mu s$ ). The time step during the simulation varies, since a variable step solver appropriate for stiff differential equations was used (*ode23tb*). The rotor is held fixed in the simulation by setting the rotor moment of inertia to infinity.

The large inflections in the response curve are the controller sampling times, when new duty cycles are generated. The rise time,  $175 \mu s$ , is faster than that determined from the closed-loop

transfer function. The overshoot is slightly greater for the simulation than that determined from the transfer function (7.8 % *vs* 7 %). The cause of the difference in delay between the simulation model and transfer function is unclear. The current control simulation model is located in appendix C.5.

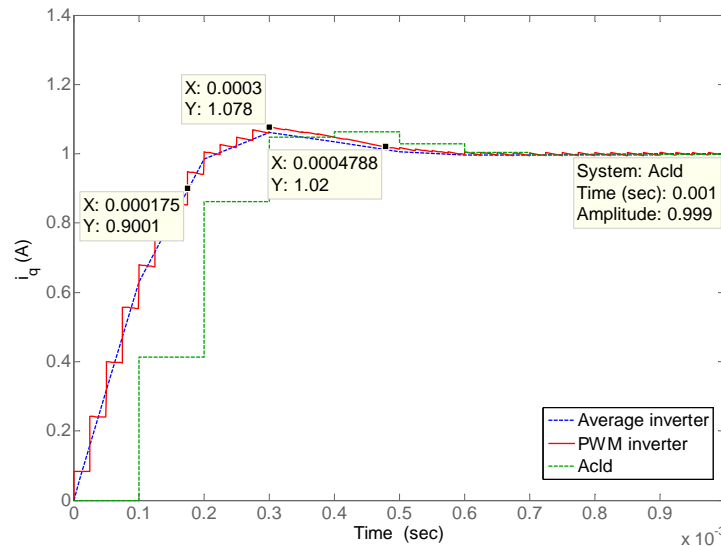


Figure 3.18: Current step response with performance measures.

### 3.2.2 Speed signal extraction

Before the speed controller can be designed, the method by which the speed value is extracted from the angular position measurement is developed. The method determines the bandwidth of the speed signal, which in turn determines the choice of the speed controller gains.

#### 3.2.2.1 Numerical differentiation

The obvious method of obtaining the speed signal from the position signal is via numerical differentiation, such as the backward difference method. Figure 3.19, shows the model for calculating the speed from the position via the backward difference approximation.

The angular position input cannot increase indefinitely and has to reset at some point, hence the saw-tooth nature of the input. The discontinuous edge denotes one revolution. The range of the angular position sensor is  $[0, 2\pi]$ . Due to the discontinuity in the input signal, the backward difference formula cannot be applied directly and requires a form of edge detection. Depending on the edge being falling or rising (rotation direction) a constant is added to the newest sampled position to bridge the discontinuity with the previously sampled value. The implementation of the numeric differentiation is listed in algorithm 3.1.

The angular position input is sampled and held by the ZOH, after which it is quantized to the numerical accuracy of the ADC. Quantization noise causes low frequency harmonics in the speed

[72]. Another problem is the amplification of high frequency noise in the position signal by the differentiator. Due to the aforementioned noise, a second order low pass filter is used.

The output of the numerical differentiation algorithm is shown in figure 3.20. The magnification box shows the attenuated high frequency ripple superimposed on a low frequency harmonic due to quantization noise. The quantization disturbance is larger at lower speeds. The quantization noise seems negligible in the shown (open-loop) response. In a closed-loop system the quantization noise is more severe as it tends to circulate and amplify in the controller. The backward difference simulation model is included in appendix C.6.

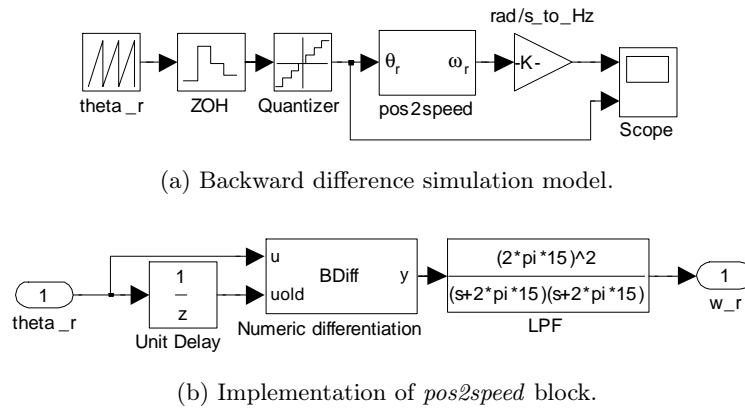


Figure 3.19: Speed from position via backward difference.

---

**Algorithm 3.1** Calculation of backward difference with falling/rising edge detection.

---

```

function y = BDiff(u, uold)

    Ts = 1/10e3;

    %Detect angular revolution
    if (u-uold) < (-0.7*2*pi)
        rot = 2*pi;
    elseif (u-uold) > (0.7*2*pi)
        rot = -2*pi;
    else
        rot = 0;
    end

    %Backward difference formula
    y = ((u + rot) - uold) / Ts;

end

```

---



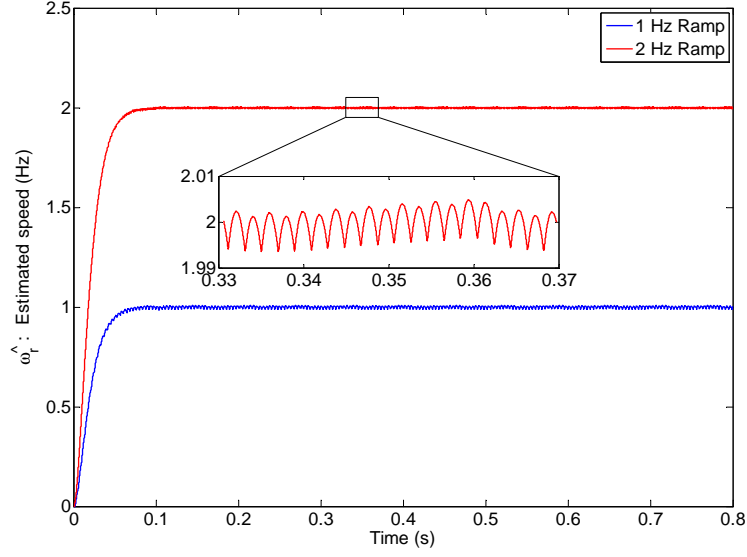


Figure 3.20: Numerical differentiation algorithm response.

### 3.2.2.2 Speed observer

The problem of quantization noise can be addressed by using an observer instead of the backward difference method. Roche *et al.* analysed quantization noise in position servo systems and the reduction thereof. Their analysis shows that the current ripple (and the increased losses) is quadratically dependent on the speed loop bandwidth. Suggested methods of reducing the quantization noise are oversampling (to increase resolution) and the use of a speed observer [72].

The speed observer can be extended to estimate the load torque. By estimating the load torque and including it in the control loop, better load torque disturbance rejection can be achieved. The set of differential equations describing the speed and load-torque observer is given by [30]:

$$p\hat{\theta} = \hat{\omega}_r + l_1 (\theta - \hat{\theta}) \quad (3.33)$$

$$p\hat{\omega}_r = \frac{1}{J} (T_e - \hat{T}_l - B\hat{\omega}_r) + l_2 (\theta - \hat{\theta}) \quad (3.34)$$

$$p\frac{\hat{T}_l}{J} = l_3 (\theta - \hat{\theta}) \quad (3.35)$$

where the electromechanical torque is approximated by:  $T_e = K_t i_q$ .

With the observer gains,  $l_{1..3}$ , set equal to zero, the differential equations are just the state-space model describing the rotational dynamics with a load torque of zero. If the simulation model starts with initial values equal to the actual initial states and run in parallel to the actual system, it will track the actual states assuming ideal conditions. In fact, the ideal assumption is invalid and the real world system will always differ (even though it might only be slightly) with the simulation model. Thus after a time, the actual and simulated state variables diverge. This is

the purpose of the “correction” term,  $\theta - \hat{\theta}$ . An error between the simulated and actual position drives the estimated position back to the actual position. The correction term also drives the other state variables, although a non-zero steady state error is possible.

In order to design the observer gains, it is useful to set the differential equations in state-space form:

$$\begin{aligned} \begin{bmatrix} p\hat{\theta} \\ p\hat{\omega}_r \\ p\frac{\hat{T}_l}{J} \end{bmatrix} &= \begin{bmatrix} -l_1 & 1 & 0 \\ -l_2 & -\frac{B}{J} & -1 \\ -l_3 & 0 & 0 \end{bmatrix} \begin{bmatrix} \hat{\theta} \\ \hat{\omega}_r \\ \frac{\hat{T}_l}{J} \end{bmatrix} + \begin{bmatrix} l_1 & 0 & 0 \\ l_2 & \frac{K_t}{J} & 0 \\ l_3 & 0 & 0 \end{bmatrix} \begin{bmatrix} \theta \\ i_q \\ 0 \end{bmatrix} \\ y &= \begin{bmatrix} 1 & 0 & 0 \end{bmatrix} \mathbf{x} \end{aligned} \quad (3.36)$$

The roots of the observer characteristic equation can be set with the use of Ackermann’s formula [73]:

$$\mathbf{L} = p(\mathbf{A}) \mathbf{P}_o^{-1} \begin{bmatrix} 0 & \dots & 0 & 1 \end{bmatrix}^T \quad (3.37)$$

where  $p(\mathbf{A})$  is the desired characteristic polynomial, evaluated for  $\mathbf{A}$ , and  $\mathbf{P}_o$  is the observability matrix, defined as [73]:

$$\mathbf{P}_o = \begin{bmatrix} \mathbf{C} & \mathbf{CA} & \dots & \mathbf{CA}^{n-1} \end{bmatrix}^T \quad (3.38)$$

A first choice for the observer characteristic polynomial is that determined by the ITAE criterion for a step input [73]:

$$p(s) = s^3 + 1.75\omega_n s^2 + 2.15\omega_n^2 s + \omega_n^3 \quad (3.39)$$

where  $\omega_n$  is the natural frequency related to (although not equalling) the bandwidth, which can be obtained from the Bode diagram for use in the speed control design. The chosen bandwidth is a compromise on speed of response and noise disturbance rejection, such as the aforementioned quantization noise.

The ITAE criterion for a step is not optimal for the speed observer, because the transfer function from rotational to estimated speed has a zero:

$$T_{\hat{\omega}\omega}(s) = \frac{sl_2 - \frac{l_3}{J}}{s^3 + s^2 \left( \frac{B}{J} + l_1 \right) + s \left( l_1 \frac{B}{J} + l_2 \right) - \frac{l_3}{J}} \quad (3.40)$$

The ITAE criterion for a ramp input includes a zero, but requires a relationship between the denominator and numerator coefficients. The coefficient requirement is obtained if the relationship:  $l_1 \frac{B}{J} \ll l_2$ , holds. The polynomial satisfying the ITAE criterion with a ramp input is [73]:

$$p(s) = s^3 + 1.75\omega_n s^2 + 3.25\omega_n^2 s + \omega_n^3 \quad (3.41)$$

The bandwidth related parameter,  $\omega_n$ , is chosen as  $2\pi 5$ , after observation of the simulation response which included quantization noise with a precision of 8 bits. The low precision of the high-speed position sensor restricts the selected bandwidth. The resulting observer gains are

calculated as:

$$\mathbf{L} = \begin{bmatrix} l_1 \\ l_2 \\ l_3 \end{bmatrix} = \begin{bmatrix} 54.9 \\ 3206 \\ -44.2 \end{bmatrix} \quad (3.42)$$

The Bode diagram of the observer speed transfer function is shown in figure 3.21, from which the observer bandwidth is noted as 12 Hz.

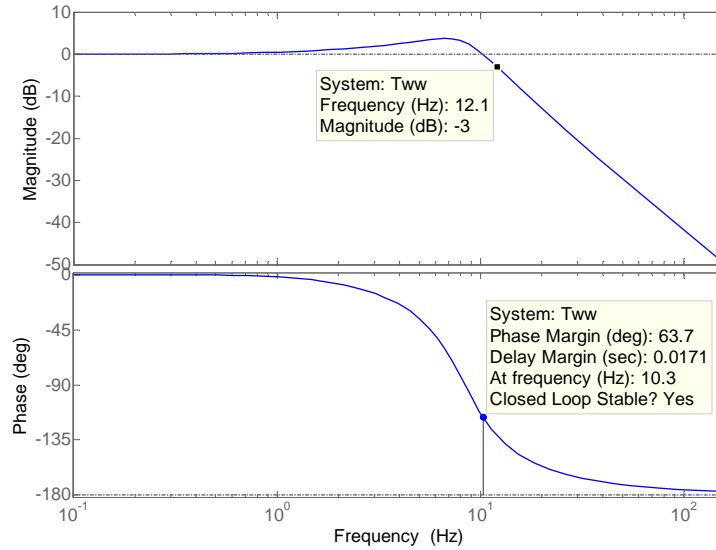
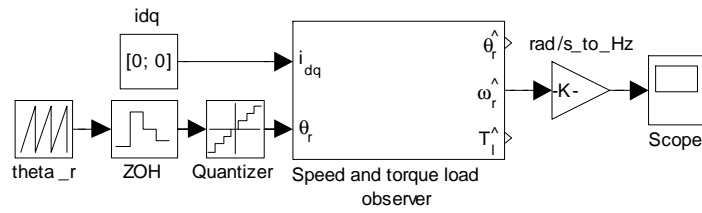


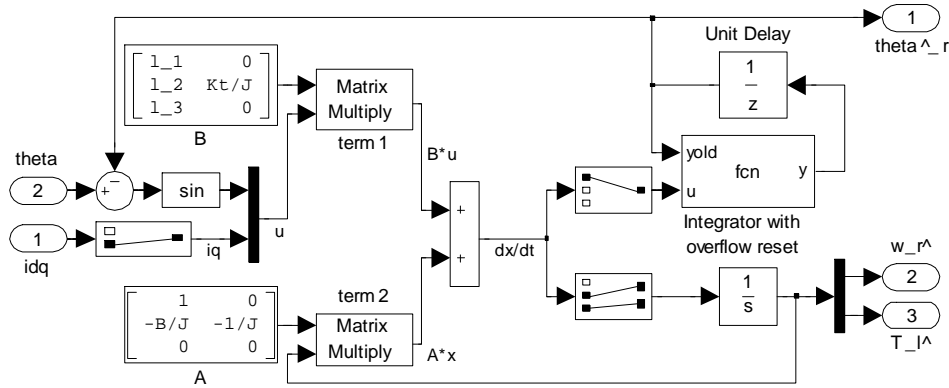
Figure 3.21: Bode diagram for observer speed transfer function.

The simulation model of the speed observer is shown in figure 3.22. A special integrator had to be implemented which resets the angular position each revolution. The first order, forward Euler numerical integration formula is used. A slight difference between the presented state-space model of equation 3.36 and that which is implemented in figure 3.22b exists, i.e. the input to the implemented observer is the position estimation error,  $\hat{\theta}_e$ . This reduces the number of computations of the implemented observer.

The implementation of the observer also has to address the problem due to the discontinuity experienced each revolution in the position and estimated position. The same revolution detection scheme as for the numerical differentiation is possible. The problem with that implementation is the computational burden due to the numerous *If*-statements. A second solution is to notice that the trigonometric sine function is invariant to the discontinuity from zero to  $\pm 2\pi$ . Since the estimated position tracks the input position closely, the estimation error operates near zero and the gain of the trigonometric sine is approximately unity. Therefore, the discontinuity in the position error,  $\hat{\theta}_e$ , is rejected with the use of the *sin* block.



(a) Top level connections to speed observer simulation model.



(b) Implementation of speed observer.

Figure 3.22: Speed and load torque observer.

Figure 3.23, depicts the step response of the speed observer for a 100 rpm (1.67 Hz) reference input. The large overshoot, nearly 40 %, is due to the zero of the observer. The small undershoot and drifting of the response on top of the reference before settling is caused by the ITAE criterion being optimal for a *ramp* input. The improvement in noise rejection compared to the numerical differentiation, claimed in the literature, is not apparent in figure 3.23. The estimated load torque used for feed-forward disturbance rejection is still an advantage of the observer over numerical differentiation. Load disturbance rejection can also be obtained by adding a differential term to the PI speed controller.

The speed observer design code and simulation model is included in appendix C.7.

### 3.2.2.3 Modified speed observer

The bandwidth of the speed and torque load observer was chosen extremely low due to the quantization noise of the 8-bit position sensor. This low bandwidth causes the torque load output of the observer to have no beneficial effect in the speed control loop.

The solution to the observer bandwidth problem is to reduce the quantization noise by another means than by reducing the observer bandwidth. By considering the nature of the quantization noise a solution becomes apparent. It is the discontinuities in the position signal input which are responsible for the noise. Since the input to the implemented observer is the position estimation error, filtering of the observer output alone, such as choosing a low observer bandwidth

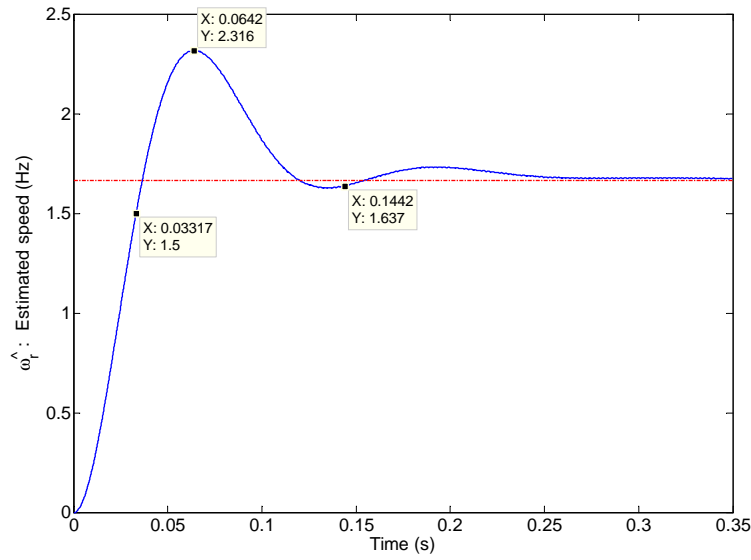


Figure 3.23: Speed observer step response.

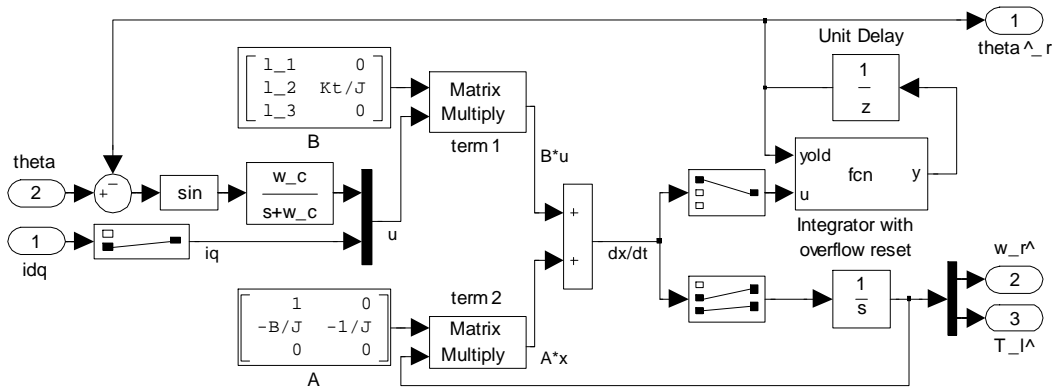


Figure 3.24: Modified speed and load torque observer.

will not reduce the noise in the observer input, because the observer output tries to track the discontinuities in the position input. The position input with the quantization noise has to be smoothed before it is used in the observer. This poses a problem, because the discontinuity due to a revolution may not be filtered. Therefore, the quantization noise due to the input has to be filtered *after* a revolution discontinuity has been removed from the signal.

The position estimation error,  $\hat{\theta}_e$ , which has been processed by the sine function, as in figure 3.22b, is invariant to the revolution discontinuity but still has the quantization noise discontinuity. This signal can be smoothed by a low pass filter, thereby allowing the observer gains to be recalculated to yield a larger bandwidth. The modified speed observer model is shown in figure 3.24.

The equivalent state-space model for the speed observer, modified with a first order low-pass filter, is extended by two states, i.e. one for the filtered input and another for the estimated

filter input. The state-space model is then given by:

$$\begin{bmatrix} p\hat{\theta} \\ p\hat{\omega}_r \\ p\frac{\hat{T}_l}{J} \\ p\hat{\theta}_f \\ p\hat{\theta}_f \end{bmatrix} = \begin{bmatrix} 0 & 1 & 0 & -l_1 & l_1 \\ 0 & -\frac{B}{J} & -1 & -l_2 & l_2 \\ 0 & 0 & 0 & -l_3 & l_3 \\ \omega_c & 0 & 0 & -\omega_c & 0 \\ 0 & 0 & 0 & 0 & -\omega_c \end{bmatrix} \begin{bmatrix} \hat{\theta} \\ \hat{\omega}_r \\ \frac{\hat{T}_l}{J} \\ \hat{\theta}_f \\ \theta_f \end{bmatrix} + \begin{bmatrix} 0 & 0 \\ 0 & \frac{K_t}{J} \\ 0 & 0 \\ 0 & 0 \\ \omega_c & 0 \end{bmatrix} \begin{bmatrix} \theta \\ i_q \end{bmatrix} \quad (3.43)$$

$$y = \begin{bmatrix} 1 & 0 & 0 & 0 & 0 \end{bmatrix} \mathbf{x} \quad (3.44)$$

where the filter cut-off frequency is given by  $\omega_c$ . If  $\omega_c$  is selected high enough, then the filter dynamics may be assumed much faster than that of the observer, so that the observer gains can still be determined with the procedure for the original state-space model. The filter cut-off frequency is selected to be 150 Hz. With the aid of the speed observer simulation model, the observer natural frequency is chosen as 15 Hz. The resulting observer gains for the modified speed observer is then:

$$\mathbf{L} = \begin{bmatrix} l_1 \\ l_2 \\ l_3 \end{bmatrix} = \begin{bmatrix} 165 \\ 28.9 \times 10^3 \\ -1.19 \times 10^3 \end{bmatrix} \quad (3.45)$$

The observer step response, with the newly determined gains, is shown in figure 3.25. The reference amplitude corresponds to 100 rpm (1.67 Hz). The high frequency ripple has been attenuated as desired. For higher speeds the ripple is attenuated even more. The overshoot is slightly larger, which suggests that the negligible filter dynamic assumption is not entirely valid. The settling time is approximately three times faster than for the original observer response of figure 3.23. Therefore, the speed observer bandwidth is also approximately three times larger, which is confirmed by the Bode diagram in figure 3.26.

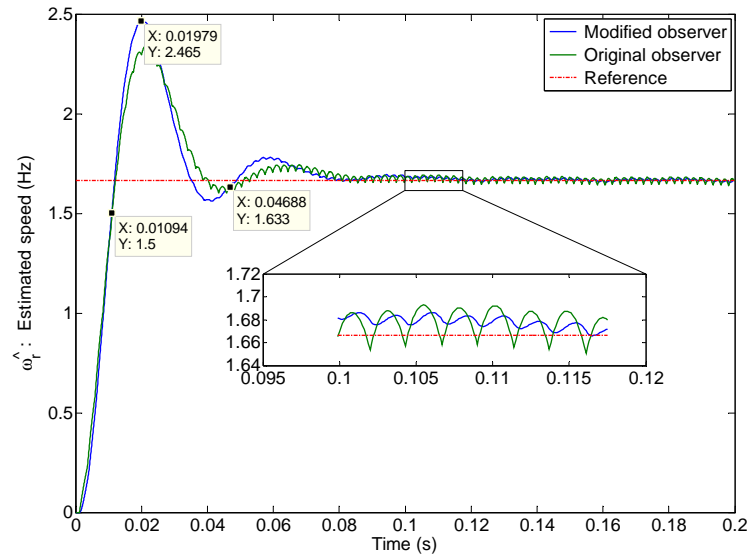


Figure 3.25: Modified speed observer step response.

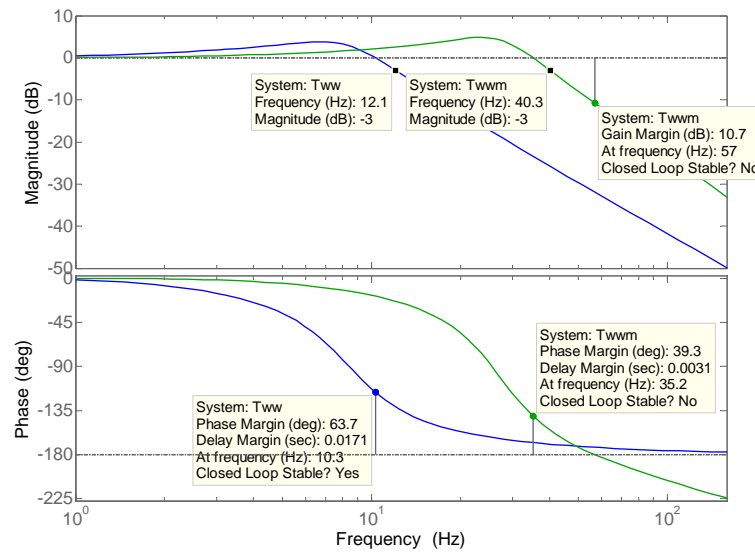


Figure 3.26: Modified speed observer Bode diagram.

Since the transfer function considers only the single input,  $\theta$ , the observer prediction capability due to the known torque producing current is ignored. If the system is modelled exactly by the observer, the bandwidth of the transfer function for measured position to estimated speed is infinite. Thus, it is difficult to get an estimate of the actual observer bandwidth, because it is either under or over estimated.

A better estimate of the observer bandwidth can be obtained if its second input,  $i_q$ , is also considered. The prediction capability is degraded by uncertainty in the model parameters and

noisy measurements. A better estimate of the observer is obtained with the use of system identification. The observer is excited with a chirp signal and instead of setting the second input zero (as with the transfer function), it is set to what would have been present in a system under rotational acceleration. The relationship of the current input to the speed (without a load torque) is:

$$i_q = \alpha \frac{J}{K_t} \frac{d\omega_r}{dt} \quad (3.46)$$

where  $\alpha$  is a degradation factor. The purpose of the degradation factor is to acknowledge uncertainty in the PMSM parameters and in the motor current measurement. The most uncertainty is in the moment of inertia as observed in section 3.1.1. If  $\alpha < 1$  the speed is underestimated in the observer which leads to overshoot in the controlled speed, hence oscillatory behaviour. If  $\alpha > 1$  the speed is overestimated and the controlled speed is over-damped.

If  $\alpha = 1$ , the observer has nearly unity gain and almost no phase shift and when  $\alpha = 0$ , the system response equals that determined by the transfer function. With  $\alpha = 0.65$ , the bandwidth of the system is seen to be much reduced as shown in figure 3.27.

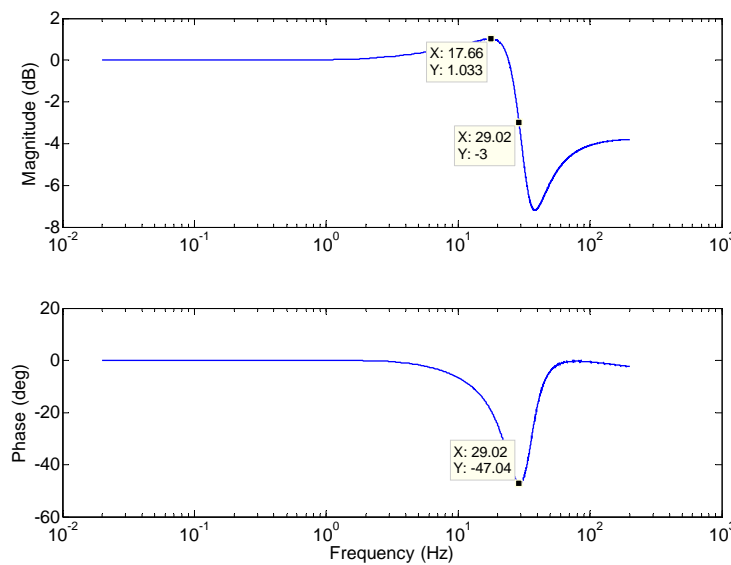


Figure 3.27: Observer frequency response,  $\alpha = 0.65$ .

The bandwidth via system identification is 29 Hz, compared to the transfer function bandwidth of 41 Hz, which was unrealistically high due to the high degree of peaking. The phase shift is also seen to be much reduced when the current prediction term aids the observer, in comparison to the worst case scenario represented by the transfer function which only had a phase margin of  $30^\circ$ .

Therefore, it is more realistic to use a first order pole, located at the  $-3$  dB frequency, to model the effect of the observer in the feedback path of the speed control loop, as depicted in figure 3.27. This first order pole is used as an approximation of the observer when determining the loop gain during the speed controller design.



Appendix C.8, includes the design code and simulation model for the modified speed observer.

### 3.2.3 Speed control

#### 3.2.3.1 Speed control design

The speed control block diagram is depicted in figure 3.28. The plant model is:

$$G_p(s) = \frac{z_p}{sJ + B} \quad (3.47)$$

where  $J$  is the rotor moment of inertia,  $B$  is the viscous friction coefficient and  $z_p$  is the number of pole pairs. The model assumes that the current control bandwidth is much larger than the speed control bandwidth, thus instantaneous torque control is assumed by using the torque gain,  $K_t$ . A more detailed speed control loop is derived by Krishnan [28]. The simplified control loop is sufficient for the speed control loop design.

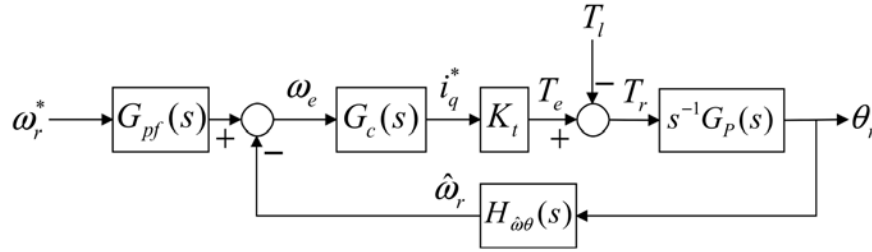


Figure 3.28: Speed control block diagram.

The transfer function in the feedback path,  $H_{\hat{\omega}\theta}(s)$ , is that of the observer. The pure integrator in the servo plant model,  $s^{-1}G_p(s)$ , can be combined with the observer in the feedback path, so that the observer transfer function becomes:

$$H_{\hat{\omega}\omega}(s) = \frac{H_{\hat{\omega}\theta}(s)}{s} \quad (3.48)$$

so that the block diagram output changes to rotational speed. As discussed at the end of section 3.2.2.3, the single-input single-output (SISO) transfer function of the observer does not represent the system dynamics of the multiple-input multiple-output (MIMO) observer accurately. Instead, the observer is modelled as:

$$H_{\hat{\omega}\omega}(s) = \frac{\omega_o}{s + \omega_o} \quad (3.49)$$

where  $\omega_o$  is the observer bandwidth determined by the system identification procedure (with  $\alpha = 0.65$ ).

The closed-loop transfer function, with  $G_c$  selected as a PI controller, is:

$$A_{cl} = \frac{K_t}{J} \frac{s^2 K_p + s(K_i + K_p \omega_o) + K_i}{s^3 + s^2 \left( \frac{B}{J} + \omega_o \right) + s(B + K_p K_t) \frac{\omega_o}{J} + K_i K_t \frac{\omega_o}{J}} \quad (3.50)$$

The zeros of the speed transfer function can be cancelled by the pre-filter,  $G_{pf}(s)$ , in the forward path of the reference input. It can be shown that if the observer bandwidth is assumed infinite, then the complex zeros reduces to a single zero, which can be cancelled by the pre-filter [4]:

$$G_{pf}(s) = \frac{K_i}{sK_p + K_i} \quad (3.51)$$

Note that the disturbance rejection transfer function still has the zero.

Assuming the zero is cancelled, the speed control closed-loop transfer function is in appropriate form to equate the characteristic equation coefficients to those specified by some performance criterion, in this case the deadbeat response. The reader is referred to [73] for the details of designing for deadbeat response. Note that the second order coefficient,  $(\frac{B}{J} + \omega_o)$ , has no unknowns, hence the natural frequency for the deadbeat response is found in reverse order of the usual design steps. The natural frequency is found to be 15.3 Hz, which yields a settling time of 42 ms. The PI controller gains are determined as:  $K_p = 2.84$  and  $K_i = 124$ .

The stability margins in the Bode diagram of the open-loop control system, is shown in figure 3.29. The phase margin of  $38^\circ$  is a worst-case estimate, because the observer is modelled with  $\alpha = 0.65$ . The actual speed control performance is better than what would be obtained with such a large error in the observer input, but by ensuring stability under the parameter variation the implemented system is more robust.

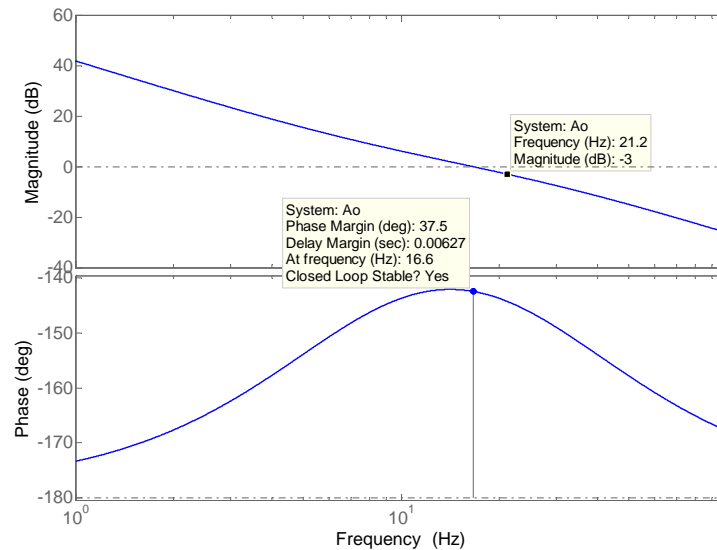


Figure 3.29: Speed control stability margins.

The closed-loop bandwidth of the speed control is verified with the Bode diagram, as shown in figure 3.30.

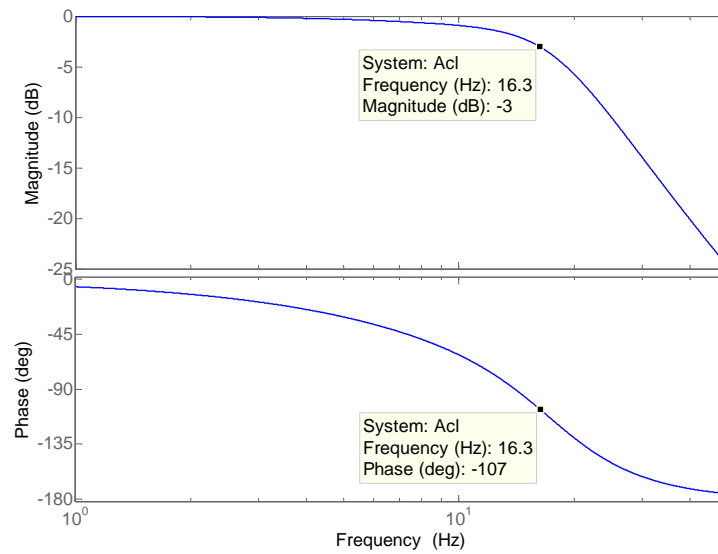


Figure 3.30: Speed control closed-loop Bode diagram.

The step response of the system with approximated observer, pre-filter and gains (as designed), is shown in figure 3.31.

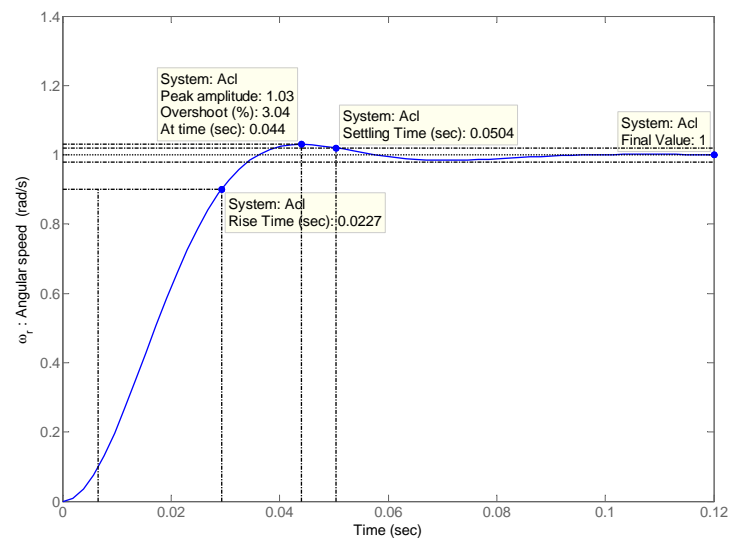


Figure 3.31: Closed-loop speed-control step response.

The speed control design code is included in appendix C.9.

### 3.2.3.2 Speed reference generator

Instead of using a pre-filter to cancel the zeros of the closed-loop speed control, a rate limiter is used to limit the high frequency content in the reference input (such as a reference speed step change), which would have been amplified by the zeros.

The rate limiter also serves as a method of protecting the DC bus capacitors from an over voltage condition, if the PMSM is in generator mode, by limiting the rate at which kinetic energy is extracted and stored in the DC bus capacitors. This protection method is required because the DC bus capacitors do not have a protection braking circuit, which has been initially deemed unnecessary due to the low moment of inertia of the high-speed rotors.

If the kinetic energy stored in the rotors spinning at maximum speed could instantaneously be displaced to the DC bus capacitors, the voltage after such a brake would be:

$$\begin{aligned}
 V_{end} &= \sqrt{V_{init} + \frac{J}{C}\omega_{init}^2} \\
 &= \sqrt{310 + \frac{1.15 \times 10^{-3}}{13.2 \times 10^{-3}} (2\pi 500)^2} \\
 &= 927 \text{ V}
 \end{aligned} \tag{3.52}$$

where  $C$  is the total DC bus capacitance. The designed capacitance value, from section 4.2.4, is 13.2mF. Although the rotors have little stored kinetic energy, it is more than what the capacitors can safely absorb with a maximum voltage rating of 450 V.

The rate limit value is chosen such as to allow the rotor to be braked by the frictional losses. The maximum allowed deceleration is thus:

$$\begin{aligned}
 \check{\alpha} &= -\frac{d\omega_r}{dt}_{min} \\
 &= -\frac{1}{J} (B\omega_r + T_l) \\
 &\approx -(0.046\omega_r + 64) \text{ rad.s}^{-2}
 \end{aligned} \tag{3.53}$$

Due to the large uncertainty in the viscous and coulomb friction, the deceleration coefficients need to be tuned during implementation, since those calculated serve only as a guide.

The rate limit for acceleration is much larger than for deceleration, since it is limited by the maximum torque producing current:

$$\begin{aligned}
 \hat{\alpha} &= \frac{1}{J} \hat{T}_e \\
 &= \frac{1}{J} K_t \hat{i}_q \\
 &\approx 767 \text{ rad.s}^{-2}
 \end{aligned} \tag{3.54}$$

The rate limits may be calculated using the reference speed, i.e. the output of the rate limiter,

instead of the actual speed due to the limited speed control error. This is useful in the case of the V/f controller, for which a speed sensor measurement is assumed not available.

The method of limiting the DC bus voltage by constraining the rotor deceleration is only applicable to the PMSM controlled in motoring mode. If the motor and generator runs simultaneously and the motor drive shuts down, it is still possible for the generator to charge the DC bus capacitors to a dangerous level. Therefore, a second protection mechanism is used as presented in section 4.3.6.

The Simulink<sup>®</sup> model which performs the reference speed generation is as shown in figure 3.32. The *Discrete Integrator* is listed in algorithm 3.2. The rate at which the integrator's output changes is determined by the *Acceleration Limits* and *Deceleration Limits*. The final integration step has a magnitude dependent on the reference speed error which adds just the right amount in order to yield zero difference between the desired speed reference and the final instantaneous speed reference.

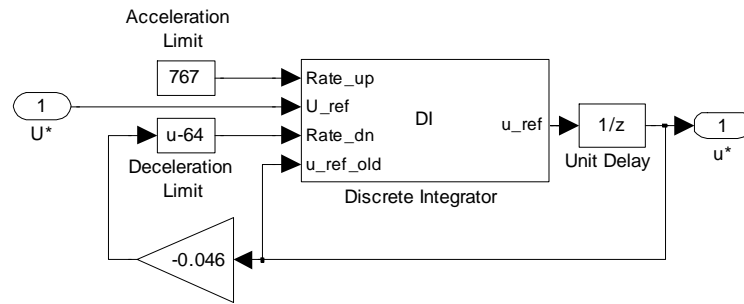


Figure 3.32: Speed reference generator for vector control.

### 3.2.3.3 Simulation model

The speed controller is verified in a Matlab/Simulink<sup>®</sup> simulation. The top level model is as shown in figure 3.33. Note that the simulated speed is no longer one of the feedback variables.

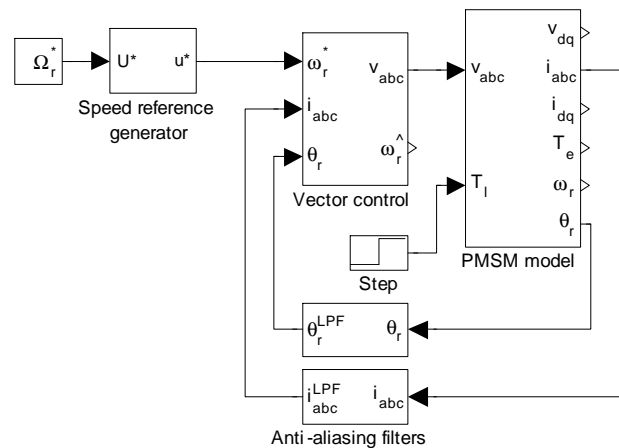


Figure 3.33: Top level of speed control simulation model.

**Algorithm 3.2** Discrete integrator with variable amplitude step.

```

function u_ref = DI(Rate_up, U_ref, Rate_dn, u_ref_old)

Ts = 1/10e3;
Du = Rate_up*Ts;
Dd = Rate_dn*Ts;

%Difference between desired speed and present speed:
u_error = U_ref - u_ref_old;

%Calculate speed step according to rate limit:
if u_error>Du
    dy = Rate_up;
elseif u_error<Dd
    dy = Rate_dn;
else
    %Final speed adjustment has a smaller step to yield zero
    %and therefore non-oscillating error:
    dy = u_error/Ts;
end

u_ref = u_ref_old + Ts*dy; %Forward Euler

end

```

The lower level model (of the *Vector control* subsystem) is as shown in figure 3.34. The inputs to the model are followed by a ZOH and quantizer. The current is measured by 16-bit ADCs, whilst the angular position is measured by an 8-bit ADC. Since the speed observer utilise the DQ transformed currents for computation of the electromagnetic torque, it is combined with the feed-forward decoupling subsystem.

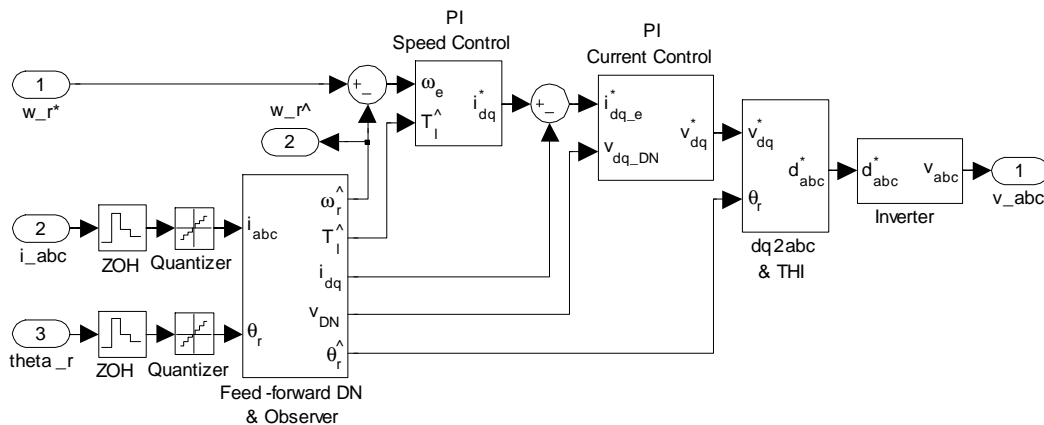


Figure 3.34: Combined speed and current control.

The integration of the previously developed anti-aliasing decoupling, speed observer and voltage feed-forward terms is shown in figure 3.35. The angular position used in the transforms (and output) is not the estimated output of the observer, but is the measured position compensated for the measurement delay,  $\frac{T_s}{2}$ . This position is used instead of the estimated position so that the estimator delay, caused by a torque disturbance, is not included in the position used for the current transformations.

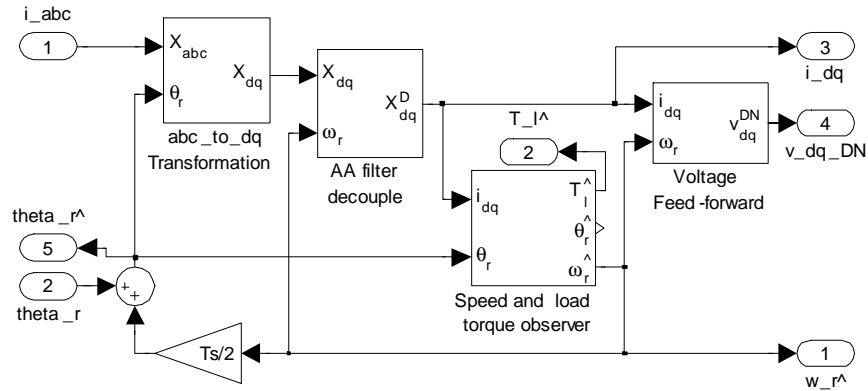


Figure 3.35: Measurement decoupling, speed observer and voltage feed-forward linearization.

The PI speed controller model is as shown in figure 3.36. It includes the same anti-windup structure used for the current control. The observed torque is scaled to current units, before added as a feed-forward term. The saturation block's limit is in current units.

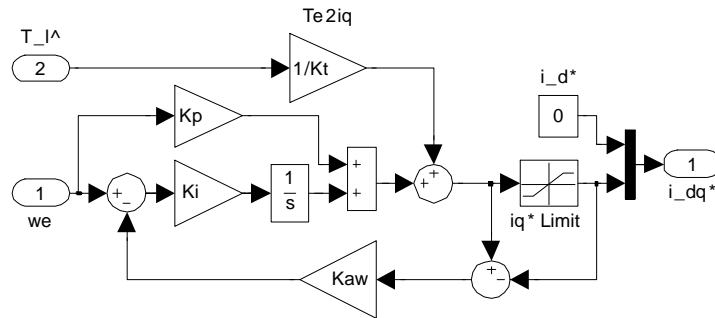


Figure 3.36: PI speed controller.

### 3.2.3.4 Simulation results

The step response in the design is confirmed via simulation as shown in figure 3.37, where the current input and motor parameters of the observer are assumed exactly known. To confirm the control stability when the observer input and parameters are non-ideal, the step response is repeated with a non-unity degradation factor as shown in figures 3.38 and 3.39.

Figure 3.40, shows the speed control response to a speed ramp up to 20 krpm, including a load torque step of 1 N.m at 3 s. Note how the d-axis current deviates only slightly from zero. Figure

3.41, shows the response for the same test, but without the measurement decoupling and the feed-forward linearization terms, respectively. The d-axis current has a steady-state error, which is load dependent without the measurement decoupling. Without the feed-forward linearization term, an oscillatory response results due to the non-linear nature of the current control loop.

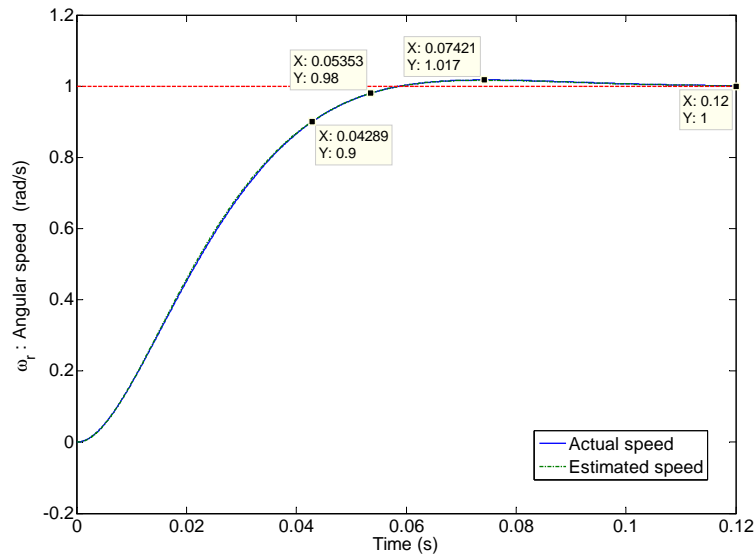


Figure 3.37: Speed control step response,  $\alpha = 1$ .

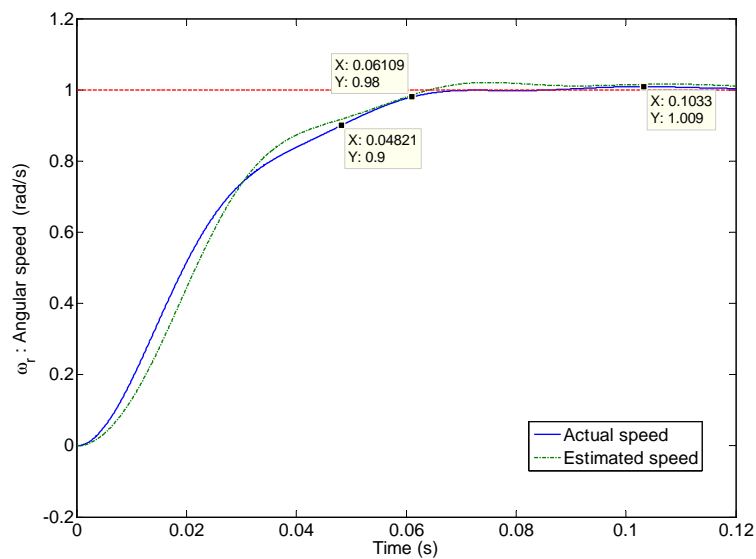


Figure 3.38: Speed control step response with underestimated motor parameters and input,  $\alpha = 0.65$ .



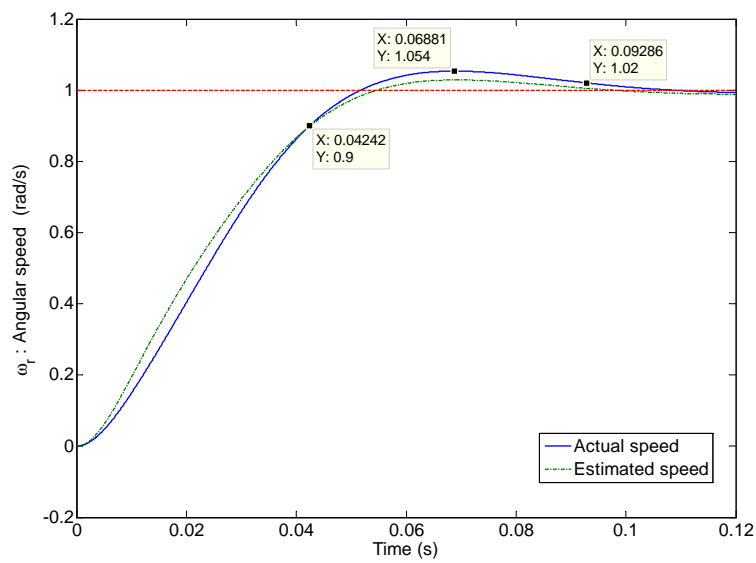


Figure 3.39: Speed control step response with overestimated motor parameters and input,  $\alpha = 1.35$ .

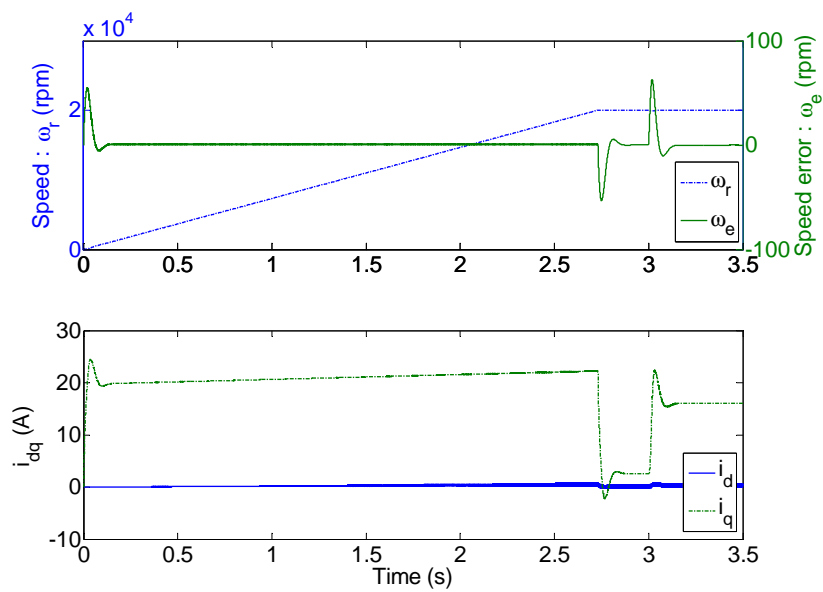


Figure 3.40: Speed ramp and torque load step response.

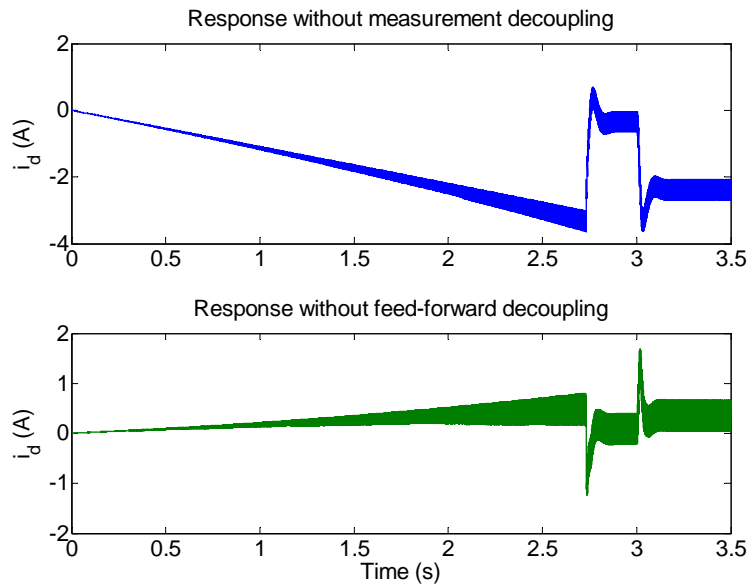


Figure 3.41: Current response to speed ramp and load torque step without measurement decoupling and feed-forward linearization.

In the previous plots, quantization has not been included. Figure 3.42, shows the speed response with the quantization added to the simulation. The ripple in the speed error and torque producing current can clearly be seen.

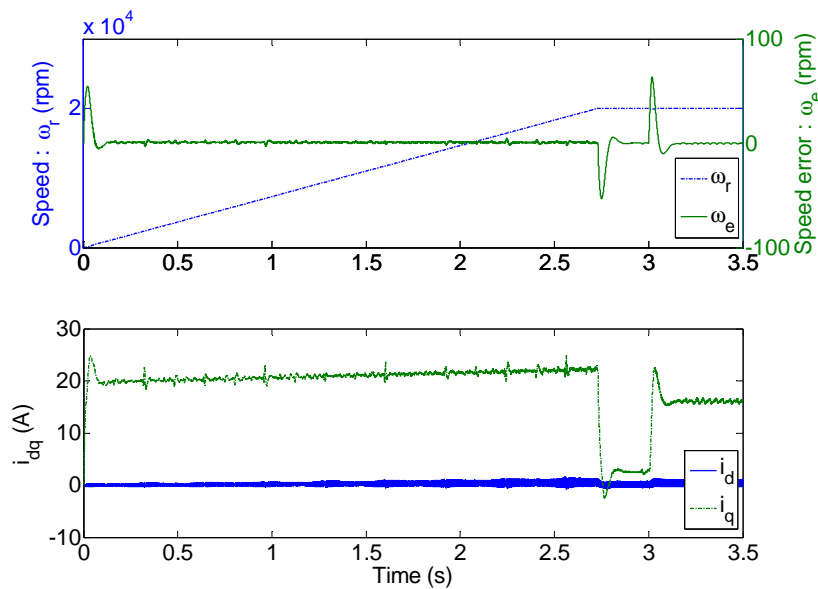


Figure 3.42: Response with quantizer included.

The advantage of third harmonic injection over sine triangle modulation is illustrated in figure 3.43. Instead of using the specified DC bus voltage, a reduced voltage of 20 V is used in the example. The response illustrates the maximum speed which each of the inverter modulation

schemes can attain. With third harmonic injection the maximum speed is increased by approximately 15 %, which is the same percentage increase in the voltage fundamental.

The speed control simulation file is included in appendix C.10.

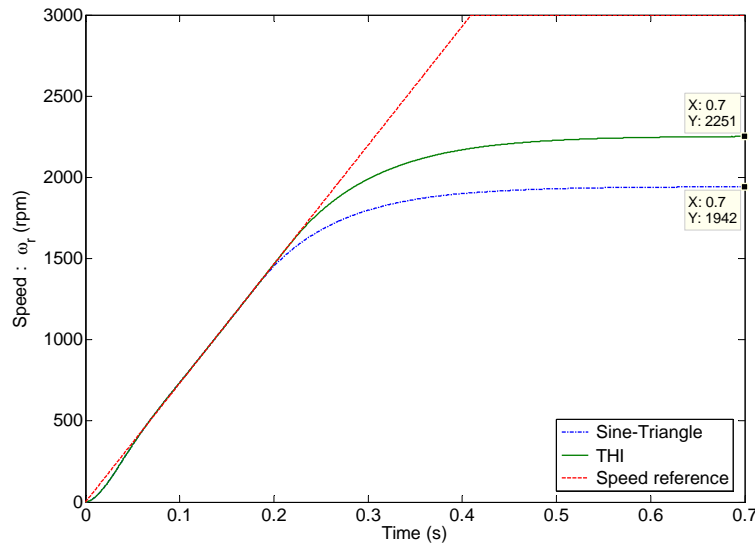
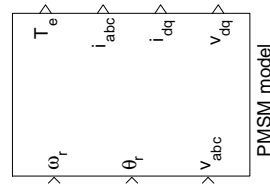


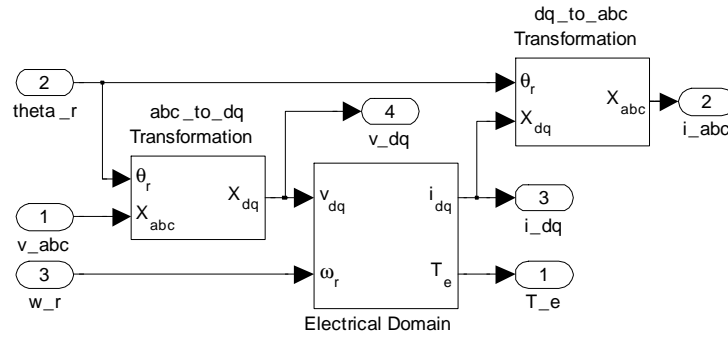
Figure 3.43: Speed response comparison with different modulation schemes.

### 3.2.4 Load torque control

A fictitious torque load for testing the step response as in section C.10 is not available in the real world. In order to test the PMSM motor control, a second PMSM functioning as a torque load is operated in generator mode. For the purpose of simulation, only the electrical domain of the generator is modelled. The mechanical domain of the motor-generator coupled system resides in the motor. Thus, the generator is modelled as in figure 3.44. The dynamics of the linked DC bus capacitors is not modelled.



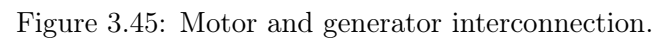
(a) PMSM generator model I/O.



(b) Subsystem interconnection.

Figure 3.44: PMSM simulation model (generator).

The motor and generator is connected as shown in figure 3.45. Note that the diagonal lines emphasise the crossing lines are non-touching. The controller inputs for the generator differ from the motor control inputs. The angular position input to the generator has an offset,  $Du$ , since the motor and generator is not necessarily aligned. For example, if the phase-a winding of each PMSM alternately carry a DC current, the resulting physical alignment of the coupled motor and generator rotors may differ. Since the generator has the same speed as the motor, only one speed observer is required, hence the generator has the estimated angular speed as an input from the motor control.



in the generator. The input is added slowly by using a weighting factor, since the speed will overshoot if the generator receives the motor's current reference as a step command. A simple method by which the generator can be switched softly, without causing a speed disturbance, is shown in figure 3.47.

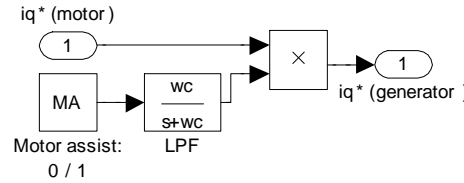


Figure 3.47: Motor assist soft-switching.

With the motor assist activated the current to the motor's speed observer accounts for only half of the produced torque. The generator's contribution to the torque is sensed as a negative load torque by the torque load observer.

Since the torque load controller essentially corresponds to the vector controller without a speed control loop, simulations of the torque load controller is not performed.

### 3.3 V/f Control

#### 3.3.1 Constant flux linkage control

The terminal voltage is controlled proportional to the reference rotational speed of the PMSM. The back-emf of the machine in steady state is:

$$\mathbf{e}_s = \omega_r \boldsymbol{\lambda}_s \quad (3.55)$$

By controlling the voltage proportional to the frequency, the ratio of the back-emf to the rotational speed equals the stator flux linkage. If the contribution of the stator current to the flux linkage is considered negligible, then the stator flux linkage is simply equal to the rotor permanent magnet flux linkage. Hence, V/f control aims to keep the stator flux linkage constant.

The back-emf expression alone is not sufficient for use as a feed-forward term to set the terminal voltage, due to the resistive voltage drop which has to be accounted for in order for enough torque producing current to result. At startup, a boost voltage is added to ensure that the resistive voltage drop is overcome. Also, to ensure that the feed-forward voltage is sufficient, reference acceleration is limited so that the steady state condition is approximately satisfied.

A feed-forward expression which accounts for the different voltage drops in the machine, yields better performance than the previous oversimplification used to explain the principle of operation. Since the rotor position is assumed unavailable in the open-loop control, the PMSM model

in the rotor reference frame is less useful for implementation purposes. Instead, the motor variables may be transformed to the synchronous reference frame, i.e. instead of using the rotor angular position,  $\theta_r$ , in the dq0 coordinate transformation the reference voltage vector angle,  $\theta_e$ , is used. The synchronous reference frame is expressed in  $\gamma\delta$  coordinates, as depicted in figure 3.48.

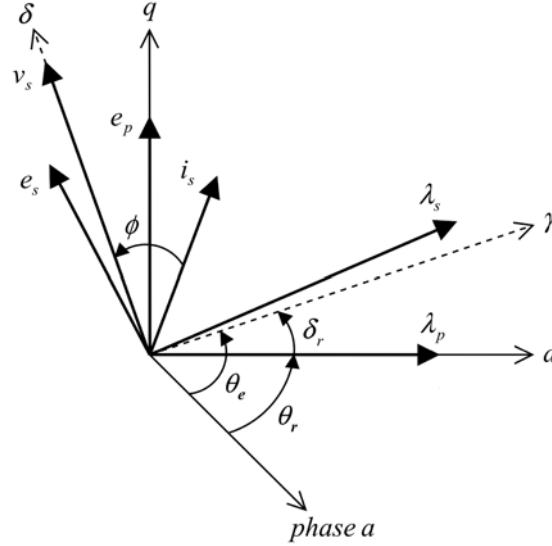


Figure 3.48: PMSM variables in the synchronous reference frame.

As can be seen, if the load angle,  $\delta_r$ , is small, then the  $\delta$ -axis variables are an approximation to the  $q$ -axis variables and the same for the  $\gamma d$  pair. Therefore,  $\delta$ -axis current is associated with real power and the  $\gamma$ -axis current with reactive power [45].

The PMSM model expressed in the synchronous reference frame is [45]:

$$\begin{bmatrix} v_\gamma \\ v_\delta \end{bmatrix} = \begin{bmatrix} r_s + pL_s & -\omega_e L_s \\ \omega_e L_s & r_s + pL_s \end{bmatrix} \begin{bmatrix} i_\gamma \\ i_\delta \end{bmatrix} + \omega_r \lambda_p \begin{bmatrix} \sin(\delta) \\ \cos(\delta) \end{bmatrix} \quad (3.56)$$

where the in-phase and quadrature inductance is assumed equal to  $L_s$  and  $\omega_e$  is the synchronous frequency.

An expression for the terminal voltage for constant flux linkage control as derived by Perera *et al.* is [24]:

$$v_{s0} = i_{s0} r_s \cos(\phi_0) + \sqrt{e_{s0}^2 + [i_{s0} r_s \cos(\phi_0)]^2 - [i_{s0} r_s]^2} \quad (3.57)$$

where  $\phi_0$  is the steady state power-factor angle. Perera *et al.* chose to approximate the back-emf as  $e_{s0} = \omega_{e0} \lambda_p$ . In order to justify this assumption the back-emf is computed from the  $\gamma\delta$  model (equation 3.56) as:

$$\begin{aligned} e_{s0} &= \omega_{e0} (\lambda_{\gamma 0} + j \lambda_{\delta 0}) \\ &= \omega_{e0} [(L_s i_{\gamma 0} + \lambda_p \cos(\delta_{r0})) + j (L_s i_{\delta 0} - \lambda_p \sin(\delta_{r0}))] \end{aligned} \quad (3.58)$$

The magnitude of the back-emf vector is obtained as:

$$\begin{aligned} |\mathbf{e}_{s0}| &= \omega_{e0} \sqrt{\lambda_p^2 + (L_s i_{s0})^2 + 2L_s \lambda_p [i_{\gamma 0} \cos(\delta_{r0}) - i_{\delta 0} \sin(\delta_{r0})]} \\ &\approx \omega_{e0} \lambda_p \end{aligned} \quad (3.59)$$

since we are only interested in the magnitude of the back-emf vector in the steady state. The approximation is justified by noting that:

$$\because \lambda_p^2 \gg L_s^2 \quad (3.60)$$

$$\because \lambda_p > L_s \quad (3.61)$$

If the motor load is known prior to the implementation, then the back-emf approximation may be modified accordingly, as long as the expression is simplified to be independent of the *unknown* load angle,  $\delta_r$ .

Substituting the approximated expression for the back-emf into equation 3.57 and noting that  $i_s \cos(\phi_0) = i_\delta$ , the reference terminal voltage is obtained as:

$$\begin{aligned} v_s^* &= r_s i_\delta + \sqrt{(\omega_e^* \lambda_p)^2 + (r_s i_\delta)^2 - (r_s i_s)^2} \\ &= r_s i_\delta + \sqrt{(\omega_e^* \lambda_p)^2 - (r_s i_\gamma)^2} \end{aligned} \quad (3.62)$$

Note that equation 3.62 uses the instantaneous variables. In order to limit large perturbations in the instantaneous variables, which could cause instability, the inputs to the feed-forward voltage terminal equation has to be filtered.

One might argue that a single filter is sufficient if the reference terminal voltage is filtered instead of its inputs. This is not the case, because the contribution of the (possibly accelerating) reference speed should not be filtered, otherwise the phase lag will cause the reference voltage to be valid for a past reference frequency, instead of the current frequency.

The term under the square root can become negative, especially during startup transients. Therefore, the absolute value is computed before computing the square root.

### 3.3.2 Linearized PMSM model

In order to test the stability of the V/f control, the non-linear PMSM model is linearized in the steady state operating point. The linear system of equations is stable if all the eigenvalues of the linearized model are in the left hand side of the complex plane [24].



To linearize the state-space model of the PMSM, all the state variables are substituted by a steady state value plus a perturbation:

$$x = x_0 + \Delta x \quad (3.63)$$

After this substitution, the system of equations is simplified by expanding the expressions and grouping the steady state and perturbation terms. Second order (and higher) perturbation terms, i.e. products between two perturbation terms are dropped. The steady state and perturbation terms are orthogonal. Hence the steady state and perturbation equations may be grouped separately. The perturbation terms describe the dynamics of the linearized system and can be written in the form [24]:

$$\Delta \dot{x} = A(x_0) \Delta x + B(x_0) \Delta u \quad (3.64)$$

Note that the state transition matrix  $A(x_0)$  is dependent on the operating point, since after expanding the perturbed set of equations, cross product terms of the form  $x_0 \Delta x$  result.

The system of linearized equations can be interpreted as a tangent plane in  $\mathbb{R}^n$ , where  $n$  is the number of state variables. Another method of determining the tangent plane is with the use of a multidimensional Taylor series and dropping the second and higher order derivative terms. With the non-linear system equations written in the form:

$$\dot{x} = f(x, u) \quad (3.65)$$

the first derivative term in the Taylor series of  $f(x, u)$  is the Jacobian matrix of the set of equations. Note that  $f$  is a function vector, i.e.  $f = \begin{bmatrix} f_1(x, u) & f_2(x, u) & \dots & f_n(x, u) \end{bmatrix}^T$ . The state transition and input matrices using the Jacobian linearization around the equilibrium point  $(x_0, u_0)$  is [74]:

$$A(x_0) = \left. \frac{\partial f}{\partial x} \right|_{(x_0, u_0)} \quad (3.66)$$

$$B(x_0) = \left. \frac{\partial f}{\partial u} \right|_{(x_0, u_0)} \quad (3.67)$$

where  $\frac{\partial f}{\partial x}$  is a shorthand notation for the Jacobian matrix defined as:

$$\frac{\partial f}{\partial x} = \frac{\partial (f_1, f_2, \dots, f_n)}{\partial (x_1, x_2, \dots, x_n)} \quad (3.68)$$

The advantage of using the Jacobian linearization is that its use is more general than the manual perturbation substitution method. The set of equations have to be cast in the form of equation 3.65 after which a computer algebra system can be used to compute the Jacobian matrix symbolically and substitute the steady state operating point.

The non-linear PMSM state-space equation 2.43 is in appropriate form for the Jacobian linea-

rization. The linearization computation of the open-loop V/f control is performed in appendix C.11, which results in the state transition matrix given by:

$$\mathbf{A}(\mathbf{x}_0) = \begin{bmatrix} -\frac{1}{\tau_s} & \omega_0 \sigma & i_{q0} \sigma & -\frac{v_{s0} \cos(\delta_{r0})}{L_d} \\ -\frac{\omega_0}{\sigma} & -\frac{1}{\tau_s \sigma} & -\frac{\frac{\lambda_p}{L_d} + i_{d0}}{\sigma} & -\frac{v_{s0} \sin(\delta_{r0})}{L_d \sigma} \\ \frac{3L_d i_{q0}(1-\sigma)z_p^2}{2J} & \frac{3(i_{d0}L_d(1-\sigma) + \lambda_p)z_p^2}{2J} & -\frac{B}{J} & 0 \\ 0 & 0 & -1 & 0 \end{bmatrix} \quad (3.69)$$

with the perturbation state vector defined as  $\Delta \mathbf{x} = [\Delta i_d \quad \Delta i_q \quad \Delta \omega_r \quad \Delta \delta]$ .

The PMSM model in the rotor reference frame is used for the linearization, because after adding the high efficiency control loop presented in section 3.3.4, the substitution of the steady state operating point, on which the linearized state transition matrix depends, is simplified. With the high efficiency control loop added, the steady state operating point is determined from:

$$\mathbf{x}_0 = \begin{bmatrix} i_{d0} \\ i_{q0} \\ \omega_{r0} \\ \delta_{r0} \end{bmatrix} = \begin{bmatrix} 0 \\ \frac{1}{3\lambda_p z_p^2} (2\omega_0 B + T_l z_p) \\ \omega_0 \\ \tan^{-1} \left( -\frac{v_{d0}}{v_{q0}} \right) \end{bmatrix} \quad (3.70)$$

$$\mathbf{u}_0 = \begin{bmatrix} v_{d0} \\ v_{q0} \\ \omega_{e0} \end{bmatrix} = \begin{bmatrix} r_s i_{d0} - \omega_0 L_q i_{q0} \\ r_s i_{q0} + \omega_0 L_d i_{d0} + \omega_0 \lambda_p \\ \omega_0 \end{bmatrix} \quad (3.71)$$

In the actual control the terminal voltage is determined from equation 3.62, which depends on the current in the  $\gamma\delta$  coordinates. Due to the high efficiency loop, the resultant terminal voltage operating point is not equal to the steady state feed-forward voltage, put differently:

$$v_{s0} \neq r_s i_{\delta 0} + \sqrt{(\omega_{e0} \lambda_p)^2 - (r_s i_{\gamma 0})^2} \quad (3.72)$$

It is more accurate to determine the resultant terminal voltage from the steady state current, by constraining the rotor reference frame current such that the reactive current is zero and the torque producing current is in equilibrium with the load, as done in equation 3.70, thereby accounting for the contribution of the high efficiency loop to the resultant terminal voltage.

The resultant terminal voltage in equation 3.69 and the rotor reference frame voltage in equation 3.70 are related by:

$$\begin{bmatrix} v_{d0} \\ v_{q0} \end{bmatrix} = v_{s0} \begin{bmatrix} -\sin(\delta_{r0}) \\ \cos(\delta_{r0}) \end{bmatrix} \quad (3.73)$$

which may be used to eliminate the trigonometric terms present in equation 3.69.

### 3.3.3 Stabilization

#### 3.3.3.1 Unstable open-loop operation

The stability of the open-loop V/f controller is tested by calculating the eigenvalues of the state transition matrix of the linearized system. Since the linearized system depends on the operating frequency and load conditions, the eigenvalues vary accordingly. Hence, a root locus as a function of the operating frequency can be constructed.

The root locus of the open-loop V/f controller is as shown in figure 3.49. A set of complex conjugate pairs are shown for the fast electrical stator dynamics and another complex conjugate pair (as shown in the zoomed axes) for the slow rotor dynamics. It can be deduced that the open-loop V/f control becomes unstable at approximately 55 Hz. The code which computes the eigenvalues and that generates the root locus is included in appendix C.12.

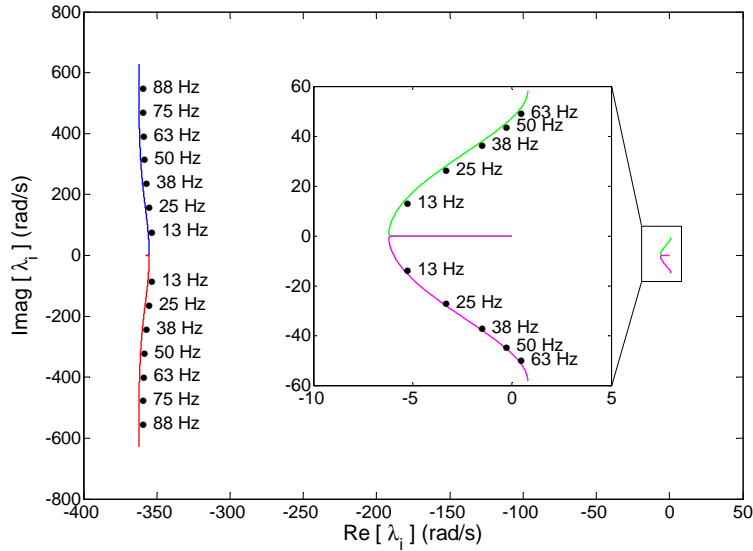


Figure 3.49: Root loci of open-loop V/f control.

#### 3.3.3.2 Reduced order model

Although the stability of the PMSM can be checked by computing the eigenvalues of the linearized model, the high order model itself does not yield much insight into the cause of the instability. To gain such insight, the model is simplified into a reduced order model, which is used to calculate an approximate damping ratio.

The perturbed speed is related to the perturbed electromechanical and load torque as follows:

$$\begin{aligned} \Delta \dot{\omega}_m &= \frac{1}{J} (\Delta T_e - \Delta T_l - \Delta \omega_m B) \\ \therefore \frac{\Delta \omega_r(s)}{\Delta T_{res}(s)} &= \frac{z_p}{sJ + B} \end{aligned} \quad (3.74)$$

where  $\Delta T_{res}$  is the resultant torque acting on the rotor given by  $\Delta T_{res} = \Delta T_e - \Delta T_l$ . Equation 3.74 is simply the transfer function of the rotor dynamics, where the differential equation has been Laplace transformed.

The perturbed speed in turn has its own feedback to the perturbed electromechanical torque, because a perturbation in speed will cause the magnetic axis of the current to align differently with respect to the rotor after the perturbation in speed has had time to cause a perturbation in load angle.

The total perturbed electromechanical torque is dependent on both the dq-axis perturbed currents:

$$\begin{aligned}\Delta T_e(s) &= \Delta T_{i_q}(s) + \Delta T_{i_d}(s) \\ &= T(i_{d0}) \Delta i_q(s) + T(i_{q0}) \Delta i_d(s)\end{aligned}\quad (3.75)$$

where the operating point dependent gains are obtained from equation 3.69 via inspection:

$$T(i_{d0}) = \frac{3}{2} (i_{d0} L_d (1 - \sigma) + \lambda_p) z_p \quad (3.76)$$

$$T(i_{q0}) = \frac{3}{2} L_d i_{q0} (1 - \sigma) z_p \quad (3.77)$$

Therefore, the transfer function of perturbed speed to perturbed electromechanical torque can be decomposed using an approach similar to the chain rule for differentiation using Leibniz notation:

$$\frac{\Delta T_e(s)}{\Delta \omega_r(s)} = \frac{\Delta T_{i_q}(s)}{\Delta i_q(s)} \frac{\Delta i_q(s)}{\Delta \delta_r(s)} \frac{\Delta \delta_r(s)}{\Delta \omega_r(s)} + \frac{\Delta T_{i_d}(s)}{\Delta i_d(s)} \frac{\Delta i_d(s)}{\Delta \delta_r(s)} \frac{\Delta \delta_r(s)}{\Delta \omega_r(s)} \quad (3.78)$$

If the rotor saliency is assumed unity, i.e.  $\sigma = 1$ , then the transfer function in equation 3.78 reduces to:

$$\frac{\Delta T_e(s)}{\Delta \omega_r(s)} = \frac{\Delta T_{i_q}(s)}{\Delta i_q(s)} \frac{\Delta i_q(s)}{\Delta \delta_r(s)} \frac{\Delta \delta_r(s)}{\Delta \omega_r(s)} \quad (3.79)$$

From the previous discussion, the mechanical dynamics of the linearized model can be depicted as in figure 3.50.

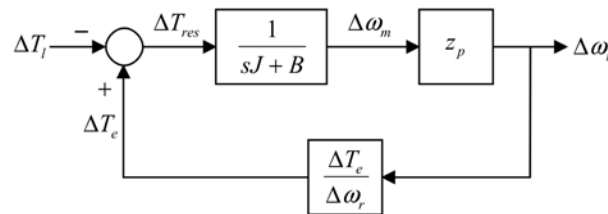


Figure 3.50: Block diagram of linearized mechanical dynamics.

In order to obtain the transfer function in equation 3.79, each of its sub-transfer functions are required. The transfer function from perturbed speed to load angle is obtained by Laplace

transforming the fourth row in equation 3.69:

$$\frac{\Delta\delta_r(s)}{\Delta\omega_r(s)} = -\frac{1}{s} \quad (3.80)$$

The perturbed torque producing current, as a function of the load angle, is obtained by solving the Laplace transform of the system of equations formed by the first and second row of equation 3.69:

$$\begin{bmatrix} s\Delta i_d \\ s\Delta i_q \end{bmatrix} = \begin{bmatrix} -\frac{1}{\tau_s} & \omega_0\sigma & i_{q0}\sigma & -\frac{v_{s0}\cos(\delta_{r0})}{L_d} \\ -\frac{\omega_0}{\sigma} & -\frac{1}{\tau_s\sigma} & -\frac{\lambda_p+i_{d0}}{\sigma} & -\frac{v_{s0}\sin(\delta_{r0})}{L_d\sigma} \end{bmatrix} \begin{bmatrix} \Delta i_d \\ \Delta i_q \\ \Delta\omega_r \\ \Delta\delta_r \end{bmatrix} \quad (3.81)$$

Equation 3.81 is reduced to contain only the unknowns of interest by noting that  $\Delta\omega_r$  is assumed known from the feed-forward path in figure 3.50 and  $\Delta\delta_r$  is known via its relation to  $\Delta\omega_r$  in equation 3.80. Hence, the system of equations can be written in an adjoint form and solved as:

$$s\Delta\mathbf{x}_i = \begin{bmatrix} \mathbf{A}_i & | & \mathbf{c} \end{bmatrix} \begin{bmatrix} \Delta\mathbf{x}_i \\ - \\ \Delta\delta_r \end{bmatrix} \quad (3.82)$$

$$\therefore \frac{\Delta\mathbf{x}_i}{\Delta\delta} = (s\mathbf{I} - \mathbf{A}_i)^{-1} \mathbf{c} \quad (3.83)$$

where

$$\frac{\Delta\mathbf{x}_i}{\Delta\delta} = \begin{bmatrix} \frac{\Delta i_d}{\Delta\delta} & \frac{\Delta i_q}{\Delta\delta} \end{bmatrix}^T \quad (3.84)$$

$$\mathbf{c} = \begin{bmatrix} -\left(s i_{q0}\sigma + \frac{v_{s0}\cos(\delta_{r0})}{L_d}\right) & \left(s \frac{\lambda_p+i_{d0}}{L_d\sigma} - \frac{v_{s0}\sin(\delta_{r0})}{L_d\sigma}\right) \end{bmatrix}^T \quad (3.85)$$

$$\mathbf{A}_i = \begin{bmatrix} -\frac{1}{\tau_s} & \omega_0\sigma \\ -\frac{\omega_0}{\sigma} & -\frac{1}{\tau_s\sigma} \end{bmatrix} \quad (3.86)$$

Therefore, after simplifying, the solution for the transfer function of load angle to torque producing current is:

$$\frac{\Delta i_q(s)}{\Delta\delta_r(s)} = \frac{1}{L_d} \frac{as^2 + bs + c}{(s + \omega_s)^2 + \omega_0^2} \quad (3.87)$$

where the placeholder terms are defined as:

$$a = \lambda_p + L_d i_{d0} \quad (3.88)$$

$$b = \omega_0 L_d i_{q0} + \omega_s L_d i_{d0} + \omega_s \lambda_p + v_{d0} \approx \omega_s \lambda_p \quad (3.89)$$

$$c = (\omega_0 v_{q0} + \omega_s v_{d0}) \approx \omega_0^2 \lambda_p \quad (3.90)$$

$$\omega_s = \frac{1}{\tau_s} \quad (3.91)$$

The transfer function from perturbed torque producing current to electromechanical torque is equal to the DC gain,  $T(i_{d0})$ , defined in equation 3.76.

By substituting the previously obtained sub-transfer functions, the transfer function from perturbed speed to electromechanical torque, corresponding to the transfer function in the feedback path of the block diagram in figure 3.50, is:

$$\frac{\Delta T_e(s)}{\Delta \omega_r(s)} = -\frac{3}{2} \frac{\lambda_p}{L_d} z_p \frac{as^2 + bs + c}{s((s + \omega_s)^2 + \omega_0^2)} \quad (3.92)$$

The open-loop V/f control becomes unstable if the transfer function in equation 3.92 cause positive feedback, which happens when its open-loop gain is greater than one and has a phase shift equal to or greater than  $180^\circ$ . The block diagram in figure 3.50 with equation 3.92, has the same order as the linearized model of equation 3.69.

In order to obtain a reduced order model, the transfer function in the feedback path is written in the form:

$$\frac{\Delta T_e(s)}{\Delta \omega_r(s)} = \frac{\Delta T_e(s)}{\Delta \delta_r(s)} \frac{\Delta \delta_r(s)}{\Delta \omega_r(s)} \quad (3.93)$$

The bandwidth of the transfer function in the feedback path is relatively large in comparison to the slow rotor dynamics. Hence, an approximation of the transfer function can be made by approximating it by its DC gain, which is dependent on the operating point. The DC gain is obtained with the aid of the final value theorem, assuming the input to the feedback transfer function is an impulse function (the signal after the integrator of  $\frac{\Delta \delta_r(s)}{\Delta \omega_r(s)}$  corresponds to a step input):

$$\begin{aligned} K_{e0} &= \lim_{s \rightarrow 0} s \frac{\Delta T_e(s)}{\Delta \delta_r(s)} \frac{1}{s} \\ &= \frac{3}{2} \frac{\lambda_p}{L_d} z_p \frac{\omega_0 v_{q0} + \omega_s v_{d0}}{\omega_s^2 + \omega_0^2} \\ &\approx \frac{3}{2} \frac{z_p}{L_d} \frac{(\omega_0 \lambda_p)^2}{\omega_s^2 + \omega_0^2} \end{aligned} \quad (3.94)$$

In the literature  $K_{e0}$  is named the electromechanical spring constant [24], since  $\Delta \delta_r(s)$  can be thought of as an angular displacement and  $\Delta T_e(s)$  as the resulting angular force due to the displacement on the spring. A speed perturbation has oscillatory behaviour due to the mass-spring system formed by the rotor's moment of inertia and the electromechanical spring constant.

With the reduced order model in the feedback path, a second order closed loop transfer function results:

$$\frac{\Delta \omega_r(s)}{\Delta T_l(s)} = \frac{z_p}{J} \frac{s}{s^2 + \frac{B}{J}s + \frac{1}{J}K_{e0}z_p} \quad (3.95)$$

Hence, for the open-loop V/f control the approximate natural frequency and damping of the

second order model is:

$$\omega_{n\_ol} = \sqrt{\frac{1}{J}K_{e0}z_p} \quad (3.96)$$

$$\zeta_{ol} = \frac{B}{2\sqrt{Jz_pK_{e0}}} \quad (3.97)$$

Hence, the open-loop V/f control has very little damping, due only to the viscous friction.

The reduced order model is confirmed by comparing it to the higher order model's frequency response. Figure 3.51 shows the bode diagram for a rotational frequency of 50 Hz and figure 3.52 for a rotational frequency of 60 Hz. As expected, the exact model predicts that the PMSM is marginally stable for the lower frequency and unstable for the higher frequency. The smallest steady state rotational speed which yields unstable behaviour corresponds to that predicted by the root locus method, i.e.  $\approx 55$  Hz. Since the root locus and frequency response methods yield the same result, the derivation of the exact transfer function is verified.

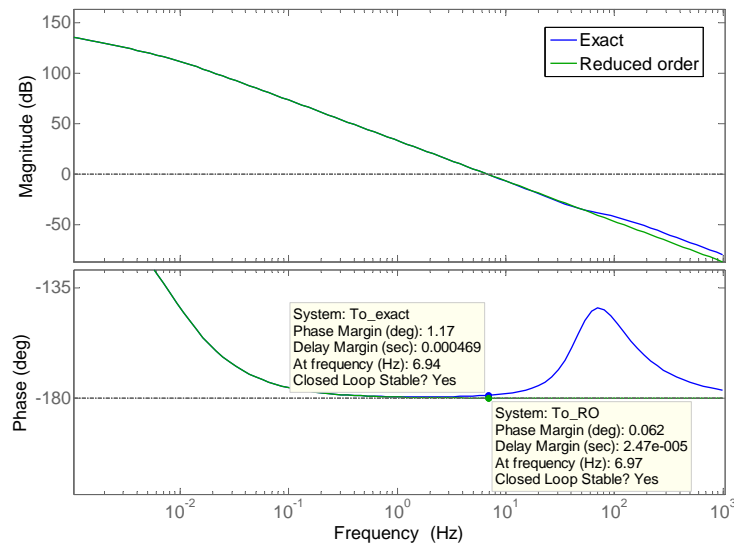


Figure 3.51: Bode diagram of exact and reduced order model for  $\omega_{r0} = 2\pi 50 \text{ rad.s}^{-1}$ .

The reduced order model does not reveal the unstable response directly, because the phase response approaches  $180^\circ$  asymptotically, which corresponds to the analytical approximation of the damping in equation 3.97. Nevertheless, common sense suggests that a system with a phase margin which exceeds some threshold close to  $0^\circ$ , although not strictly unstable, should be assumed unstable in order to be conservative with the assessment of the stability margins.

A better insight into the cause of the unstable behaviour (and therefore how to compensate for it), can be obtained by rearrangement of the open-loop V/f control block diagram. Instead of setting the load torque as an input, it is considered as a disturbance and the new input is a speed perturbation reference,  $\Delta\omega_r^*$ , which is ideally zero. Figure 3.53, shows this new arrangement.

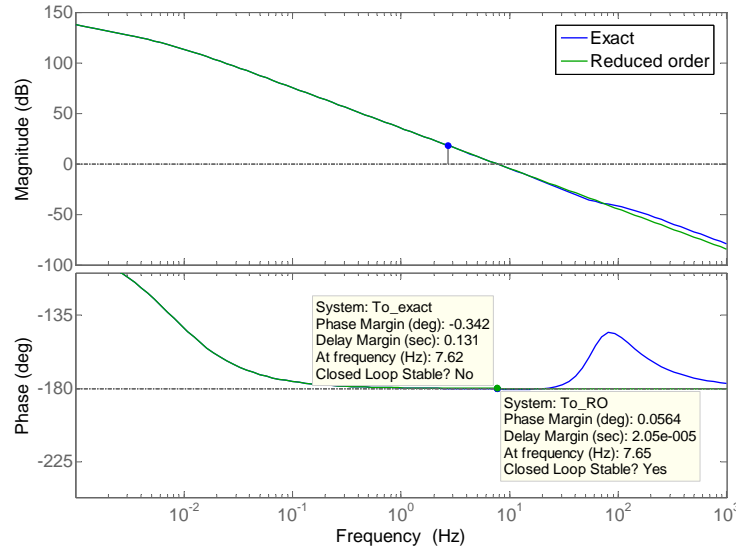


Figure 3.52: Bode diagram of exact and reduced order model for  $\omega_{r0} = 2\pi 60 \text{ rad.s}^{-1}$ .

For low frequencies, the phase shift due to the pure integrator and the plant is less than  $180^\circ$ , hence the speed perturbation feedback is required for the stability of the machine at low frequencies. The gain in the forward path of the loop,  $K_{e0}$ , increases as the speed increases, as shown in figure 3.54. This increase in gain reduces the phase margin and at some critical speed the loop becomes unstable. If the d-axis current can be controlled constant, such as the case with the high efficiency control loop, then  $K_{e0}$  is independent of the load torque.

If a zero could be inserted to compensate the phase of the speed perturbation error,  $\Delta\omega_{re}$ , then the system would be stable for higher frequencies.

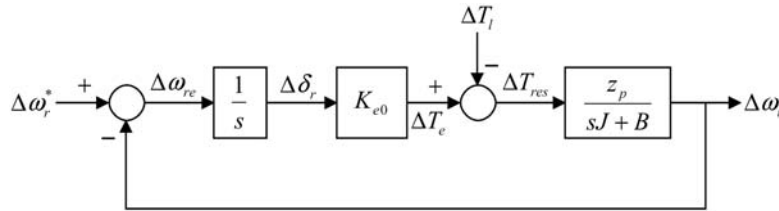


Figure 3.53: Rearranged open-loop V/f control block diagram.

### 3.3.3.3 Stabilization via synchronous frequency modulation

In order to compensate the phase of the speed perturbation error, an estimate of the rotor speed perturbation is required. Figure 3.55, shows the estimation of the speed perturbation by some hypothetical function,  $f(\Delta\omega_r)$ . The superscript,  $c$ , indicates that the estimation function also acts as a compensator. The dotted line in the feedback path emphasizes that it is not a direct feedback of  $\Delta\omega_r$  as is the case with the solid feedback line which forms part of the open-loop



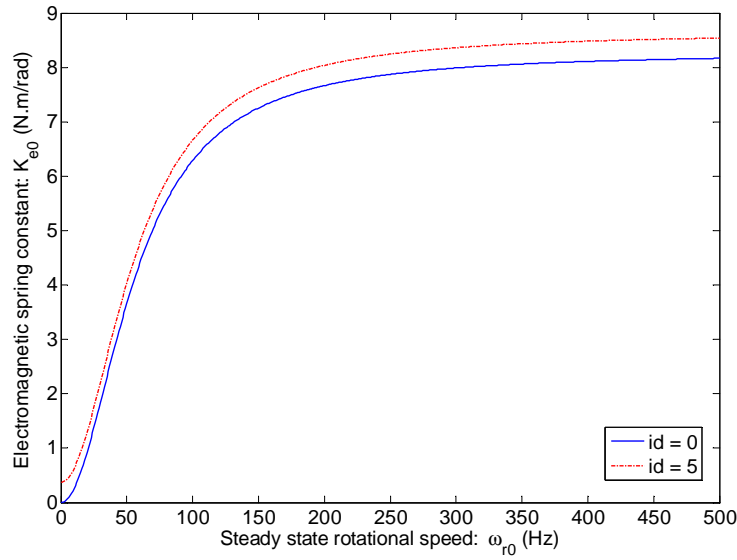


Figure 3.54: Dependence of electromechanical spring constant ( $K_{e0}$ ) on operating point.

V/f control model. The gain,  $k_c$ , serves as a gain adjustment of the compensator term if the compensator's gain is not inherently adjustable. Note that the estimated speed perturbation in the feedback path and the speed perturbation reference does not necessarily have the same units. This is not of importance, because the speed perturbation reference is a fictitious regularization input, i.e.  $\Delta\omega_r^* = 0$ .

The synchronous frequency perturbation is used to compensate the inverter's reference angle, as shown in equation 3.98.

$$\begin{aligned}\theta_e^* &= \int (\omega_{e0}^* + \Delta\omega_e^*) dt \\ &= \theta_{e0}^* + \Delta\theta_e^*\end{aligned}\quad (3.98)$$

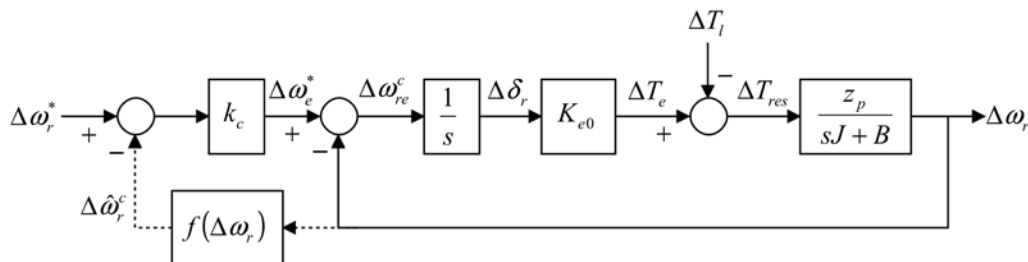


Figure 3.55: Compensation of speed perturbation in the feedback path.

The method of estimating the rotor speed perturbation is presented in [44, 45, 24], which is based on extracting the rotor speed perturbation from the perturbation in measured power. The power perturbation expression is obtained from the power balance equation which relates

the input power  $p_e$  to the different loads which absorb or dissipate the energy [24]:

$$\begin{aligned} p_e &= P_e + \Delta p_e \\ &= p_{loss} + \frac{dW_{em}}{dt} + \frac{1}{z_p^2} \frac{J}{2} \frac{d\omega_r^2}{dt} + \frac{1}{z_p^2} B \omega_r^2 + \frac{1}{z_p} T_l \omega_r \end{aligned} \quad (3.99)$$

where  $p_{loss}$  is the motor and inverter losses,  $\frac{dW_{em}}{dt}$  is the change in stored electromagnetic energy,  $\frac{1}{z_p^2} \frac{J}{2} \frac{d\omega_r^2}{dt}$  is the change in rotor kinetic energy,  $\frac{1}{z_p^2} B \omega_r^2$  is the power loss due to viscous friction and  $\frac{1}{z_p} T_l \omega_r$  is the power transferred to a load torque which is externally coupled to the rotor shaft.

The perturbation in input power is obtained by perturbing the load variables. The motor losses can be assumed to be relatively constant and does not contribute to input power perturbation. The stator stores little electromagnetic energy and can also be neglected. The power perturbation is obtained by perturbing the state variables in the power balance equation (higher order terms are dropped):

$$\begin{aligned} P_e + \Delta p_e &= \frac{1}{z_p^2} \frac{J}{2} \frac{d}{dt} (\omega_{r0} + \Delta\omega_r)^2 + \frac{1}{z_p^2} B (\omega_{r0} + \Delta\omega_r)^2 + \frac{1}{z_p} T_l (\omega_{r0} + \Delta\omega_r) \\ &= \frac{1}{z_p^2} \frac{J}{2} \frac{d}{dt} (\omega_{r0}^2 + 2\omega_{r0}\Delta\omega_r) + \frac{1}{z_p^2} B (\omega_{r0}^2 + 2\omega_{r0}\Delta\omega_r) + \frac{1}{z_p} T_l (\omega_{r0} + \Delta\omega_r) \\ \therefore \Delta p_e (\Delta\omega_r) &= \frac{1}{z_p^2} J \omega_{r0} \Delta\dot{\omega}_r + 2 \frac{1}{z_p^2} B \omega_{r0} \Delta\omega_r + \frac{1}{z_p} T_l \Delta\omega_r \end{aligned} \quad (3.100)$$

The power perturbation in equation 3.100 is dependent on a feed-forward term of the speed perturbation,  $\left(2 \frac{1}{z_p^2} B \omega_{r0} + z_p T_l\right) \Delta\omega_r$ , but also on the derivative of the speed perturbation,  $\frac{1}{z_p^2} J \omega_{r0} \Delta\dot{\omega}_r$ . Thus, the measured power perturbation meets the phase compensation requirement and can be used for the synchronous frequency modulation. Substituting the power perturbation into the position of the estimation function,  $f(\Delta\omega_r)$ , in figure 3.55 yields the synchronous frequency modulation as:

$$\begin{aligned} \Delta\omega_e^* &= k_c (\Delta\omega_r^* - \Delta p_e (\Delta\omega_r)) \\ &= -k_c \Delta p_e (\Delta\omega_r) \end{aligned} \quad (3.101)$$

where  $k_c$  is required to adjust the gain of the power perturbation.

For implementation the power perturbation is obtained by measuring the power to the motor and extracting the perturbation component with a high-pass filter. In the  $\gamma\delta$  coordinates the power is measured as:

$$p_e = \frac{3}{2} (v_\delta i_\delta + v_\gamma i_\gamma) \quad (3.102)$$

Thus, the power perturbation is given by:

$$\Delta p_e = \frac{s}{s + \omega_c} p_e \quad (3.103)$$

where  $\omega_c$  is the high-pass filter cut-off frequency. The cut-off frequency is chosen low compared to the dynamics of the rest of the system, so that its transfer characteristic is assumed unity and can be ignored in the reduced order stability analysis.

The transfer function from rotor speed perturbation to synchronous speed modulation reference can be written in the form of a proportional plus derivative (PD) controller:

$$\frac{\Delta\omega_e^*}{\Delta\omega_r} = k_c (K_d (\omega_{r0}) s + K_p (\omega_{r0})) \quad (3.104)$$

The dependence of the PD gains on the operating speed is removed by varying the compensator gain,  $k_c$ , inversely proportional to the magnitude of the steady state reference speed,  $\omega_{r0}^*$ . Hence the compensator gain is:

$$k_c = \frac{c}{|\omega_{r0}^*| + \epsilon_z} \quad (3.105)$$

where  $\epsilon_z$  is a small constant added to prevent division by zero.

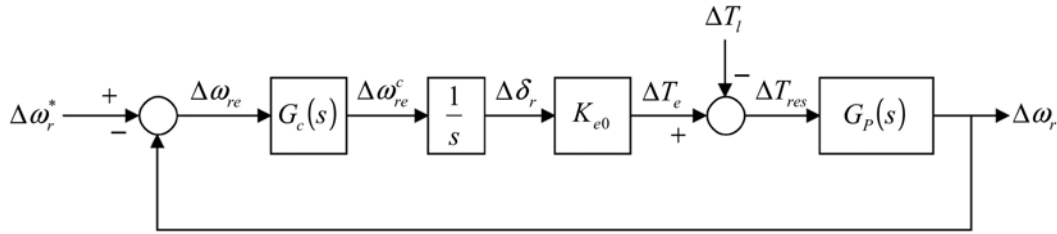


Figure 3.56: Simplified block diagram of open-loop V/f control with stabilization loop.

The open-loop V/f control with stabilization loop block diagram is simplified and represented as in figure 3.56, where the plant is defined as:

$$G_p(s) = \frac{z_p}{sJ + B} \quad (3.106)$$

and the compensator is defined as:

$$G_c(s) = 1 + k_c K_d s + k_c K_p \quad (3.107)$$

where the derivative gain and proportional gain is given by:

$$K_d = \frac{1}{z_p^2} J \omega_{r0} \quad (3.108)$$

$$K_p = 2 \frac{1}{z_p^2} B \omega_{r0} + z_p T_l \quad (3.109)$$

Note that the negative gain in equation 3.101 has been absorbed in the negative feedback of figure 3.56. The characteristic equation of the closed-loop transfer function is:

$$\Delta = s^2 + s \frac{1}{J} (B + z_p k_c K_e0 K_d) + \frac{1}{J} z_p K_e0 (1 + k_c K_p) \quad (3.110)$$

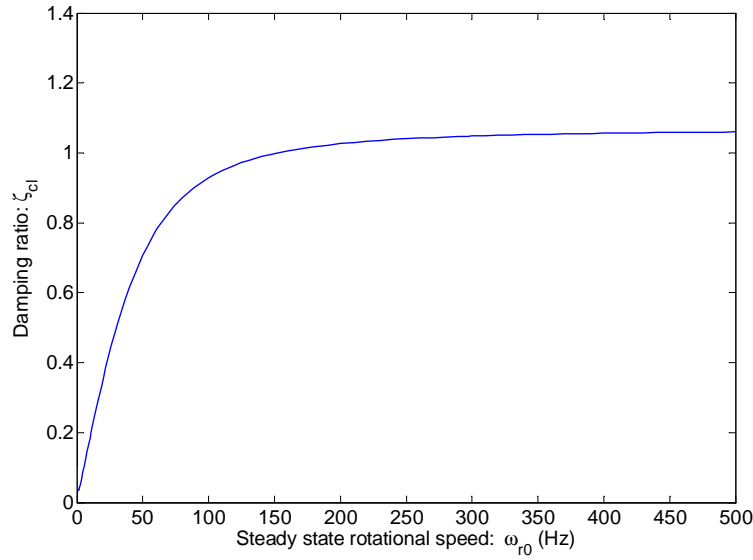


Figure 3.57: Damping ratio as a function of operating speed.

The natural frequency and damping for the stabilized system is determined from the characteristic equation to be:

$$\omega_{n\_cl} = \sqrt{\frac{z_p K_{e0}}{J} (1 + k_c K_p)} \quad (3.111)$$

$$\zeta_{cl} = \frac{B + z_p k_c K_{e0} K_d}{2\sqrt{J z_p K_{e0} (1 + k_c K_p)}} \quad (3.112)$$

where it can be seen that the damping and natural frequency has been increased. As a check on the calculation note that if the compensator gain,  $k_c$ , is set equal to zero then the natural frequency and damping of the system without the stabilization loop results.

In order to obtain an over-damped system (i.e.  $\zeta_{cl} > 1$ ) the gain constant in equation 3.105 is required to be  $c \gtrsim 17$ . The power perturbation high-pass filter's cut-off frequency is chosen as 0.5 Hz.

#### 3.3.3.4 Low speed boost voltage

The over-damped characteristic is obtainable only after a minimum rotational speed as shown in figure 3.57, which is generated with the approximated damping ratio in equation 3.112. Therefore, successful startup of the PMSM is still a problem due to the lack of damping at low speeds, which for this particular motor corresponds to speeds below 25 Hz.

Increasing the startup current on purpose (by adding a boost voltage at low speeds) helps to ensure successful startup. With no-load at startup, the increase in terminal voltage corresponds to an increase in  $d$ -axis current, which in turn corresponds to an increase in the electromechanical spring constant. Therefore, any deviation of the rotor magnetic axis with respect to the stator

field will experience an increased restoring force by the electromechanical spring constant.

Since the increased  $d$ -axis current is an inefficient method of stabilizing the motor<sup>5</sup>, the boost voltage is gradually decreased as the operating frequency increases.

### 3.3.3.5 Verification of stabilization with synchronous frequency modulation

In order to confirm the improved damping of the open-loop V/f control, the stabilization loop is added to the non-linear system model. The eigenvalues of the new linearized system can be used to confirm the stability in the form of a root locus. The stability loop is added to the set of non-linear equations by noting that the inverter frequency perturbation,  $\Delta\omega_e$ , is no longer arbitrary but is related to the rotor speed perturbation by the power perturbation feedback. For the reduced order system, this relation is expressed by equation 3.104, but for the accurate high order system, this relationship is expressed by relating the power perturbation to the instantaneous power. In the rotor reference frame the instantaneous power is [24]:

$$\begin{aligned} p_e &= \frac{3}{2} (v_d i_d + v_q i_q) \\ &= \frac{3}{2} V_s (-\sin(\delta) i_d + \cos(\delta) i_q) \end{aligned} \quad (3.113)$$

Substituting the instantaneous power into equations 3.103 and 3.101, yields the inverter frequency modulation as:

$$\Delta\omega_e = -\frac{3}{2} V_s k_c \frac{s}{s + \omega_c} (-\sin(\delta) i_d + \cos(\delta) i_q) \quad (3.114)$$

The state equation is obtained by performing the inverse Laplace transform, resulting in:

$$\Delta\dot{\omega}_e = -\omega_c \Delta\omega_e - \frac{3}{2} V_s k_c \left( -\sin(\delta) \dot{i}_d + \cos(\delta) \dot{i}_q - (\cos(\delta) i_d + \sin(\delta) i_q) \dot{\delta} \right) \quad (3.115)$$

The linearized system with stabilization loop results in:

$$\mathbf{A}_{stab}(\mathbf{x}_0) = \begin{bmatrix} -\frac{1}{\tau_s} & \omega_0 \sigma & i_{q0} \sigma & -\frac{v_{q0}}{L_d} & 0 \\ -\frac{\omega_0}{\sigma} & -\frac{1}{\tau_s \sigma} & -\frac{\frac{\lambda_p}{L_d} + i_{d0}}{\sigma} & \frac{v_{d0}}{L_d \sigma} & 0 \\ \frac{3L_d i_{q0}(1-\sigma)z_p^2}{2J} & \frac{3(i_{d0}L_d(1-\sigma) + \lambda_p)z_p^2}{2J} & -\frac{B}{J} & 0 & 0 \\ 0 & 0 & -1 & 0 & 1 \\ A_{51} & A_{52} & A_{53} & A_{54} & A_{55} \end{bmatrix} \quad (3.116)$$

where the matrix placeholder variables are equal to:

<sup>5</sup>Which by itself is not a sufficient stabilizer at higher frequencies, thus necessitating the stabilization loop.

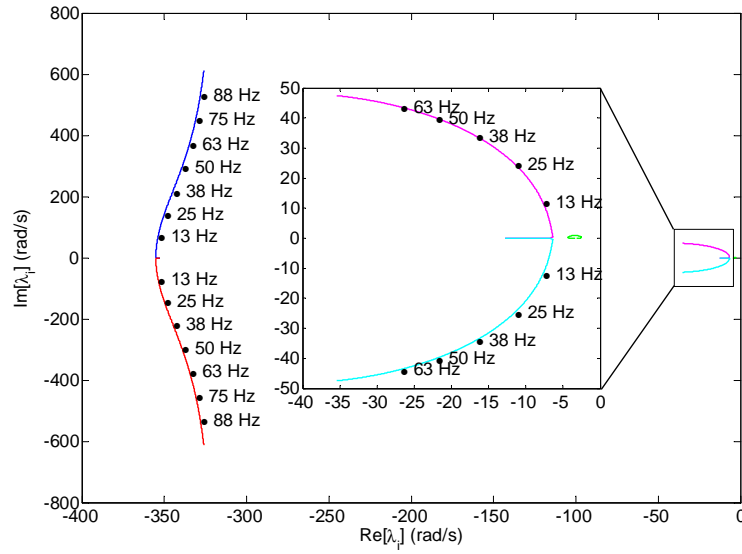


Figure 3.58: Root loci of open-loop V/f control with stabilization loop ( $k_c = \frac{10}{|\omega_{r0}^*|}$ ).

$$\begin{aligned}
 A_{51} &= \frac{k_1}{\sigma} (\omega_{r0} v_{q0} + \sigma \omega_s v_{d0}) \\
 A_{52} &= \frac{k_1}{\sigma} (\omega_s v_{q0} - \sigma^2 \omega_{r0} v_{d0}) \\
 A_{53} &= \frac{k_1}{\sigma} \left( \left( \frac{\lambda_p}{L_d} + (1 - \sigma) i_{d0} \right) v_{q0} + (1 - \sigma) \sigma i_{q0} v_{d0} \right) \\
 A_{54} &= \frac{k_1}{\sigma L_d} \left( (1 - \sigma) v_{s0} \sin(2\delta_{r0}) + \sigma (\sigma \omega_0 i_{q0} - \omega_s i_{d0}) v_{q0} + \left( \omega_s i_{q0} + \omega_{r0} \left( \frac{\lambda_p}{L_d} + i_{d0} \right) \right) v_{d0} \right) \\
 A_{55} &= -k_1 (v_{d0} i_{q0} - v_{q0} i_{d0}) - \omega_c \\
 k_1 &= \frac{3}{2} k_c
 \end{aligned}$$

The root locus of the open-loop V/f control with stabilization loop is as shown in figure 3.58. The stability is verified, since the eigenvalues does not cross over into the right hand plane. The damping ratio is low at small rotational speed, but increases and converges at higher rotational speed, which corresponds to the damping ratio obtained with the reduced order model (figure 3.57).

### 3.3.4 High efficiency control

Besides the stabilization control loop, another control loop can be added in order to obtain high efficiency, i.e.  $i_d = 0$ . The stabilization control loop operates on the principle of suppressing power perturbations, whilst the high efficiency control loop operates on the principle of suppressing reactive power.

The reactive power in the synchronous reference frame is given by [45]:

$$Q_{\gamma\delta} = \frac{3}{2} (v_\delta i_\gamma - v_\gamma i_\delta) \quad (3.117)$$

$$= \frac{3}{2} v_\delta i_\gamma \quad (3.118)$$

where,  $v_\gamma$ , equals zero by definition of the synchronous reference frame.

In order to realize the control objective, the control constraint  $i_d = 0$  has to be expressed in the synchronous reference frame. The control constraint is found by imposing it on the reactive power in the rotor reference frame and noting that the reactive power in the different reference frames are equal. Hence, the reactive power in the rotor reference frame is:

$$Q_{dq} = \frac{3}{2} (v_q i_d - v_d i_q) \quad (3.119)$$

Equation 3.119 contains too many unknowns, since the rotor angular position is assumed unknown for the open-loop control. Therefore, it is expanded into known terms by setting derivative terms in the PMSM state-space model (equation 2.43) equal to zero and substituting the terminal voltage into equation 3.119, which yields:

$$Q_{dq} = \frac{3}{2} \left[ L_q \left( \frac{\omega_r}{\sigma} \left( \frac{\lambda_p}{L_d} + i_d \right) + \frac{1}{\sigma \tau_s} i_q \right) i_d - L_d \left( \frac{1}{\tau_s} i_d - \omega_r \sigma i_q \right) i_q \right] \quad (3.120)$$

$$= \frac{3}{2} \omega_r [L_d (i_d^2 + \sigma i_q^2) + \lambda_p i_d] \quad (3.121)$$

For high-speed surface mount PMSMs, the saliency is assumed unity. Noting that  $i_s^2 = i_d^2 + i_q^2$ , so that the reactive power may be further simplified into:

$$Q_{dq} \approx \frac{3}{2} \omega_r (L_d i_s^2 + \lambda_p i_d) \quad (3.122)$$

The ideal reactive power is obtained by constraining equation 3.122 so that:

$$Q_{dq}^* = \frac{3}{2} \omega_r L_d i_s^2 \quad (3.123)$$

Note that the ideal reactive power can also be calculated in the synchronous reference frame, since  $i_s^2 = i_\delta^2 + i_\gamma^2$ , thereby allowing a special case of the reactive power to be controlled with known  $\gamma\delta$  variables.

The difference between the ideal reactive power and the actual reactive power in the synchronous reference frame yields the error reactive power as:

$$Q_e = Q_{dq}^* - Q_{\gamma\delta} \quad (3.124)$$

$$= \frac{3}{2} (\omega_r L_d i_s^2 - v_\delta i_\gamma) \quad (3.125)$$

$$= \frac{3}{2} \omega_r \lambda_p i_d \quad (3.126)$$

where equation 3.126 may be interpreted to be the residual error due to an error in  $v_\delta$  required to cancel with  $\omega_r L_d i_s^2$  in equation 3.125. Therefore, the reactive power error may be used to adjust the  $\delta$ -axis voltage to drive the reactive power to zero, thereby obtaining optimal efficiency.

The high efficiency control loop is shown in figure 3.59, where the sum of the correction voltage,  $\Delta v_\delta^*$ , and the open-loop V/f voltage,  $v_\delta^{FW*}$ , yields the total reference voltage. The reference voltage is processed by a PI controller. It was found that the transients in the PI controller's output caused a speed disturbance, which is corrected by the addition of the low pass filter.

The gains of the PI controller and low pass filter cut-off frequency were chosen by a trial-and-error method during simulation. The chosen parameters are:  $K_p = 0.05$ ,  $K_I = 0.05$ ,  $\omega_c = 2\pi$ .

The high efficiency loop conflicts with the boost voltage (see section 3.3.3.4) required to stabilize the system at low speeds, hence the high efficiency loop is activated after the boost voltage is switched off.

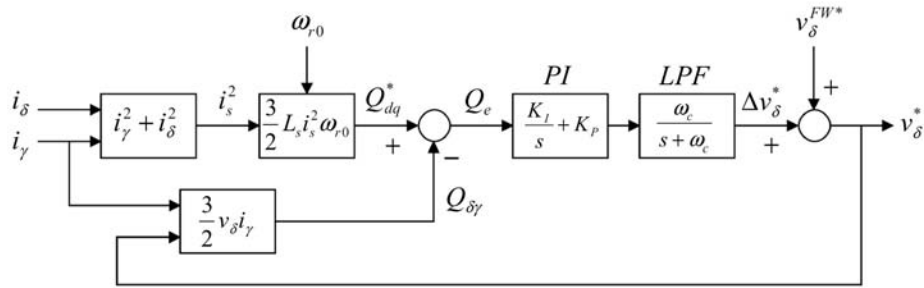


Figure 3.59: Zero reactive power control loop.

### 3.3.5 Current measurement decoupling

The anti-aliasing filters and measurement delay cause a coupling in the synchronous reference frame current similar to the coupling in the rotor reference frame as discussed in section 3.2.1.1.

The coupling causes the power perturbation measurement to be decreased, hence a decrease in the stabilization loop gain. An error also results in the calculated reactive power, thereby causing the high-efficiency loop to function sub-optimally.

A decoupling correction term for the synchronous reference frame current is obtained by noting the similarity between the  $\gamma\delta$  and  $dq$  coordinates. The inverter angle,  $\theta_e$ , is measured with respect to the (lagging)  $\gamma$ -axis (see figure 3.48), similar to the rotor reference frame convention in which the rotor angle,  $\theta_r$ , is measured with respect to the (lagging)  $d$ -axis. Hence, the current cross-coupling term for the synchronous reference frame is given by:

$$\mathbf{i}_{\gamma\delta}^X = \omega_r \begin{bmatrix} 0 & \frac{1}{\omega_C} \\ -\left(\frac{1}{\omega_C} + \frac{T_s}{2}\right) & 0 \end{bmatrix} \mathbf{i}_{\gamma\delta} \quad (3.127)$$



The measured current is then corrected by subtracting the cross-coupling term:

$$\mathbf{i}_{\gamma\delta}^D = \mathbf{i}_{\gamma\delta} - \mathbf{i}_{\gamma\delta}^X \quad (3.128)$$

where  $\mathbf{i}_{\gamma\delta}^D$  is the decoupled current.

### 3.3.6 V/f control simulation

#### 3.3.6.1 Simulation model

The top level of the V/f control simulation model is shown in figure 3.60. The speed reference is held zero by the zero weight input of the *Pre-Align* step block, at  $t = 0$  s. This allows the rotor to align with the stator magnetic axis before the reference speed starts to ramp. The alignment phase helps to ensure successful startup. The *Speed reference generator* block, start to generate a speed ramp after the *Pre-Align* step block had its transition.

When the rotor turns it experiences Coulomb friction, but not at standstill, therefore the *Pre-Align* step block also serves as the condition that triggers the Coulomb friction input to the *PMSM model*. The *Load Torque* step input occurs at a user defined time of interest.

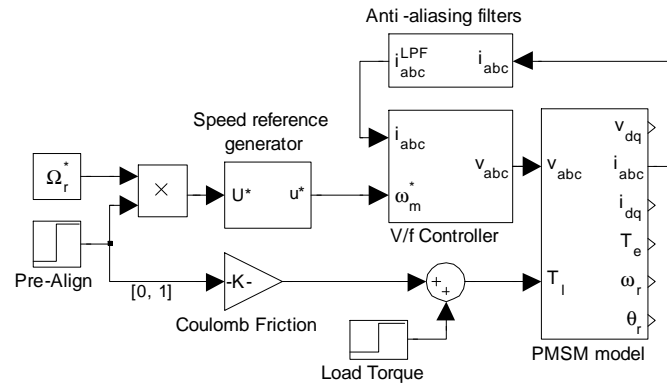


Figure 3.60: Top level of V/f control simulation model.

The *Speed reference generator* block is the same block used for the reference speed generation of the vector controller, except that the acceleration and deceleration constants limit the rate of change more than for the vector controller. Another difference is the inclusion of a low pass filter to the output of the V/f controller's speed reference generator. The purpose of the low pass filter is to ensure a smooth transition from a constant to an accelerating speed reference, which helps to ensure synchronism between the stator and rotor magnetic fields. The V/f controller's speed reference generator, with modifications, is shown in figure 3.61.

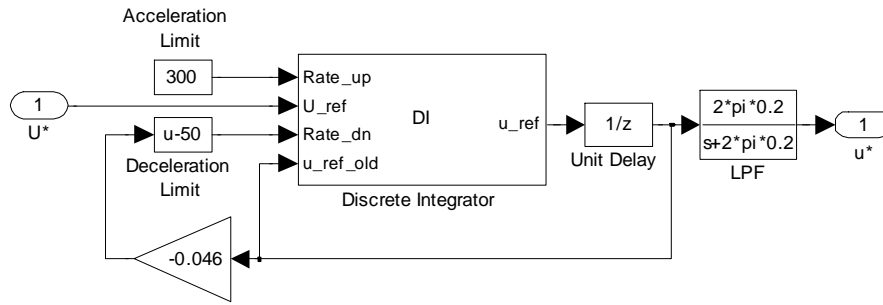


Figure 3.61: Speed reference generator for V/f control.

Figure 3.62, shows the integration of subsystems comprising the V/f controller. The mechanical speed reference input is first converted to an electrical speed reference. The sum of the nominal electrical speed reference,  $\omega_{r0}^*$ , and the stabilizing speed perturbation,  $\Delta\omega_e^*$ , yields the instantaneous synchronous speed reference,  $\omega_e^*$ . The integrated synchronous speed reference yields the inverter angle,  $\theta_e^*$ , which is used to project the synchronous voltage vector,  $v_\delta^*$ , to obtain the instantaneous three-phase voltage reference,  $v_{abc}$ , in the *dg2abc* & *THI* subsystem.

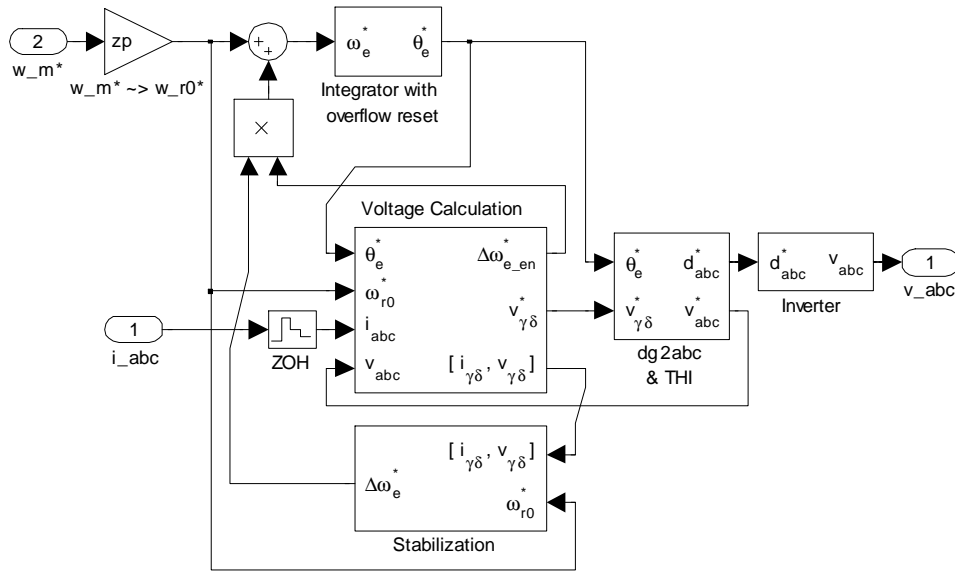


Figure 3.62: Lower level of V/f control simulation model.

The transformation from  $\gamma\delta$  coordinates to three-phase stationary coordinates, third harmonic injection and the inverter model used in the V/f control is essentially the same as that used in the vector control (see figures 3.16 and 3.17).

The integrator which calculates the inverter angle resets on each revolution to prevent an overflow in the controller. In order to utilize the advantage of the variable time step solver, a continuous integrator (which does not reset) is combined with a secondary reset function (e.g.  $\text{rem}(\theta_e^*, 2\pi)$ ) in simulation. For the actual controller a discrete integrator, which resets on each revolution, is

used. The integrator with such functionality has been developed previously with regard to the speed observer in section 3.2.2.2.

Implementation of the *Stabilization* subsystem is shown in figure 3.63. The instantaneous power is calculated from the synchronous reference frame current,  $i_{\gamma\delta}$ , and voltage,  $v_{\gamma\delta}$ . The power perturbation is obtained by high-pass filtering the instantaneous power. The synchronous frequency modulation term is obtained by normalizing the power perturbation with the rotational speed (thereby obtaining a torque perturbation) and amplification with the compensator gain.

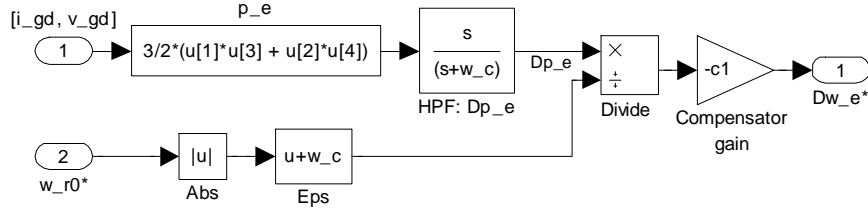


Figure 3.63: V/f control stabilization from power perturbation

Figure 3.64, shows the implementation of the *Voltage calculation* subsystem. The nominal rotor speed reference,  $\omega_{r0}^*$ , instantaneous inverter angle reference,  $\theta_e^*$ , and instantaneous three-phase current and voltage serve as the inputs. The three-phase current and voltage is transformed to the synchronous reference frame. The synchronous reference frame current is decoupled to compensate for measurement delays and combined with the voltage vector into a single vector output for use in the *Stabilization* subsystem. Since the angular position and three-phase voltage is not sampled by an ADC, it does not require delay compensation. The synchronous reference frame current and nominal speed is used in the calculation of the feed-forward reference voltage,  $v_{\delta}^{FW*}$ .

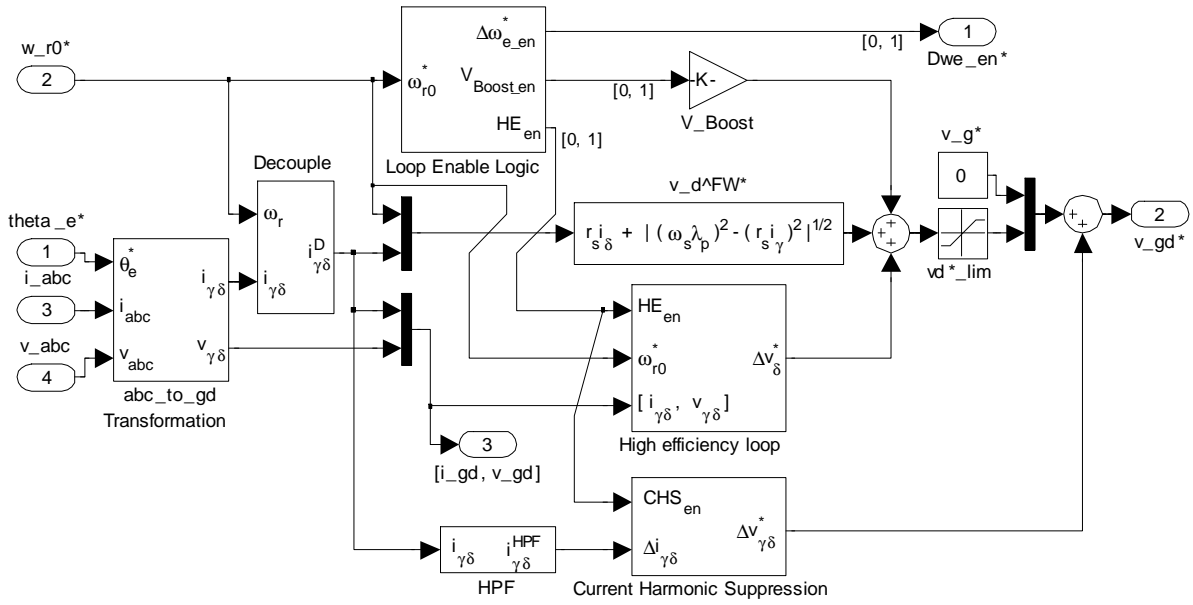


Figure 3.64: Calculation of resultant terminal voltage.

The synchronous reference frame current and voltage, as well as the nominal speed are used in the *High efficiency loop* subsystem, which is implemented as shown in figure 3.65. The loop has an enable input, which weighs the reactive power error before the integrator, in order to deactivate the high efficiency loop at low speed.

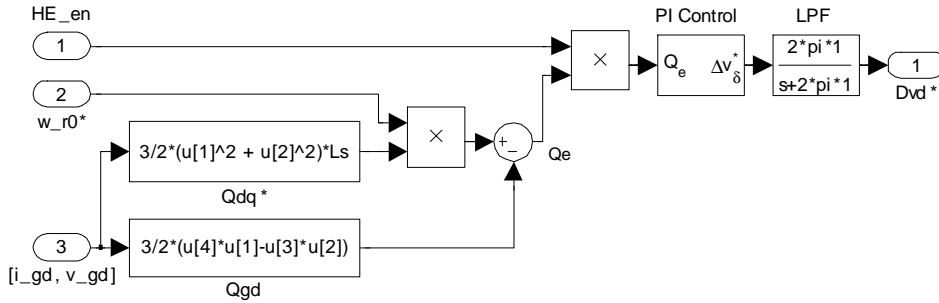


Figure 3.65: V/f control high efficiency loop implementation.

The current harmonic suppression loop is discussed in section 3.4.1.3, with regard to DC bus voltage disturbance rejection. The loop is not enabled in the simulation results of section 3.3.6.2.

The activation signals for the different loops: boost voltage, stabilization and high efficiency loop is calculated in the *Loop Enable Logic* subsystem in figure 3.64. The implementation of the activation signal calculation is shown in figure 3.66. The different loops are (de)activated in the vicinity of the frequency for which the stabilization loop would yield sufficient damping. Hence, the reference speed is normalized by this frequency,  $\omega_n = 2\pi 20 \text{ rad.s}^{-1}$ . The per unit speed is then compared to unity speed which yields an error per unit speed which indicates how close the reference speed is to the normalization frequency. For speeds below the normalization frequency

the boost voltage is activated, by inverting the speed error and limiting it with a saturation block. The saturation block limits each enable signal to the range  $[0, 1]$ . As the speed approaches the normalization speed, the boost voltage is gradually decreased, whilst simultaneously the enable signal for the stabilization loop increases. The speed at which the high efficiency loop is enabled, is delayed by the  $-1$  bias with respect to the stabilization loop enable which is advanced in time by the  $+0.5$  bias. The method of activation and sequencing of the enable signals are reminiscent of fuzzy logic. The exact values of the normalization frequency and activation biases were determined with a trial-and-error process.

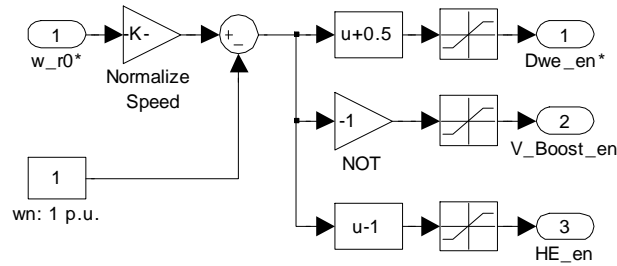


Figure 3.66: Calculation of enable signals of the different control loops.

The Simulink<sup>®</sup> simulation model for the V/f controller is included in Appendix C.14.

### 3.3.6.2 Simulation results

The effect of the different control loops on the V/f control is investigated in this section using the simulation model presented in the previous section. Each simulation considers the effect of a single control loop removed, whilst keeping the other loops in place.

The unstable operation of the V/f controller without stabilization loop is confirmed by simulation as shown in figure 3.67. At the lower operating speed the machine is still stable, but as predicted by the root locus it becomes unstable at approximately, 55 Hz. A load torque of 1 N.m is applied at  $t = 20$  s. The control without stabilization loop, but which were stable at low speed, loses synchronism. With the stabilization loop added, the speed could be ramped up to 20 krpm and remains stable despite the load torque step. It can be seen that the speed error response is over-damped (due to the lack of overshoot when the speed error returns to zero), as designed. The peak speed error due to the load torque step for the V/f control is  $\approx 150$  rpm vs. the peak error for the vector control which is  $\approx 50$  rpm (see figure 3.40)

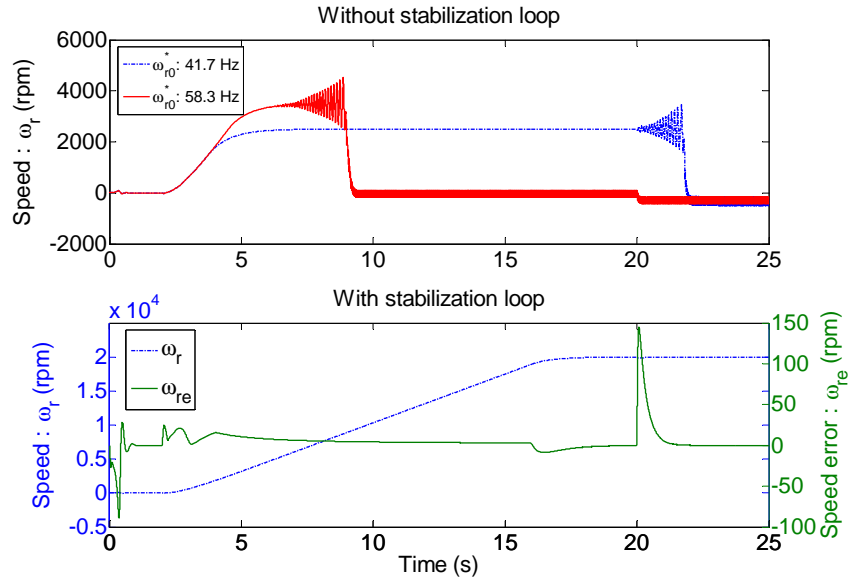


Figure 3.67: V/f control response with and without stabilization loop.

The effect of the boost voltage on the startup current is shown in figure 3.68. The current ripple during the period:  $0\text{ s} \leq t \leq 2\text{ s}$ , is due to the rotor lining up with the stator magnetic axis. Together with the alignment step, the boost voltage ensures that the d-axis current is positive, which is more stable at startup.

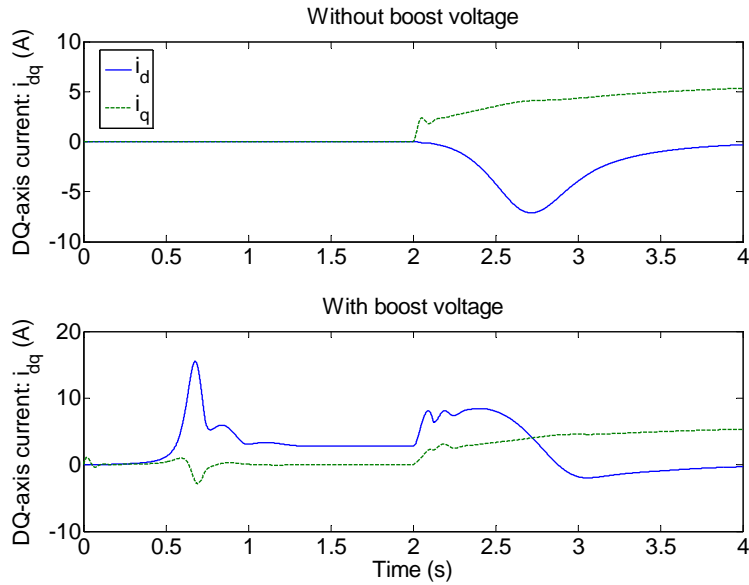


Figure 3.68: Startup response with and without boost voltage.

Suppression of reactive power by the high efficiency loop is demonstrated in figure 3.69, in which the motor is ramped up to 20 krpm and a load torque of 1 N.m is applied at  $t = 20\text{ s}$ . The deviation of the d-axis current with the high efficiency loop is noticeably improved, compared to

the response without the high efficiency loop. Therefore, with the high efficiency loop added, the same efficiency as the constant current angle vector control is obtained, but with slower dynamic response. An advantage of the V/f control over the vector control for high-speed operation is that it is free from low frequency speed harmonics due to quantization noise in the angular position.

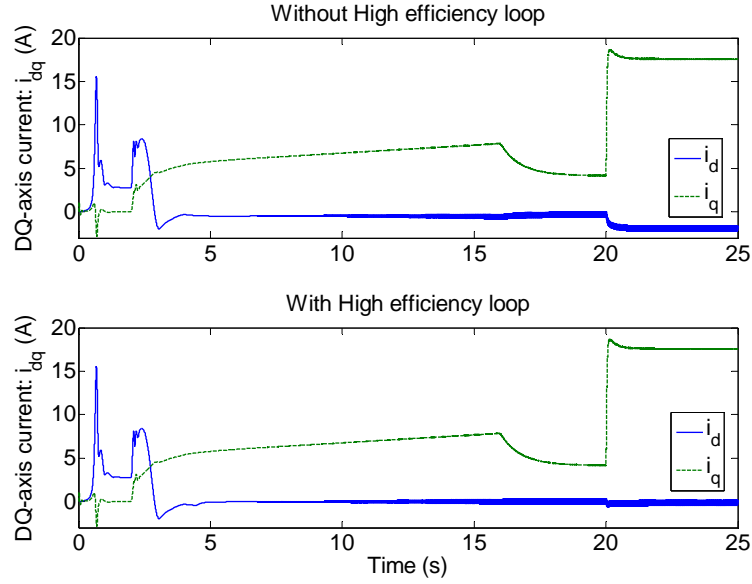


Figure 3.69: Torque load step response, at  $\omega_{r0} = 20$  krpm, with and without the high efficiency loop.

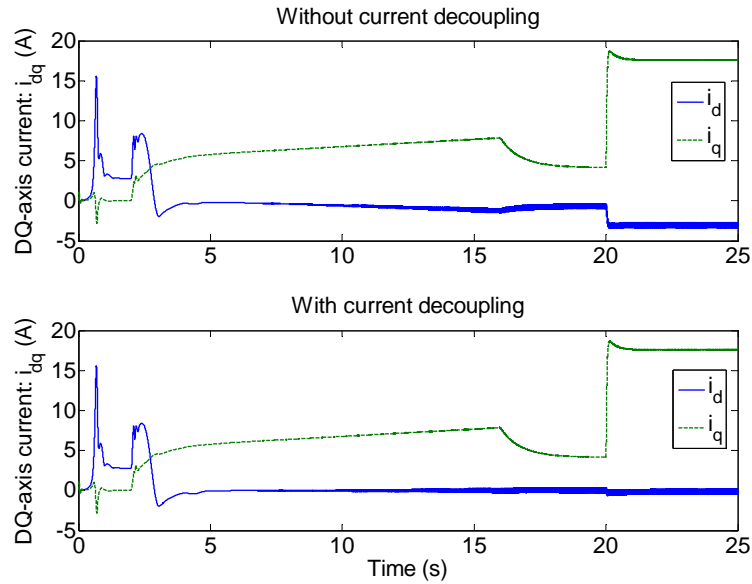


Figure 3.70: Response with and without current measurement decoupling.

The importance of the current measurement decoupling is illustrated in figure 3.70, with the

same torque load step conditions as the previous test setup. The high efficiency loop is active in both tests, but current decoupling is included only in the second test. The correct operation of the high efficiency loop relies to a great extent on the correct measurement of the current. In fact, the current deviation without the high efficiency loop is less than the erroneous operation of the high efficiency loop due to absent current decoupling.

Parameter mismatch between the controller and the PMSM connected to the drive has to be considered in order to evaluate the control fairly. Since the control is open-loop, it is more severely affected than a closed-loop controller such as vector control (non-sensorless versions). The current response to a run-up test with a load torque step of 1 N.m at 20 krpm, is depicted in figure 3.71, in which the stator flux linkage due to the rotor permanent magnet is mismatched in the control with respect to that of the PMSM model. It can be seen that an overestimated flux linkage is better tolerated in comparison to an underestimated flux linkage. The overestimated flux linkage, which would have caused an increase in reactive power, is compensated by the high efficiency loop, whilst the underestimated flux linkage degrades the stability and is not compensated by the high efficiency loop.

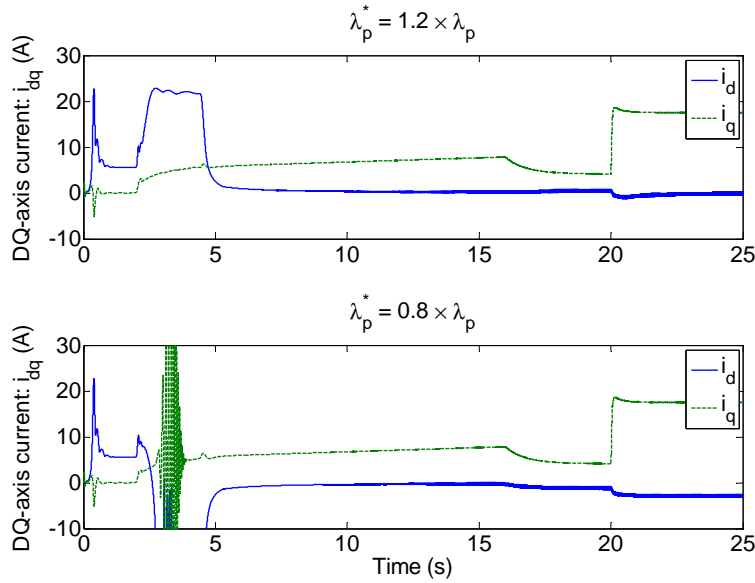


Figure 3.71: Current response with mismatch in controller's permanent magnet flux linkage.

The response due to mismatch in the stator inductance, with the same test setup as for the mismatched flux linkage, is shown in figure 3.72. As can be seen, an even larger mismatch can be tolerated compared to the response for mismatched permanent magnet flux linkage. Due to the mismatched stator inductance, the high efficiency loop no longer operates optimally: the *d*-axis current offset polarity corresponds to the mismatch being either over- or underestimated.



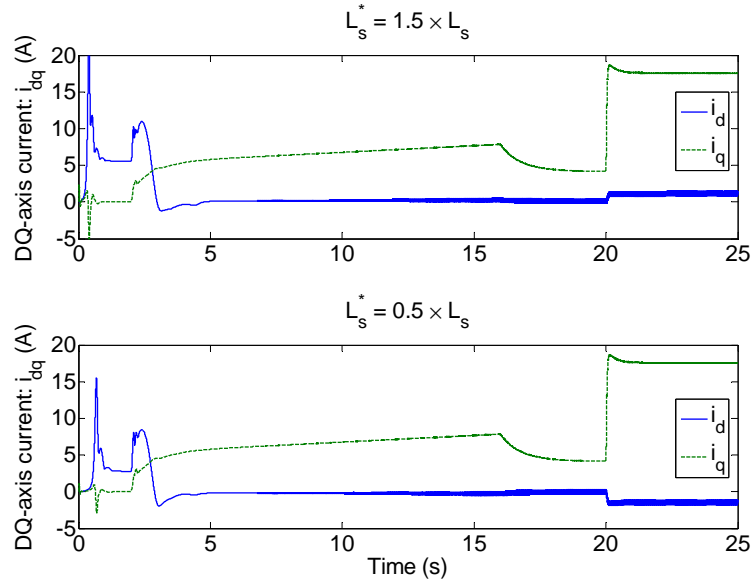


Figure 3.72: Current response with mismatch in controller's stator inductance.

The different types of PMSM parameter mismatch each have its own characteristic. Besides illustrating the importance of using accurate PMSM parameters in the controller, the simulation response for the different types of mismatch serve as a symptom guide for identifying culprit mismatched parameters in the control.

All of the previously presented V/f control simulation responses intentionally used an underestimated stator resistance ( $r_s^* = 0.14 \Omega$  vs  $r_s = 0.158 \Omega$ ) in the feed-forward calculation of the reference terminal voltage. It has been found that if the exact (or an overestimated) stator resistance is used, the current control becomes unstable. The importance of including the stator resistance voltage drop in the open-loop V/f control is stressed in [24, 45], but the importance of using an underestimated resistance has not been observed. The simulation response with mismatch between the controller's stator resistance and PMSM model is shown in figure 3.73, which confirms the previous discussion.

The cause of the instability becomes apparent by modelling the loop gain of the resistance feed-forward term. Figure 3.74, depicts the situation for normal feed-forward terms. The example considers only the winding impedance without the back-emf.

A current reference is used to obtain a voltage reference by the inverse of the plant impedance. The resulting current is simply equal to the reference current if the command parameters in the control are equal to the plant parameters. For the V/f controller an explicit current reference is not available. The voltage reference is instead generated by the use of equation 3.62. The actual current is used to compensate the resistive voltage drop, which is in fact positive feedback. Figure 3.75, depicts a simplified version of compensating the resistive voltage drop with a positive feedback. An initial voltage reference is generated by a current reference and the feed-forward inductive impedance. It needs to be stressed that in the actual control a current reference is not

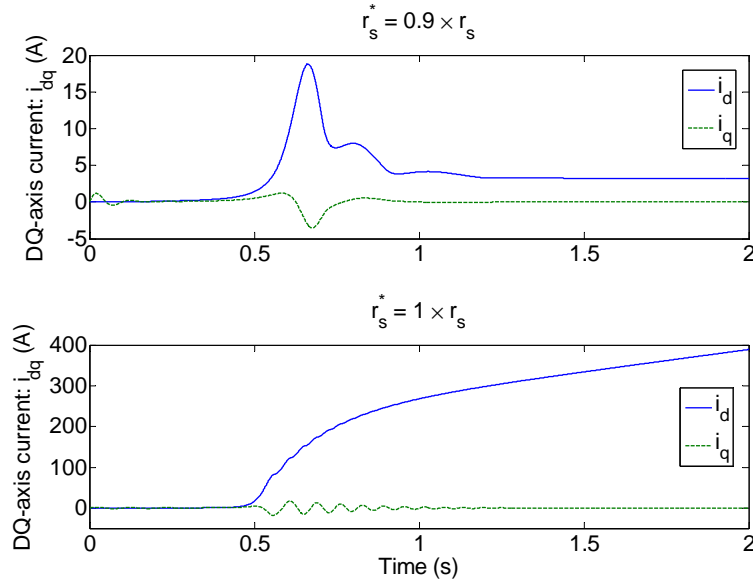


Figure 3.73: Current response with mismatch in controller's stator resistance.

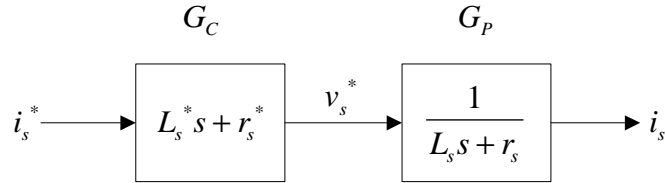


Figure 3.74: Open-loop feed-forward control of phase current.

available, but is used in this example only in order to generate an initial voltage reference.

For analysis, the positive feedback case can be simplified even more, by assuming the dynamics of the inductor sufficiently fast and all other delays negligibly small, which results in an algebraic loop as shown in figure 3.76. The output is in equilibrium<sup>6</sup> to the input for a certain range of the ratio of the command resistance to the plant resistance,  $\frac{r_s^*}{r_s}$ . The transfer function from the current reference to the output current is:

$$\frac{i_s}{i_s^*} = \frac{r_s^*}{r_s - r_s^*} \quad (3.129)$$

Hence, in order to obtain unity DC gain with the positive feedback system, the commanded resistance,  $r_s^*$ , used in the control should actually be:  $r_s^* = \frac{1}{2}r_s$ . Unlike a dynamical instability caused by a lack of phase-margin, this instability results in a non-oscillatory, exponential response when  $r_s^* \geq r_s$ , as observed from figure 3.73. The positive feedback method of compensating the voltage drop tends to amplify any disturbance measured in the current, such as measurement noise or an actual current disturbance due to dead-time or quantisation. Therefore, the current

<sup>6</sup>The condition for equilibrium can be determined by noting that this algebraic loop can be represented as a geometric series.

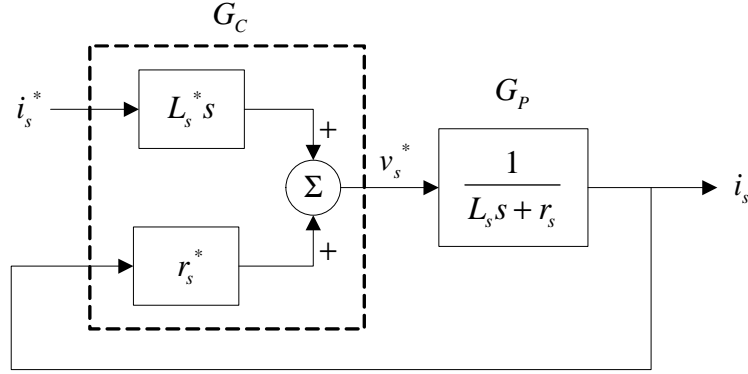


Figure 3.75: Feed-forward control of phase current with positive feedback compensation of resistive voltage drop.

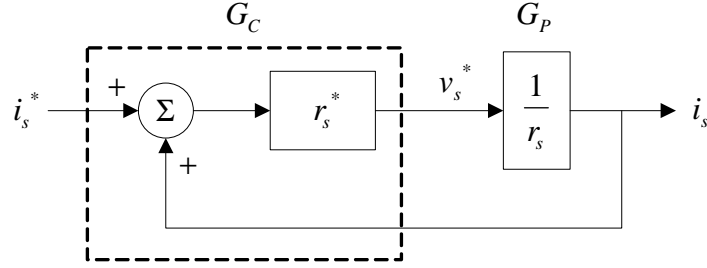


Figure 3.76: Current control with positive feedback.

should be low pass filtered before it is used in the feed-forward calculation of equation 3.76.

### 3.4 Inverter non-ideality compensation

The design of the vector and V/f controllers, assumed that the inverter is an ideal voltage source. As found in the literature study (see section 2.2.4.2), the inverter has non-idealities which has to be compensated in order for the designed control to perform as desired.

#### 3.4.1 DC bus disturbance rejection

##### 3.4.1.1 Introduction

The bus voltage,  $V_{dc}$ , is regulated by rectifying a utility voltage supply and filtering the rectified voltage with a capacitor. The resulting capacitor voltage contains a DC and a ripple component. The inverter gain varies, due to the ripple component of the bus voltage. Therefore, the PMSM current (torque) also contains a ripple component if the inverter gain is not compensated to reject the bus voltage disturbance. The frequency of the ripple voltage for a passively rectified supply voltage is equal to:

$$f_r = 2f_s \times \phi_{\#} \quad (3.130)$$

where  $f_s$ , is the supply frequency and  $\phi_{\#}$ , is the number of supply phases. For a 50 Hz, three-phase supply voltage (as used in this project), the resulting ripple frequency is equal to 300 Hz.

The mechanical time constant of the rotor is much larger than the period of the voltage ripple and would by itself prevent the high frequency torque disturbance from becoming a significant speed ripple. Although not significant with respect to the speed response, the disturbance causes mechanical vibration, audible noise and increased losses in the PMSM and drive.

### 3.4.1.2 DC bus rectifier and capacitor model

In order to inspect the influence of the ripple on the control response, a rectifier model is incorporated into the vector and V/f control simulation models. The rectifier and DC bus capacitor is modelled as in figure 3.77.

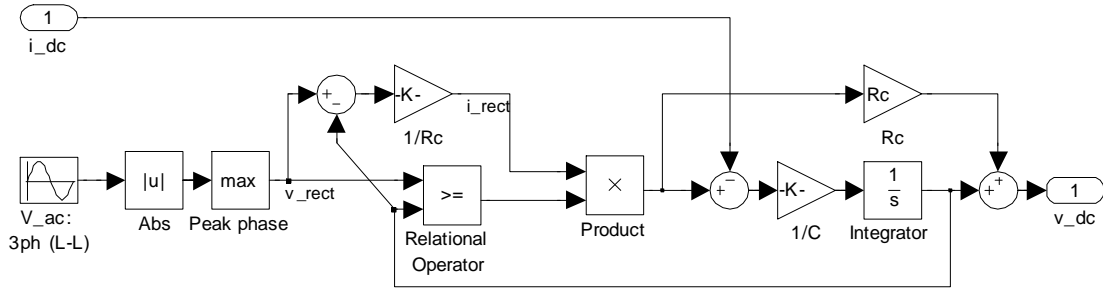


Figure 3.77: Rectifier and bus capacitor model.

The model has the AC voltage source as an internal input and DC link current,  $i_{dc}$ , as an external input, where the DC-link current is as defined in figure 2.4. The integrator output is the capacitor voltage, where the term that is integrated is the capacitor current. The rectifier supplies current to the capacitor and load, when the rectified input voltage exceeds the capacitor voltage (detected by the *Relational Operator* block). The input voltage is rectified by the absolute value function block. To accommodate a multiphase input, the *Peak phase* block detects which input phase has the largest voltage, since this is the voltage that the capacitor charges to. When the rectifier conducts, its output current is equal to the load current,  $i_{dc}$ , plus the voltage difference between the capacitor and the rectified source voltage divided by the capacitor's equivalent series resistance,  $R_c$ .

The model assumed zero filter inductance between the rectifier output and the DC bus capacitor. Thus, a worst-case DC bus voltage ripple results which is used to illustrate the importance of compensating for the DC bus voltage ripple in the motor control. The rectifier designed in section 4.2.4, includes a filter inductor.

The rectifier simulation model is verified by comparing it to the same circuit modelled with Simulink® *SymPowerSystems* components. The model comparison is included in appendix C.15a.

The DC-link current is dependent on the three-phase PMSM load current and is obtained by observing that each phase is equivalent to a buck converter so that the resulting DC-link current is [75]:

$$\begin{aligned} i_{dc} &= d_a i_a + d_b i_b + d_c i_c \\ &= \mathbf{d}_{abc} \cdot \mathbf{i}_{abc} \end{aligned} \quad (3.131)$$

where  $\mathbf{d}_{abc}$  and  $\mathbf{i}_{abc}$  are the three-phase duty cycle and current vectors, respectively.

### 3.4.1.3 Control simulation models with disturbance rejection

The V/f control simulation model is modified with the DC bus voltage model as shown in figure 3.78. The input to the rectifier is the actual three-phase current, whereas the three-phase current to the control is low pass filtered by an anti-aliasing filter. The three-phase voltage reference,  $\mathbf{v}_{abc}^*$ , is converted to a three-phase duty cycle reference,  $\mathbf{d}_{abc}^*$ , by the *v2d* block, which uses the measured DC bus voltage for the conversion as shown in figure 3.79. The *Average value inverter* block models the inverter which has the instantaneous DC bus voltage as input, which determines the gain of the inverter as shown in figure 3.80.

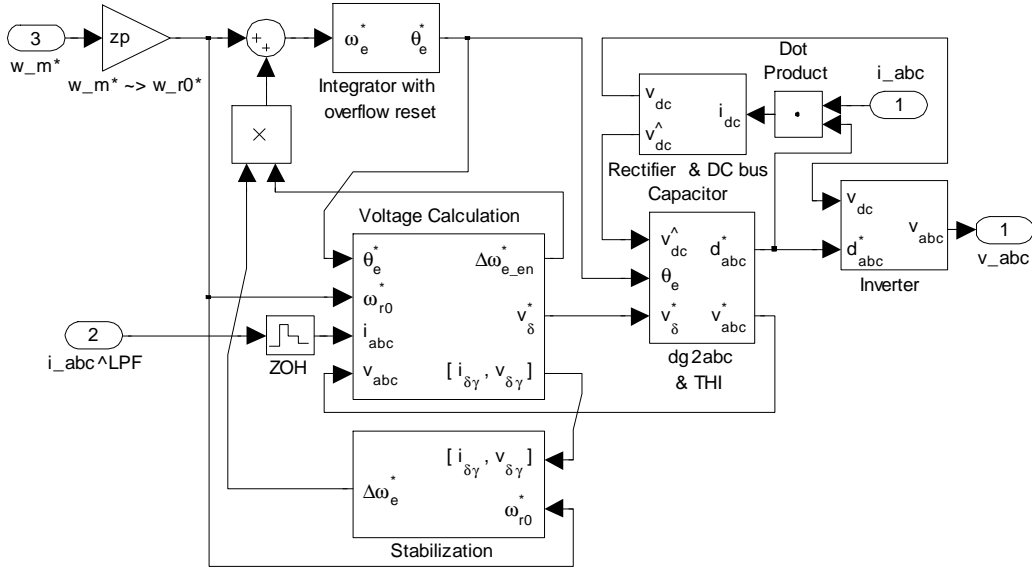


Figure 3.78: V/f control with DC bus disturbance rejection.

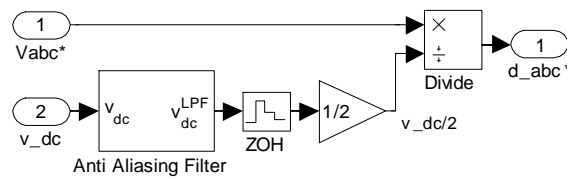


Figure 3.79: Voltage reference to duty cycle conversion.

The implementation of the *Voltage calculation* subsystem is shown in figure 3.64. In order to control the current fundamental the rotor position is required, either with a position sensor or a position observer. The current fundamental is load dependent and is not directly controlled in a V/f controlled PMSM. This does not negate the possibility of controlling the current harmonics, which yields higher DC bus voltage disturbance rejection. The current harmonic suppression control loop input is obtained by high-pass filtering the  $\gamma\delta$  current and utilizes a PI current controller as shown in figure 3.81. Suppressing the current harmonics at low speed actually suppresses self stabilizing current transients at low speed. Therefore, the control loop is activated after the speed is high enough with the same enable input used for the high efficiency loop. The current control gains are selected in the same order of magnitude as the current control gains calculated for the vector current control (approximately one-half of the gain). The cut-off frequency of the high-pass filter, which extracts the current harmonics, is chosen one decade below the rectified voltage frequency, in order to ensure no phase shift in the current harmonics due to the DC bus voltage ripple. The requirement of minimum phase shift has to be met in order for effective disturbance rejection of the DC bus voltage.

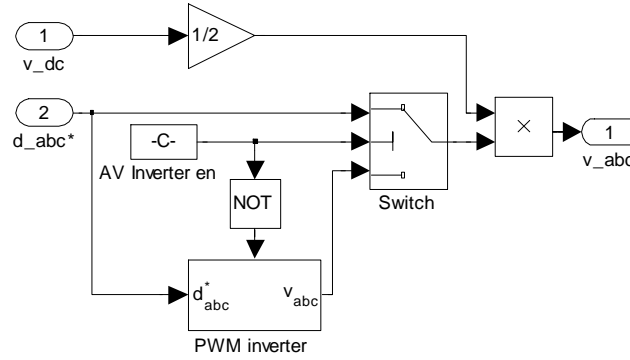


Figure 3.80: Average value inverter model.

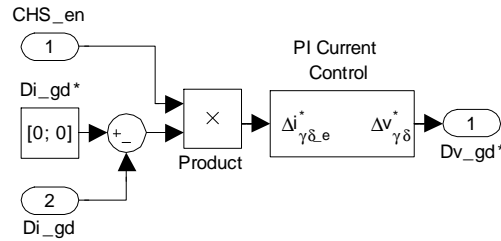


Figure 3.81: Current harmonic suppression.

The vector control simulation model, modified to include the DC bus voltage model is shown in figure 3.82. The *v2d* block inside the *dq2abc & THI* subsystem (figure 3.16), is replaced by that of figure 3.79.

The simulation models of vector and V/f control with the DC bus model and disturbance rejection are included in appendices C.15b and C.15c.

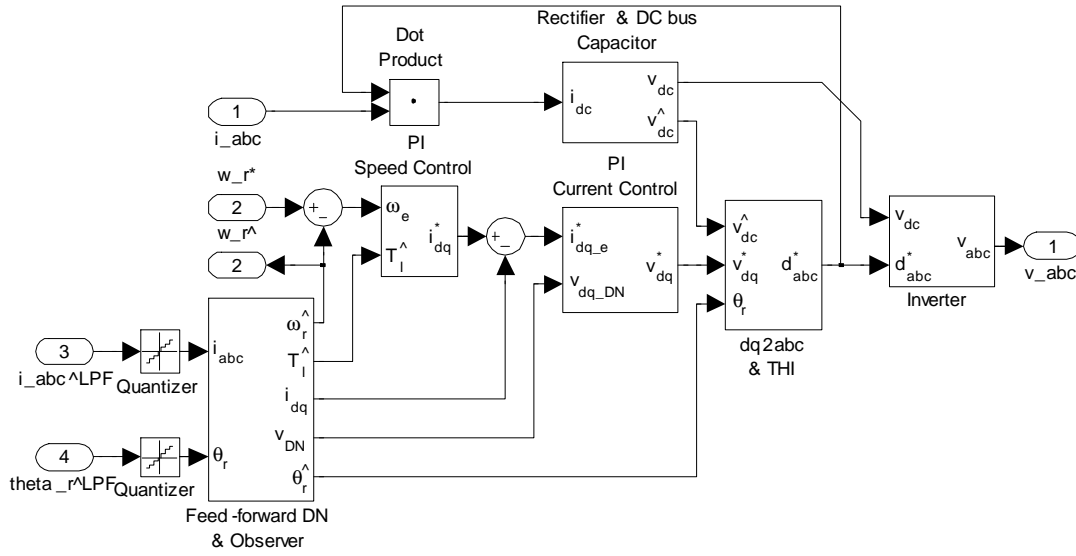


Figure 3.82: Vector control with DC bus disturbance rejection.

#### 3.4.1.4 Disturbance rejection simulation response

The response of the PMSM to vector control with DC bus disturbance rejection is shown in figure 3.83. The motor operating condition for the simulation is 1 N.m at 20 krpm. At  $t = 3.2$  s the DC bus disturbance rejection is enabled, prior to which the inverter inverse gain is calculated with a nominal DC bus value of  $v_{dc0} = 310$  V. The disturbance rejection is enabled by using the measured DC bus voltage. The reduction in peak-peak torque producing current ripple from  $0.5 A_{pp}$  to  $150 mA_{pp}$  can clearly be seen.

The response of the DC bus for this test setup is shown in figure 3.84. Note the change in the DC-link current waveform. Before the disturbance rejection is enabled, the current peaks during the recharge period of the capacitor. After enabling the disturbance rejection, the current has a sawtooth inversely proportional to DC bus voltage ripple, thereby keeping the power to the PMSM constant.

The PMSM current response to the V/f controller with DC bus disturbance rejection is shown in figure 3.85. The motor operating condition is the same as for the vector controller. At  $t = 11$  s the current harmonic suppression loop is enabled. The current harmonic suppression does not provide as much disturbance rejection compared to the vector current control, due to lower control gain. At  $t = 11.02$  s the inverter inverse gain is switched from a nominal to a measured value. With both disturbance rejection loops enabled, the disturbance rejection is comparable to that of the vector control with disturbance rejection. At  $t = 11.04$  s the current harmonic suppression is disabled and the inverter inverse gain is the only source of disturbance rejection. Hence, the total disturbance rejection with both loops active is better than the combined effect of each separate loop.

The large scale current response without disturbance rejection for V/f control is shown in figure

3.86. The test is for a speed ramp to 30 krpm with no load. The DC bus ripple causes amplitude modulation in the three-phase current. The amplitude modulated current is balanced and does not cause a torque disturbance. The peak amplitude of the modulated current is 15 A compared to a peak current of 13 A with disturbance rejection, which may exceed the maximum inverter current rating or may trigger protective current limiting, which interferes with the normal drive operation. Note the sharp peaking in the rotor reference frame current as the rotational frequency crosses the DC bus voltage ripple frequency. This would cause excessive rotor vibration at this frequency<sup>7</sup>.

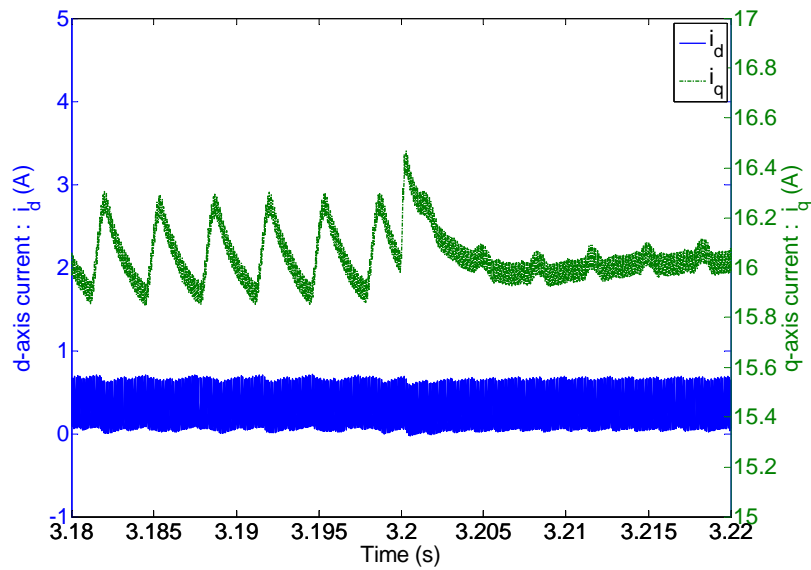


Figure 3.83: Vector control response without DC bus disturbance rejection.

<sup>7</sup>For the AMB FESS system in [17], which uses a single phase 50 Hz rectified supply, this peaking occurs at 6000 rpm.



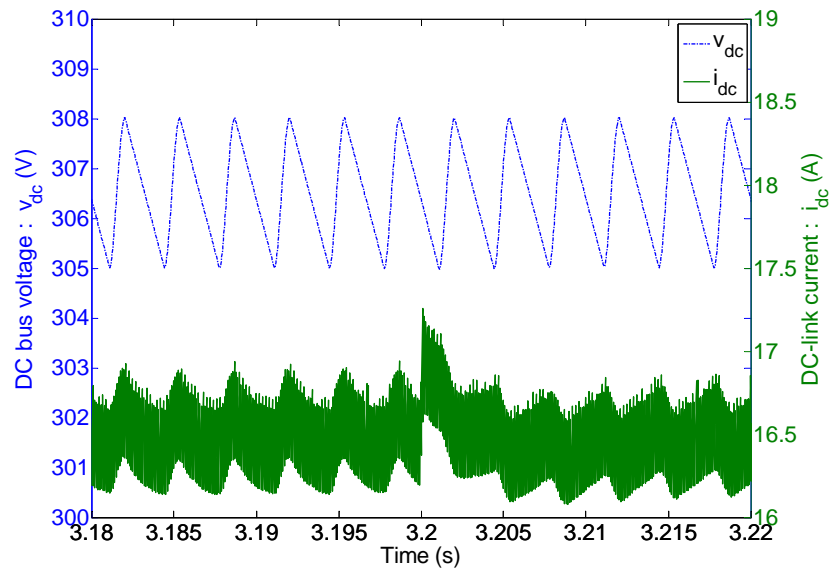


Figure 3.84: DC bus response to vector control without disturbance rejection.

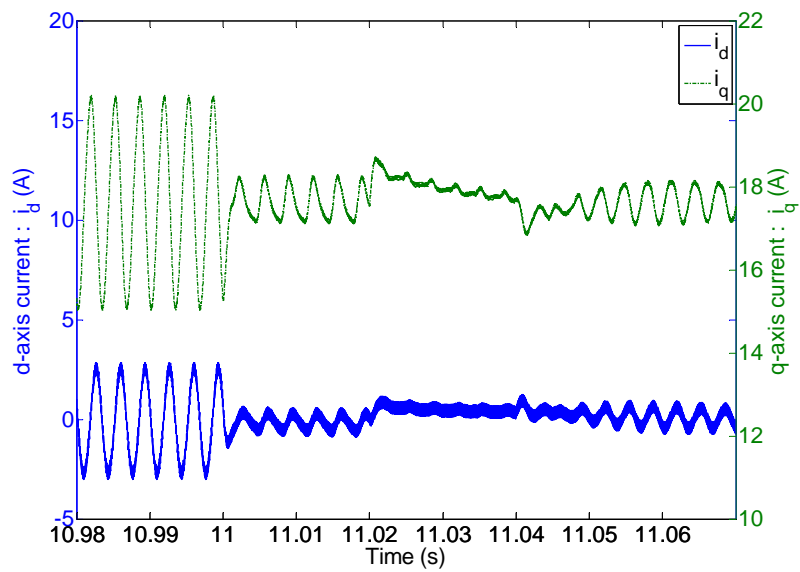


Figure 3.85: V/f control response without DC bus disturbance rejection.

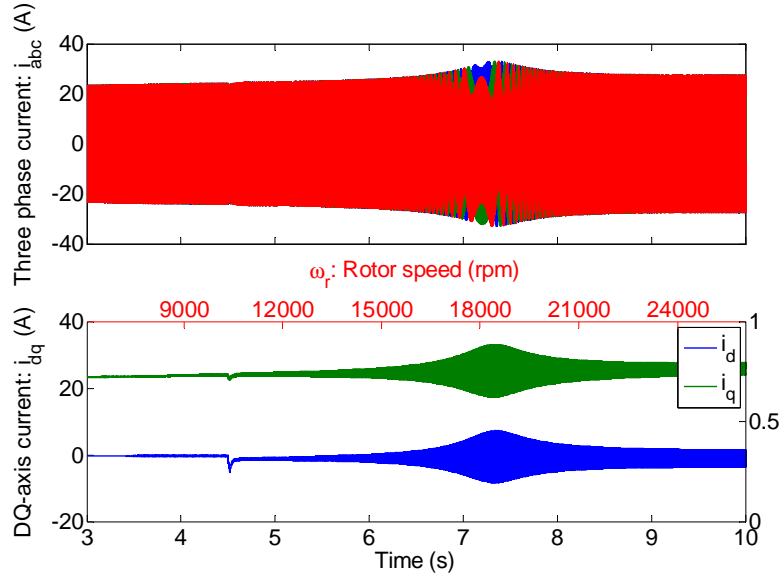


Figure 3.86: Large scale V/f control response without DC bus disturbance rejection.

### 3.4.2 Dead-time compensation

#### 3.4.2.1 Dead-time average value model

The effect of dead-time on the PMSM response may be modelled by adding the dead-time to each PWM pulse. This would require a simulation time step at least an order of magnitude smaller than that which is used for the PMSM with a switching inverter, i.e.  $h_{max} = 5 \times 10^{-7}$  s. A simulation of the drive with the pulse model of dead-time is unwieldy for simulations longer than a few milliseconds.

Since the current *simulation* is free from measurement noise, the current zero-crossing is exactly known, hence the fast average model of dead-time may be used for longer simulations. The average value model of the dead-time is modelled as in figure 3.87.

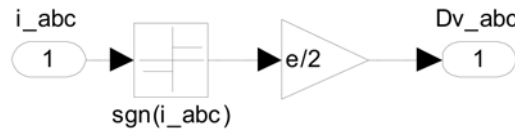


Figure 3.87: Dead-time average value model.

A comparison of an inverter switched with PWM signals including dead-time and the average dead-time model is included in appendix C.16a.

#### 3.4.2.2 Control models with dead-time compensation

Similar to the DC bus disturbance rejection, the exact currents are used in the calculation of the disturbance model, but low-pass filtered and sampled currents are used in the compensation

terms.

The average value model which accounts for dead-time is included in the inverter model as in figure 3.88. The offset voltage, which depends on the current polarity, is simply added to the reference duty cycle.

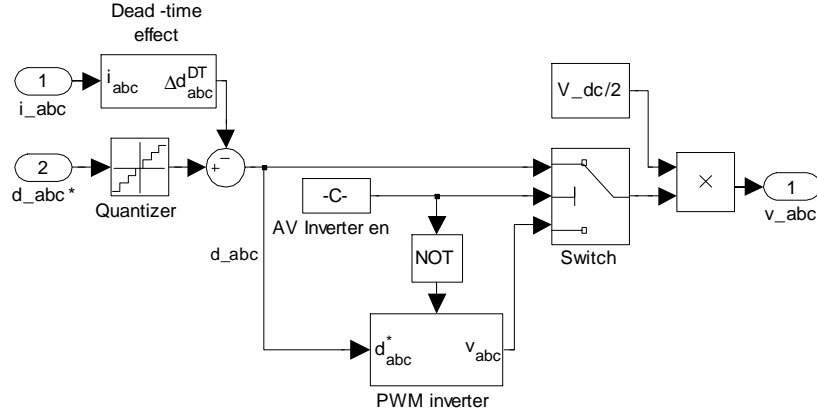


Figure 3.88: Dead-time average value model included with inverter.

The dead-time compensation for vector control is modelled as in figure 3.89. In case of V/f control, the input current is in the synchronous reference frame and the inverter reference angle is used instead of the rotor angle. The fundamental of the current, used for polarity detection, is extracted by low pass filtering and transforming back to the stationary reference frame. Instead of using the sign function as in the dead-time model, the current polarity is detected by amplification (*DTC Slope* block) and limiting (*Saturation* block), which result in a smoother transition. A hard transition in the compensation would not correspond exactly in time with the zero current clamping. Hence, a soft transition reduces the mean error between the exact time that the effect occurs and the time that it is compensated.

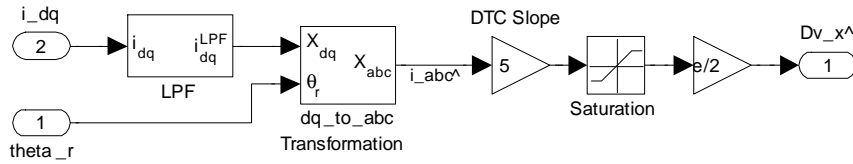


Figure 3.89: Dead-time compensation.

The dead-time compensation is added to the reference three-phase duty cycle before it enters the inverter model, as shown in figures 3.90 and 3.91, for vector and V/f control, respectively.

The simulation models for vector and V/f control with dead-time compensation is included in appendices C.16b and C.16c, respectively.



in figure 3.93. With DTC included the startup transient current is reduced to an acceptable range.

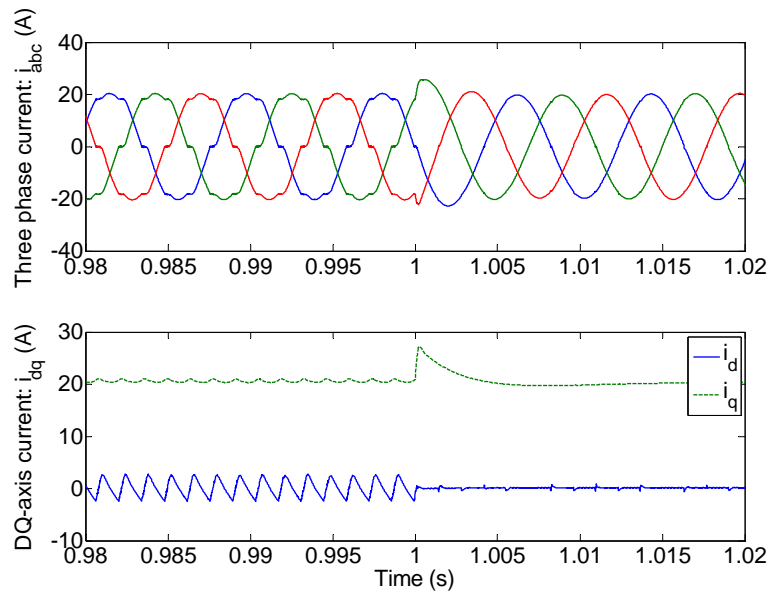


Figure 3.92: Vector control with dead-time compensation.

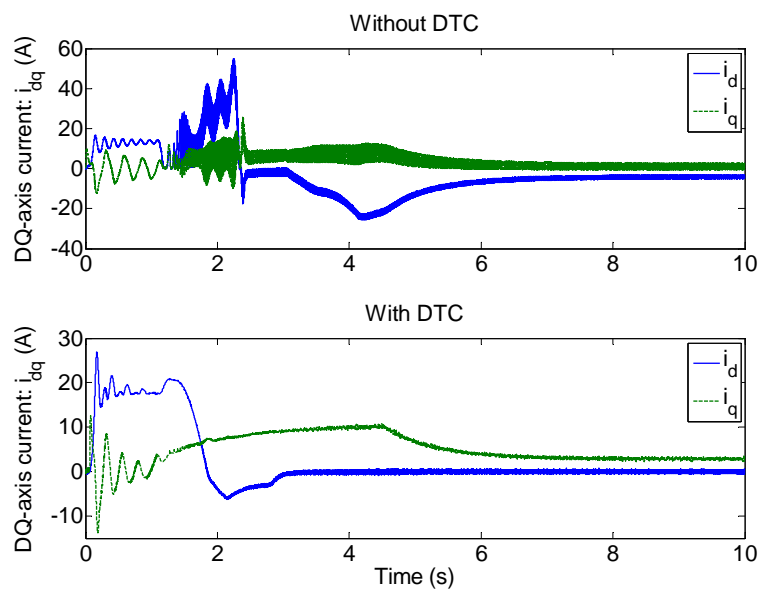


Figure 3.93: V/f control with dead-time compensation

### 3.4.3 Duty cycle quantization noise suppression

#### 3.4.3.1 Introduction

The duty cycle has two sources of quantization, namely the finite word length of the digital controller and the obtainable resolution of the PWM period which is restricted by its clock frequency. For medium to high switching frequencies, the quantization due to the PWM generator period resolution is greater than the finite word length representation of the duty cycle.

The quantization interval of the duty cycle due to the PWM generator is:

$$\Delta d = \frac{1}{f_c T_{PWM}} \quad (3.132)$$

where  $f_c$  is the PWM carrier frequency and  $T_{PWM}$  is the base period of the PWM generator.

The PWM generator used in this project is the dSPACE<sup>®</sup> DS5101, which has a time base of 25 ns. Thus, a switching frequency of 50 kHz has 800 duty cycle intervals, which is equivalent to representing the duty cycle with 9.64 bits. For a rated frequency of 30 krpm, an error in the least significant bit (LSB) of the duty cycle corresponds to 37.5 rpm. Also, a current ripple due to quantization in the duty cycle results, which is worse for machines with low input impedance, such as high-speed PMSMs.

The quantization noise can be suppressed, without a change in hardware, by oversampling the duty cycle in software with a delta-sigma modulator (DSM)<sup>8</sup>. Given a high resolution reference, the DSM switches an output signal between two quantization levels, so that the average output error is not as large as it would have been if the output signal had been represented by the non-switching quantized output.

The effect of quantization noise on the duty cycle, and the suppression thereof with a DSM, has been studied with regard to high switching frequency DC-DC converters and class-D amplifiers in [76, 77, 78].

#### 3.4.3.2 Control models with quantization noise suppression

The quantization noise is modelled in the inverter, by quantizing the reference duty cycle, before the addition of the dead-time effect as shown in figure 3.88. The quantization noise suppression for vector and V/f control is shown in figures 3.90 and 3.91, respectively.

The implementation of the DSM modulator is shown in figure 3.94. Each phase of the input signal vector has a DSM (hence there are actually three DSMs implemented in figure 3.94). The input to the DSM is the difference between the high resolution input signal and the quantized output signal. The *Quantizer* block in the feed-forward path has the same quantization interval as the quantization that occurs in the digital PWM generator. The quantization error is amplified by

<sup>8</sup>Also known as a sigma-delta modulator in the literature.

a high gain and is integrated. When the output of the integrator causes the quantizer output to increase with one LSB, the sign of the quantization error changes, which causes the integrator output to change direction. Hence, the DSM oscillates around the desired high resolution input. The DSM spreads the input quantization noise to a higher frequency bandwidth in the output, which is better filtered by the low-pass characteristic of the plant.

The DSM has an inherent delay due to the integrator, although small due to the high gain. Therefore, the dead-time compensation has to be added *after* the DSM, so that it is not delayed by the DSM with respect to the current zero-crossing.

Control simulation models which include quantization noise suppression are included in appendices C.17a and C.17b.

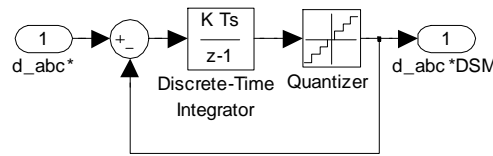


Figure 3.94: Delta-sigma modulator.

### 3.4.3.3 Quantization noise suppression simulation results

The response of vector control with and without the delta-sigma modulator is shown in figure 3.95. The current control loop cause suppression of the duty cycle quantization, as it can be seen that the response is practically identical with and without the DSM. The current control loop dithers the duty cycle in response to the current ripple caused by the quantization, therefore in effect, the current control loop acts as a DSM itself with regard to the duty cycle quantization noise.

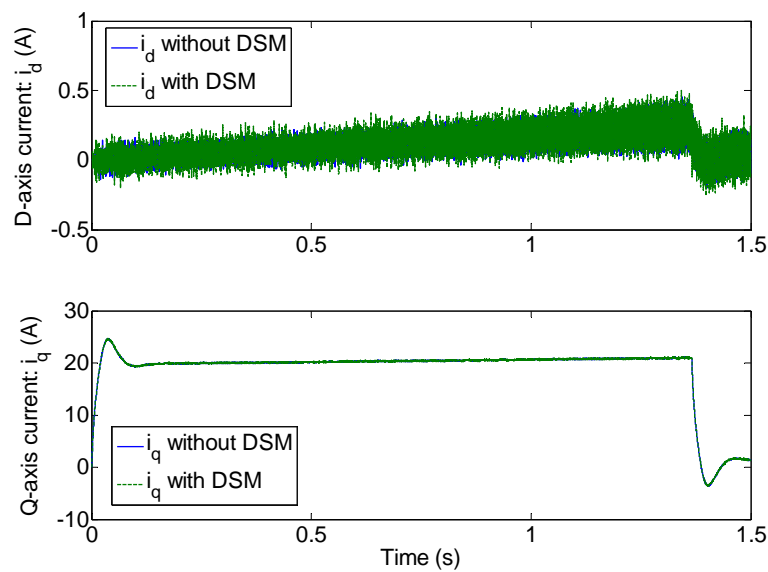


Figure 3.95: Current response to vector control with quantization noise suppression.

Figure 3.96 depicts the current response for V/f control with and without the DSM. The DSM causes a marked improvement in the current ripple, which would have caused problems at startup.

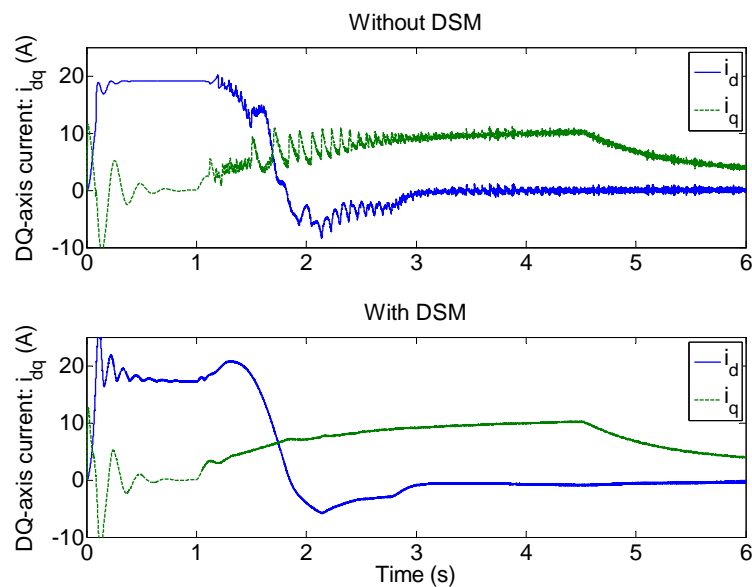


Figure 3.96: V/f control response with quantization noise suppression.

### 3.5 Summary

The design performed in this chapter can be summarized as follows:



- Identification of the PMSM parameters was performed. The identified parameters were used throughout the design process.
- The vector control's current and speed loops were designed. Special decoupling terms which are important for the high-speed PMSM were derived.
- The V/f controller with stabilization was designed. A high efficiency loop has been added which improves the V/f control efficiency to the same level as the vector controller in steady-state. The V/f control was expressed in a vector formulation, which made it possible to use the same decoupling terms (which become important at high speed) as used for the vector controller. This formulation also made it possible to recognize the possibility of controlling the high frequency currents via the current harmonic suppression loop.
- Both the vector and V/f controls were verified thoroughly, via simulation of the drive system.
- The effects of a non-ideal voltage source inverter were investigated. Compensation for these effects in order for successful operation or at least improved performance (depending on the severity of the effect) was also investigated via simulation.



## Chapter 4

# Implementation issues

This chapter presents practical implementation issues of the different controllers which also had to be addressed in order for the successful operation of the different control strategies. It starts off with a layout of the drive configuration which explains how the different subsystems have been integrated. This is followed by the inverter design, which consists out of the rating selection of the IGBTs and a thermal verification of the inverter. The input rectifier and filter is designed as part of the drive component specification.

The inverter design is followed by isolation and protection of the different subsystems, in order to protect the controller from faults in the power electronics.

A section dedicated to the different types of sensors required for the control and monitoring of the PMSM is presented.

The cause of electromagnetic interference in the drive and the measures taken to reduce the interference are presented.

The chapter concludes with computational improvements of the control algorithm, required for the controller to be executed in real-time at the chosen control frequency.

### 4.1 Drive layout

The drive subsystem integration is shown in figure 4.1. Note that the connections from the controller to only one inverter and PMSM are shown. The second PMSM is mechanically coupled to the first and its drive connects to the same controller and rectifier as the first.

The controller used is the dSPACE<sup>®</sup> DS1005, which uses a PowerPC processor. It interfaces to the outside world with various IO expansion cards which slot into a high speed bus for data exchange with the control processor. It samples the ADC inputs, processes the control algorithm and updates the PWM outputs for each control period.

The controller does not interface directly with the sensors and power amplifiers, in order to protect it from electrical faults on the connected hardware. Instead, the sensor inputs and control

outputs are passed through the *Interface Board*<sup>1</sup> (IB). The IO which does connect directly to the controller is already electrically isolated. The IB also contains the anti-aliasing filters for signal conditioning.

The PWM signals, generated on the DS5101 board, are passed through the IB in order to protect the IGBTs from invalid inputs during the control program compilation period. The PWM signals and an enable signal (from the DS4002 board) are passed through combinational logic circuitry, which prevents invalid inputs to the *IGBT Driver Board*.

The IGBT driver board (SKHI61 from Semikron<sup>®</sup>) control inputs are electrically isolated, with optocouplers, from its gate outputs. The driver board also contain over current detection (OC) and soft-shutdown functionality. In case an over current condition is detected by the driver board, the driver outputs are pulled low over a longer time period than a normal shutdown, in order to prevent an over voltage condition due to high  $\frac{di}{dt}$ . The controller is also notified by the driver board that the drive has been shutdown. A soft-shutdown can also be commanded by the controller via the DS4002 board.

The DC bus capacitors are connected to the inverter via the *IV Sensor Board* in order to measure the DC bus voltage and DC-link current. The three-phase output of the inverter is connected to the PMSM also via the sensor board. As mentioned previously the sensor board outputs connect to the controller via the *Interface Board*.

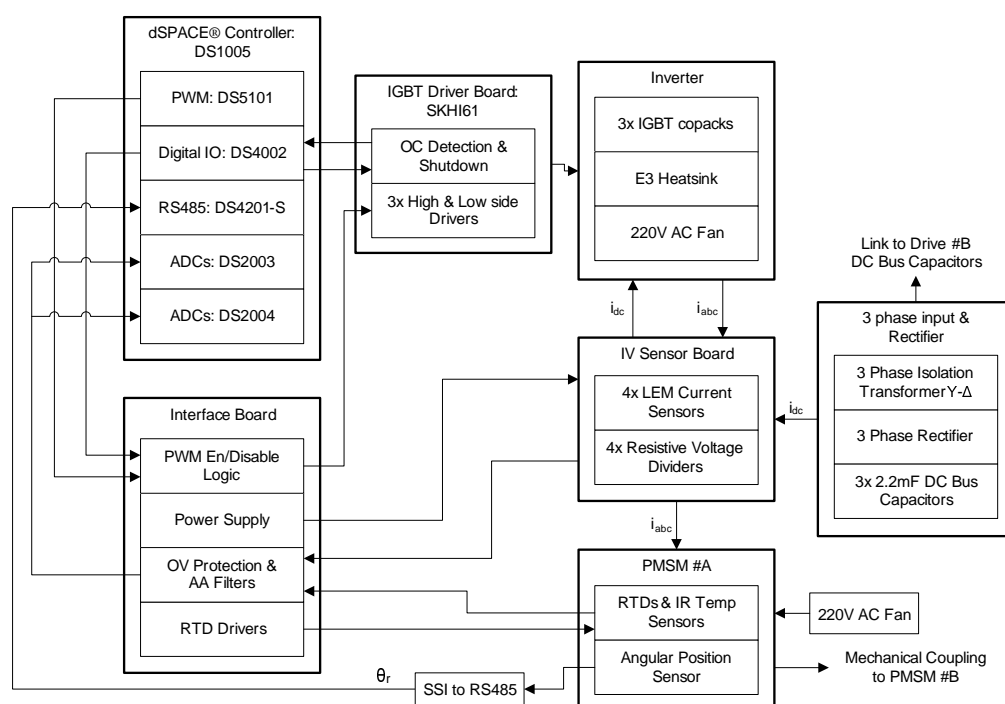


Figure 4.1: Functional relationship block diagram.

<sup>1</sup>Capitalized italics are used for referencing and drawing attention to the subsystem blocks of the discussed figure.

## 4.2 Specification of drive components

### 4.2.1 IGBT Voltage rating

The required voltage rating is determined by the DC bus voltage and the PMSM back-emf constant. At rated speed the back-emf in a phase is  $2\pi\omega_r\lambda_p \approx 156$  V. The DC bus voltage has to be approximately double the back-emf voltage<sup>2</sup>, due to the limited phase voltage which can be imposed by the inverter, hence 312 V. The IGBT parallel diodes ensure that the maximum voltage across an IGBT is clamped to the bus voltage. This value has to be compensated further, e.g. 50 V, to account for voltage spikes during a switch transition due to leakage inductance in the DC-link. IGBT voltage ratings are available in a discrete incremental range, so that the IGBT voltage rating is chosen as 600 V.

### 4.2.2 IGBT Current rating

The required current rating is determined by a combination of the PMSM rated current and IGBT losses. An IGBT with a slightly higher current rating than required has less switching and conduction losses compared to one which barely meets the current specification. The conduction and switching losses decrease as the current density in the devices decreases, but only to a point because the gate input capacitance also increases which in turn increases the switching losses.

The current rating can be determined from the rated peak electromagnetic torque, which is equal to:

$$\begin{aligned} T_e &= \frac{P_r}{\omega_r} \\ &= \frac{4 \times 10^3}{2\pi 500} \\ &= 1.27 \text{ N} \cdot \text{m} \end{aligned} \tag{4.1}$$

where,  $P_r$ , is the rated power at rated speed,  $\omega_r$ . The peak torque producing current is obtained by dividing the peak torque by the torque constant,  $K_t$ , which yields 17.72 A. For the power variant dq0 transformation this corresponds to the peak phase current. Again this value should be modified by a safety factor, e.g.  $\times 2$  the peak current, to account for higher peak currents during startup transients<sup>3</sup>.

Another method of determining the required current rating is by noting the current rating of the winding which has been designed for a current density of  $5 \text{ A} \cdot \text{mm}^{-2}$ , which yields a current rating of  $18.5 \text{ A}_{\text{rms}}$ . Therefore, the PMSM has a higher torque rating than that which is achieved at maximum speed. The peak torque rating according to the winding current rating is thus  $1.875 \text{ N} \cdot \text{m}$  and rated power is already achieved at a rotational speed of 340 Hz. Beyond this

<sup>2</sup>If sine-triangle modulation is conservatively assumed.

<sup>3</sup>For the vector controller, the startup current is limited to a maximum allowed value by the current control, which is not possible for the V/f controller.

speed the torque is derated (thereby keeping the power constant), in order to limit the PMSM losses. Hence, the peak inverter current is 26.2 A, which corresponds roughly to the inverter current requirement of 30 A stated in section 1.3.

The IGBT selected for the project is the SKM50GB063 IGBT module from Semikron<sup>®</sup>, which has a rating of 600 V, 50 A. Each module is an IGBT half-bridge configuration with an anti-parallel diode per IGBT. Thus, three modules combine to form the three-phase inverter configuration. The devices in the module are electrically isolated with  $\text{Al}_2\text{O}_3$  from a copper base plate, providing excellent thermal performance.

### 4.2.3 Inverter thermal verification

In order to confirm that the chosen IGBT can operate in the inverter configuration with the specified operating conditions a thermal analysis is performed in order to verify that the IGBT junction temperature does not exceed its maximum allowed value.

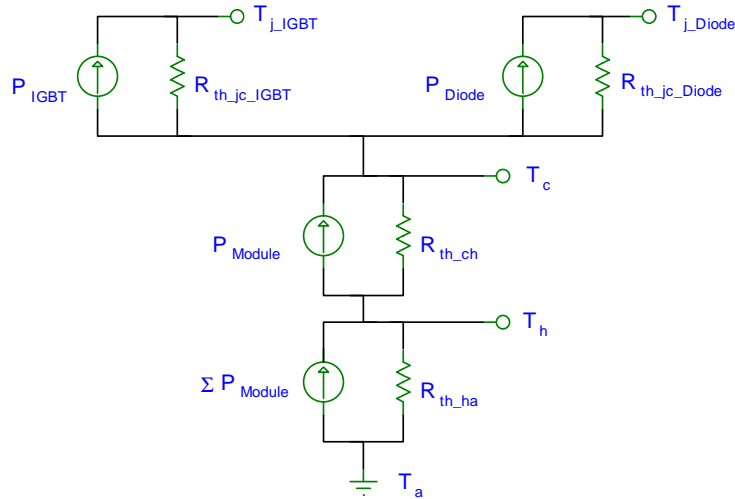


Figure 4.2: Inverter thermal model.

Figure 4.2, depicts the lumped parameter thermal model of the IGBT module. The parameters of the model are defined as follows:

$P_{IGBT}$  Power loss of an IGBT in a module.

$P_{Diode}$  Power loss per diode in a module.

$P_{Module}$  The total power loss generated per module.

$\Sigma P_{Module}$  The total power loss generated by all the modules per heatsink.

$R_{th\_jc\_X}$  Junction to case thermal resistance of a device, where  $X$  is either an IGBT or an inverse diode. The base-plate is included in this resistance.

$R_{th\_ch}$  Case to heatsink thermal resistance.

$R_{th\_ha}$  Heatsink to ambient thermal resistance.

$T_a, T_h, T_c$  Temperature of the ambient, heatsink and case, respectively.

$T_{j\_IGBT}, T_{j\_Diode}$  Junction temperature of the IGBT and diode, respectively.

Since the model does not include thermal capacitance, steady state conditions are assumed. High frequency losses would have been absorbed (averaged) by the thermal capacitance, therefore the resistive model is a conservative (yet simple) verification of the inverter thermal response.

The power losses of a device, required in the thermal model, are the sum of the conduction and switching losses. Since the PMSM current is sinusoidal, the conduction loss is calculated by averaging the power over a period of the fundamental component. The nonlinear V-I characteristic of the device is linearized by substituting the voltage across a device as a linear function of the device current. The averaging and linearization allow the following simplification of the device conduction loss:

$$\begin{aligned} P &= \frac{1}{T} \int_0^T v(i(t)) i(t) dt \\ &= \frac{1}{T} \int_0^T (v_0 + ri(t)) i(t) dt \\ &= v_0 \bar{i} + r i_{rms}^2 \end{aligned} \quad (4.2)$$

where,  $v_0$ , is the voltage across the device with zero device current,  $\bar{i}$ , the average device current,  $i_{rms}$ , the rms device current and  $r$  is the linearized device resistance. The generality of equation 4.2, makes it useful for the conduction loss calculation of any converter configuration.

The calculation of the average and rms current for the IGBT and anti-parallel diode in an inverter using sine-triangle modulation is performed by Perruchoud *et al.* in [79], which after substitution yields the conduction losses as:

$$P_I = v_{CE0} \hat{i}_{ph} \left( \frac{1}{2\pi} + \frac{m_i}{8} \cos(\phi) \right) + r_{CE} \hat{i}_{ph}^2 \left( \frac{1}{8} + \frac{m_i}{3\pi} \cos(\phi) \right) \quad (4.3)$$

$$P_D = v_{F0} \hat{i}_{ph} \left( \frac{1}{2\pi} - \frac{m_i}{8} \cos(\phi) \right) + r_D \hat{i}_{ph}^2 \left( \frac{1}{8} - \frac{m_i}{3\pi} \cos(\phi) \right) \quad (4.4)$$

where the voltage and resistances are the IGBT and diode linearized parameters,  $\hat{i}_{ph}$ , is the peak phase current,  $m_i$ , the modulation index and  $\phi$  is the load power factor angle. Bierhoff and Fuchs derived the conduction losses for the inverter with third harmonic injection and found that it is nearly equal to the sine-triangle modulation case [80].

The switching losses can be approximated analytically from the device voltage and current switching waveforms averaged over a switching period as in equation 4.5 [81].

$$P_{sl\_fc} = \frac{1}{2} V_{dc} \hat{i}_{ph} f_c (t_{c(on)} + t_{c(off)}) \quad (4.5)$$

where  $t_{c(on)}$  and  $t_{c(off)}$  is the time during which the device voltage and current passes through the linear region for the device turn on and turn off (the other parameters have been defined previously). Manufacturers have their own definition of the device turn-on and off times, which is often incompatible with the switching times used in equation 4.5. Also, as stated, equation 4.5 is only an approximation, because it does not account for the increase in device current due to diode reverse recovery when the IGBT turns on and it also neglects the losses due to the IGBT tail current and increased device voltage caused by parasitic inductance during device turn-off. In order to account for the switching losses being higher than the theoretical amount, manufacturers provide the switching loss energy determined with a standard test circuit as a function of the gate resistance and collector current.

Hence, the switching losses (for an IGBT and inverse diode pair) averaged over a switching period can alternatively be expressed as in equation 4.6 [80].

$$\begin{aligned} P_{sl\_fc} &= (E_{on,I} + E_{off,I} + E_{off,D}) f_c \\ &= E_{tot} f_c \end{aligned} \quad (4.6)$$

where  $E_{on,I}$  and  $E_{off,I}$  is the IGBT turn-on and turn-off switching energy and  $E_{off,D}$  is the diode turn-off energy. The diode turn-on switching energy may be neglected. Since the inverter current is sinusoidal the switching losses have to be averaged over the fundamental modulation period [79]:

$$P_{sl\_ws} = \frac{1}{2\pi} \int_0^\pi P_{sl\_Tc} d\theta \quad (4.8)$$

$$= \frac{1}{2\pi} \int_0^\pi f_c \hat{E}_{tot} \sin(\theta) d\theta \quad (4.9)$$

$$= \frac{f_c}{\pi} \hat{E}_{tot} \quad (4.10)$$

where the integral is carried out over half a period because this is the period for which an IGBT and opposite inverse diode conducts. Note that  $\hat{E}_{tot}$  is the peak switching energy during the modulation period.

With the losses known, the junction temperature for the IGBT and diode is calculated as:

$$T_{j\_IGBT} = T_a + \Sigma P_{mod} R_{th\_ha} + P_{mod} R_{th\_ch} + P_{IGBT} R_{th\_jc\_IGBT} \quad (4.11)$$

$$T_{j\_Diode} = T_a + \Sigma P_{mod} R_{th\_ha} + P_{mod} R_{th\_ch} + P_{Diode} R_{th\_jc\_Diode} \quad (4.12)$$

The calculation for the thermal verification is included in appendix C.18, which assumed an operating condition of 25 A PMSM load current, switching at 20 kHz with a conservative ambient temperature of 40 °C. The SKM50GB063D datasheet is included which shows the linearization of the IGBT and diode V-I characteristics as well as the linear approximation of the switching losses as a function of the gate resistance. The heatsink parameters are obtained from the Semikron® P3/180 heatsink datasheet, which is derated (to account for the difference in heatsink length



Table 4.1: Summary of thermal verification.

Symbol	Description	$\hat{I}_{max} = 25 \text{ A}$	$\hat{I}_{rated} = 17 \text{ A}$
$P_{IGBT}$	Losses of an IGBT in a module	26.9 W	22.4 W
$P_{Diode}$	Losses of a diode in a module	4.18 W	3.87 W
$P_{mod}$	Losses per module	62.2 W	52.6 W
$\Sigma P_{mod}$	Total inverter losses	187 W	158 W
$T_h$	Heatsink temperature	77.3 °C	71.6 °C
$T_c$	Module case temperature	80.4 °C	74.2 °C
$T_{j\_IGBT}$	IGBT junction temperature	93.9 °C	85.4 °C
$T_{j\_Diode}$	Diode junction temperature	84.6 °C	78.1 °C

and number of fins) to approximate the Semikron<sup>®</sup> E3 heatsink parameters (of which an official datasheet could not be found). The heatsink thermal resistance has also been derated in order to account for altitude.

A clarification of the switching frequency used is required. Most of the simulations performed in Chapter 3, assumed a switching frequency of 50 kHz. In fact, the current control was originally designed for a switching frequency of 50 kHz. The thermal calculations showed that a switching frequency of 50 kHz, with the assumed current load is possibly out of reach for the chosen IGBTs (which were already procured). Hence, the switching frequency was lowered to a more acceptable value of 20 kHz. The most important sections in the design were iterated with the newly chosen switching frequency. Due to the decreased switching frequency, the inverter non-idealities which are frequency depended, namely the dead-time effect and duty cycle quantization are decreased. The relative importance of compensating each of the inverter non-idealities has to be reconsidered with the reduced switching frequency. The disadvantage is increased switching current ripple and the corresponding increased motor losses.

Table 4.1 lists the key results of the calculation. Thus, the device junction temperature operates well below the recommended junction temperature of 125 °C<sup>4</sup> with a safety margin of at least 1.25.

#### 4.2.4 Rectifier design

The three-phase inverter is fed from a DC bus capacitor which is charged by a full-wave rectified three-phase voltage source, which is filtered by an inductor, as shown in figure 4.3.

Without the filter inductor,  $L_f$ , the capacitor would be recharged by a sawtooth-like rectifier current, which would have a low power factor and has a large total harmonic distortion. The rectifier has a lagging power factor, even without an inductive load, since a diode pair is forward biased when the line-line voltage is near its peak. Also the high capacitor current peaks could easily surpass the peak rated current of the rectifier diodes. By reducing the peak amplitude of

<sup>4</sup>The maximum allowed junction temperature is 150 °C.

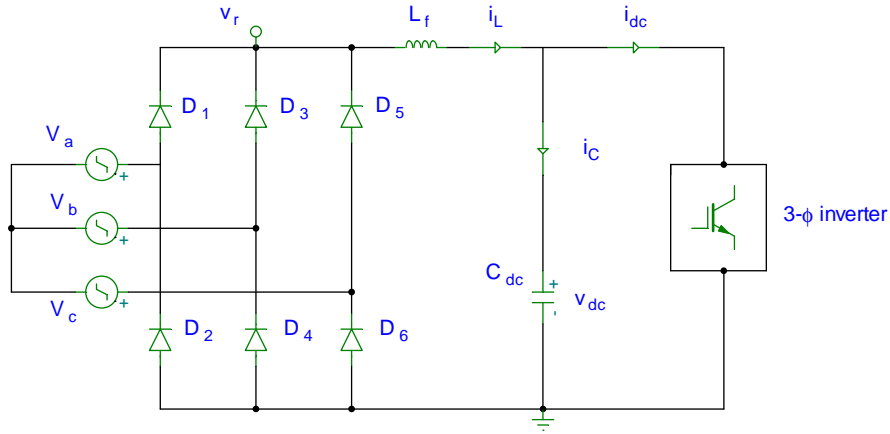


Figure 4.3: Three-phase rectifier.

the capacitor current, the filter inductor improves the power factor, protects the rectifier diodes and reduces the capacitor rms current.

The design of the rectifier components comprises the following:

- Selection of the rectifier diodes in order to meet the maximum current demand.
- Filter inductor specification and design, such that the benefits of improved power factor is obtained but simultaneously specifying a component which is realizable in terms of constraints such as cost, space and operating efficiency.
- Selection of the filter capacitor such that an expected capacitor operating lifetime and voltage ripple specification is met.

Since the resulting diode current is dependent on the LC filter values, the filter components are designed first, after which a simulation of the rectifier with a load corresponding to rated PMSM load, yields the required diode rating.

#### 4.2.4.1 Filter inductance design

The influence of the filter inductor on the line current harmonics and power factor of the rectifier has been analyzed by Kelley and Yadusky [82]. Their analysis was carried out in the form of a simulation on a rectifier circuit in which all parameters were normalized by a special procedure. The derived diagrams relating power factor and total harmonic distortion are thus useful for specifying an inductance value given a required power factor and/or maximum allowed total harmonic distortion.

Since this project focused on a prototype system for motor control evaluation, with relatively low power, a desired power factor has not been specified, but the inductance value was specified

according to a trial and error simulation approach with the capacitor rms current as the main concern. With the currents defined as in figure 4.3, the capacitor current is equal to:

$$i_C = i_L - i_{dc} \quad (4.13)$$

where the currents consist of an average and a ripple component, e.g. the DC-link current can be written as:

$$i_{dc} = \bar{i}_{dc} + \tilde{i}_{dc} \quad (4.14)$$

Note that the capacitor average current equals zero, so that the total capacitor rms ripple current is given by:

$$\tilde{i}_{C, rms}^2 = \tilde{i}_{L, rms}^2 + \tilde{i}_{dc, rms}^2 \quad (4.15)$$

The inductor rms ripple current can be calculated by noting that the sixth harmonic dominates the rectifier output voltage. The n-th harmonic voltage component for the full-wave three-phase rectifier is given by [83]:

$$v_{r, n} = \frac{6\hat{V}_L}{\pi(n^2 - 1)} \quad (4.16)$$

where  $\hat{V}_L$  is the peak line-line voltage of the three-phase source. Voltage harmonics higher than six cause negligible current due to the low-pass characteristic of the LC filter and the hyperbolic decreasing harmonic amplitude. Hence, the 6th current harmonic is a good approximation of the ripple component of the filter inductor and is approximated by:

$$\tilde{i}_{L, B} \approx \frac{v_{r, 6}}{6\omega L_f} \quad (4.17)$$

$$= \frac{\hat{V}_L}{35\pi\omega L_f} \quad (4.18)$$

where the denominator represents the equivalent impedance at the frequency of the rectified voltage, i.e. six times higher than the source frequency,  $\omega$ . The impedance is dominated by the filter inductor, since the impedance of the load is in parallel with the essentially zero impedance (at this frequency) of the filter capacitor. Note that equation 4.18 is oddly not a function of the load current. This is due to the assumption that the current can be approximated by the sixth harmonic which is most valid when the load current is such that the inductor current is on the boundary between discontinuous and continuous mode, hence the use of the  $B$  subscript denoting this boundary mode of operation. For smaller load currents resulting in discontinuous mode, it has been found experimentally that the ripple current can be calculated as the geometric mean between the average load current and the ripple current corresponding to the boundary mode of operation. Thus, the ripple current as a function of the average load current is:

$$\tilde{i}_L = \sqrt{\bar{i}_{dc} \times \tilde{i}_{L, B}} \quad (4.19)$$

Equation 4.19 is useful for estimating the filter inductance required for a current ripple specifi-

cation of the DC bus capacitor.

The filter inductance is selected as  $450\ \mu\text{H}$ , which results in a peak inductor ripple current of 16.2 A. With a rated motor load of 4 kW and a phase voltage of  $133\ \text{V}_{\text{rms}}$ , the *normalized* inductance results in  $5.1 \times 10^{-3}$  (unitless). This corresponds to a rectifier power factor of approximately 0.73 using the normalized diagrams presented in [82].

The toroidal core, T400-26, from MICROMETALS<sup>®</sup> is selected for the inductor. Its parameters are listed in table 4.2.

Table 4.2: T400-26 core parameters.

Symbol	Description	Value
$A_L$	Core permeance	130 nH/N <sup>2</sup>
$l$	Mean reluctance length	25 cm
$A_e$	Effective cross-sectional area	3.46 cm <sup>2</sup>
$\mu_r$	Relative permeability	75
$id, od$	Inner and outer diameter	5.72, 10.2 cm
$h$	Height	1.65 cm
$V_c$	Core volume	86.5 cm <sup>3</sup>

The required number of turns is calculated as:

$$\begin{aligned}
 N &= \sqrt{\frac{L_f}{A_L}} \\
 &= \sqrt{\frac{450 \times 10^{-6}}{130 \times 10^{-9}}} \\
 &\approx 59 \text{ turns}
 \end{aligned} \tag{4.20}$$

The core is checked for saturation by calculating the peak flux density excursion by:

$$\begin{aligned}
 \hat{B} &= \frac{N \times \hat{i}_L \times A_L}{A_e} \\
 &= \frac{59 \times 32.4 \times 130 \times 10^{-9}}{3.46 \times 10^{-4}} \\
 &= 0.72 \text{ T}
 \end{aligned} \tag{4.21}$$

where the peak current has been calculated as  $2 \times \tilde{i}_L$ , because the inductor ripple current is DC biased. Since this flux density is a bit high for the chosen core, two cores are stacked, which effectively doubles the core permeance and cross-sectional area. In order to maintain the inductance constant, the number of turns is reduced by a factor of  $\sqrt{2}$ , yielding 42 turns, which reduces the mmf and hence the peak flux density with the same factor. The resulting peak flux density is 0.51 T.

The core loss is checked with the aid of a polynomial fit found in the core's datasheet [84]:

$$\begin{aligned}
 P_c &= \left[ \frac{f}{\frac{a}{B_{pk}^3} + \frac{b}{B_{pk}^{2.3}} + \frac{c}{B_{pk}^{1.65}}} + d (f \cdot B_{pk})^2 \right] \cdot V_c \\
 &= \left[ \frac{300}{\frac{1 \times 10^9}{2530^3} + \frac{1.1 \times 10^8}{2530^{2.3}} + \frac{1.9 \times 10^6}{2530^{1.65}}} + 1.9 \times 10^{-13} (300 \cdot 2530)^2 \right] \cdot (2 \times 86.5) \\
 &= 6.12 \text{ W}
 \end{aligned} \tag{4.22}$$

where  $B_{pk}$  is the peak AC flux density in gauss, taken as half of the peak-peak flux density.

The winding is designed by noting that the winding loss is a function of the inductor rms current which is computed as:

$$i_{L,rms} = \sqrt{\bar{i}_{L,rms}^2 + \bar{i}_L^2} \tag{4.23}$$

$$\begin{aligned}
 &= \sqrt{\left( \frac{\hat{i}_L}{\sqrt{2}} \right)^2 + \bar{i}_L^2} \\
 &= \sqrt{\left( \frac{16.2}{\sqrt{2}} \right)^2 + 12.5^2} \\
 &= 17 \text{ A}_{rms}
 \end{aligned} \tag{4.24}$$

where the average inductor current,  $\bar{i}_L$ , corresponds to rated load and the peak ripple current is taken as the sixth harmonic component. The required copper area for the winding is calculated as:

$$\begin{aligned}
 A_{cu} &= \frac{i_{L,rms}}{J} \\
 &= \frac{17}{4} \\
 &= 4.24 \text{ mm}^2
 \end{aligned} \tag{4.25}$$

where  $J$  is the maximum allowed current density. The required wire diameter is calculated as:

$$\begin{aligned}
 D &= 2 \sqrt{\frac{A_{cu}}{\pi}} \\
 &= 2.32 \text{ mm}
 \end{aligned} \tag{4.26}$$

The winding resistance is calculated as:

$$\begin{aligned}
 R &= \rho \frac{l_{cu}}{A_{cu}} \\
 &= 1.68 \times 10^{-8} \frac{6.53}{4 \times 10^{-6}} \\
 &= 27.3 \text{ m}\Omega
 \end{aligned} \tag{4.27}$$

where  $l_{cu}$  is the total winding length ( $N \times$  turn circumference) and  $\rho$  is the resistivity of copper. The resulting winding loss is thus:

$$\begin{aligned} P_w &= i_{L,rms}^2 R \\ &= 17^2 \times 0.027 \\ &= 7.85 \text{ W} \end{aligned} \quad (4.28)$$

The total inductor loss is the sum of the core and winding copper loss, which results in 14 W.

#### 4.2.4.2 DC bus capacitor design

The filter capacitor current is the sum of the rectifier and the DC-link current. The previous section analyzed the rectifier contribution to the capacitor ripple current. An analysis of the ripple component of the DC-link current due to the switching inverter is performed by Kolar and Round in [85]. The analytical equation of the rms DC-link current is quite complex and is dependent on the load power factor and the inverter modulation index. Assuming a load with near unity power factor (such as the PMSM), a simplified equation for the rms ripple component of the DC-link current, corresponding to worst-case DC bus capacitor loading is given as [85]:

$$\tilde{i}_{dc,rms} \simeq \frac{1}{\sqrt{2}} i_{ph,rms} \quad (4.29)$$

where  $i_{ph,rms}$  is the maximum phase current of the inverter load. Hence, the total rms ripple current, assuming a maximum phase rms current of 12.5 A<sub>rms</sub>, is calculated as:

$$\begin{aligned} i_{c,rms} &= \sqrt{\tilde{i}_{dc,rms}^2 + i_{L,rms}^2} \\ &= \sqrt{\left(\frac{12.5}{\sqrt{2}}\right)^2 + \left(\frac{16.2}{\sqrt{2}}\right)^2} \\ &= 14.5 \text{ A}_{rms} \end{aligned} \quad (4.30)$$

The ripple current handling capability<sup>5</sup> of an electrolytic capacitor is specified at some reference frequency, usually 100 Hz [85]. The ripple component of the DC-link current and the rectifier current can be up/derated, due to the frequency dependency of the electrolytic capacitor's ESR, in order to obtain an equivalent 100 Hz rms ripple current. The selected capacitor is the AYY-HR222X450DC1 from Itelcond<sup>®</sup>. Table 4.3 lists some of its key parameters [86].

<sup>5</sup>The ripple current rating is that current which would cause a rise of 10 °C in the capacitor's core temperature. For every 10 °C increase of the capacitor core temperature the expected lifetime of the capacitor is approximately halved [83].

Table 4.3: Electrolytic capacitor parameters.

Symbol	Description	Value
$V_n$	Rated voltage	450 V
$C$	Rated capacitance	2.2 mF
$\tilde{i}_{C,rms} @ 55^\circ\text{C}$	Ripple current	12.8 A
$\tilde{i}_{C,rms} @ 85^\circ\text{C}$	“	9.1 A
$K_t @ 40^\circ\text{C}$	Temperature scaling factor	1.65
$K_f @ 300 \text{ Hz}$	Frequency scaling factor	1.24
$K_f @ > 1 \text{ kHz}$	“	1.37

The capacitor ripple current is transformed into an equivalent 100 Hz ripple current by [86]:

$$\begin{aligned}
 i_{c,rms,100\text{Hz}} &= \sqrt{\left(\frac{\tilde{i}_{dc,rms}}{K_{f,>1k}}\right)^2 + \left(\frac{\tilde{i}_{L,rms}}{K_{f,300}}\right)^2} \\
 &= \sqrt{\left(\frac{8.84}{1.37}\right)^2 + \left(\frac{11.5}{1.37}\right)^2} \\
 &= 11.3 \text{ A}_{\text{rms}}
 \end{aligned} \tag{4.31}$$

Thus, as long as the ambient temperature is below  $45^\circ\text{C}$ , the capacitor will obtain an operational lifetime exceeding  $150 \times 10^3$  hours, based on operational lifetime curves in the datasheet. If the capacitor is forced cooled, its ripple current rating and/or operational lifetime can also be increased.

The capacitance is determined from a voltage ripple specification. The filter inductor design assumed that the capacitor impedance is negligibly small, but in actuality the ripple voltage due to the capacitor impedance can be computed as the integral of the sixth harmonic current:

$$\begin{aligned}
 i_C &= C \frac{dv}{dt} \\
 \tilde{v}_c &= \frac{1}{C} \int \tilde{i}_L \cos(6\omega t) dt \\
 \therefore \tilde{v}_c &= \frac{1}{6\omega C} \tilde{i}_L \sin(6\omega t)
 \end{aligned} \tag{4.32}$$

Substituting equation 4.19, yields the peak-peak capacitor voltage as:

$$\tilde{v}_{c,pp} = \frac{1}{3\omega C} \sqrt{\tilde{i}_{dc} \times \tilde{i}_{L,B}} \tag{4.33}$$

Substituting the peak-peak ripple voltage as a percentage of the average output voltage and solving for the capacitance yields:

$$C = \frac{\pi}{9\omega v_{r,\%} \hat{V}_L} \sqrt{\tilde{i}_{dc} \times \tilde{i}_{L,B}} \tag{4.34}$$

where  $v_{r,\%}$  is the required peak-peak ripple percentage of the nominal output voltage. Due to the

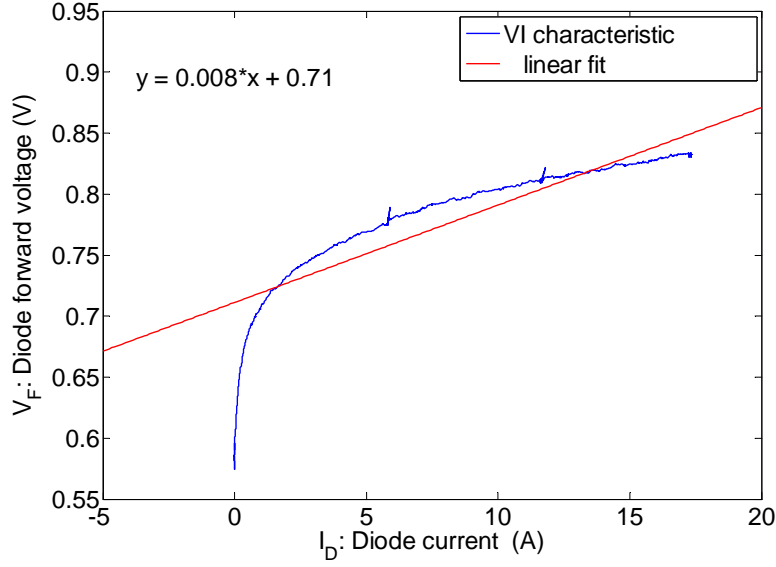


Figure 4.4: Three-phase diode bridge rectifier forward characteristic.

assumption that the capacitor ripple current is dominated by the sixth harmonic, equation 4.34 is only valid for a percentage ripple of  $\lesssim 3.5\%$ . Specifying a maximum percentage ripple of 1.5%, the required capacitance is 3.7 mF. Hence, two capacitors are required per drive (ignoring the interconnected DC bus of each drive). Note that the analysis did not consider the contribution of the PMSM acting as a load which recharges the DC bus capacitor bank. By designing each drive independently, the prototype is flexible in the number of configurations it can achieve<sup>6</sup>.

#### 4.2.4.3 Three-phase diode bridge

The filter inductor current operates in the discontinuous mode so that the rectifier diodes have essentially zero switching losses due to the zero current switching. The diode conduction losses can be calculated following the same approach followed for the inverter thermal verification. The rectifier bridge module is mounted on the same heatsink as the inverter. The three-phase diode bridge (MDS110-12:B6U) has a voltage blocking rating of 1200 V and a current rating of 110 A. A datasheet of this component could not be found, hence its V-I characteristic has been measured as shown in figure 4.4. The linear fit parameters are used in the conduction loss calculation.

The diode rms and average current, required for the conduction loss calculation, is obtained via an LTspice<sup>®</sup> simulation of the rectifier and LC filter loaded with rated current. The diode rms and average current equalled 10 A<sub>rms</sub> and 4.3 A, respectively. The diode bridge rectifier losses are determined as 23.1 W.

The simulation model has also been used to verify the equations used for the calculation of the

<sup>6</sup>The preliminary capacitor design assumed a much higher capacitor ripple current, due to a larger assumed load and the absence of the filter inductor, so that the total DC-link capacitance in the test system is 13.2 mF.



rectifier contribution to the capacitor ripple current. The rectifier design file and simulation model is included in appendix [C.19](#).

## 4.3 Isolation and protection

### 4.3.1 Three-phase transformer

The three-phase utility supply has a line-line voltage of  $380 - 420 \text{ V}_{\text{rms}}$ . If this voltage were to be rectified with a three-phase full-wave rectifier, the DC bus would be charged to  $563 - 622 \text{ V}$ , which would be mismatched with the voltage required by the PMSM used in this project. The inverter losses and current ripple would be unnecessarily high with this DC bus voltage.

The DC bus voltage is reduced by connecting three single phase transformers with a winding ratio of  $380 : 220$  in a  $Y - Y$  configuration, which reduces the voltage by a factor of  $\sqrt{3}$ . Hence the resulting DC bus voltage is in the range of  $325 - 359 \text{ V}$ . The isolation transformers has a winding ratio slightly larger than  $380 : 220$ , in order to account for the voltage drop caused by a rated load connected to the secondary. The single phase transformers used has a rating of  $5 \text{ kVA}$ , which is more than sufficient.

The transformers also serves the purpose of isolating the input voltage from the rest of the control electronics, so that the rectified voltage ground may be connected safely to the ground of the dSPACE<sup>®</sup> controller.

### 4.3.2 DC bus inrush current limiting

When the voltage source to the rectifier is switched on, the uncharged DC bus draws high inrush currents which would damage the rectifier and cause an overvoltage condition due to the overshoot caused by the filter inductor. In order to solve this problem the capacitor inrush current is limited with a series resistance placed in the line preceding the rectifier. After the capacitor bank has reached steady state, the current limiting resistors are bypassed with a  $30 \text{ A}$  contactor. The switching of the contactor is done with a timed relay option build into the contactor.

The series resistance per line is obtained by paralleling eight  $3.3 \text{ k}\Omega$ ,  $5 \text{ W}$  resistors, which yields a  $413 \Omega$ ,  $40 \text{ W}$  resistor. Via simulation, the time constant for the three-phase rectifier has increased by a factor of  $\approx \frac{2\pi}{3}$ , compared to the RC time constant required for a DC bus capacitor to charge up to  $68\%$  of its final value. The DC bus capacitor reaches its final value in approximately four (modified) time constants, i.e.  $46 \text{ s}$ . Hence the contactor's timer circuit which bypasses the capacitors are set to approximately  $60 \text{ s}$ .

### 4.3.3 Inverter dead-time selection

The amount of dead-time required in order to prevent a short circuit in the top and bottom switches is determined by considering the switching times of the IGBT. Before an IGBT may be turned on, the switch in the complementary part of the inverter leg has to be off. Therefore, the switch-off delay and fall time serve as a guide for selecting the dead-time.

The switch-off time is defined as the sum of the switch-off delay and fall times. A definition of the switching characteristics of the IGBT can be found in [87]. For a gate resistance of  $22\ \Omega$ , a collector current of 50 A and a DC bus voltage of 300 V, the resulting turn-off time for the SKM 50 GB 063 D from its datasheet is 330 ns.

From the characteristic curves in the datasheet, the switching times are not a strong function of the collector current, but do depend strongly on the gate resistance. The gate resistance used in this project is  $12\ \Omega$ . Hence, the actual switching time is even lower.

Selecting the dead-time equal to  $1\ \mu\text{s}$  is therefore deemed sufficient. With a switching frequency of 20 kHz, the dead-time constitutes 2 % of the switching period. Thus a low amount of distortion due to the dead-time effect is expected and the maximum obtainable voltage fundamental of the inverter is not reduced by a considerable amount.

### 4.3.4 Inverter snubber capacitors

The leakage inductance between the electrolytic DC bus capacitors and the DC bus terminals of the IGBT module cause voltage overshoot when one of the IGBTs switches off. The series resistance of the electrolytic capacitors form part of the total leakage inductance. In order to prevent excessively dangerous voltage overshoot, a snubber capacitor is placed directly across the terminals of the DC bus connection of the IGBT module. It is important to make the connection of the snubber capacitors to the IGBT module as short as possible, in order to reduce the contribution of the capacitor leads to the leakage inductance.

The required capacitance in order to limit the voltage overshoot at the DC bus terminals of the IGBT, given a specified allowable maximum voltage,  $\hat{v}_{dc}$ , can be determined by considering an energy relation, without solving the differential equations of the circuit under consideration. This is done by noting that the maximum voltage is attained after all of the leakage inductance energy is transferred to the capacitor. The moment just before the IGBT switches off, the electrolytic capacitor and snubber capacitor is charged to the same average value,  $\bar{v}_{dc}$ . Thus when the IGBT switches off and the inductor transfers its energy to the capacitor, the capacitor appears uncharged, because the voltage difference across the inductor before switch off is zero. Hence, the required capacitance can be determined as follows:

$$\frac{1}{2}C_s(\Delta v_{dc})^2 = \frac{1}{2}L_l\hat{i}_{dc}^2 \quad (4.35)$$

$$\therefore C_s = \frac{\hat{i}_{dc}^2 L_l}{(\hat{v}_{dc} - \bar{v}_{dc})^2} \quad (4.36)$$

where  $\hat{i}_{dc}$  is the peak DC-link current and  $L_l$  is the total leakage inductance of the loop which carried the current just before turn-off.

The inductance of the cable connecting the electrolytic capacitors to the DC bus terminals of the IGBT modules were measured as 380 nH, with the *RLC 300* measurement unit from digimess<sup>®</sup>. The leakage inductance of the electrolytic capacitors proved to be an elusive parameter. The capacitor leakage inductance can be calculated from the capacitor impedance, assuming the capacitor impedance is dominated by the leakage inductance at high frequency. From the capacitor datasheet [86], its impedance at 10 kHz is 43 mΩ. This corresponds to an equivalent series inductance (ESL) of 684 nH. Even though there are capacitors in parallel, which reduces the equivalent inductance, this is not taken into account in order to yield a conservative snubber capacitance.

Although the selected IGBT modules have a blocking voltage of 600 V, it is not good to push the limits of operation to this point, in order to obtain a minimum snubber capacitance. One reason is for safety and another for EMI considerations, i.e. a higher voltage overshoot corresponds to higher  $\frac{dv}{dt}$  and thus common-mode current in parasitic capacitance near the IGBT modules. Hence, the peak allowed DC bus voltage is chosen as 365 V, slightly higher than the DC bus voltage.

The peak DC-link current for sizing the snubber capacitor corresponds to average DC-link current at maximum inverter power, thus  $\approx 12$  A. With the chosen constraint, operating conditions and determined leakage parameters, the required capacitance is determined to be 680 nF. Including a safety factor in order to acknowledge unmodelled leakage inductance, the chosen snubber capacitance is 2 μF.

#### 4.3.5 Inverter current limiting

The IGBTs are protected from an overcurrent condition by three methods. Firstly, the peak torque producing current is limited in the control (vector control) to a value which corresponds to slightly higher than rated load<sup>7</sup>. Secondly, the control sends an error signal to the driver board to soft shutdown the IGBTs, if the control cannot maintain the peak current limit and a current value has been detected which is higher than the limit in the first case. A short circuit through low impedance in the output of the inverter could result in a current which is far higher than the maximum allowed value for the IGBTs, which would be detected too late by the time the controller executes its next control period. In order to protect the inverter from such an overcurrent condition, the IGBT driver board detects an overcurrent condition via a method known as  $V_{ce}$  saturation monitoring (third method).

Saturation monitoring utilizes the relationship of the IGBTs saturation voltage to its collector current. In parallel to the IGBT, the driver board measures the collector-emitter voltage during the IGBT on-time, and trips the drive if this voltage is higher than a threshold voltage. The

<sup>7</sup>The first method, is not applicable to V/f control

threshold voltage is configured via a resistor on the driver board. The IGBT monitoring is only active during the IGBT on-time, since during an off-time the collector-emitter voltage is high, which would appear as a short circuit. When the IGBT switches on, there is a small delay before the saturation monitoring activates, in order to reject switching noise which would falsely trip the drive. This delay is known as blanking time (not to be confused with dead-time, although dead-time is also referred to as blanking time in the literature). The blanking time is configured with a capacitor on the driver board. The blanking time should be set high enough for the switching transients to have decayed, but small enough in order to protect the inverter<sup>8</sup>.

The threshold value and blanking time is set by a resistive divider and low-pass filter capacitor, hence the resistance and capacitance required for configuring the driver board's over current detection is interrelated. The equations are found in the SKHI61 datasheet [88]:

$$R_{V_{ce}} = \frac{11.86}{5.4 - 0.93V_{ce}} - 4.75 \quad (4.37)$$

$$C_{V_{ce}} = \frac{t_{blank} (72.75 + R_{V_{ce}})}{(R_{V_{ce}} + 4.75) \times 36.08} - 0.1 \quad (4.38)$$

where  $C_{V_{ce}}$  is the filter capacitance in nF,  $R_{V_{ce}}$  is the voltage divider resistance in k $\Omega$  and  $t_{blank}$  is the desired blanking time in  $\mu$ s. The inverter blanking time is chosen as 2.5  $\mu$ s. The threshold value has been chosen the lowest possible value, which is set by shorting the threshold resistor. The resulting saturation threshold voltage is 3.12 V, which corresponds to a collector current of 85 A at  $T_j = 125^\circ\text{C}$  (read from the collector-emitter voltage and collector current characteristic in the SKM50GB063D datasheet). Since the selected device is a non-punch through (NPT) IGBT, the current is higher for lower junction temperatures corresponding to this threshold voltage. Note that this is higher than the continuously rated collector current of the IGBT. For short periods (on the order of 10  $\mu$ s), the IGBT can withstand short circuit current levels of up to ten times its rated current. Therefore, although the drive short circuit current is detected at a relatively high level, the IGBT is able to handle this current, but for only a short period, which is why it is important to detect a short circuit and trip the drive as soon as possible. With the specified blanking time and threshold voltage:  $R_{V_{ce}} = 0\Omega$  and  $C_{V_{ce}} \approx 1$  nF. The calculations for the current limiting are included in appendix C.20.

The high current present during a short circuit represent energy stored in the leakage inductance, formed by the short circuit loop. In order to limit high induced voltage by the leakage inductance, the IGBTs are switched off with a soft-shutdown, by the SKHI61 driver board. Another reason for the soft-shutdown requirement of the IGBTs is due to the phenomenon known as latchup. An IGBT can withstand high levels of operating current, but only to a certain extent. At a high current level, exceeding a certain threshold, the base of a parasitic npn region inside the IGBT becomes forward biased, at which point the IGBT gate no longer has control over the switching of the device. This condition is known as latchup and like a normal thyristor, the switch has to be turned off by forced commutation of the current, i.e. the device current has to be forced to

<sup>8</sup>A simple check on the blanking time is to note that it should be in the same order of magnitude as the dead-time.

zero external to the device in order for the latchup to end. Latchup can also be triggered during device turn-off. The region causing static device latchup has a higher current which depends on the rate at which the MOSFET structure in the device turns off. If the device switches off too quickly, the IGBT can enter latchup, known as dynamic latchup (the result is the same, the name only differs to identify its cause). The collector current required for dynamic latchup, is lower than the static case. The manufacturer's peak current rating usually corresponds to dynamic latchup. Modern IGBTs are designed and guaranteed to be latchup proof for the normal rated operating range. A short circuit condition is out of range of the guaranteed region [81], hence short circuit currents also require soft-shutdown in order to prevent dynamic latchup.

#### 4.3.6 DC bus overvoltage protection

Since a brake resistor is not added to the drive, an overvoltage due to regenerative braking on the DC bus capacitors is possible. With respect to the control operation, this has been addressed by limiting the deceleration rate of the motor in the speed signal reference generator, as discussed in section 3.2.3.2. In the event that the deceleration constants are no longer valid<sup>9</sup> or if the control becomes unstable, an overvoltage condition is still possible.

In order to address this risk, the DC bus voltage measurement is compared to a threshold value. If the measured value exceeds the threshold value, both drives are shutdown and the rotors are allowed to decelerate due to the frictional losses.

Ideally a brake resistor should be added to the system. This can be achieved by replacing the driver board with one which supports a seventh IGBT driver. The control of the brake would impose minimal extra computation burden to the controller. This has not been done due to resource constraints.

#### 4.3.7 Controller protection from sensor signals

The output signals of the sensors presented in section 4.4, pass through an interface board before connecting to the dSPACE® controller. The signal conditioning circuitry and overvoltage protection reside on the interface board. The overvoltage protection is achieved via a zener diode clamping circuit.

Figure 4.5 shows the clamping circuit combined with the anti-aliasing filter. With the back-to-back configuration of the zener diodes, with a breakdown voltage of 10 V, an external rail voltage of  $\pm 10$  V is not required for the clamping circuit. The filter resistance forms part of the clamping circuit: if the input voltage is too high, a large current is drawn by the clamping diodes, which cause a voltage drop across the filter resistance such that the output voltage is limited to  $\pm 10$  V.

---

<sup>9</sup>The deceleration constants may become invalid if the rotor inertia increases due to an external coupling to the rotor, e.g. if a blower is connected to the rotor.

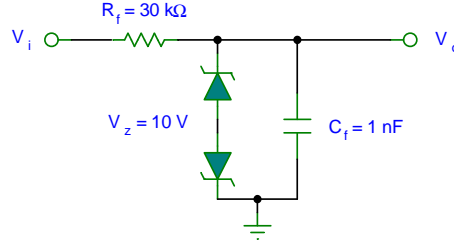


Figure 4.5: Anti-aliasing filter and zener voltage clamp circuit.

The overvoltage protection circuitry used in this project provides safe protection up to  $V_i \approx 100$  V. A thermal fuse, with the appropriate voltage rating and trip current, should be placed in series with the filter resistance in a follow-up project, in order to provide protection up to  $V_i = V_{dc}$ .

## 4.4 Drive sensors

### 4.4.1 Voltage and current sensors

The PMSM voltage and currents are measured with a sensor board<sup>10</sup>, which is mounted on the side of the inverter heatsink. The voltages are measured with resistive voltage dividers. Ideally the voltage measurement should be isolated, using a Hall-effect voltage sensor, or a resistive voltage divider combined with an isolation amplifier, in order to protect the dSPACE<sup>®</sup> controller.

The resistive voltage divider network has a maximum voltage input equal to  $\hat{v}_{dc} = 350$  V. The analogue-to-digital converter boards (DS2003 & DS2004) have a voltage range of  $\pm 10$  V. Hence, the input signal needs to be attenuated by a factor of at least 35. After including a safety margin of  $\approx \sqrt{2}$ , the voltage divider resistances are chosen as  $550$  k $\Omega$  and  $12$  k $\Omega$ , which results in an attenuation factor of 46.8. In the control, the measured voltage is not multiplied by this calculated attenuation factor, but is instead multiplied by a factor determined by a calibration procedure, in order to account for attenuation due to all of the signal conditioning circuitry preceding the ADCs.

The currents are measured with isolated LEM LAH 25-NP current sensors, which can measure a maximum current of  $25 A_{rms}$  continuously and a peak current of  $55$  A for a limited duration. The current is measured using the Hall-effect. Thus, unlike current transformers, these sensors can also measure the DC component. The sensors require a voltage supply of  $\pm 15$  V. The sensor output is a current which is proportional to the input current. The sensor gain is thus set with a load resistor that converts the measured current to a voltage which is sampled by the ADCs. The gain resistor is chosen as  $220 \Omega$ , which yields a total attenuation factor of  $0.22 \frac{V}{A}$ .

<sup>10</sup>The sensor and interface board schematics and PCB layout were outsourced to Mr. D. Herbst.

#### 4.4.2 Temperature sensors

The permanent magnets fitted onto the rotor have a shrink-fitted shielding cylinder. The usual purpose of the shielding cylinder is to reduce eddy current loss in the permanent magnets, if made from a good conductive material. The cylinder had to be shrink-fitted in order to limit the centrifugal growth of the rotor at high speed. For mechanical strength the shielding cylinder is made from *Inconel*<sup>®</sup> 718, which has a resistivity comparable to that of the permanent magnets. A temperature rise in the rotor causes thermal expansion of the rotor, which in turn increases stress in the permanent magnets, which is constrained by the shielding cylinder. From the mechanical design, the maximum rotor temperature allowed is 80 °C [7].

In order to monitor the rotor temperature for safe operation, an infrared temperature sensor is fitted onto the motor housing cover, which measures the rotor temperature. The infrared sensor (EL101A from Callex<sup>®</sup>) requires a voltage supply of 24 V. It has an output of 4 – 20 mA which is converted into a voltage with a 750  $\Omega$  resistor. By placing the current-to-voltage conversion resistor on the interface board, a voltage drop on the long leads from the sensor is prevented.

The PMSM winding temperature is also monitored with resistive temperature detectors (RTDs). Since the RTD (PT-100 RTD from Wika Instruments<sup>®</sup>) is a passive component, it requires driver circuitry in order to measure the resistance. The driver circuit, which requires a voltage supply of  $\pm 15$  V, acts as a constant current source. The voltage resulting from the driver current consists of a nominal and a deviation component. The nominal voltage represents a known value for a certain operating temperature. This voltage is subtracted and the deviation voltage (which is a function of the RTD temperature) is amplified and measured by the ADC. The amplification is performed by a difference amplifier which also subtracts the nominal voltage. The RTD driver circuitry resides on the interface board. The RTD measurement is scaled with an amplification factor in the controller, which is determined by a calibration procedure. The nominal voltage which has been subtracted, corresponds to a 0 °C operating point, thus only the scale factor is required to determine the temperature, given the measured voltage.

The sensor and interface board schematics are included appendix C.21.

#### 4.4.3 Position sensor

For the vector controlled drive, the rotor angular position is required for the transformation of the three-phase currents into the rotor reference frame. The rotor position is also used to derive the rotor speed via an observer. The rotor angular position is obtained with a high-speed rotary magnetic encoder (RM22S from RLS<sup>®</sup>). In order to protect the sensed position signal from the switching interference caused by the three-phase inverter, the sensed signal is transmitted via a digital signal to the controller.

#### 4.4.3.1 Sensor mounting

A magnetic actuator which is placed on the tip of the rotor is sensed via a separate Hall-effect sensor inside an encoder IC (AM512BD01). The encoder IC is inside a housing which is not in contact with, but in close proximity to the magnetic actuator as shown in figure 4.6.

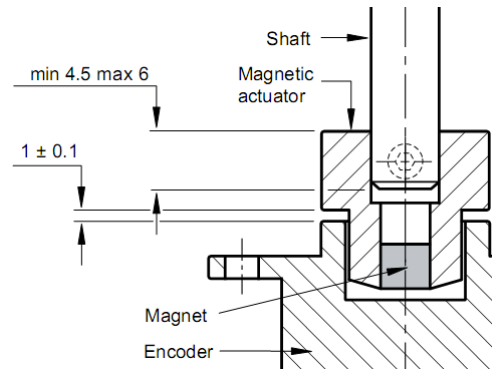


Figure 4.6: Non-contact, angular position sensor [6].

#### 4.4.3.2 Communication to controller

The measured signal from the encoder is read out digitally using a serial synchronous interface (SSI). The SSI consists of a clock and data line. A rising edge of the clock signal instructs the encoder IC to present the next bit of the measured signal on the data line, which can be read after a minimum specified delay has passed after the clock's rising edge. After the complete value (9-bits) has been read by the controller, a period has to elapse before the next measured byte is latched into the SSI shift register.

The dSPACE<sup>®</sup> controller does not have native support for the SSI protocol and would require excessive resources if it is to be implemented on a digital I/O card of the controller. Hence, a PIC<sup>®</sup> microcontroller from Microchip<sup>®</sup> is used to read the rotational position value using the SSI protocol, after which it is transmitted via RS485 to the DS4201-S card (which has RS485 support). The majority of the distance that the signal has to be transmitted is via RS485, which is more noise immune than the SSI protocol, because the data signal is transmitted differentially on two data lines. Balanced common-mode noise is rejected by the difference amplifier inside the RS485 driver IC on the receiver side.

Figure 4.7, shows the functional diagram of the circuit interfacing the position sensor to the controller. The microcontroller requires a voltage supply of 5 V. The SSI converter schematic and microcontroller source code is included in appendix C.22. The downsampling also depicted in the figure is discussed in section 4.5.2.



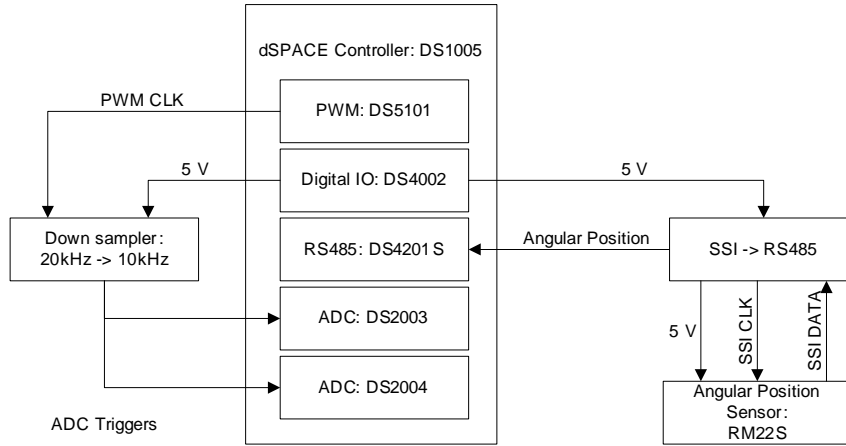


Figure 4.7: Functional diagram of position sensor interfaced with controller.

#### 4.4.3.3 Offset zeroing

The zero position of the encoder is not necessarily aligned with the zero position as defined by the controller's reference frame. Hence, the offset of the encoder should be measured and subtracted from the measured value, in order to obtain a value which can be used by the transformations in the control.

The encoder is zeroed by measuring the encoder offset when the rotor is aligned with its defined zero position. The rotor is aligned with its defined zero position, by exciting the three-phase winding with a DC voltage vector of small amplitude which excites the phase-a magnetic axis. The rotor d-axis aligns with this stator magnetic axis, which is chosen as the origin of the angular position. The encoder output corresponding to this alignment is stored in the controller memory and is used to zero the encoder signal. The zeroing value should be tested by advancing the DC voltage vector to other known values. The resulting rotor position should correspond to the voltage vector angle. It may happen that the direction of the angular increase for the voltage vector and position sensor may be opposite, in which case the measured angular position polarity should be reversed by multiplying it with  $-1$  and repeating the previous offset zeroing procedure.

## 4.5 EMI

### 4.5.1 Shielding and filtering

Figure 4.8, depicts one leg of the three-phase inverter. The line connecting the phase output of the inverter to the load has a parasitic capacitance to ground. The switching of the inverter causes high  $\frac{dv}{dt}$  in the phase output, which results in a current flowing in the parasitic capacitance. Ideally, the sum of the three-phase currents should be zero, since all of the current leaving one

phase output is returned via the other two phases. In the actual system the sum of the three-phase currents, measured directly at the output of the inverter is not zero, because some of the output current, has a return path via the parasitic capacitance, known as the common-mode current.

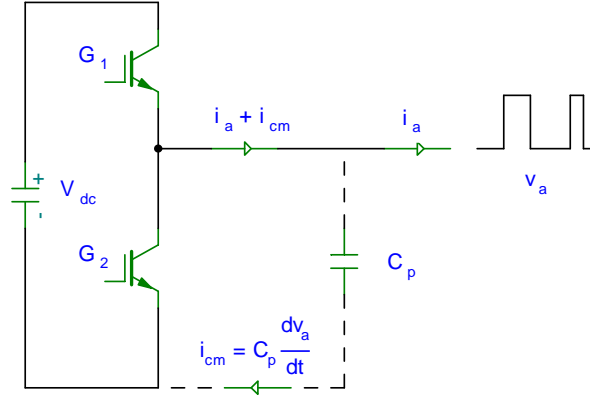


Figure 4.8: Common mode current due to parasitic capacitance.

The common-mode current has a return path which covers a large area from where it is emitted, due to fringing of the electric field. Common-mode current also returns along sensor conductors and measurement circuitry. Figure 4.9, shows a hypothetical difference amplifier, usually present in the signal conditioning circuitry preceding an analogue-to-digital converter. If the signal lines carry an unequal common-mode current, i.e.  $i_{cm1} \neq i_{cm2}$ , then the common-mode signal will be converted into a differential-mode voltage,  $v_{dm}$ , which is amplified by the gain of the difference amplifier. Also, even if the common-mode current is balanced, but the input impedance in each of the difference amplifier lines are not balanced over the frequency range of interest, then a differential-mode voltage also results. The conversion of common-mode current into a differential-mode voltage represents unwanted interference in the desired output signal:  $v_o = G(v_1 - v_2) + Gv_{dm}$ . Placing a cross-capacitor between the two inputs of a difference amplifier, *before* the common-mode current has been converted into a differential-mode signal, helps to balance the common-mode current in the two inputs.

The interference caused by the common-mode current has to be minimized by shielding the cable carrying the high  $\frac{dv}{dt}$  and/or to filter the inverter three-phase output with an  $LC$  filter, in order to have uncorrupted sensor signals for use in the control and to be electromagnetic interference (EMI) compliant. The shield has to be grounded with a low impedance path as close as possible to the noise source.

The common-mode current due to parasitic capacitance represents one source of interference; another source of interference is that due to parasitic mutual inductance. Parasitic mutual inductance causes coupling of the differential-mode and common-mode signals to sensor cables in close proximity. The mutual inductance carrying differential-mode signals should be reduced by minimizing the loop area of the cable. Without shielding, the common-mode current has a

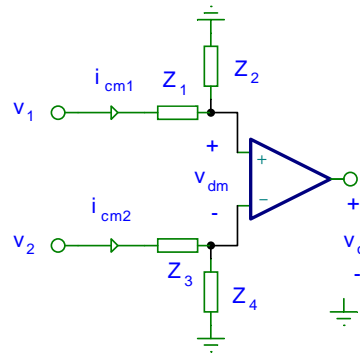


Figure 4.9: Conversion of common mode to differential mode signals.

large return path, covering a large area. If this area is thought of as a loop, then a potentially significant mutual inductance exist between the path of the common-mode current and all other signal carrying cables. The shield of the cable connecting the inverter and PMSM restricts parasitic capacitance to sensor cabling. It also helps to reduce mutual inductance between the common-mode current and the sensor cabling, which would have induced common-mode current in the sensor cable, even if the sensor cable is shielded.

Electromagnetic interference resulting from parasitic capacitance and mutual inductance represents *conducted* EMI. The second part of the EMI dichotomy is that due to *radiated* electromagnetic interference, which becomes important especially in communication equipment.

With the preceding introduction in mind, appendix C.24, contains photos with descriptions of the measures taken in order to counteract EMI in the PMSM drive. Reducing EMI is quite complex and deals with unseen/parasitic components, of which the surface has only been scratched in this section. The electromagnetic interference had to be addressed in this project in order to have a useful drive for control experiments. EMI standards and compliance certification<sup>11</sup> as such is still to be addressed.

#### 4.5.2 Synchronized sampling of sensor signals

Example gate signals for the top switches of the three-phase inverter is shown in figure 4.10, along with a PWM clock signal used in the generation of the gating signals. Each transition of a gate signal causes a common-mode current transient response in the parasitic capacitance as explained in the previous section. The common-mode current during this transient pervades through the measurement circuitry. If the signals required for motor control are sampled by the ADCs during such a switching transient, the noise component of the measured signals would be considerably increased.

<sup>11</sup>For EMI compliance, the common and differential-mode noise is measured at the line input of the rectifier using a circuit known as a Line Impedance Stabilization Network (LISN). The measured common and differential-mode noise spectrum has to be lower than a specified amount according to the standard used (dependent on region).

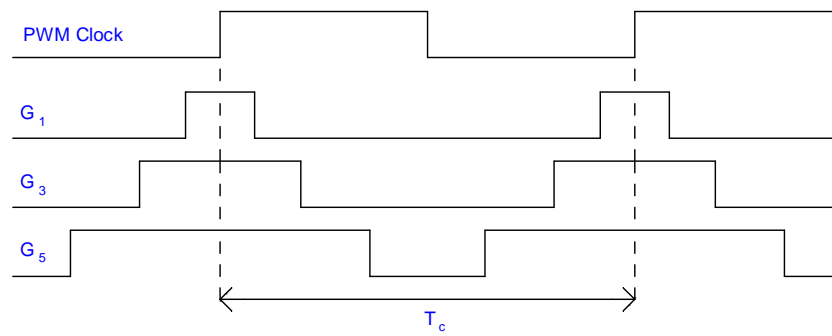


Figure 4.10: IGBT gate and synchronization clock.

The sampled signals' S/N ratio is greatly improved by synchronizing the ADC sampling circuitry with the clock of the generated PWM signals, so that signals are sampled during periods which are far from a switching transient. Ideally, the signals should be sampled just *before* a switch transition, which allows the most amount of time for the transients of a previous switch transition to have decayed. This is however impractical, because there are multiple phases and a variable delay would be introduced into the control loop.

The PWM generator board (DS5101) used for generation of the inverter gating signals has a clock output which is synchronized with the gating signals. The synchronized sampling is performed by connecting the PWM clock output to the ADC board's trigger inputs. The DS2004 ADC board converts sampled signals at a high speed and has a high resolution, whilst the DS2003 ADC board can sample more inputs, but its conversion time is much longer. If the DS2003 board receives an ADC trigger before it has completed conversion of the previously sampled signals, it discards the current conversion and starts over. This is the case with the current system setup. In order to solve this problem, the PWM clock is downsampled to the same frequency as that of the controller. The downsampled PWM clock is used for synchronized sampling of the ADCs.

The downsampling of the PWM clock period is performed without causing a delay between the optimal triggering instant and the downsampled signal, using a low cost PIC<sup>®</sup> microcontroller from Microchip<sup>®</sup>. This is done by introducing a precise delay in the downsampling, equal to the number of PWM clock periods (minus the delay caused by program overhead) which needs to be skipped in order to achieve the required downsample ratio. The clock output of the PWM generator board serves as an interrupt input for the downsampling operation, thereby preventing drift in the phase between the PWM clock and the downsampled signal.

Figure 4.7, depicts the functional relationship of the downsampling circuit to the controller and its power requirements. Source code of the synchronized downsampling is included in appendix C.23.

## 4.6 Computation improvements

The simulation models presented in chapter 3, attempt to represent the mathematics of the PMSM and controller as closely as possible. For instance, the coordinate transformations are performed with matrix multiplication. This clarified which transformations are used during the simulation model construction.

For controller implementation, the control program, which has to execute on the dSPACE<sup>®</sup> controller, is compiled from the control model implemented in Simulink<sup>®</sup>. Hence, the matrix representation of the transformations used is quite inefficient with respect to controller resources, since each entry in the matrix represents a trigonometric function call. The transformation and inverse transformations were also constructed separately.

A much more efficient manner of performing the transformations is possible. This can be achieved by noting that the phase shifted evaluation of the sine and cosine functions, can be represented as a linear combination of the aforementioned base functions. Therefore, the entries in the transformation matrix can be obtained with only two trigonometric function calls. The other entries can be obtained via multiplication and addition. Once the set of entries in the transformation matrix has been calculated, the same set of entries can be re-used in order to construct the inverse transformation, with minimal extra computations.

The final optimized models of the two controllers are included in appendix C.25.

## 4.7 Summary

The developments of this technical oriented chapter can be summarized as follows:

- The requirements of the IGBTs used in the inverter were specified and a selection of the IGBT modules was made accordingly.
- A thermal analysis of the inverter was performed based on the lumped parameter representation of thermal impedance and losses. An overview of the expressions required for the three-phase inverter switching and conduction loss calculation was presented. The analysis result predicts that the inverter should be able to drive the PMSM at a rated power of 4 kW.
- It was found that the three-phase rectifier supplying the DC bus required a filter inductor in order to limit the capacitor ripple current. A filter inductor was designed accordingly. The losses of the three-phase rectifier for a rated load were also calculated to verify its safe operation.
- Many aspects regarding protection of the inverter and controller were covered. This included the following:

- isolation of the three-phase voltage supply so that the controller and drive may safely share a common ground;
  - inrush current limiting in order to prevent large DC bus charging currents and a dangerous voltage overshoot due to the rectifier filter inductor;
  - dead-time selection for the inverter in order to prevent shoot-through;
  - calculation of the required inverter snubber capacitance to prevent large voltage overshoot on the DC bus terminals of the IGBT modules;
  - calculation of the component values required to set the inverter overcurrent detection of the IGBT driver board;
  - voltage clamping of the sensor signals in order to protect the dSPACE<sup>®</sup> controller.
- Selection of all the sensors used in the drive, their power requirements and interfacing to the controller was presented.
  - The origin of EMI in the drive has been explained and the measures which were taken to isolate, suppress and/or filter are presented in appendix [C.24](#).
  - Modification of the controllers used in the simulation in order to better re-use calculated variables aimed towards the implementation of the control was discussed.

# Chapter 5

## Controller results

This chapter serves as validation of the designed controllers on the physical system. The time domain simulations of the designed controllers in chapter 3 served as verification. Chapter 5, presents the controller test results of the physical system, using the same control references as used in the simulations of chapter 3. The measured response of the actual system is compared to the simulation response. This is done for both the designed controllers. In the context of this project, this comparison is defined as the validation of the designed controllers.

Where applicable, discrepancies between the simulation and measured response of the controller are discussed.

After the controller results have been presented, the vector and V/f controllers are evaluated.

The test results presented in this chapter were obtained with short test runs, due to the excessively high friction losses of the tested PMSMs. The PMSM temperatures were also monitored closely to ensure safe operation.

### 5.1 PMSM drive protection

Before the vector and V/f controllers are tested, the drive protection is tested in order to assure it is functional when required. The order in which the different protection mechanisms are tested follows in a logical sequence: each test relies on the successful operation of the protection mechanisms in the preceding tests.

#### 5.1.1 Inrush current limiting

Figure 5.1, shows the charging of the DC bus capacitors through the current limiting resistors. The final jump in the voltage is due to the switching of the contactor, which bypasses the inrush current limiting resistors. The jump corresponds to a charging of approximately 12% of the total stored capacitor energy. As can be seen, the DC bus capacitors charge safely, without causing

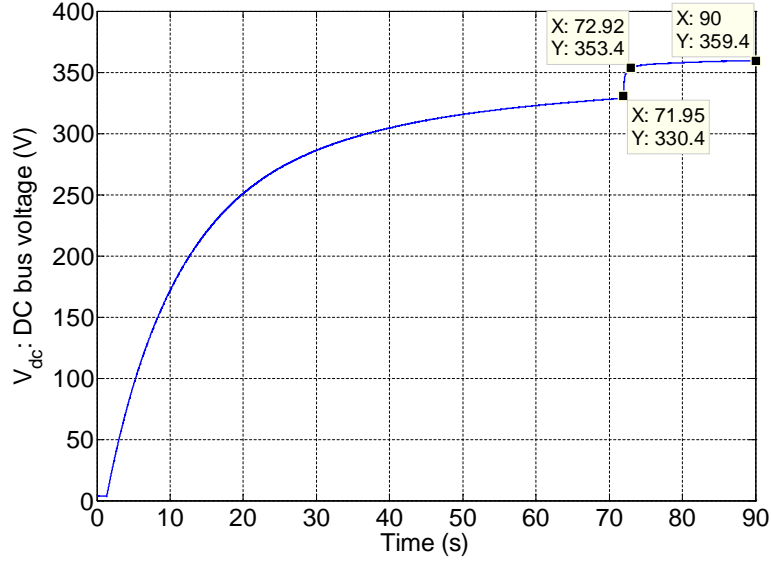


Figure 5.1: Charging of DC bus capacitors with inrush current limiting.

a dangerous voltage overshoot or strenuous loading of the source. The switching time of the contactor ( $\approx 70$  s) exceeds that specified in section 4.3.2.

### 5.1.2 Inverter current limiting

The inverter overcurrent protection (OCP) is tested by generating a current level which is high enough in order to activate the  $V_{ce}$  saturation monitoring of the IGBT driver board. By reducing the DC bus capacitance for this test, the energy in a short circuit pulse is limited. Therefore, even if the current limiting protection should fail to respond to the overcurrent condition, the IGBT inverter is not harmed by the limited energy.

The circuit used for the overcurrent protection is shown in figure 5.2. The DC bus capacitance is chosen as  $C_{DC} = 5 \mu\text{F}$ . The short circuit impedance is limited by an inductor, chosen as  $L_{sc} = 5 \mu\text{H}$ . The DC bus capacitor is charged to 120 V from a laboratory DC voltage source. Switch  $S_1$ , is open-circuited after the capacitors are charged. Hence, without accounting leakage inductance and other losses, the peak inductor current is 120 A. Assuming the over current protection did not respond, the peak inductor current freewheels through the Schottky diode,  $D_s$ , preventing a negative voltage on the DC bus capacitance.

The DC bus capacitance of the test circuit is constructed by placing  $1 \mu\text{F}$ , low ESR and ESL, polypropylene capacitors (WIMA<sup>®</sup> MKP4) in parallel. The inductor is designed with the same T400-26 core used for the rectifier filter designed in section 4.2.4. The same design procedure is used, with different inductor specifications. Core loss is not a problem, due to the low average power of the single pulse. The core saturates only after approximately 300 A, due to the low inductance.



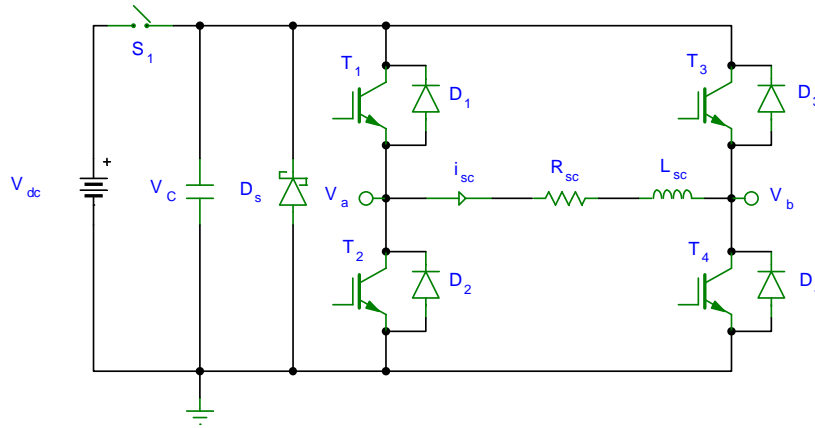


Figure 5.2: Over current protection test circuit.

During the testing procedure, the DC bus capacitance was increased to  $7\ \mu\text{F}$ , the load inductance was lowered to  $3.5\ \mu\text{H}$  and the DC bus voltage was increased to  $125\ \text{V}$ . This was done to increase the short circuit current amplitude in order to trigger the overcurrent protection monitoring. The relationship of the saturation voltage to collector current is highly dependent on temperature. The tests were performed with the heatsink at room temperature, which is why the current had to be higher in order to trigger the saturation voltage monitoring.

The high frequency, large amplitude short circuit current is measured with a Lecroy<sup>®</sup> AP015 ( $50\ \text{A}_{pk}$ ,  $50\ \text{MHz}$ ) current probe by splitting the current with three parallel conductors. The splitting conductors are of equal, medium length. The length is not too short in order to counter a large percentage impedance imbalance in the conductors. The splitting measurement is calibrated by characterizing the ratio of the current in a parallel branch to the main branch current, using two current probes. This is performed at a reduced current value (by lowering the DC bus voltage) which is in range of the current probe used in the main branch. The calibration of the divided current measurement is performed not for high accuracy but to insure that the measurement does not have a large error.

Figure 5.3, shows the overcurrent protection responding to an overcurrent condition. At room temperature, the saturation voltage monitoring detects the overcurrent condition at roughly  $140\ \text{A}$ . The soft turn-off of the IGBT is visible in the gate-emitter voltage. It appears to use a multi-step switch-off approach in order to reduce the chance of latchup in comparison to other turn-off strategies [89]. The gate signals of phase-a were disabled, but not that of phase-b. Once phase-a had turned off, the current could no longer increase in order to trigger the current limiting of phase-b. Phase-b did not shut its gate signals down. It appears that an overcurrent condition has to persist in the other phases, for the drive to be completely shut down by the driver board overcurrent protection.

If a single phase has shut down due to an overcurrent condition from a phase-to-ground fault, the motor current in the other two phases will become unbalanced. The magnitude of the

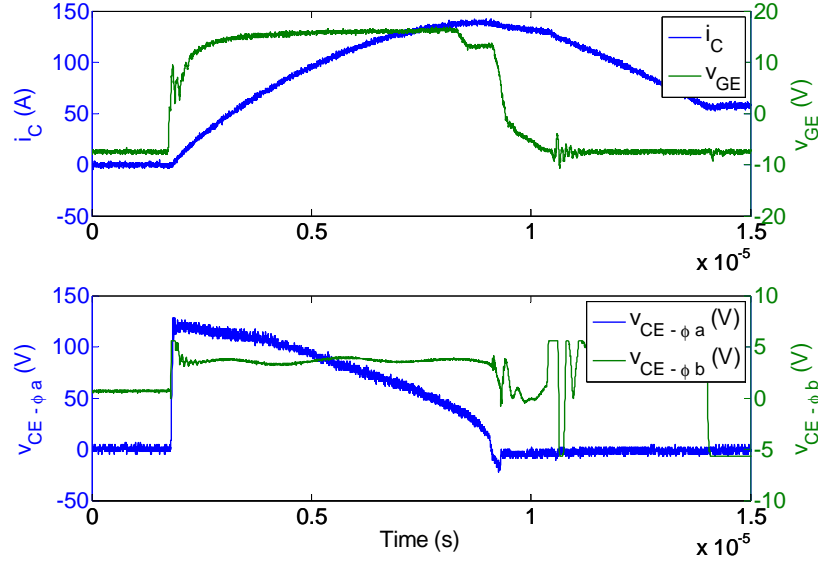


Figure 5.3: Overcurrent protection measurement.

unbalanced current will be increased, but will not necessarily cause the overcurrent protection of the driver board to respond. For this reason, the drive control shuts down the drive at a much lower current value than the IGBT driver board protection, i.e. at a current value of 30 A.

### 5.1.3 Inverter dead-time

In order to assure the top and bottom switches do not conduct simultaneously when the drive is used, the dead-time is measured first. Initially, this is performed by measuring the top and bottom IGBT gate-emitter voltages in an inverter leg, with zero DC bus voltage. When the dead-time is confirmed, the test is repeated at successively higher voltages. Due to the Miller capacitance, the IGBT switching transient takes longer at higher DC bus voltages. The gate-emitter voltage of the top switch is measured with a Lecroy<sup>®</sup> ADP305 differential voltage probe.

Figure 5.4, shows the final result of the dead-time test for a DC bus voltage of 350 V. The signals are measured with a Lecroy<sup>®</sup> WaveRunner 6030A oscilloscope at a sampling rate of  $1 \text{ GSs}^{-1}$ . Instead of measuring the top IGBT gate signal, the bottom collector-emitter voltage is shown. The duty cycle is set such that a positive current is sourced by the inverter leg so that the freewheeling current pulls the collector-emitter voltage low as soon as the top IGBT switches off. Otherwise the collector-emitter voltage would be pulled to ground only after the bottom IGBT had switched on, which would drive the charged parasitic capacitance low. Hence, with this test configuration the top (bottom) switch is clearly off before the bottom (top) switch turns on, with a delay corresponding to the chosen dead-time of  $1 \mu\text{s}$ .

The absent voltage overshoot when the IGBT switches off, is also an indication that the DC bus voltage is clamped effectively by the DC bus snubber capacitors.

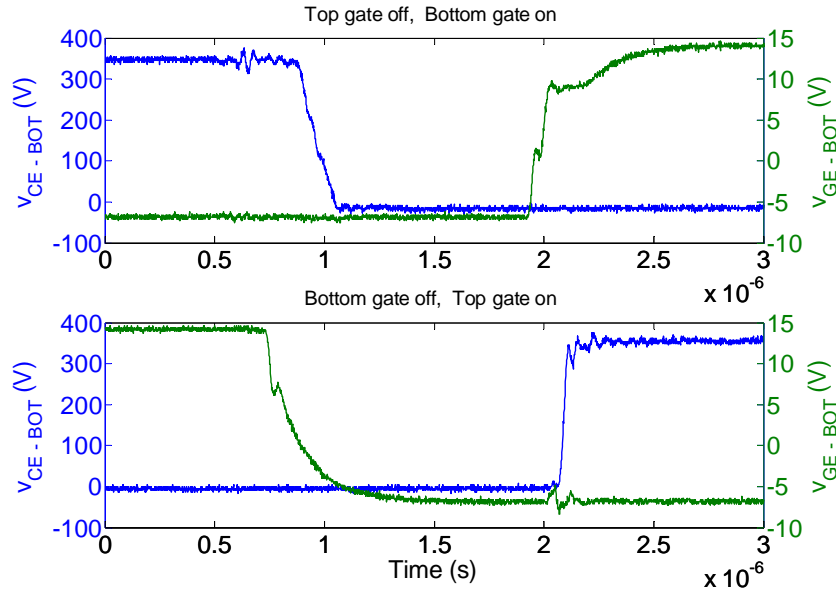


Figure 5.4: Inverter dead-time protection verification.

## 5.2 Vector Control

### 5.2.1 Current control results

The current control step response of the d-axis current is shown in figure 5.5, with a current reference of 4 A. The d-axis current is stepped instead of the q-axis so that the rotor need not be locked to perform this test at zero speed.

The response without dead-time compensation has a much longer rise time than without dead-time compensation. The response with dead-time compensation used the current reference (instead of the measured current) to estimate the zero-current-crossings. The reason for this is that the current zero-crossing estimator is only appropriate for relatively slowly varying sinusoidal currents. If the measured current is used as input for the dead-time compensation and is initialized with zero current, such as with the step response, then the dead-time compensation oscillates around zero, which does not effectively compensate for the dead-time. Thus, the dead-time causes a decrease in the current control gain for low amplitude current references.

The current control proportional gain used ( $K_p = 2$ ), is lower than the designed value, in order to yield a satisfactory response. With the designed gain, the current control exhibited large overshoot. The settling time is still in the same order as designed, i.e. 600  $\mu$ s. The source of the apparent steady state error is due to the rotor being not aligned perfectly at 90°, as assumed in the dq0 transformation of the captured three-phase current.

The frequency characteristic of the current control is determined by chirping the d-axis current reference from 0 Hz to 2500 Hz. The current response is captured by the dSPACE<sup>®</sup> controller. The same system identification method is used to process the captured data as done for the speed control observer in section 3.2.2.3. The chirp signal is applied in increments of 200 Hz.

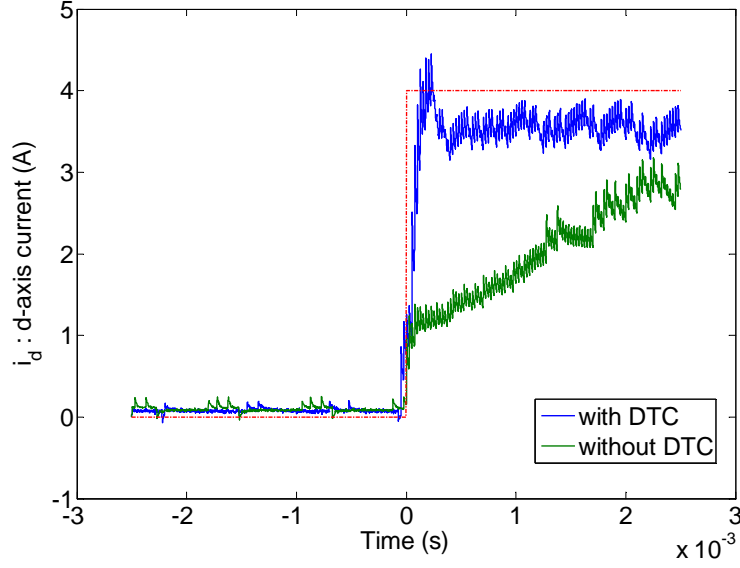


Figure 5.5: Current control step response.

Each frequency sub-range is linearly increased over a period of 20 s. Hence the total bandwidth is swept over a period of 250 s. The reason for this slowly increasing frequency is twofold. Firstly, at 2500 Hz, each sine period has only four measured data points. This is still below the Nyquist rate. Hence, in order to obtain a measured signal with a good enough signal-to-noise ratio (S/N), the system has to be excited at a specific frequency for an extended period. The second reason is that if the reference signal frequency increases too rapidly, the phase of the reference signal may experience a sign reversal. The chirp method is done with the feedback loop closed.

The resulting closed-loop frequency response is as shown in figure 5.6 (compare with figure 3.9). The open-loop transfer characteristic is computed from the closed-loop transfer characteristic with:

$$G_o = \frac{G_{cl}}{1 - G_{cl}} \quad (5.1)$$

The resulting open-loop characteristic is as shown in figure 5.7 (compare with figure 3.8). In order to obtain the desired cross-over frequency of 1 kHz, the proportional gain had to be lowered further to  $K_p = 1.8$ . The designed integral gain,  $K_i = 990$ , was used. The desired phase margin of  $60^\circ$  is obtained. Due to the significant peaking in the gain response, the current control loop bandwidth is artificially increased to 2.3 kHz. The peaking is also the cause of the decreased gain margin of 6.65 dB, compared to the gain margin of 15 dB predicted in the design.

The decrease in current control gain due to the dead-time as noted in the current control step response, has been circumvented by performing the system identification with a chirp signal with a DC bias of 5 A. The chirp signal amplitude was set to 2 A, which also helped to improve the S/N of the measured current response in the presence of a current ripple of  $0.5 \text{ A}_{pp}$  due to the PWM switching, as can be observed in figure 5.5.

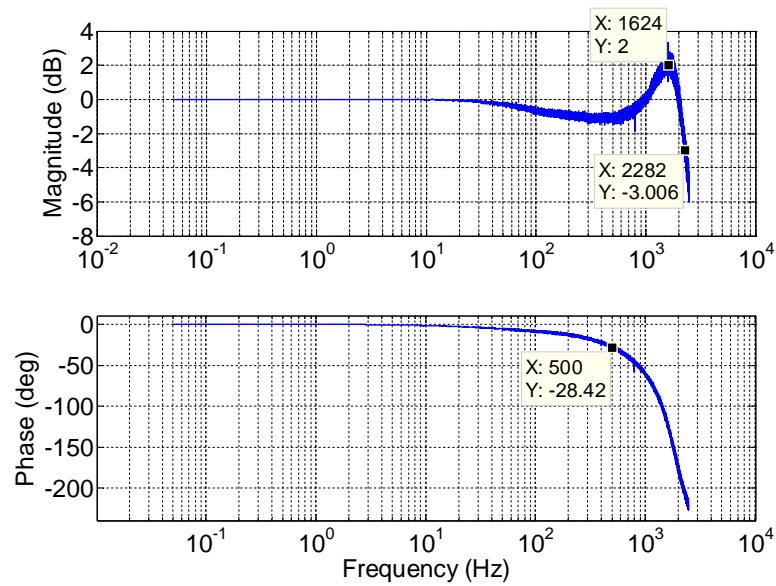


Figure 5.6: Bode diagram of closed-loop current control closed-loop transfer characteristic.

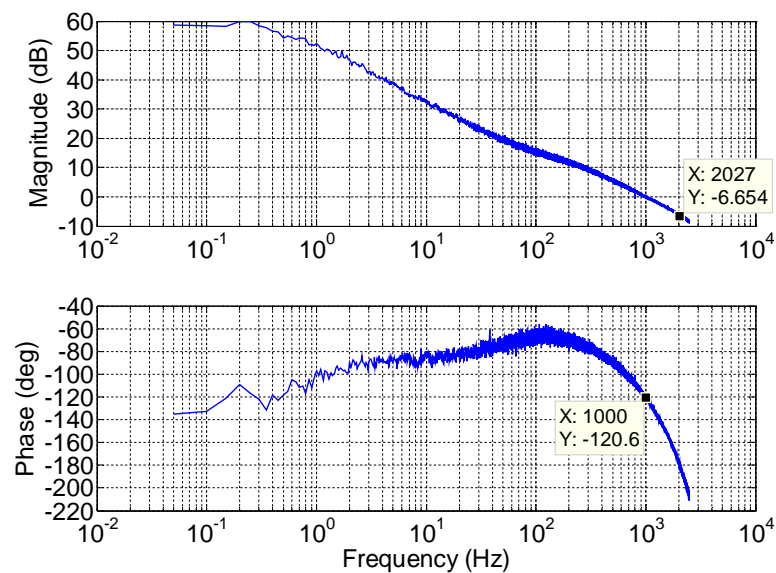


Figure 5.7: Bode diagram of closed-loop current control open-loop transfer characteristic.

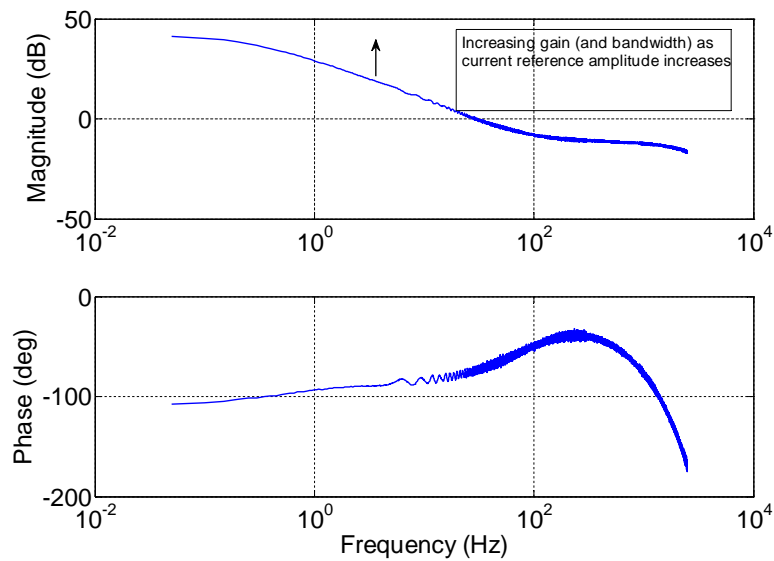


Figure 5.8: Reduced gain and bandwidth of current control open-loop transfer characteristic, due to dead-time effect.

The loop gain with a zero current bias, is much smaller and the phase delay much larger, due to the dead-time effect, as shown in figure 5.8. With dead-time compensation enabled, the chirp frequency has to be ramped up even slower in order for the zero-current-crossing estimator of the dead-time compensator to track the measured signal. Thus, although the current control has a large bandwidth, this bandwidth is applicable only for a small-signal disturbance. For a large-signal reference, the bandwidth is only usable to the extent that the dead-time compensation can sufficiently counter the loss in gain. This can be performed by limiting the rate of change of the reference speed. Therefore, it has been found that the dead-time not only causes unwanted current harmonics which increase losses, but it also adversely affects the current control stability.

The vector controller can still function without dead-time compensation, because the outer speed control loop simply generates a larger torque producing current reference in order to compensate for the decreased current gain due to the dead-time.

## 5.2.2 Speed control results

### 5.2.2.1 Speed control ripple

The designed speed controller results displayed a much higher speed ripple than what could be attributed to the quantization noise in the measured position signal. The cause of this speed ripple was investigated and it was found that the rotor experienced a variable frictional load. The result of applying a small, but constant driving torque to the rotor is shown in figure 5.9. The frictional load occurs at a specific angle. Hence, the speed control will experience a periodic torque load disturbance. For a certain rotational speed range, the torque disturbance frequency is within the speed controller bandwidth. For this bandwidth the speed controller tries to

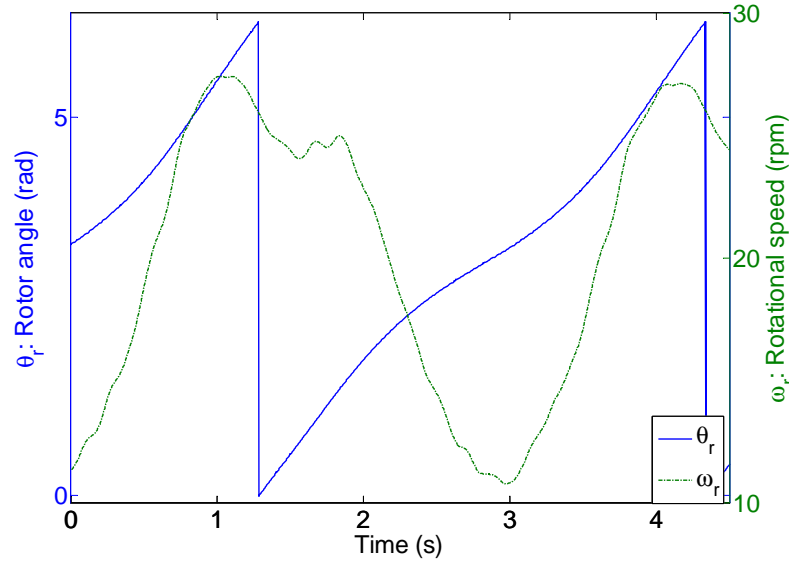


Figure 5.9: Rotor response to small motoring torque (0.07 Nm).

reject the speed ripple due to the torque disturbance and causes motor current harmonics. The speed ripple combined with the resulting current harmonics, cause a jitter in the input of the zero-current-crossing estimator of the dead-time compensator. The resulting lack of dead-time compensation increases the current harmonics even more.

The current control results of the previous section showed the decreased current control bandwidth in the case of non-functioning dead-time compensation. Since the current reference of the speed controller cannot be properly actuated, the speed controller in turn cannot properly compensate for the speed ripple due to the torque disturbance. The speed ripple can be rejected by the speed controller only at very low rotational speed. The measured speed and current harmonics, are compared for the designed speed control gain and for a reduced gain ( $K_p = 0.5$ ,  $K_i = 10$ ), as shown in figure 5.10. The test is performed at a rotational speed of 8.3 Hz. The x-axis for the two plots are biased with a small offset, so that the spectral lines for the two cases are distinguishable. The speed harmonics due to the torque disturbance are only slightly improved with the high gain speed controller, but with increased current harmonics.

At higher rotational speed, the speed ripple is reduced because the pulsating torque is filtered by the rotor inertia, resulting in improved current harmonics and dead-time compensation. The control can reject the effect of the torque disturbance on the current harmonics by considerably reducing the speed controller gain as shown in figure 5.10. For the low and intermediate speed range, a reduced speed control gain is a serious option, because the controller is not able to reject the *periodic* torque disturbance in any case.

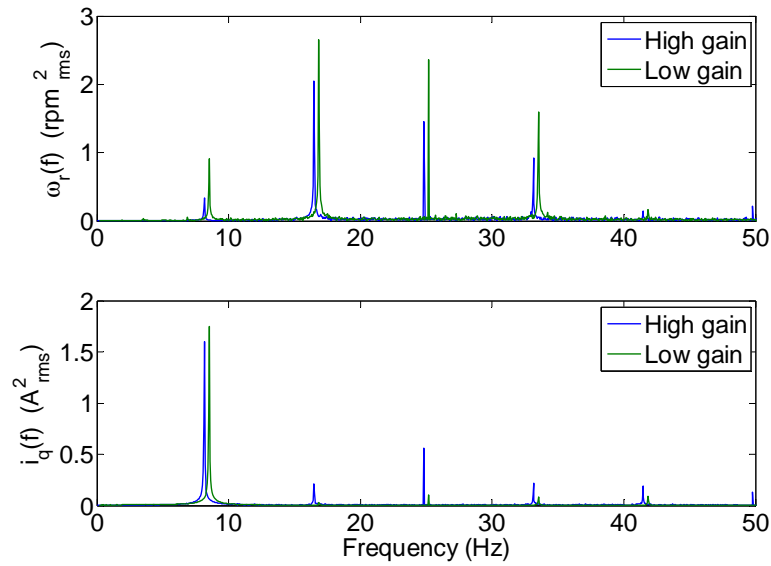


Figure 5.10: Spectral comparison of speed controller results with high (designed) and low gain.

### 5.2.2.2 Speed control ramp response

The response of the vector controller for the designed gain, to a speed ramp up to 20 krpm with a 1 N.m torque load step is shown in figure 5.11. The speed error due to the torque load step compares favourably to that predicted by the simulation (compare with figure 3.42). The mean value of  $i_d$  is centred on 0 A, which indicates that the current measurement decoupling required for high-speed, operated as intended.

The main difference in the actual response compared to the simulation is in the current ripple. The simulation was performed with a PWM carrier frequency of 50 kHz. As explained in section 4.2.3, the implemented switching frequency was 20 kHz. Note how the current ripple increases as the speed increases. The actual current ripple obtained has been confirmed by repeating the simulation included in appendix C.10, with a switching frequency of 20 kHz, in order to verify that the switching frequency is the cause of the difference.

### 5.2.2.3 Speed control frequency response

The predicted speed control bandwidth for the designed gain is validated by performing system identification on the speed control loop. This is done by performing a frequency sweep on the reference speed. The test is performed with the motor operating at 2 krpm, in order for the motor to operate in a region free of the speed ripple which causes the dead-time compensation to become ineffective. The rate at which the frequency is swept determines if the dead-time compensation can track the current zero-crossings. Therefore, the speed control bandwidth is also only applicable to a small signal disturbance as was the case for the current control bandwidth.



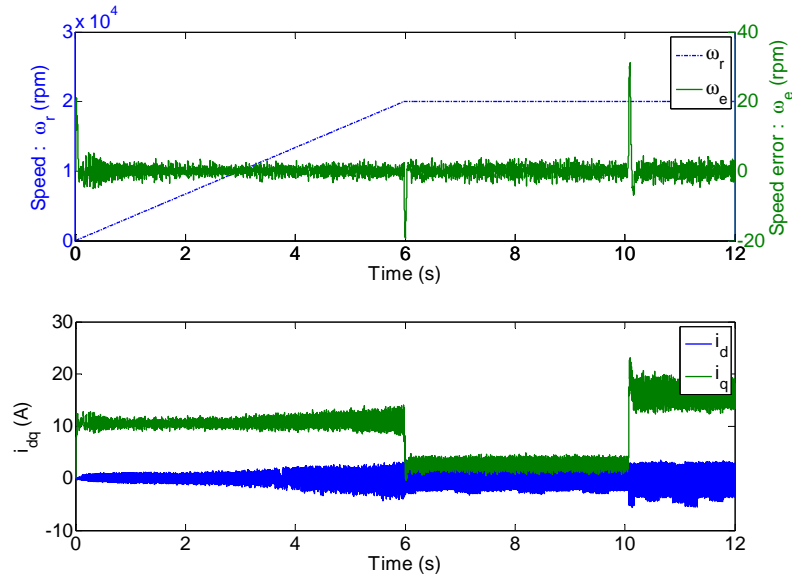


Figure 5.11: Speed ramp response of vector control with 1 N.m torque load step.

The frequency transfer characteristic of the closed-loop speed controller with the designed gain is as shown in figure 5.12. The control bandwidth is larger than designed (compare with figure 3.30). This indicates that the parameters in the implemented observer better matches the actual system than the assumed transfer function of the observer (which was conservatively determined by the degradation factor of  $\alpha = 0.65$ ). Note the presence of a zero in the speed control loop in the vicinity of 21 Hz. The Bode diagram of the speed controller with reduced gain ( $K_p = 0.5$ ,  $K_i = 10$ ) is shown in figure 5.13.

## 5.3 V/f Control

### 5.3.1 Speed control ramp response

The speed control ramp response, with test conditions similar to the ramp response of the vector controller is as shown in figure 5.14. The stability of the V/f controller is confirmed by the 1 N.m torque load step. The dq currents are only calculated in order to verify the control response, but were not used for control.

The control did not perform entirely as desired. A speed error of 330 rpm resulted for the torque load step, compared to the simulated speed error of 150 rpm. The high efficiency control loop operated as desired at no-load, but experienced a d-axis current bias after the torque load step. The bias is similar to the case without measured current decoupling (compare with figure 3.70). This suggests further investigation of the current decoupling method used to compensate measurement delays.

The startup current of nearly 30 A, is due to an increased boost voltage of 3 V, which was

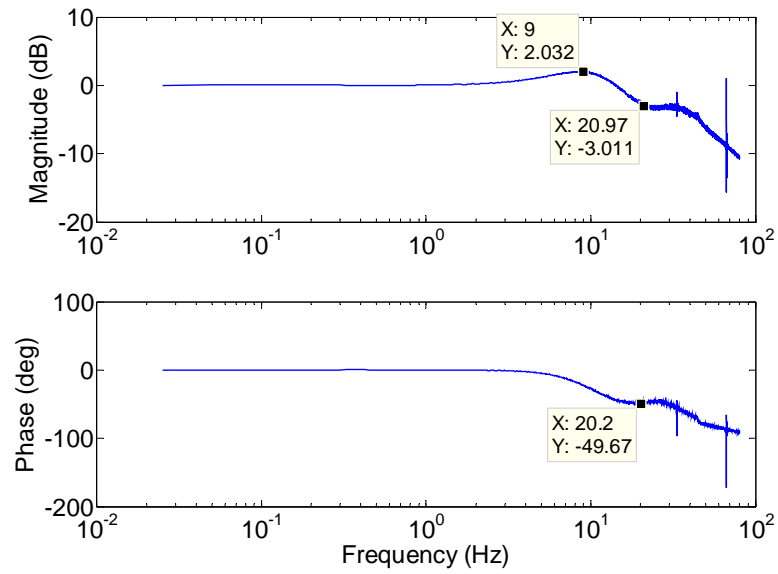


Figure 5.12: Bode diagram of closed-loop speed controller with designed gain.

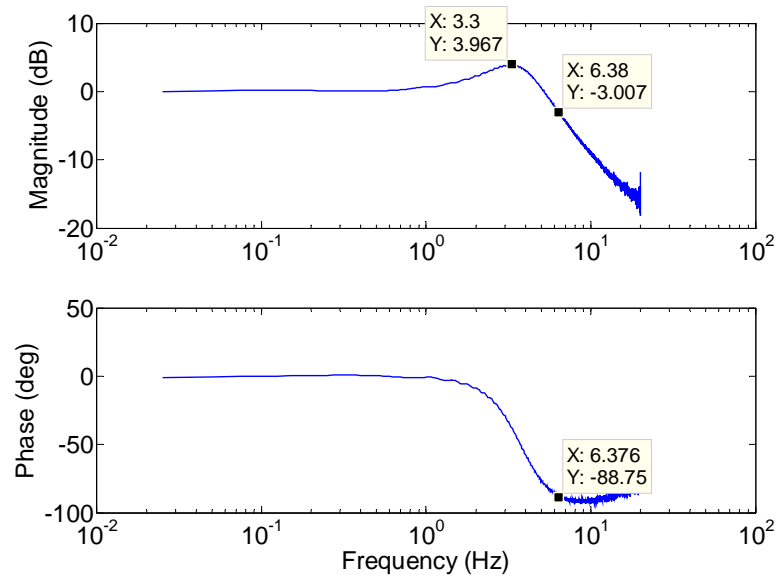


Figure 5.13: Bode diagram of speed control with reduced gain.

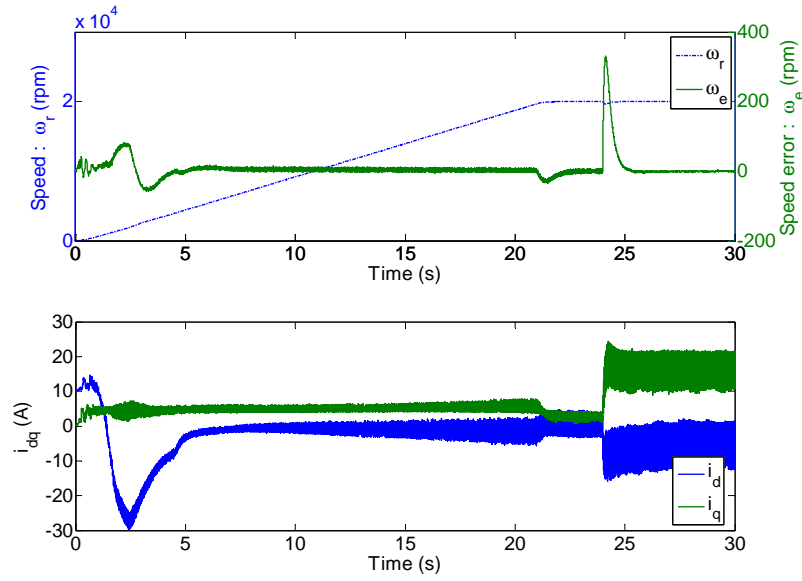


Figure 5.14: Speed ramp response of V/f control with 1 N.m torque load step.

required for reliable startup under the increased disturbance of the switching current ripple. Also to provide reliable startup, the boost voltage cut-out frequency was increased from the designed 25 Hz to 32 Hz.

The theoretically calculated dead-time compensation was used at low speed. Without this term the V/f controller current was insufficient to start the PMSM. It was found that at higher speed, the theoretically calculated dead-time compensation caused severe current distortion and resulted in a destabilizing limit cycle. The limit cycle was caused by the inability of the dead-time compensator's zero-current-crossing estimator, to estimate the zero-current-crossings properly (probably due to the increased disturbance of the current switching ripple). In order to solve this problem, the dead-time compensation was gradually reduced to only half its theoretical value at approximately 3 krpm, which was performed similar to the boost voltage enable logic.

The most significant difference in the designed and actual V/f controller was the stabilization gain required to stabilize the actual system. The compensator gain used was 40. The designed stabilization gain was  $\approx 17$ . In simulation, the stabilizing perturbation for a gain of 40 overshoots too much and is unable to stabilize the system. The strong dependence on the rotor inertia for a chosen stabilizing gain as in equation 3.112, together with the large parametric error index of the rotor inertia as in table 3.1, suggest that the difference in stabilization gain may be due to an incorrect rotor inertia used in the design.

### 5.3.2 Speed control frequency response

The frequency response for the speed control loop of the V/f controller is shown in figure 5.15, from which a bandwidth of approximately 4 Hz can be observed. Therefore, the vector controller, even for the reduced speed control gain which yielded satisfactory current harmonics, has a higher

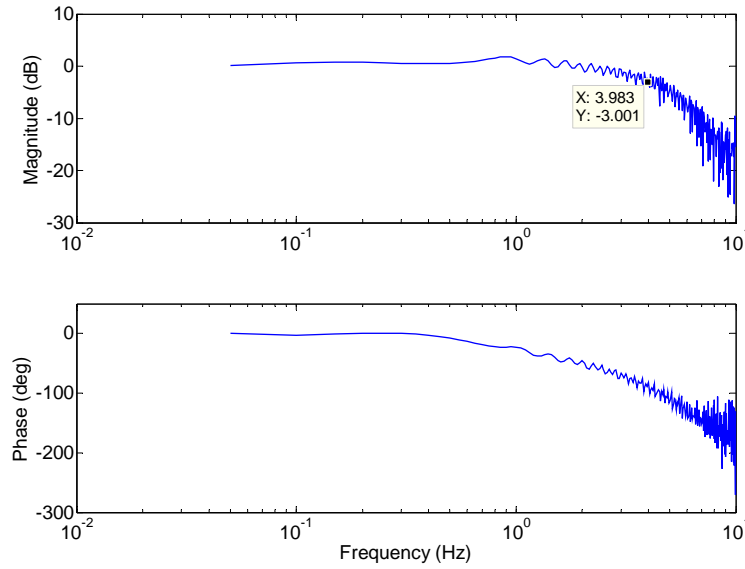


Figure 5.15: Bode diagram of V/f speed control.

speed control bandwidth. The chirp reference was added to the V/f controller *after* the speed reference generator which would have limited the chirp reference bandwidth.

## 5.4 Control efficiency

A comparison between the two controllers' efficiency, as a function of rotational speed, is as shown in figure 5.16. The test is performed by loading the motoring PMSM with 50 % rated load torque (0.637 N.m) and ramping the speed from 3 krpm to 20 krpm. The efficiency is computed by calculating the input power as  $p_i = v_{dc}^m i_{dc}^m$ , and the output power as  $p_o = v_{dc}^g i_{dc}^g$ , where superscripts  $m$  and  $g$  denote the motor and generator variables, respectively. The efficiency is calculated as:

$$\eta(\omega_r) = \frac{p_o(\omega_r)}{p_i(\omega_r)} \times 100\%$$

Since the input and output power is calculated with the DC-link variables, the resulting efficiency calculation includes the inverter losses.

The relatively low efficiency is due to the high frictional losses. At low speed, the total input power is dominated by the frictional losses, whilst as the speed increases, the efficiency improves. This is because the total power increases as the speed increases ( $P = T_e \omega_r$ ) such that the relatively constant frictional losses allocates less of the total input power. The obtained efficiency should only be used for comparison in a qualitative sense, because the losses of the high-speed PMSM in this project are not representative of a typical high-speed motor. What is important to note is that the V/f control obtains a lower efficiency than the vector controller up to about 4 krpm, 13 % of the rated speed, after which, the two controllers yield essentially the same efficiency. This is despite the fact that the V/f controller's high efficiency loop did not operate

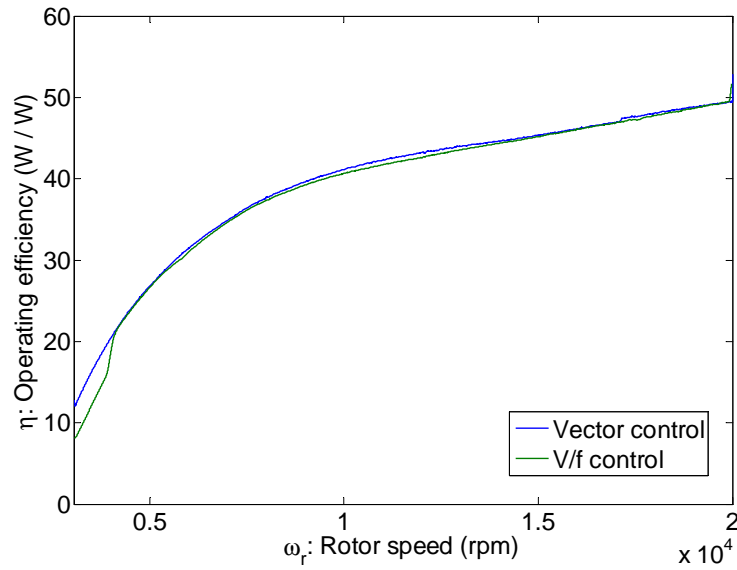


Figure 5.16: Efficiency comparison between vector and V/f control with 50 % rated load torque.

optimally. With further work on the V/f controller the cause of the malfunctioning high efficiency loop can be resolved and the V/f controller may be assumed to be just as efficient as the vector controller for speeds greater than 15 % of rated speed.

## 5.5 Control evaluation

Based on the experience gained from implementing the vector and V/f control and the measurement results obtained, the two controllers are compared. The comparison is done with respect to the following criteria: efficiency, speed control bandwidth, the difference in implementation complexity and stability.

From the results of section 5.4, the two controllers' efficiency is comparable for an operating speed range above 15 % of rated speed.

The main difference in the two controllers is in the startup characteristic and speed control bandwidth. Due to the high startup current of the V/f controller, it cannot start with full load. The load torque characteristic has to be such that the torque load increases as the speed increases. Even though it has been shown that V/f control can withstand a torque load step, an actual application faces the mechanical problem of how a constant load should be applied after startup. Hence, the V/f controller is suited for fan and pump applications.

The vector controller displayed a much higher speed control bandwidth, even for a reduced speed control gain (approximately  $5\times$  less than the designed gain). The vector controller can reliably startup even with a rated load.

The basic V/f controller requires a less powerful control processor than the vector controller. With all the extra control loops required to improve the V/f controller performance and in

order to make its performance more comparable to that of the vector controller, it requires a processor which is comparable (if not even more powerful) than that required for the vector controller. In terms of complexity, implementation time and fine-tuning, the V/f controller is much more difficult and time consuming to implement correctly. Its sensitivity towards the inverter non-idealities makes it extremely difficult to implement. For example, the standard dead-time compensation had to be modified so that it is dependent on rotational speed. This dependency is not predicted by the analytical models of the dead-time effect.

With a position sensor, the vector controller is much easier to understand, which decreases implementation time and fine-tuning. Its control robustness cannot be overemphasized. The vector controller is much less influenced by the inverter non-idealities, reducing the development time to obtain a relatively good performing controller. It can operate without dead-time compensation, in which case the dead-time effect increases motor current harmonics. The current control loop automatically rejects DC bus voltage disturbances.

For the V/f controller, to obtain comparable DC bus disturbance rejection (especially due to the ripple caused by the rectifier), a novel current harmonic suppression loop was developed. Although the fundamental current of the V/f controller cannot be controlled, by representing the V/f controller in a vector formulation it became apparent that a current control loop, controlling the non-fundamental current component could be realized.

For those PMSM drive applications, in which the cost of the position sensor is a fraction of the total cost of the drive, the vector controller is recommended. Low power applications, which are cost sensitive should carefully consider the V/f controller, since the cost of the position sensor is not the only factor to be considered. Although not implemented in this dissertation, the sensorless vector controller, using Hall-effect position sensors at startup, is a good alternative to V/f control for position sensorless applications.

## 5.6 Summary

The tests and results presented in this chapter can be summarized as follows:

- The drive protection mechanisms were tested methodically, before operating the drive in order to test the two controllers safely.
- The step response and frequency characteristic of the vector controller current and speed loops were presented. In general the vector controller compared favourably compared to the simulation of the designed controller.
- The modification of the current control loop gain, in order to obtain the chosen cross-over frequency has also been shown. The decreased current control bandwidth due to the dead-time has been shown. Future designs should investigate the influence on stability due to the temporarily decreased bandwidth during a large signal transient.

- A discrepancy in the vector controller speed control loop has been identified, i.e. the speed ripple due to the variable frictional load. It is suggested that the speed controller should make use of gain scheduling: use a lower gain at low speed, so that the motor current does not become excessively distorted. The designed speed control gain can be used at a rotational speed greater than approximately 5 krpm.
- With the designed speed control gain, the vector controller had stable operation, with a small speed error with under a 1 N.m load torque step.
- The step response and frequency characteristic of the V/f controller were presented. The motor had stable operation and did not lose synchronism even with a 1 N.m load torque step. The speed error was significantly larger than that predicted by simulation.
- The high efficiency loop of the V/f controller was effective at speeds greater than approximately 15 %, but did not operate optimally at full load. The implementation of the high-efficiency loop requires further work.
- Assuming the fault with the high-efficiency loop has been resolved, V/f and vector control have similar efficiencies, especially at high-speed.
- It was shown that the V/f controller speed control bandwidth is much smaller than the vector controller's, even for a vector speed controller with a relatively small gain.
- Given the test results and experience gained during the implementation, the vector and V/f controllers were compared, which will be useful for selecting a controller given a certain application.
- Despite the initial complexity of the vector control, its implementation and fine-tuning required less time than that of the V/f controller. The vector control is more robust than the V/f control.
- The operational principle of the V/f controller at first is much simpler, but the loops required to improve its efficiency, disturbance rejection and reliable startup is much more time consuming. Fine-tuning the control parameters of the V/f controller also took longer, due to its sensitivity to inverter non-idealities.





## Chapter 6

# Conclusion and recommendations

### 6.1 Conclusions

#### 6.1.1 Vector control

The current and speed control loops of the vector controller were designed analytically. The design was verified with detail simulations of the controller, inverter and PMSM models. The measured ramp response and frequency characterization results presented in chapter 5 compared favourably to that predicted by the simulations in chapter 3.

#### 6.1.2 V/f control

The V/f control fine-tuning was more problematic than for the vector controller due to its increased sensitivity to parameter variations and disturbances. The main discrepancies between the designed and actual controller, was the requirement of an increased stabilization gain and the dead-time compensation which had to gradually decrease as a function of the rotational speed. After these modifications, the V/f control operated as desired, e.g. it could stabilize even after a 1 N.m torque load step.

The existence of these discrepancies, between the designed and actual controller, emphasizes the importance of validation. No design is perfect, because there are always some unaccounted effects during the design. Hence, validation actually forms part of an iterative design and implementation process. Verification ensures that the calculations have been performed correctly given the models representing the actual system. Validation rectifies differences between the models used during the design and the actual system.

#### 6.1.3 Design methodology

The design process followed, yielded sufficiently functional controllers, although some flaws in the process existed. For example, the inverter thermal verification which caused a change of the

chosen switching frequency from 50 kHz to 20 kHz, should have been performed before all of the motor control simulations were performed for a switching frequency of 50 kHz. The resulting high current ripple noted in the results combined with the relatively low IGBT junction temperature at a rated PMSM current of 17 A, suggest that the newly chosen switching frequency is perhaps a bit too low and cleaner measurement results could have been obtained at a higher switching frequency. Instead of aiming for an efficient, continuously operable inverter, the focus should have been smoother measurements due to a smaller current ripple. The results would then be less ambiguous, e.g. is the current ripple band around  $i_q$  in figure 5.14, truly due to the switching ripple or in part due to peaking in the current control loop? IGBTs better suited to the current range of the application, which has lower switching losses could have been chosen. During the selection of the IGBTs, there was uncertainty in the intended PMSM operating current and the IGBT with the higher current rating was chosen.

## 6.2 Recommendations

This section states recommendations for future work related to theoretical development and experiments which should be performed to clarify some uncertainties which arose during the course of this dissertation.

### 6.2.1 Sensorless vector control

In order to be fair in the comparison between vector and V/f control, sensorless vector control should also be developed and compared to vector and V/f control.

### 6.2.2 Unification of V/f and sensorless vector control

The main difference between vector and V/f control is that one uses a position sensor to determine the alignment of the control currents, whilst the other allows the current transients to largely settle by itself. Sensorless vector control estimates the rotor position with an observer and uses the estimated rotor angular position in the vector control of the currents.

With the development of the current harmonic suppression loop for the V/f controller, which damps the non-fundamental currents, the question arose: why not control the fundamental also? Two elements are required to do so, namely a reference current and estimation of the rotor angle so that the reference currents may be transformed back to the stationary reference frame. In the V/f controller, after the high-efficiency loop has settled, the steady state condition is equal to that of the vector controller. When this condition is satisfied, it should be possible to estimate the torque angle,  $\hat{\delta}_r$ . If the torque angle can be estimated, then the rotor angle is simply:  $\hat{\theta}_r = \theta_e - \hat{\delta}_r$  (see figure 3.48). Given that the V/f controller is still operating and the estimation in the background, then the dq-axis current can be obtained with the aid of the estimated rotor angle. From the estimated rotor angle, the speed can be estimated. With the estimated speed,

$\hat{\omega}_r$ , and reference speed,  $\omega_e$ , a current reference can be generated, similar to the vector speed control loop.

After this waving in the air, the reader may wonder: “Why is this important?” The reason is that the description given is close to what actually occurs in a sensorless vector controller (e.g. [4]). The motor is started with some open-loop control technique, with an estimator running in the background. After the state variables have settled, the control is switched over to the sensorless vector controller. In effect, there are two controllers executing simultaneously in the same processor. Since the PMSM reaches a unique state vector due to the high-efficiency loop and a current control loop is already in place (due to current harmonic suppression loop), then why not try to add a “correction term” to the inverter angle and slowly inject a fundamental current component to the current harmonic suppression loop reference? The aim of this recommendation is so that many of the already existing control components in the V/f control loop can be reused (more efficient use of the processor), and allowing for a soft transposition (transient free) from the one control type to the other in a sensorless vector control drive.

### 6.2.3 Mechanical vibration and bearing losses

The PMSM losses were mainly due to the mechanical friction of the bearings as determined from the model parameter identification. It is suspected that this is due to misalignment of the bearings. During initial development, the motors also experienced a rapid increase in vibration above  $\approx 20$  krpm, signifying a mechanical resonance of the motor housing. After validation of the rotor mechanical design up to 30 krpm as presented in [7], it was decided not to operate the PMSM above 20 krpm, until its source could be identified and resolved. The source of the mechanical vibration, which excites the resonant structure, may have been caused by the variable frictional load which caused the observed speed ripple. The variable frictional load was discussed in section 5.2.2.1.

The control used during the mechanical validation was a rudimentary form of the V/f controller which was eventually implemented and tested in this dissertation. In particular, the V/f control used a *constant* nominal value of the DC bus voltage in order to obtain a duty cycle reference. Also, a filter inductor between the rectifier and DC bus capacitors had not been added to the system, resulting in a larger DC bus voltage ripple during the mechanical validation<sup>1</sup>. The effect of lacking DC bus voltage disturbance rejection on the control, has been investigated in section 3.4.1.4 (especially refer to figure 3.86). Hence, another possible source of the vibration in the problematic frequency range has been identified. The sharp increase in the resonant frequency near 20 krpm was not noticed during testing of the eventual controllers, which both had DC bus voltage disturbance rejection.

Therefore, it is recommended that the mechanical vibration of the PMSM housing should be

---

<sup>1</sup>During the mechanical validation, the DC bus ripple current was not dangerously high, because the PMSMs were run essentially without a load. Yet the DC bus voltage ripple was relatively high, compared to after the addition of the filter inductor.

quantified using accelerometers, with the DC bus voltage disturbance rejection enabled and disabled, in order to verify if this is indeed the source of the vibration.

Irrespective of the outcome of the proposed test, due to the excessively high frictional losses of the bearings, which should be apparent to any layperson by a simple turn of the rotor by hand, it is recommended that the current bearings be replaced with self-aligning bearings. Self-aligning bearings have very low friction and due to the self-aligning capability, the chances of increased friction due to improper alignment of the housing end-plate is reduced (sensitivity on the load torque, given a slight tightening or loosening on an end plate bolt has been observed during testing). For the rotor diameter, the highest speed self-alignment bearing is 20 krpm. The functionality of self-alignment requires more space on the outer diameter, which explains the reduced speed rating for the same inner diameter. Due to a larger outer diameter, another set of end plates need to be designed. The larger bearings also make it impossible for the placement of the infrared sensor at the same location. This can be solved by noting that the highest losses of the current system are the bearings, hence re-orientation of the infrared sensor to sense near the bearings is a logical alternative.

## 6.2.4 Drive recommendations

### 6.2.4.1 Sensor and interface board redesign

The redesign of the sensor and interface boards is recommended. The sensor board should be redesigned, making use of *isolated* voltage measurement, since the protection of the dSPACE<sup>®</sup> controller warrants top priority due to the cost of the controller.

The RTD sensor output should also be isolated from dSPACE<sup>®</sup> controller for the same safety reason. Some of the RTDs are embedded inside the stator winding and failure of the winding and RTD isolation could result in a disaster. Therefore, it is recommended to provide a separate interface board, with an isolated supply and isolated output.

Many ground loops exist on the current sensor and interface boards. This is mainly due to the ground of the different controller cards inside the dSPACE<sup>®</sup> system sharing a common ground on the interface board. The true “star point” connection is already made *inside* the dSPACE<sup>®</sup> controller. The erroneous measurements made due to the ground loops could lead to false conclusions of discovered anomalies in the control. Thus, this is a second reason for the redesign of the sensor and interface boards from a signal integrity point of view.

### 6.2.4.2 Brake circuit

The risk of an overvoltage on the DC bus has been addressed by limiting the PMSM deceleration in the control and also by commanding a drive shutdown in the case of an overvoltage. For future work, researchers who are unaware of these safety mechanisms may unawares circumvent these safety mechanisms. Hence, it is recommended to implement a brake circuit to limit the DC bus

voltage to a threshold voltage. Preferably, the brake circuit control should operate independent of the PMSM control.

#### **6.2.4.3 Three-phase transformer**

The three single-phase transformers used for isolation has a power handling capability which far exceeds the requirement. Since energy circulates back into the DC bus for this experimental drive setup, the power requirement of the isolation transformer may be reduced. Hence, it is recommended to replace the three single-phase transformers, with a single three-phase transformer with a rating of 3 kVA. If the bearing losses in the system can be solved, a transformer with an even lower rating may be selected.

#### **6.2.4.4 Influence of PWM switching frequency on total drive losses**

The uncertainty regarding the choice of the PWM switching frequency can be clarified by inspecting the influence of the switching frequency on the total drive losses. By increasing the PWM switching frequency, the inverter losses are increased, but the motor losses are decreased due to a smaller current ripple.

Suppose a local minimum in the total drive losses as a function of the switching frequency exist. With the efficiency measurement setup for the efficiency measurement presented in section 5.4, this hypothesis can be tested empirically.

### **6.3 Closure**

The aim of this project was to implement and evaluate V/f and vector control on high-speed PMSM drives. The design of the controllers was presented thoroughly. Issues surrounding the implementation of the control algorithms on the real-time controller and design of the drive power electronics were also presented. With either controller, the motoring PMSM could be spun up to 20 krpm and could withstand a torque load step of 1 N.m produced by the second PMSM which is controlled as a generator. The two control strategies were evaluated separately, i.e. tests on the actual system were performed and compared to the response predicted by simulation. Based on the control results, the characteristics of the two controllers were contrasted.



# References

- [1] B. K. Bose, *Modern Power Electronics and AC Drives*. Prentice Hall, 2002.
- [2] P. Pillay and R. Krishnan, “Application characteristics of permanent magnet synchronous and brushless DC motors for servo drives,” *IEEE Transactions on Industry Applications*, vol. 27, pp. 986–996, Sep./Oct. 1991.
- [3] T. D. Batzel, *Electric propulsion using the permanent magnet synchronous motor without rotor position transducers*. PhD thesis, The Pennsylvania State University, 2000.
- [4] P. Kshirsagar, R. Burgos, A. Lidozzi, J. Jang, F. Wang, D. Boroyevich, and S.-K. Sul, “Implementation and sensorless vector-control design and tuning strategy for SMPM machines in fan-type applications,” in *Conference Record of the 2006 IEEE Industry Applications Conference. 41st IAS Annual Meeting*, vol. 4, pp. 2062–2069, Oct. 2006.
- [5] M. Zordan, P. Vas, M. Rashed, C. Ng, S. Bolognani, and M. Zigliotto, “Field-weakening in high-performance PMSM drives,” *COMPEL: The International Journal for Computation and Mathematics in Electrical and Electronic Engineering*, vol. 21, no. 2, pp. 338–354, 2002.
- [6] “RM22 series non-contact rotary encoders datasheet,” tech. rep., RLS®, 2009.
- [7] C. J. G. Ranft, “Stress in a multi-ring speed rotor of a permanent magnet synchronous machine,” tech. rep., North West University, Potchefstroom campus, 2008.
- [8] P. Pillay and P. Freere, “Literature survey of permanent magnet AC motors and drives,” in *Conference Record of the 1989 IEEE Industry Applications Society Annual Meeting*, pp. 74–84, Oct. 1989.
- [9] R. Monajemy, *Control Strategies and Parameter Compensation for Permanent Magnet Synchronous Motor Drives*. PhD thesis, Virginia Polytechnic Institute and State University, 2000.
- [10] P. Pillay and R. Krishnan, “Modeling, simulation, and analysis of permanent-magnet motor drives, part i: The permanent-magnet synchronous motor drive,” *IEEE Transactions on Industry Applications*, vol. 25, pp. 265–273, Mar./Apr. 1989.

- 
- [11] T. Batzel and K. Lee, "Electric propulsion with the sensorless permanent magnet synchronous motor: Model and approach," *IEEE Transaction on Energy Conversion*, vol. 20, pp. 818–825, Sep. 2005.
  - [12] Y. Dai, L. Song, and S. Cui, "Development of PMSM drives for hybrid electric car applications," *IEEE Transactions on Magnetics*, vol. 43, pp. 434–437, Jan. 2007.
  - [13] S. Chi and L. Xu, "Development of sensorless vector control for a PMSM running up to 60,000 rpm," in *2005 IEEE International Conference on Electric Machines and Drives*, pp. 834–839, May 2005.
  - [14] A. Lidozzi, L. Solero, F. Crescimbin, and A. D. Napoli, "SVM PMSM drive with low resolution hall-effect sensors," *IEEE Transactions on Power Electronics*, vol. 22, pp. 282–290, Jan. 2007.
  - [15] B. Bae, S.-K. Sul, J. Kwon, and J. Byeon, "Implementation of sensorless vector control for super-high-speed PMSM of turbo-compressor," *IEEE Transactions on Industry Applications*, vol. 39, pp. 811–818, May/Jun. 2003.
  - [16] A. de Klerk, "Drive implementation of a permanent magnet synchronous motor," Master's thesis, The School of Electrical, Electronic and Computer Engineering, North-West University, 2007.
  - [17] S. Myburgh, "The development of a fully suspended AMB system for a high-speed flywheel application," Master's thesis, The School of Electrical, Electronic and Computer Engineering, North-West University, 2007.
  - [18] M. Hadziselimovic, G. Stumberger, B. Stumberger, and I. Zagradisnik, "Magnetically nonlinear dynamic model of synchronous motor with permanent magnets," *Journal of Magnetism and Magnetic Materials*, vol. 316, pp. 257–260, Sep. 2007.
  - [19] Z. Jing, C. Yu, and G. Chen, "Complex dynamics in a permanent-magnet synchronous motor model," *Journal of Chaos, Solitons and Fractals*, vol. 22, pp. 831–848, Nov. 2004.
  - [20] S. B. Ozturk, "Modelling, simulation and analysis of low-cost direct torque control of PMSM using hall-effect sensors," Master's thesis, Texas A&M University, December 2005.
  - [21] R. H. Park, "Two-reaction theory of synchronous machines: Generalized method of analysis - part i," *Transactions of the American Institute of Electrical Engineers*, vol. 48, pp. 716–727, Jul. 1929.
  - [22] O. Mohammed, S. Liu, and Z. Liu, "Physical modeling of PM synchronous motors for integrated coupling with machine drives," *IEEE Transactions on Magnetics*, vol. 41, pp. 1628–1631, May 2005.



- [23] K. Chang, T. Low, and T. Lee, "An optimal speed controller for permanent-magnet synchronous motor drives," *IEEE Transactions on Industrial Electronics*, vol. 41, pp. 503–510, Oct. 1994.
- [24] P. Perera, F. Blaabjerg, J. Pedersen, and P. Thogersen, "A sensorless, stable V/f control method for permanent-magnet synchronous motor drives," *IEEE Transactions on Industry Applications*, vol. 39, pp. 783–791, May/Jun. 2003.
- [25] P. C. Krause, O. Wasynczuk, and S. D. Sudhoff, *Analysis of Electric Machinery and Drive Systems*. Wiley-IEEE Press, 2002.
- [26] C.-M. Ong, *Dynamic Simulations of Electric Machinery: Using MATLAB/Simulink*. Prentice Hall, 1997.
- [27] J. Edwards, *Electrical machines: an introduction to principles and characteristics*. Aylesbury: International Textbook, 1973.
- [28] R. Krishnan, *Electric Motor Drives: Modeling, Analysis, and Control*. Prentice Hall, 2001.
- [29] A. E. Fitzgerald, C. Kingsley, and S. D. Umans., *Electric Machinery*. McGraw-Hill, 6 ed., 2003.
- [30] J. Chiasson, *Modeling and High-Performance Control of Electric Machines*. Wiley-IEEE Press, 2005.
- [31] H. de Kock, "Dynamic control of the permanent magnet assisted reluctance synchronous machine with constant current angle," Master's thesis, University of Stellenbosch, 2006.
- [32] N. P. Quang and J.-A. Dittrich, *Vector Control of Three-Phase AC Machines*. Springer, 2008.
- [33] M. J. Hoeijmakers, "A fundamental approach of the derivation of AC-machine equations by means of space vectors," in *AFRICON, 1996., IEEE AFRICON 4th*, vol. 1, pp. 178–183, 1996.
- [34] M. J. Hoeijmakers, *Modelvorming bij draaistroommachines*. Technische Universiteit Delft, November 1996.
- [35] A. J. Blauch, M. Bodson, and J. Chiasson, "High-speed parameter estimation of stepper motors," *IEEE Transactions on Control Systems Technology*, vol. 1, pp. 270–279, 1993.
- [36] R. J. Kerkman, D. Leggate, B. J. Seibel, and T. M. Rowan, "Operation of PWM voltage source-inverters in the overmodulation region," *IEEE Transactions on Industrial Electronics*, vol. 43, no. 1, pp. 132–141, 1996.
- [37] L. Ben-Brahim, "On the compensation of dead time and zero-current crossing for a PWM-inverter-controlled AC servo drive," *IEEE Transactions on Industrial Electronics*, vol. 51, no. 5, pp. 1113–1117, 2004.

- 
- [38] J.-W. Choi and S.-K. Sul, "Inverter output voltage synthesis using novel dead time compensation," *IEEE Transactions on Power Electronics*, vol. 11, no. 2, pp. 221–227, 1996.
- [39] Ben-Brahim, "The analysis and compensation of dead-time effects in three phase PWM inverters," in *IEEE Industrial Electronic Soc. Annu. Conf.*, pp. 792–797, 1998.
- [40] G. L. Wang, D. G. Xu, and Y. Yu, "A novel strategy of dead-time compensation for PWM voltage-source inverter," in *Twenty-Third Annual IEEE Applied Power Electronics Conference and Exposition, 2008. APEC 2008.*, pp. 1779–1783, Feb. 2008.
- [41] D. Leggate and R. J. Kerkman, "Pulse based dead time compensator for PWM voltage inverters," *IEEE Transactions on Industrial Electronics*, vol. 44, pp. 191–197, Apr. 1997.
- [42] R. Crowder, *Electric Drives and Electromechanical Systems: Applications and Control*. Newness, 2006.
- [43] B. K. Bose, *Power Electronics and Motor Drives: Advances and Trends*. Elsevier, 2006.
- [44] R. Colby and D. Novotny, "An efficiency-optimizing permanent-magnet synchronous motor drive," *IEEE Transactions on Industry Applications*, vol. 24, pp. 462–469, May/Jun. 1988.
- [45] J.-I. Itoh, N. Nomura, and H. Ohsawa, "A comparison between V/f control and position-sensorless vector control for the permanent magnet synchronous motor," in *Proceedings of the Power Conversion Conference (PCC Osaka 2002)*, vol. 3, pp. 1310–1315, 2002.
- [46] R. Ancuti and I. Boldea, "V/f control of PMSM super high speed drives with flux and power angle stabilizing loops," in *Proc. 10th Int. Conf. on Optimization of Electrical and Electronic Equipment (OPTIM)*, vol. 3, pp. 17–22, May 2006.
- [47] L. Zhao, C. Ham, Q. Han, T. Wu, L. Zheng, K. Sundaram, J. Kapat, and L. Chow, "Design of an optimal V/f control for a super high speed permanent magnet synchronous motor," in *30th Annual Conference of IEEE Industrial Electronics Society (IECON 2004)*, vol. 3, pp. 2260–2263, Nov. 2004.
- [48] C. Mademlis, J. Xypteras, and N. Margaris, "Loss minimization in surface permanent-magnet synchronous motor drives," *IEEE Transactions on Industrial Electronics*, vol. 47, pp. 115–122, Feb. 2000.
- [49] T. M. Rowan and R. J. Kerkman, "A new synchronous current regulator and an analysis of current-regulated PWM inverters," *IEEE Transactions on Industry Applications*, vol. 22, no. 4, pp. 678–690, 1986.
- [50] F. B. del Blanco, M. W. Degner, and R. D. Lorenz, "Dynamic analysis of current regulators for AC motors using complex vectors," *IEEE Transactions on Industry Applications*, vol. 35, no. 6, pp. 1424–1432, 1999.

- 
- [51] M. Bodson, J. Chiasson, R. Novotnak, and R. Rekowski, "High-performance nonlinear feedback control of a permanent magnet stepper motor," *IEEE Transactions on Control Systems Technology*, vol. 1, pp. 5–14, 1993.
  - [52] M. S. Sarma, *Electric Machines: Steady-State Theory and Dynamic Performance*. Thomson Learning, 2 ed., 1994.
  - [53] L. Xu and C. Wang, "Implementation and experimental investigation of sensorless control schemes for PMSM in super-high variable speed operation," in *The 1998 IEEE Industry Applications Conference, 1998. Thirty-Third IAS Annual Meeting*, vol. 1, pp. 483–489, Oct. 1998.
  - [54] A. Bunte and S. Beineke, "High-performance speed measurement by suppression of systematic resolver and encoder errors," *IEEE Transactions on Industrial Electronics*, vol. 51, pp. 49–53, Feb. 2004.
  - [55] T. Batzel and K. Lee, "Slotless permanent magnet synchronous motor operation without a high resolution rotor angle sensor," *IEEE Transaction on Energy Conversion*, vol. 15, pp. 366–371, Dec. 2000.
  - [56] P. Vas, M. Rashed, A. Joukhadar, and C. Ng, "Recent developments in sensorless and quasi-sensorless drive," *COMPEL: The International Journal for Computation and Mathematics in Electrical and Electronic Engineering*, vol. 21, no. 2, pp. 307–322, 2002.
  - [57] S. Bolognani, R. Oboe, and M. Zigliotto, "Sensorless full-digital PMSM drive with EKF estimation of speed and rotor position," *IEEE Transactions on Industrial Electronics*, vol. 46, pp. 184–191, Feb. 1999.
  - [58] J. Hu, L. Xu, and J. Liu, "Magnetic pole identification for PMSM at zero speed based on space vector PWM," in *CES/IEEE 5th International Power Electronics and Motion Control Conference (IPEMC 2006)*, vol. 1, pp. 1–5, August 2006.
  - [59] T. Batzel and K. Lee, "Starting method for sensorless operation of slotless permanent magnet synchronous machines," in *Power Engineering Society Summer Meeting, 1999. IEEE*, vol. 2, pp. 1243–1247, 1999.
  - [60] S. Ostlund and M. Brokemper, "Sensorless rotor-position detection from zero to rated speed for an integrated PM synchronous motor drive," *IEEE Transactions on Industry Applications*, vol. 32, pp. 1158–1165, Sep./Oct. 1996.
  - [61] S. Shinnaka, "New "D-State-Observer"-based vector control for sensorless drive of permanent-magnet synchronous motors," *IEEE Transactions on Industry Applications*, vol. 41, pp. 825–833, May/Jun. 2005.
  - [62] X. Yue, D. Vilathgamuwa, and K. Tseng, "Observer based robust adaptive control for PMSM with initial rotor position uncertainty," *IEEE Transactions on Industry Applications*, vol. 39, pp. 645–656, May/Jun. 2003.

- 
- [63] M. Tursini, F. Parasiliti, and D. Zhang, “Real-time gain tuning of PI controllers for high-performance PMSM drives,” *IEEE Transactions on Industry Applications*, vol. 38, pp. 1018–1026, Jul./Aug. 2002.
  - [64] J. Salomäki, *Sensorless Control of AC Drives equipped with an Inverter Output Filter*. PhD thesis, Helsinki University of Technology, 2007.
  - [65] S. Dan, F. Weizhong, and H. Yikang, “Study on the direct torque control of permanent magnet synchronous motor drives,” in *Proceedings of the Fifth International Conference on Electrical Machines and Systems, 2001. ICEMS 2001.*, vol. 1, pp. 571 – 574, 2001.
  - [66] M. Kadjoudj, S. Taibi, N. Golea, and H. Benbouzid, “Modified direct torque control of permanent magnet synchronous motor drives,” *International Journal of Sciences and Techniques of Automatic control & computer engineering*, vol. 1, no. 2, pp. 167–180, 2007.
  - [67] M. S. Merzoug and F. Naceri, “Comparison of field-oriented control and direct torque control for permanent magnet synchronous motor (PMSM),” *World Academy of Science, Engineering and Technology*, vol. 45, pp. 299–304, 2008.
  - [68] R. B. Sepe and J. H. Lang, “Implementation of discrete-time field-oriented current control,” *IEEE Transactions on Industry Applications*, vol. 30, no. 3, pp. 723–728, 1994.
  - [69] C. L. Phillips and H. T. Nagle, *Digital Control System Analysis and Design*. Prentice Hall, 3 ed., 1995.
  - [70] R. B. Ridley, *A New Small-Signal Model for Current-Mode Control*. PhD thesis, Virginia Polytechnic Institute and State University, 1990.
  - [71] T. E. Seiphethlho, “Power electronic activation for active magnetic bearings,” Master’s thesis, The School of Electrical, Electronic and Computer Engineering, North-West University, 2006.
  - [72] P. J. Roche, J. M. Murphy, and M. G. Egan, “Reduction of quantisation noise in position servosystems,” in *Proceedings of the 1992 International Conference on Industrial Electronics, Control, Instrumentation, and Automation, 1992.*, 1992.
  - [73] R. C. Dorf and R. H. Bishop, *Modern Control Systems*. Pearson Prentice Hall, 11 ed., 2008.
  - [74] K. J. Åström and R. M. Murray, *Feedback Systems: An Introduction for Scientists and Engineers*. Princeton University Press, 2010.
  - [75] Z. Mihailovic, “Modeling and control design of VSI-fed PMSM drive systems with active load,” Master’s thesis, Virginia Polytechnic Institute and State University, 1998.
  - [76] M. Norris, L. M. P. E. Alarcon, and D. Maksimovic, “Quantization noise shaping in digital PWM converters,” *IEEE Power Electronics Specialists Conference*, pp. 127–133, 2008.

- 
- [77] A. V. Peterchev and S. R. Sanders, "Quantization resolution and limit cycling in digitally controlled PWM converters," *IEEE Transactions on Power Electronics*, vol. 18, no. 1, pp. 301–308, 2003.
  - [78] A. Kelly and K. Rinne, "High resolution DPWM in a DC-DC converter application using digital Sigma-Delta techniques," in *IEEE Power Electronics Specialists Conference*, pp. 1458–1463, 2005.
  - [79] K. Berringer, J. Marvin, and P. Perruchoud, "Semiconductor power losses in AC inverters," in *IEEE-IAS Annu. Meeting*, vol. 1, pp. 882–888, 1995.
  - [80] M. H. Bierhoff and F. W. Fuchs, "Semiconductor losses in voltage source and current source IGBT converters based on analytical derivation," in *IEEE Power Electronics Specialists Conference*, vol. 4, pp. 2836–2842, 2004.
  - [81] N. Mohan, T. M. Undeland, and W. P. Robbins, *Power Electronics - Converters, Applications and Design*. John Wiley & Sons Inc, 2003.
  - [82] A. W. Kelley and W. F. Yadusky, "Rectifier design for minimum line-current harmonics and maximum power factor," in *Conference Proceedings of the Fourth Annual IEEE Applied Power Electronics Conference (APEC '89)*, pp. 13–22, 1989.
  - [83] B. W. Williams, *Power Electronics: Devices, Drivers, Applications, and Passive Components*. McGraw-Hill, 2008.
  - [84] "Power conversion and line filter applications, issue L," tech. rep., Micrometals<sup>®</sup>, February 2007.
  - [85] J. Kolar and S. Round, "Analytical calculation of the RMS current stress on the DC-link capacitor of voltage-PWM converter systems," in *IEE Proceedings of Electrical Power Applications*, vol. 153, Jul. 2006.
  - [86] "Databook 2011: AY- / AYU- HR Series aluminium electrolytic capacitors: High ripple current," tech. rep., Itecond<sup>®</sup>, 2011.
  - [87] "Semikron<sup>®</sup> application handbook," tech. rep., Semikron<sup>®</sup>, 2011.
  - [88] "SKHI61/71 SEMIDRIVER Datasheet," tech. rep., Semikron<sup>®</sup>, 2005.
  - [89] M. Ramezani and C. A. T. Salama, "A monolithic IGBT gate driver implemented in a conventional 0.8  $\mu\text{m}$  BiCMOS process," in *Proceedings of the 10th International Symposium on Power Semiconductor Devices and ICs. ISPSD 98.*, 1998.
  - [90] R. A. Serway and J. W. Jewett, *Physics for Scientists and Engineers with Modern Physics*. Brooks Cole, seventh ed., 2008.
  - [91] D. R. Kincaid and E. W. Cheney, *Numerical Mathematics and Computing*. Brooks Cole, 5th ed., 2004.



# Appendix A

## Parameter identification

### A.1 PMSM circuit parameters from terminal measurements

Tables A.1 and A.2, lists the line-line circuit parameter measurements made with an *RLC 300* measurement unit from digimess<sup>®</sup>. The measurements were done with an excitation frequency of 100 Hz, which is in the order of the rated frequency (500 Hz) . The measurements include the impedance of the cable connecting the inverter to the PMSMs.

Table A.1: Line-Line measurements for PMSM #A.

Line-line RLC measurement	Symbols	Values
Phase-a left open circuited	$[L_{bc}, R_{bc}]$	$[493 \mu\text{H}, 280 \text{ m}\Omega]$
Phase-b left open circuited	$[L_{ac}, R_{ac}]$	$[474 \mu\text{H}, 271 \text{ m}\Omega]$
Phase-c left open circuited	$[L_{ab}, R_{ab}]$	$[490 \mu\text{H}, 282 \text{ m}\Omega]$

Table A.2: Line-Line measurements for PMSM #B.

Line-line RLC measurement	Symbols	Values
Phase-a left open circuited	$[L_{bc}, R_{bc}]$	$[508 \mu\text{H}, 270 \text{ m}\Omega]$
Phase-b left open circuited	$[L_{ac}, R_{ac}]$	$[506 \mu\text{H}, 273 \text{ m}\Omega]$
Phase-c left open circuited	$[L_{ab}, R_{ab}]$	$[500 \mu\text{H}, 266 \text{ m}\Omega]$

Note the difference in impedance balance between PMSM #A and PMSM #B, due to a difference between the winding procedures for the two PMSMs. For PMSM #A, the windings of each phase was wound simultaneously, whilst for PMSM #B, the windings of all three phases were wound successively.

The calculation of the dq PMSM parameters are done as outlined in section 2.2.3.1. The average of the phase line-line impedances are used in the following calculations. For PMSM #A the

magnetizing inductance is:

$$\begin{aligned} L_{m0} &= \frac{1}{3} \times \left( \frac{493 + 474 + 490}{3} \right) \times 10^{-6} \text{ H} \\ &= 161.9 \mu\text{H} \end{aligned}$$

From equation 2.16, the d-axis inductance is:

$$\begin{aligned} L_d &= \frac{3}{2} (L_{m0} + L_{mp}) + L_l \\ &= \frac{3}{2} (161.9) \\ &= 242.8 \mu\text{H} \end{aligned}$$

where the inductance due to saliency has been assumed negligible, since it is a surface mount PMSM and the leakage inductance is included with the mean magnetizing inductance,  $L_{m0}$ . The phase resistance is calculated as:

$$\begin{aligned} r_s &= \frac{1}{2} \times \left( \frac{280 + 271 + 282}{3} \right) \times 10^{-3} \Omega \\ &= 138 \text{ m}\Omega \end{aligned}$$

For PMSM #B, the parameter calculation results are:

$$\begin{aligned} L_d &= 252.3 \mu\text{H} \\ r_s &= 138 \text{ m}\Omega \end{aligned}$$

The cable connecting the inverter to the PMSM is about 10 m in length, of which the phase resistance has been measured as 68 m $\Omega$ . This is subtracted from the phase resistance when the copper losses in the PMSM itself are calculated.

## A.2 PMSM mechanical parameters from calculation

From the mechanical design, the rotor's moment of inertia can be calculated using the equation for the moment of inertia of a hollow cylinder [90]:

$$J = \frac{1}{2} M (r_2^2 + r_1^2)$$

where  $M$  is the mass,  $r_2$  is the outer radius and  $r_1$  is the inner radius of the cylinder. For solid sections the inner radius equals zero. Since the geometry and materials are not uniform, the calculation is done over sections of the rotor which are uniform. The inertia of the subsections is then added to obtain the total inertia. The rotor is subdivided into different sections using figure [7]. The partitioning of the rotor and the calculation for the moment of inertia is done in a



Matlab<sup>®</sup> file in appendix C.2. The moment of inertia is calculated as:  $J = 0.665 \times 10^{-3} \text{ kg.m}^2$ .

The calculation of the viscous friction loss coefficient,  $B$ , is dependent on many varying parameters. To illustrate the elusiveness and complexity of this parameter, one should merely note that not even an approximation attempt is given in the manufacturer's data sheet. The calculation of the viscous friction loss is an advanced topic, best left for mechanical engineers and is thus beyond the scope of this dissertation.

### A.3 Least squares parameter identification of the PMSM

The least squares parameter identification theory is discussed in section A.3. The Matlab<sup>®</sup> file which performs the parameter identification is dependent on many helper functions. The parameter identification, helper functions and sampled data on which the calculation is performed, are included in appendix C.3. For the least squares parameter identification to function correctly, two important issues need to be addressed:

- non-causal filtering of the measured data,
- and adequate signal excitation.

Filtering of the signals is important, since the switch mode power amplifier causes a lower signal to noise ratio of the sampled signals. By rejecting out of band noise the signal to noise ratio is enhanced. The filtering has to be non-causal, because that is the only way a phase shift due to the filtering can be undone. It is achieved by taking the average of a filtered signal and a filtered version of the signal whose time axis has been inverted, i.e.:

$$y_{non-causal}(t) = \frac{f(x(t)) + f(x(-t))(t)}{2}$$

where the function  $f$  denotes the low pass filtering operation. Hence  $f(x(-t))$  denotes the filtering of the “swapped” signal and  $f(x(-t))(t)$  denotes that the filtered signal has been “swapped” back so as to be a function of causal time. The filtered signal  $f(x(t))$  has a negative delay, which cancels with the positive delay of  $f(x(-t))(t)$ , resulting in no phase shift.

In order for the numeric differentiation not to cause a phase shift in the signals, the forward and backward difference equations are combined [91]:

$$\frac{dy}{dt} \approx \frac{2}{3h} (y(t+h) - y(t-h)) - \frac{1}{12h} (y(t+2h) - y(t-2h))$$

Note that the numeric derivative is only valid for:  $2h \leq t \leq t_{max} - 2h$ .

Adequate signal excitation is an issue, because the PMSM has low inertia which causes the motor to accelerate with little applied torque. This makes the estimation of the mechanical parameters,  $J$  and  $B$ , difficult. The problem is addressed by requiring that the PMSM have

very high acceleration, which in turn requires rapid control of the torque producing current, thus vector control is required.

The acceleration requirement appears to be problem, because the original purpose of the parameter identification was to obtain usable parameters with which the high performance control could be designed. Firstly, this problem is solved by using approximate values of the required parameters. Secondly, the problem is not as severe as it may seem, because vector control with a position sensor is robust against uncertain parameters. Accurate parameter knowledge is more important in the open loop V/f and sensorless vector control. Thus, using vector control, reasonably accurate parameters are estimated, with which the V/f control is designed.

Figure A.1 shows the torque producing current and motor speed response for the least squares parameter identification. The data corresponding to the time range [0.1 s, 2 s] is used. During system development the PMSM was sourced with a current limited DC voltage source. In order not to use the voltage source in a saturated region, the torque producing current was limited to 10 A, thus the acceleration could have been higher, e.g.  $i_q = 30$  A could easily have been obtained with the intended three-phase voltage source. The artefact at the beginning of the rotational speed is due to the numeric differentiation, for which  $h = 25$  ms was used. Note that the PMSM speed ramp started with the rotor already turning at 500 rpm.

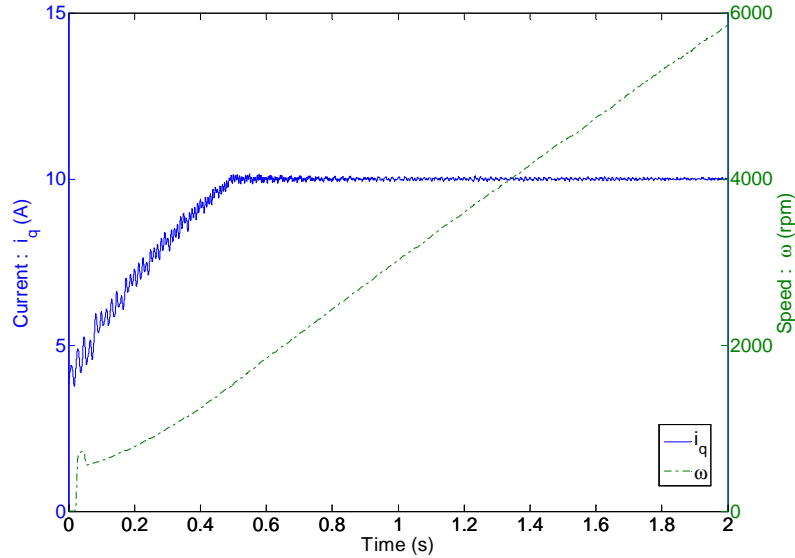


Figure A.1: PMSM excitation for least squares parameter identification.

The values determined by the least squares parameter identification is presented in table 3.1. Note that even with the care taken to improve the parameter excitation of the mechanical parameters, the uncertainty in the mechanical parameters are still much greater than for the electrical parameters. Also note the considerable difference between the inductance determined from terminal measurements and that obtained via the least squares parameter identification. Both measurements are correct for the excitation used. The inductance, from terminal measu-

rements, was excited with a small current, hence the stator back iron is operating in the initial permeability region, which has lower permeability. The resistance for the least squares identification is higher than that which has been determined by terminal measurement. Again, this is explained by nothing that the resistance is dependent on the winding temperature, which in turn is dependent on the copper loss. The least squares parameter identification excitation current was greater, therefore greater copper loss. The increase in winding resistance as a function of excitation current magnitude was not as great a for the phase inductance.

Hence, the electrical parameters as determined by the least squares method are more applicable to the PMSM operating conditions. For the mechanical parameters, the calculated rotor inertia is more accurate, whilst the viscous and coulomb friction forces could only be obtained by the least squares method.



## Appendix B

# Detail mechanical drawings

The detail assembly drawings, from the mechanical design by C.J.G. Ranft [7], are shown in figures B.1 and B.2.

### B.1 Detail rotor assembly

### B.2 Detail stator assembly

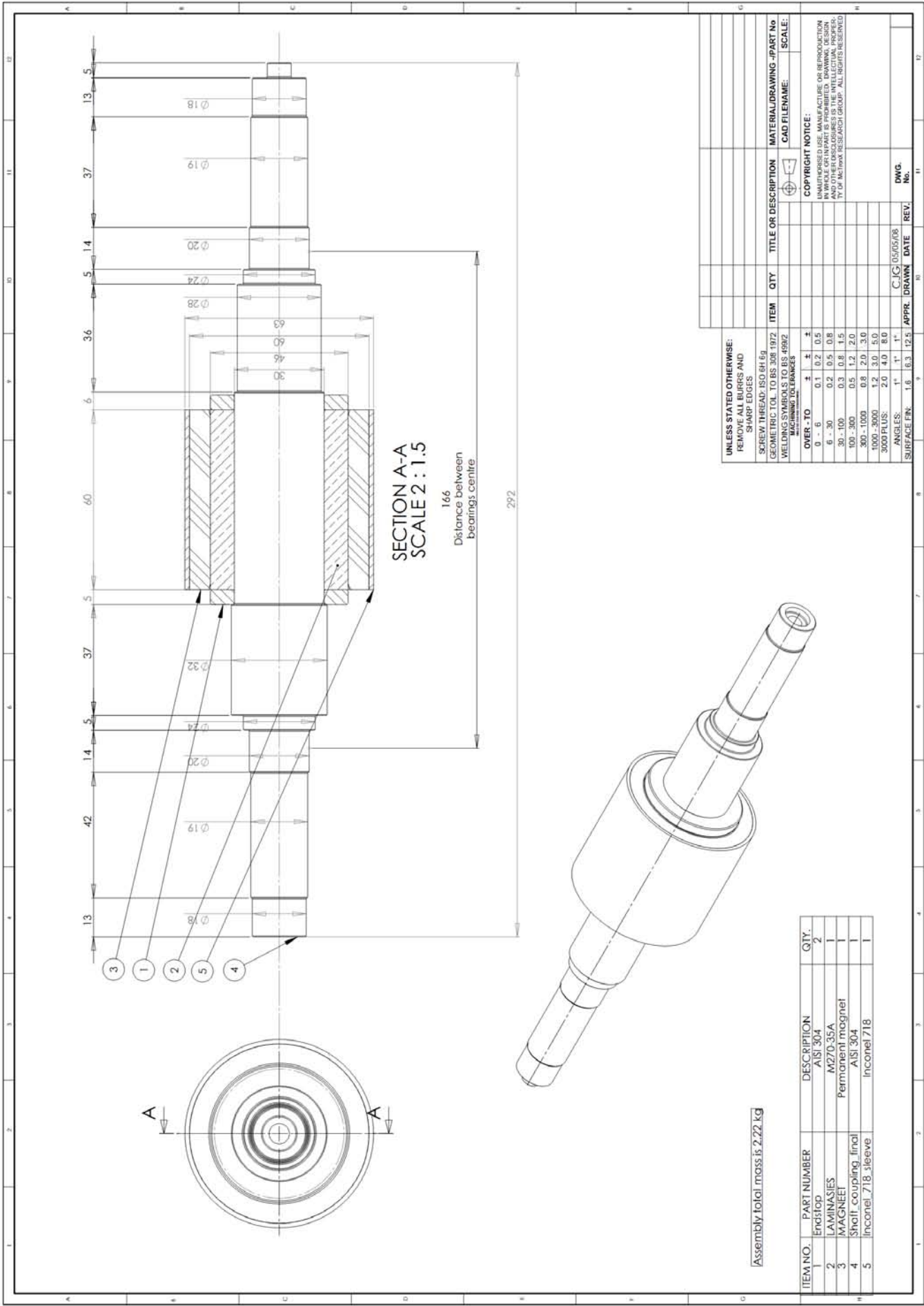


Figure B.1: Detail rotor assembly [7].

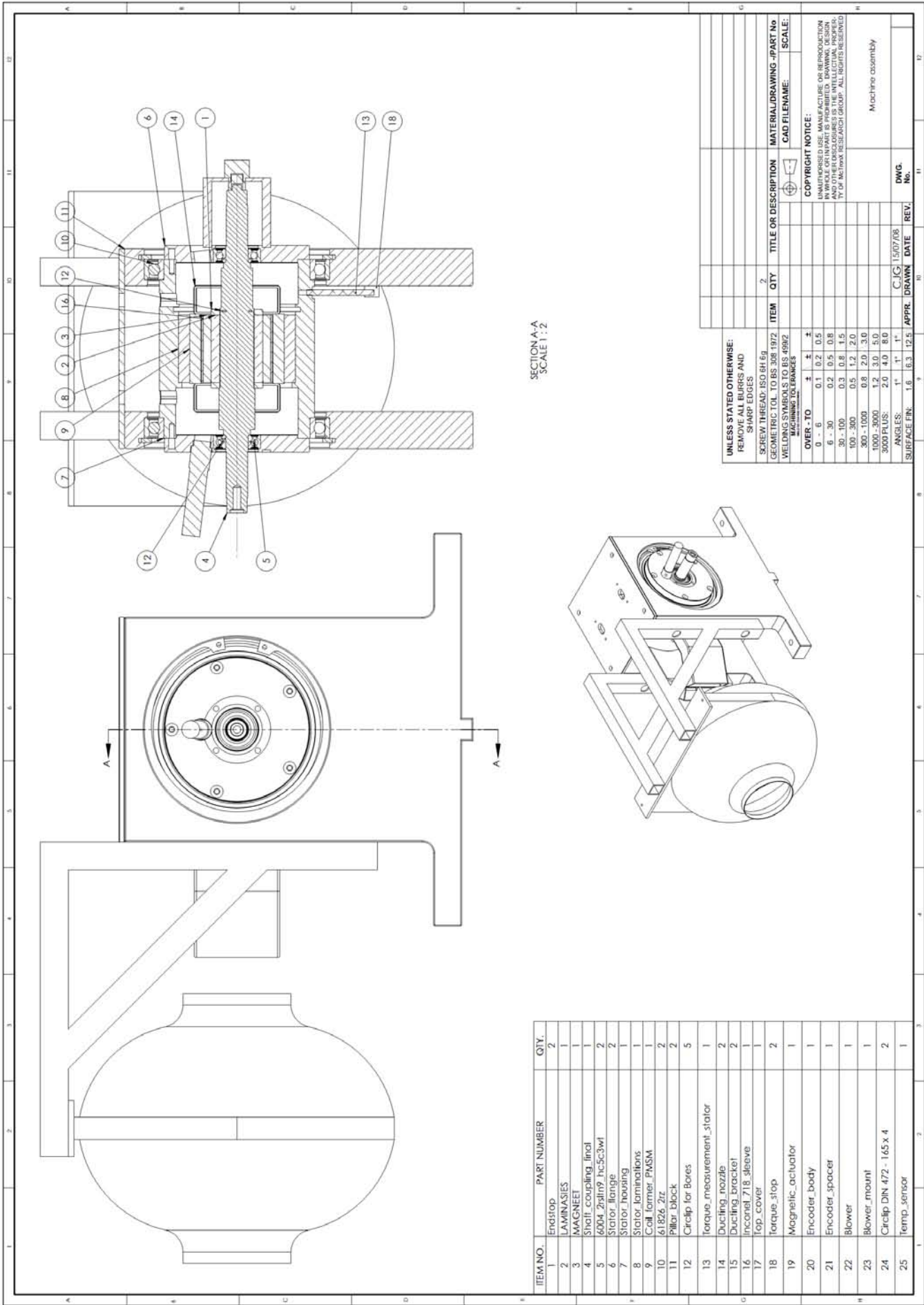


Figure B.2: Detail machine assembly [7].





# Appendix C

## Files on CD

- [C.1] Simplifications of the dq0 transformation  
Path: *CD Root:|dq0 Transformation|Symbolic\_dq\_transformation.wxm*
- [C.2] Moment of inertia calculation  
Path: *CD Root:|Parameter Identification|Moment of Inertia Calculation.m*
- [C.3] Least squares parameter identification  
Path: *CD Root:|Parameter Identification|Least Squares|LS\_Param\_Ident.m*
- [C.4] Current control design  
Path: *CD Root:|Vector Control|Current\_Control\_Design.m*
- [C.5] Current control simulation  
Path: *CD Root:|Vector Control|Vector\_Current\_Control\_Design.mdl*
- [C.6] Speed from position via numerical differentiation  
Path: *CD Root|Position to speed|Backward\_difference.mdl*
- [C.7] Speed from position via speed observer  
(a) Path: *CD Root|Position to speed|Speed\_observer\_design.m*  
(b) Path: *CD Root|Position to speed|Speed\_observer.mdl*
- [C.8] Speed from position via modified speed observer  
(a) Path: *CD Root|Position to speed|Speed\_observer\_design\_mod.m*  
(b) Path: *CD Root|Position to speed|Speed\_observer\_mod.mdl*  
(c) Path: *CD Root|Position to speed|Speed\_observer\_ident.m*
- [C.9] Speed control design  
Path: *CD Root:|Vector Control|Speed\_Control\_Design.m*

- [C.10] Speed control simulation  
Path: *CD Root: \Vector Control\Vector\_Speed\_Control\_Design.mdl*
- [C.11] PMSM model linearization  
Path: *CD Root: \V\_f Control\Linearized\_DQ\_PMSM\_w\_high\_eff\_equilibrium.wxm*
- [C.12] V/f control root locus without stabilization feedback  
Path: *CD Root: \V\_f Control\PMSM\_root\_loci\_wo\_FB.m*
- [C.13] V/f control root locus with stabilization feedback  
Path: *CD Root: \V\_f Control\PMSM\_root\_loci\_w\_FB.m*
- [C.14] V/f control simulation  
Path: *CD Root: \V\_f Control\V\_f\_Control\_Design.mdl*
- [C.15] DC bus disturbance rejection
- (a) Rectifier simulation model verification  
Path: *CD Root: \Inverter non-ideality\DC\_bus\_ripple\_ver.mdl*
  - (b) Vector control with DC bus disturbance rejection  
Path: *CD Root: \Inverter non-ideality\Vector\_Control\_w\_Vdc\_dist.mdl*
  - (c) V/f control with DC bus disturbance rejection  
Path: *CD Root: \Inverter non-ideality\V\_f\_Control\_w\_Vdc\_dist.mdl*
- [C.16] Dead-time compensation
- (a) Dead-time average value model verification  
Path: *CD Root: \Inverter non-ideality\Dead\_time\_average\_value\_ver.mdl*
  - (b) Vector control with dead-time compensation  
Path: *CD Root: \Inverter non-ideality\Vector\_Control\_w\_DTC.mdl*
  - (c) V/f control with dead-time compensation  
Path: *CD Root: \Inverter non-ideality\V\_f\_Control\_w\_DTC.mdl*
- [C.17] Quantization noise suppression
- (a) Vector control with quantization noise suppression  
Path: *CD Root: \Inverter non-ideality\Vector\_Control\_w\_quant\_sup.mdl*
  - (b) V/f control with quantization noise suppression  
Path: *CD Root: \Inverter non-ideality\V\_f\_Control\_w\_quant\_sup.mdl*
- [C.18] Inverter thermal verification
- (a) Calculation of inverter losses and device junction temperatures  
Path: *CD Root: \Inverter thermal verification\Thermal\_ver.m*

- (b) Device V-I characteristic linearization and module thermal impedance parameters  
Path: *CD Root: \Inverter thermal verification \SKM50GB063D.pdf*
- (c) Heatsink thermal impedance parameters  
Path: *CD Root: \Inverter thermal verification \P\_3\_PS503012.pdf*

[C.19] Rectifier design

- (a) Filter inductor, DC bus capacitor and diode bridge calculations  
Path: *CD Root: \Rectifier Design \Rectifier Design.m*
- (b) Rectifier with LC filter simulation  
Path: *CD Root: \Rectifier Design \Three\_Phase\_Rectifier\_LC.asc*

[C.20] Driver board overcurrent detection calculations

Path: *CD\_Root \Inverter current limit \DriverBoard\_protection.m*

[C.21] Sensor and interface board schematics

Path: *CD\_Root \Sensor and Interface Board \*

[C.22] SSI to RS485 conversion circuit schematic and source code

Path: *CD\_Root \Angular magnetic encoder \*

[C.23] Synchronized downsampling source code

Path: *CD\_Root \Synchronized downsampler \*

[C.24] Photos showing EMI reduction measures

Path: *CD\_Root \EMI photos \*

[C.25] dSPACE<sup>®</sup> control models and ControlDesk<sup>®</sup> user interface project files of the V/f and vector controllers

Path: *CD\_Root \dSPACE controller source code files \*